UNIVERSITY COLLEGE LONDON

New frequency reconfigurable antennas for wide frequency range tuning

by

Cristina Borda Fortuny

A thesis submitted for the degree of
Doctor of Philosophy
in the
Faculty of Engineering Science
University College London

Supervised by Dr Kenneth Tong and Dr Kevin Chetty

March 2017

Declaration of Authorship

I, Cristina Borda Fortuny, declare that this thesis titled, 'New frequency reconfigurable antennas for wide frequency range tuning' and the work presented in it are my own original work and that all source material used has been clearly identified and acknowledged. No part of this dissertation contains material previously submitted to the examiners of this or any other university, or any material previously submitted for any other examination.

Signed: _____

Date: _____

"All truths are easy to understand once they are discovered;
the point is to discover them"

- Galileo Galilei

UNIVERSITY COLLEGE LONDON

Abstract

by Cristina Borda Fortuny

Frequency reconfigurable antennas are becoming a compelling solution for the increasing demand of higher antenna capabilities, since they can operate at tunable narrow frequency bands while rejecting the undesirable signals from other bands. The aim of this project is to develop new designs for frequency reconfigurable antennas that can work across a wide frequency range (from 1 GHz up to 6 GHz) while maintaining stable radiation pattern and polarisation as required by the industry sponsors. A Vivaldi antenna is considered as the basis for a frequency reconfigurable design as it maintains the radiation characteristics in its operating band. Dual-band, tri-band and quad-band switched reconfigurable designs are proposed and analysed. These antennas are electronically-tuned using RF switches which adjust the impedance to reconfigure the operating band of the antenna. A prototype is tested in an anechoic chamber obtaining good performance. However, as the switches lead to several challenges, such as the effect of bias lines and the excessive insertion losses, a new approach is taken. State-of-the-art technologies are studied and fluid antennas are introduced. Current developments show that liquid antennas can have radiation efficiencies up to 90 % and conductivities close to copper, which makes them a good candidate to fulfil the requirements of this project. A hybrid Vivaldi antenna with an ionised water switch is proposed and a prototype tested. By introducing ionised water into a specific point of the feed line the operating frequency of the antenna is adjusted. The replacement of RF switches for electronically-controlled fluids brings high flexibility, suppression of the bias lines impact, dynamic adjustment and continuous frequency tuning compared to conventional antenna systems.

Acknowledgements

I would like to express my sincere gratitude to my first supervisor Dr Kenneth Tong and my second supervisor Dr Kevin Chetty for their constant support, guidance and motivation.

I cannot forget the valuable help and motivations of the Radar Group colleagues and the professors in the Friday seminars and coffee breaks.

Thanks to the funding bodies of this research project: EPSRC UK and L-3 TRL Technology.

I am very grateful for the support and good times given by my family and friends even from far away. Particularly to Jordi, Anna, Sandra and Jianling. To Paula, a good friend who never stops amazing me. And to Joan, my mentor, who convincingly conveyed a spirit of adventure in regard to research.

Finally, a special thanks to Xavi for his love, encouragement and support that were essential to carry out this thesis.

List of publications

A list of relevant publications that were produced by the work described in this thesis is presented here:

(1) **C. Borda Fortuny**, K. F. Tong, K. Chetty, D. M. Benton, "High-gain frequency reconfigurable Vivaldi antenna", *IEEE International Symposium on Antennas and Propagation 2014, Memphis (USA)*

(2) **C. Borda Fortuny**, K. F. Tong, K. Chetty, P. Brittan, "High-gain triple-band reconfigurable Vivaldi antenna", *IEEE-APS Topical Conference on Antennas and Propagation in Wireless Communications 2014, Aruba*

(3) A. Amiri, **C. Borda Fortuny**, K. F. Tong, "Reconfigurable antennas for very wide spectrum monitoring", *2014 IEEE International Workshop on Electromagnetics, Sapporo (Japan)*

(4) **C. Borda Fortuny**, A. Amiri, K. F. Tong, "Development of reconfigurable multiple wideband antenna for radar and monitoring applications", *The 9th European Conference on Antennas and Propagation, EuCAP 2015, Lisbon (Portugal)*

(5) K. F. Tong, **C. Borda Fortuny**, J.Bai, "Low cost 3D-printed monopole fluid antenna", *International Symposium on Antennas and Propagation, ISAP 2015, Hobart (Australia)*

(6) H. Li, **C. Borda Fortuny**, K. F. Tong, K. K. Wong, "Coupling-fed frequency agile monopole fluid antenna", *2016 IEEE International Conference on Antenna Measurements & Applications Focus on Antenna Systems, Syracuse (USA)*

(7) **C. Borda Fortuny**, K. F. Tong, K. Chetty, K. K. Wong, "Comparison between a Novel Liquid Switch and a GaAs MMIC Switch for Reconfiguring the Operating Frequency of a Vivaldi Antenna", *2017 IEEE International Workshop on Electromagnetics, London (UK)*

(8) **C. Borda Fortuny**, K. F. Tong, K. Chetty, "A low-cost mechanism to reconfigure the operating frequency band of a Vivaldi antenna for cognitive radio and spectrum monitoring applications", IEEE Transactions on Antennas and Propagation, *(Submitted on 13th March 2017)*

(9) **C. Borda Fortuny**, K. F. Tong, K. Chetty, "A novel liquid-switched to reconfigure the operating frequency of a Vivaldi antenna", IEEE Antennas and Wireless Propagation Letters, *(In preparation)*

(10) **C. Borda Fortuny**, H. Li, K. F. Tong, K. K. Wong, "A low-cost fluid monopole antenna for continuous frequency tuning", IEEE Antennas and Wireless Propagation Letters, *(In preparation)*

Contents

List of Figures

List of Tables

Abbreviations

AC	**A**lternating **C**urrent
AUT	**A**ntenna **U**nder **T**est
BW	**B**and**w**idth
CCW	**C**ounter**c**lock**w**ise
CPW	**C**o**p**lanar **W**aveguide
CST	**C**omputer **S**imulation **T**echnology
CW	**C**lock**w**ise
dB	**d**ecibels
DC	**D**irect **C**urrent
DIY	**D**o **I**t **Y**ourself
DPCA	**D**isplaced **P**hase **C**entre **A**ntenna
DRA	**D**ielectric **R**esonator **A**ntenna
E-field	**E**lectric field
E-plane	**E**lectric plane radiaton pattern
EGaIn	**E**utectic **Ga**llium **In**dium
EM	**E**lectro**m**agnetic
ESD	**E**lectros**t**atic **D**ischarge
FET	**F**ield-**E**ffect **T**ransistor

FIT	**F**inite **I**ntegration **T**echnique
FNBW	**F**irst-**N**ull **B**eam**w**idth
GaAs	**Ga**llium **A**rsenide
GMT	**G**round **M**oving **T**arget
GPS	**G**lobal **P**ositioning **S**ystem
GSM	**G**lobal **S**ystem for **M**obile communications
HF	**H**igh **F**requency
H-field	Magnetic field
H-plane	Magnetic plane radiation pattern
HPBW	**H**alf-**P**ower **B**eam**w**idth
IED	**I**mprovised **E**xplosive **D**evice
IFA	**I**nverted **F** **A**ntenna
KCl	Potassium chloride
LC	**L**iquid **C**rystal
LHCP	**L**eft **H**and **C**ircular **P**olarisation
LED	**L**ight **E**mitting **D**iode
LTCC	**L**ow **T**emperature **C**o-Fired **C**eramic
LTE	**L**ong **T**erm **E**volution
MGE	**M**axwell's **G**rid **E**quations
MIMO	**M**ultiple-**I**nput **M**ultiple-**O**utput
MMIC	**M**onolithic **M**icrowave **I**ntegrated **C**ircuit
NaCl	Sodium chloride
OSM	**O**pen-**S**hort-**M**atch calibration
PCB	**P**rinted **C**ircuit **B**oard

PDMS	**P**oly**dim**ethyl**s**iloxane
RCS	**R**adar **C**ross **S**ection
RF	**R**adio **F**requency
RF-MEMS	**R**adio **F**requency **M**icro-**E**lectro-**M**echanical-**S**ystems
RHCP	**R**ight **H**and **C**ircular **P**olarisation
RL	**R**eturn **L**oss
SLA	**S**tereolithography
SMA	**S**ub**M**iniature version **A**
SMT	**S**urface **M**ount **T**echnology
SNR	**S**ignal-to-**N**oise **R**atio
SOT	**S**mall-**O**utline **T**ransistor
SPST	**S**ingle-**P**ole **S**ingle-**T**hrow
SRR	**S**plit **R**ing **R**esonator
TSA	**T**apered **S**lot **A**ntenna
UAV	**U**nmanned **A**erial **V**ehicle
UAS	**U**nmanned **A**erial **S**ystem
UHF	**U**ltra **H**igh **F**requency
UMTS	**U**niversal **M**obile **T**elecommunications **S**ystem
UWB	**U**ltra-**W**ide**b**and
VHF	**V**ery **H**igh **F**requency
VNA	**V**ector **N**etwork **A**nalyser
VSWR	**V**oltage **S**tanding **W**ave **R**atio
WLAN	**W**ireless **L**ocal **A**rea **N**etwork
3D	3-**D**imensional

Symbols

a_1	incident power in port 1	W
a_2	reflected power in port 2	W
b_1	reflected power in port 1	W
b_2	incident power in port 2	W
$\vec{B}$	magnetic flux density	$\mathrm{Wb/m^2}$
c	speed of light	m/s
C	capacitance	F
D	directivity	dBi
D_{dim}	major dimension of an antenna	m
$\vec{D}$	electric flux density	$\mathrm{C/m^2}$
f	frequency	Hz
F	noise figure	dB
f_{high}	upper frequency	Hz
f_{low}	lower frequency	Hz
f_c	centre frequency	Hz
G	antenna gain	dBi
G_{AUT}	gain of the AUT	dBi
G_R	realised gain	dBi

G_{ref}	gain of the reference antenna	dBi
G_{source}	gain of the source antenna	dBi
I	radiation intensity	W/unit solid angle
$\vec{J}$	electric current density	A/m^2
k	wave phase constant	m
L	loss	dB
$L_{antenna}$	antenna length	m
L_{cut}	cut length	m
L_{flare}	flare length	m
L_{slot}	slot length	m
L_{stub}	stub length	m
M_1	impedance mismatch 1	1
M_2	impedance mismatch 2	1
P	power	W (J/s)
P_A	supplied power	W (J/s)
P_{in}	incident power	W (J/s)
P_M	power matched to a transmission line	W (J/s)
P_o	power accepted by an antenna	W (J/s)
P_{out1}	received power of experiment 1	dB
P_{out2}	received power of experiment 2	dB
P_{ref}	reflected power	W (J/s)
P_r	radiated power	W (J/s)
Pos_{stub}	stub position	m
Pos_{switch}	RF-switch position	m

Q	quality factor	1
r	sphere radius	m
R	distance to antenna center	m
R_r	radiation resistance	Ω
RL	return loss	dB
R_L	conduction-dielectric loss	Ω
S_{11}	Reflection coefficient at port 1	dB
S_{12}	Transmission coefficient from ports 2 to 1	dB
S_{21}	Transmission coefficient from ports 1 to 2	dB
S_{22}	Reflection coefficient at port 2	dB
t	time	s
V_i	incident wave	V
V_{max}	max value of standing wave	V
V_{min}	min value of standing wave	V
V_r	reflected wave	V
$W_{antenna}$	antenna width	m
W_{cut}	cut width	m
W_{HB}	aperture's narrow part width	m
W_{LB}	aperture's wide part width	m
W_{slot}	slot width	m
W_{stub}	stub width	m
Z_A	antenna impedance	Ω
Z_L	load impedance	Ω
Z_0	characteristic impedance	Ω

Γ	reflection coefficient	1
tanδ	loss tangent	rad
δ_s	skin depth	m
ε_{eff}	effective permittivity	F/m
$\varepsilon_r^{'}$	real part of relative permittivity	1
$\varepsilon_r^{''}$	imaginary part of relative permittivity	1
ε_r	relative permittivity	1
ε_0	free-space permittivity	F/m
η_0	total efficiency	1
η_r	reflection efficiency	1
η_{cd}	conduction & dielectric efficiency	1
θ	elevation angle	rad
λ	wavelength	m
λ_g	guided wavelength	m
λ_0	free-space wavelength	m
μ_r	relative permeability	1
μ_0	free-space permeability	N/A^2
ρ	resistivity of a medium	Ω·m
σ	conductivity of a medium	S/m
tanδ	loss tangent	1
υ_p	phase velocity	m/s
φ	azimuth angle	rad
χ_c	capacitive reactance	Ω

ω	angular frequency	rad/s
$\wp$	power density	W/m^2
$\wp_i$	power density of the isotropic antenna	W/m^2

For Xavi

Chapter 1

Introduction

Nowadays, electronic devices use several wireless standards to communicate: GSM, UMTS, GPS, Wi-Fi, LTE, etc. Each of these technologies operates at a specific frequency band, for example GSM-850 operates between 824 MHz and 849 MHz, while LTE in Europe operates at the bands of 700 MHz, 800 MHz, 900 MHz, 1800 MHz and 2600 MHz [1]. This means, devices need a narrowband antenna which can operate at each particular band or a system that can switch bands. For these applications one could cascade an ultra-wideband antenna with filters in the receiver, but this would increase size, cost, power consumption and insertion loss while diminishing flexibility in the design. On the other hand, narrowband frequency reconfigurable antennas are a feasible solution since they can operate in one frequency band with the necessary rejection of out-of-band signals, thereby relaxing the requirements of the receiving system and increasing signal-to-noise ratio (SNR) [2]. Multiband antennas supporting different frequency bands may not be a suitable solution in terms of high SNR and efficiency [3].

In security applications a narrowband antenna is even more critical because jamming signals can saturate the receiver in wideband systems, which may result in no communication at all. Furthermore, highly directive antennas can be used to maximise power transfer and reduce signal from unwanted directions for remote sensing. Additionally, stealth is a vital property in military camouflaged applications. Hence a reconfigurable antenna that can beam-form its radiation pattern to remain unnoticed or even suppress its RCS signature is a desirable configuration.

Moreover, with the arrival of affordable unmanned aerial vehicle (UAV) technology, rogue drones are a growing problem. UAV enable crimes to be committed without the presence of the perpetrator. Crimes such as drug smuggling, attempted assassinations or even simple interference in a controlled airspace have already been attempted. On

FIGURE 1.1: DroneGun as a countermeasure against some rogue drones [4].

the other hand, UAV can also operate as wireless communications aid systems to increase coverage as explained in [5], which would be essential in emergency situations for example. Rogue drones can interfere with such a system. Thus, the authorities are already looking into anti-UAV systems to disable any unauthorised drone using trained eagles, drone-killing drones or even a "DroneGun" that jams the drone's communications forcing it to land (see Figure 1.1). This jamming system is the safest as it can force the drone to land without disabling it while flying in the sky. Most commercial drones are controlled at the 2.4 GHz and the 5.8 GHz bands with frequency hopping or spread spectrum [6]. Although there are some DIY drones as shown in Figure 1.2 that operate at other amateur radio or unlicensed spectrum bands such at 430 MHz, 900 MHz or 1.2 GHz [7]. In order to jam drone signals the spectrum needs to be monitored to make a decision to jam only the actual operating band. Frequency reconfigurable antennas are an ideal candidate for these applications as they can operate at a selected band without affecting other bands providing high gain and high-power handling.

FIGURE 1.2: 3D-printed UAV (from University of Southampton) [8].

In addition, new technologies make it possible for antennas to meet higher demands. For example, novel materials like Galinstan, which is considered a new class of liquid metal to replace the toxic mercury [9], enable stretchable electronics that can target applications, such as biomedical devices in direct contact with the human body, that were not possible with solid antennas [10, 11].

1.1 Aim and objectives

As the growth of wireless communications demands higher antenna capabilities, the requirements given by the industry sponsors for the antenna designs in this project are:

- frequency tuning
- low cost
- low power consumption
- portability
- high gain
- wideband operation
- stable radiation patterns
- minimum isolation of 14 dB between bands

A good isolation between bands is taken to be a minimum of -14 dB because it represents a power ratio of 25 between the gain for in-band and out-band operation.

Therefore, the aim of this research project is to develop a new design of reconfigurable antenna that can operate across a wide frequency range while maintaining its radiation characteristics, such as radiation pattern and polarisation, and fulfilling the industrial requirements. The industrial sponsors demand a reconfigurable antenna for security spectrum monitoring and cognitive radio applications.

On one hand, high gain is required to recognise attenuated communications of interest, while on the other hand a stable radiation pattern across a wide frequency range is essential because the antenna is required to be pointing to a specific direction across frequency in spectrum surveillance. If an antenna changes the direction of the main lobe in its operating band, the antenna needs to be realigned depending on the operating

frequency and this is not a desirable feature. In cognitive radio an antenna is required to be dynamically adaptive and provide high isolation between frequency bands with high directivity for the desirable direction. A reconfigurable antenna with these characteristics would improve successful operations by speeding up the surveillance process and making it more reliable because of the higher SNR while maximising efficiency.

Therefore, a wideband antenna is taken as the basis for the proposed reconfigurable antenna as it will maintain the radiation characteristics in its whole band. Because part of the project requirements are wide frequency range and reconfigurable band rejection, a Vivaldi antenna is a good candidate for this research project. The Vivaldi antenna satisfies these requirements and presents high gain and efficiency [12]. These will be evaluated at a later stage. Therefore, this research project will study different methods to dynamically tune the Vivaldi antenna to achieve several highly-isolated bands.

First, RF switches are considered. However, when RF switches are introduced to reconfigure an antenna, several challenges arise. RF switches cause excessive insertion losses, add an extra cost to the system, are not easily integrated in a design and require bias lines which affect the antenna performance. Therefore, in the second part of this research project, a new approach is taken by introducing a liquid-switch into the Vivaldi reconfigurable design.

Liquid antennas are studied as a starting point to determine the feasibility of using ionised solutions as radiators. Then, an ionised solution reconfigurable monopole is proposed and its performance analysed. As satisfactory results are achieved, a novel concept is proposed: "antennas-on-demand". Antennas-on-demand can be made available or non-radiating to eliminate detection and interferences when necessary. This is advantageous for security applications where stealth capabilities are crucial.

Since ionised solutions achieve good performance capabilities as antennas and these solutions have conductive capabilities, a liquid-switch is proposed using an ionised solution as electrical contact. A liquid switch will provide a low-cost dynamic mechanism to the Vivaldi reconfigurable antenna eliminating any bias lines effect on the antenna performance. This liquid switch can be adapted to other antenna designs as it uses a 3D-printed container that can be customised to fit a required shape.

1.2 Scope

This thesis covers the antenna design in terms of operation frequency, polarisation, impedance, gain and far-field radiation pattern at the frequencies of interest. Operating

frequencies are within the microwave spectrum between 1 GHz and 6 GHz. The antennas need to be designed so that they can be fabricated at the departmental workshop. Out sourcing the design would be a possibility but for a fast and less expensive prototyping the departmental workshop is selected. Therefore, a planar design on a high performance substrate with a maximum size of an A4 satisfies the requirement. The substrate needs to be low loss as the outcome requires high gain, so FR-4 substrate is undesirable. Low-cost materials are required. A wideband antenna is chosen as the basis of the reconfigurable design to provide consistent characteristics in all bands. The research covers the physical design of new reconfigurable antennas and establishes the switching mechanism, although the automated control method of the switching mechanisms lies outside the scope of this project.

1.3 Research contributions

The research presented in this thesis is original because it presents new reconfigurable antennas that maintain consistent radiation pattern, high gain and high isolation across all operating bands for wideband applications, such as spectrum surveillance and cognitive radio.

Existing designs of reconfigurable Vivaldi antennas use electronic or mechanical components that resonate at a specific frequency to achieve high isolation but compromise the antenna gain by more than 3 dB. The proposed antennas in this project maintain the maximum gain at the operating frequencies while achieving band isolation of a minimum of 14.5 dB and up to 37.5 dB.

In the first part of the thesis RF switches are introduced in the antenna to match the impedance only at the desired bands. The second part suggests a new approach by using a novel low-cost liquid switch for frequency tuning.

Here there are several points that represent some of the outcomes from this research project:

- Original techniques have been developed to reconfigure the operating frequency of a Vivaldi antenna while maintaining its radiation characteristics, such as polarisation and radiation pattern.
- A novel and simple method for frequency reconfiguration of a Vivaldi antenna is presented in chapter 4. This method can be extrapolated to several frequency

bands. Moreover, other antenna designs that use a similar feed line with a microstrip line can also adopt this method for frequency tuning.

- An original improvement in gain of up to 2 dB more for the Vivaldi antenna is presented, based on the extension of the dielectric substrate.
- A model with empirical formulae is presented to calculate the position of the switches, the position and length of the stub and the slot for the reconfigurable Vivaldi antenna with a minimum accuracy of 96.6 % compared to simulation results.
- A low-cost liquid solution is used as the radiating part of an ionised solution monopole antenna achieving 75 % efficiency.
- The ability of a liquid antenna to replace a conventional solid metal antenna providing easy frequency tuning is demonstrated.
- A novel concept is proposed: "antennas-on-demand". Antennas-on-demand can be made available or non-radiating when needed to eliminate detection and interferences which will be advantageous for stealthy security applications.
- A novel design using a low-cost liquid switch is presented for band tuning, which can be integrated in a reconfigurable Vivaldi antenna. This technique can be used in other designs to tune various antenna characteristics since it has been demonstrated that this low-cost liquid switch can replace a conventional RF switch. Moreover, a liquid switch does not require bias lines that will affect the antenna performance.
- Ten research papers have been accepted and presented at conferences to disseminate the findings and results encountered.

1.4 The scientific method

The scientific method is an iterative process that is used in this research project for experimentation with a series of steps to explore observations and answer questions, as shown in Figure 1.3.

First of all, a question is asked. For example, this research project started with: "How can a narrowband reconfigurable antenna be achieved based on a wideband antenna?"

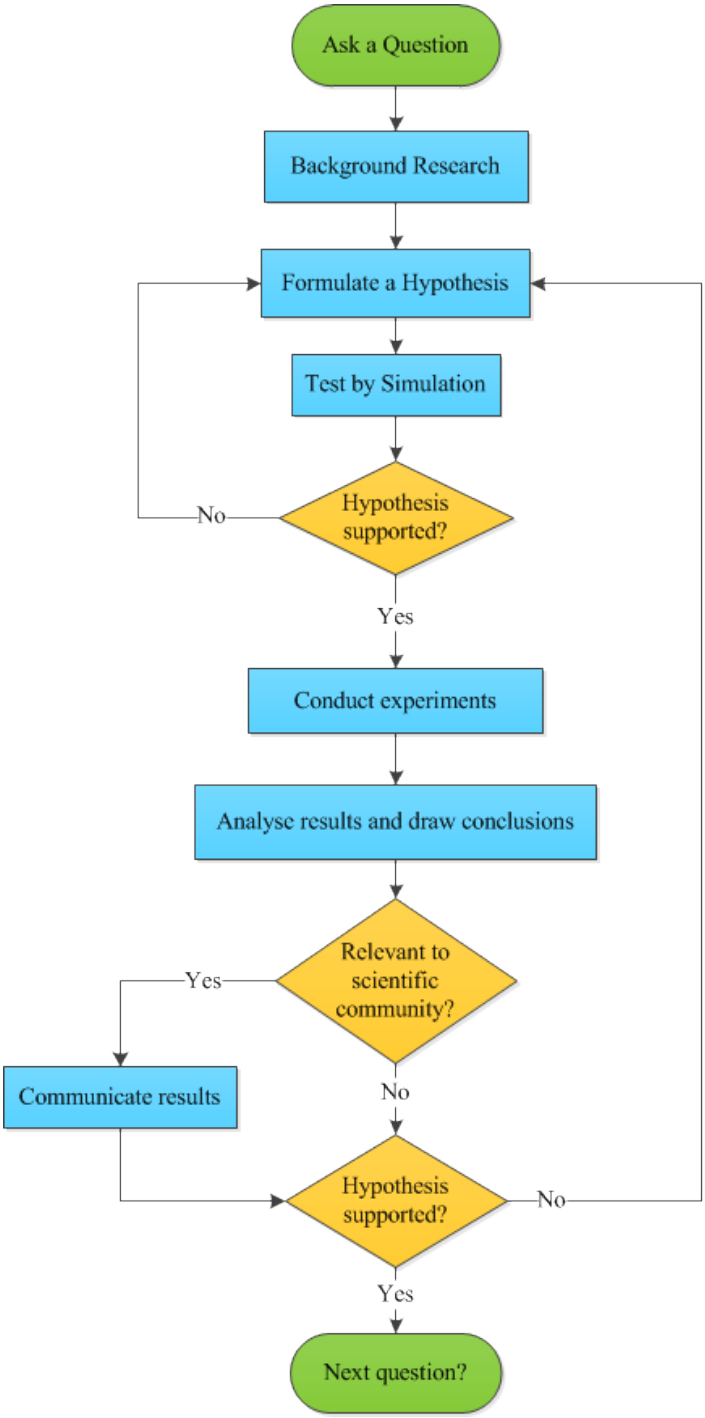

FIGURE 1.3: Scientific method applied in this project.

Next, a background research is required to analyse what has already been investigated in the selected topic. This also helps to find the best way to carry out research and not to repeat mistakes that other researchers have already overcome.

Later, a hypothesis is constructed to attempt to answer the question with an explanation that can be tested. For example: "If the impedance in the feed line of the antenna is tuned, then the operating frequency of the antenna is changed".

The first part of testing the hypothesis is by simulation. Simulation provides fast results and optimisation without the need of building a prototype and measuring it. CST Microwave Studio can calculate the reflection coefficient of a model and obtain the operating frequency. It is important for the experiment to be fair, that is by changing only one variable at a time while keeping all other conditions the same.

If the prediction is accurate, the hypothesis is supported in simulation. Then, the second part of verification is performed. In the case of antenna verification, the reflection coefficient, gain and radiation patterns are measured to obtain the operating frequency band and radiation characteristics of the prototype. These parameters can be measured using a vector network analyser (VNA) in an anechoic chamber.

The measurements are compared to the simulated results and analysed to determine if the hypothesis is supported or not. Experiments can also be repeated several times to make sure the first results are not obtained by chance. If the hypothesis is not supported, a new hypothesis and predictions are required, which will be constructed based on the experience and new information obtained. The scientific method starts over again.

The final step is to communicate the results by publishing the results in a scientific journal or by presenting the results on a poster or giving a talk at a scientific conference.

Even though it seems a straight process, new information or thinking may appear in the middle of the process and may cause the repetition of some steps at any point during the process.

1.5 Thesis Overview

The objective of this project is to produce new frequency reconfigurable antennas that can tune the operating frequency between a wide frequency range while maintaining their radiation characteristics in all the bands. The thesis is presented in six chapters and its outline will be as follows:

Chapter two reviews the fundamental background theory in the context of antenna characteristics, parameters and reconfigurable antennas.

Chapter three presents and analyses the designs that have been proposed on reconfigurable antennas categorised by the tuning parameter: frequency, polarisation or radiation pattern. Then, modern designs on reconfigurable Vivaldi antennas are analysed. Finally, state-of-the-art designs for fluid antennas are reported.

In chapter four proposed designs for reconfigurable Vivaldi antennas are described and their tests and simulations analysed. Several challenges concerning RF switches arise.

Chapter five focuses on a new approach for reconfigurable antennas: fluid antennas. The fundamentals of these types of antennas are explained and an ionised water monopole antenna is simulated and measured to demonstrate the ability of a fluid antenna to replace the conventional solid metal antennas. This chapter also covers a novel liquid-switch reconfigurable Vivaldi antenna and the simulated results and measurements for a prototype of this antenna.

Finally, chapter six covers the discussion and conclusion for the research presented in this thesis and considers improvements and future work.

Chapter 2

Background theory

This chapter is dedicated to provide the necessary antenna background for this research project. In the first section it introduces the basic antenna parameters. Next, a classification of different types of antennas is explained. Then, the difference between resonant and travelling wave antennas is considered. Wideband antennas are analysed next. Finally, the growing importance of reconfigurable antennas to fulfil the requirements of current communications systems is highlighted.

The IEEE Standard defines an antenna as "that part of a transmitting or receiving system which is designed to radiate or to receive electromagnetic waves" [13]. Therefore, the role of an antenna is to launch electromagnetic waves propagating in a transmission line into free space, or vice versa if it is a receiving antenna. In physical terms, conventionally an antenna is a conductor material which has a specific shape with certain electrical current passing through it that is able to transform waves so that they radiate into space. Lately, dielectric resonant antennas (DRA) have been proposed, where the radiating part of the antenna is not a metal part but a ceramic material [14]. Another important characteristic is that an antenna is a passive linear reciprocal device, which means an antenna does not amplify signal, but it matches this particular signal from the free space where it is radiated to a guided environment where it is propagated, in case of a receiving antenna. For a transmitting antenna the process is inverted.

The frequency response and the radiation characteristics are some of the parameters used to characterise an antenna [15]. The frequency response is the variation of input impedance of the antenna across frequency, and the radiation pattern is the power pattern usually expressed in dB of the magnitude of the electric or magnetic field as a function of the angular space [14]. The next section define these characterisations and other antenna parameters used in this research project.

2.1 Antenna parameters

In order to study the performance of antennas, the definitions of various parameters are necessary. This section explains the antenna parameters that are used in this project. It introduces the antenna field regions and then explains the basic antenna parameters: reflection coefficient, bandwidth, efficiency, directivity, gain, radiation pattern, polarisation and phase centre.

2.1.1 Field regions

The field regions surrounding an antenna can be divided into three parts as represented in Figure 2.1 depending on the distance from the antenna. Although no abrupt changes in the field configurations are identified as crossing the boundaries, each region has distinctive characteristics that separate them from others. The main characteristics and boundaries are described here.

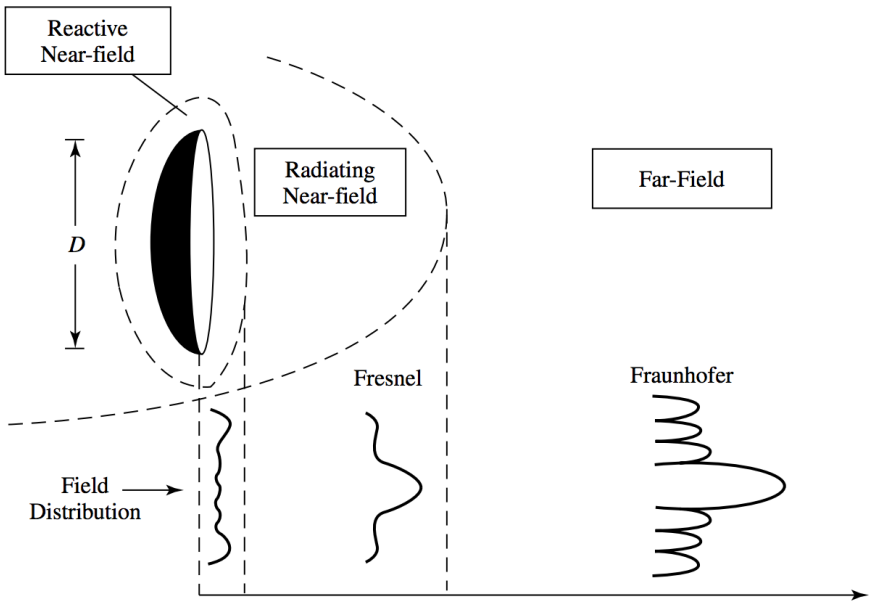

FIGURE 2.1: Antenna radiation pattern typical shape changes for the different regions in the near and far field [16].

2.1.1.1 Reactive Near-field

This region is the one immediately surrounding the antenna and where reactive fields are predominating. The fields in this region store the energy instead of dissipating

as radiation [17]. For most antennas, the outer boundary of the near-field region is commonly at a distance R as in equation 2.1, where D_{dim} is the major dimension of the antenna and λ is the free space wavelength. This region is affected by co-locating antennas or bias lines.

$$R < 0.62\sqrt{\frac{(D_{dim})^3}{\lambda}} \tag{2.1}$$

2.1.1.2 Radiating Near-field (Fresnel)

In the Fresnel region the radiation fields dominate but the radiation pattern keeps changing with the distance from the antenna. This region lies between the near-field and the far-field regions as shown in equation 2.2. If the antenna is small compared to the wavelength in the operating frequency this region may not exist [14].

$$0.62\sqrt{\frac{(D_{dim})^3}{\lambda}} < R < \frac{2(D_{dim})^2}{\lambda} \tag{2.2}$$

When co-locating antennas it is important to place them outside each others near-field so that other antennas do not interfere and change the expected performance of the antennas.

2.1.1.3 Far-field (Fraunhofer)

In the far-field region, or sometimes called Fraunhofer region, the antenna is relatively far away that EM waves behave like plane waves, thus the radiation pattern is independent of the distance from the antenna. What characterises this region is that the E-field and H-field are orthogonal to each other and to the direction of propagation. The boundary with the Fresnel region is taken to be when the radial distance is greater than shown in equation 2.3.

$$R \geq \frac{2(D_{dim})^2}{\lambda} \tag{2.3}$$

As radiative fields predominate in the far-field region, EM waves from the antenna propagate in space. Thus, this is the region of operation for almost all antennas and where the measurements of radiation pattern should be made.

2.1.2 Reflection coefficient

One of the first parameters to characterise an antenna is the reflection coefficient (Γ). The operating frequency of an antenna is represented by the reflection coefficient to display the level of impedance mismatch across frequency. There are several ways of presenting it, this section shows the most important ones:

1. The *input impedance* is the impedance presented by an antenna at its terminals and represents the relation between voltage and current at the input port called load impedance (Z_L). This impedance needs to be matched to avoid reflections. When reflections are present, most of the energy is lost in the mismatch, hence the antenna does not operate efficiently at these frequencies. Equation 2.4 represents the relation between input impedance and reflection coefficient, where Z_0 is the characteristic impedance of the transmission line. When the system is perfectly matched Γ is 0, i.e. Z_L is equal to Z_0.

$$\Gamma = \frac{Z_L - Z_0}{Z_L + Z_0} \tag{2.4}$$

2. The *reflection coefficient* which is introduced in equation 2.4, can also be represented by the ratio of the voltage reflected wave (V_r) to the incident wave amplitude (V_i), as in equation 2.5. Thus, Γ belongs to the interval $[-1, 1]$. This ratio represents the power that is actually delivered to the antenna and the power that is reflected because of an impedance mismatch.

$$\Gamma = \frac{V_r}{V_i} \tag{2.5}$$

3. The *return loss (RL)* is a measure of the dissimilarity between two impedances, usually expressed in decibels, being equal to the number of dB that corresponds to the scalar value of the reciprocal of the reflection coefficient as shown in equation 2.6, where P_{in} is the incident power and P_{ref} is the reflected power. Return loss is a measure of effectiveness of the power delivery from a transmission line to a load such as an antenna. It is a convenient way of characterising mismatch specially when the reflection is small.

$$RL(dB) = 10 \cdot \log_{10} \frac{P_{in}}{P_{ref}} \tag{2.6}$$

4. An alternative way of expressing the reflection coefficient is using the *Voltage Standing Wave Ratio (VSWR)*, which is presented in equation 2.7. VSWR can

take any value between 1 and infinity, but the perfect match is when VSWR = 1. Please note that VSWR is inversely proportional to RL.

$$VSWR = \frac{V_{max}}{V_{min}} = \frac{V_i + V_r}{V_i - V_r} = \frac{1 + |\Gamma|}{1 - |\Gamma|} \tag{2.7}$$

5. The *Scattering parameters* (S-parameters) represent how much power is transmitted or reflected in a port. Equation 2.8 shows the matrix from Figure 2.2 for a 2-port network. S_{11} and S_{21} are calculated when there are no reflected waves from the load, i.e. $a_2 = 0$. Many electrical properties, such as gain, return loss, VSWR and reflection coefficient, may be expressed using S-parameters.

$$\begin{bmatrix} b_1 \\ b_2 \end{bmatrix} = \begin{bmatrix} S_{11} & S_{12} \\ S_{21} & S_{22} \end{bmatrix} \cdot \begin{bmatrix} a_1 \\ a_2 \end{bmatrix} \tag{2.8}$$

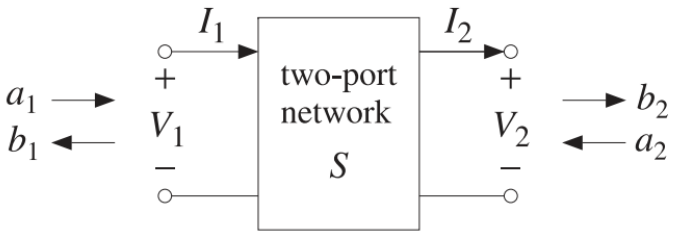

FIGURE 2.2: Two-port network inputs and outputs to create the S-parameters matrix.

Thus, the reflection coefficient can also be calculated using S_{11} as shown in equation 2.9, which represents the ratio between the returning and the incident power in port 1, when the loading impedance Z_L is matched to the system characteristic impedance Z_0. Equation 2.10 shows the transmission coefficient (S_{21}), that is the ratio between the power that leaves port 2 and the power that is accepted by port 1, when there is no mismatch on the loading impedance. In the equations, parameters are shown in linear form, but typically they are converted to dB.

$$S_{11} = \frac{b_1}{a_1} \,|_{Z_L = Z_0^*} \tag{2.9}$$

$$S_{21} = \frac{b_2}{a_1} \,|_{Z_L = Z_0^*} \tag{2.10}$$

To measure the antenna operating frequency in this research project the S_{11} parameter is used, because an antenna behaves as a one-port network. The operating bands of the

antennas will present a low S_{11} while the rejected frequencies will have an S_{11} close to 0 dB. In this project an antenna is considered to be operating in a band when the S_{11} parameter is below -10 dB, which is when more than 90 % of power is accepted by the antenna.

Note that the reflection coefficient is a measure of how much power is delivered to an antenna. A low reflection coefficient means the antenna is well-matched, but does not necessarily indicate the power delivered is also radiated. An experiment to measure the antenna radiated power is required to determine the antenna is operating properly.

2.1.3 Bandwidth

An antenna is only effective across a specific operating range of frequencies, where the reflection coefficient is low (usually < -10 dB), so that the antenna characteristics associated with pattern bandwidth (gain, side lobe level, beamwidth, beam direction, radiation efficiency and polarisation) are within acceptable value of those characteristics at the centre frequency [14]. There is no unique characterisation of the bandwidth, the specifications are set in each different field application to meet the needs of that particular application.

For wideband antennas, bandwidth is usually expressed as the ratio of upper-to-lower operating frequencies. For example, 10:1 in the case of a typical Vivaldi antenna [12]. For narrowband antennas, it is expressed as a percentage of the frequency difference over the centre frequency of the bandwidth, as shown in equation 2.11. For instance, the bandwidth of rectangular microstrip antennas is typically 3 %.

$$BW = \frac{f_{high} - f_{low}}{f_c} \cdot 100 \tag{2.11}$$

2.1.4 Efficiency

There are several losses at the input terminals and within the structure of an antenna that define its efficiency [14]. The total efficiency of an antenna (η_0) can be written as equation 2.12, where the reflection (mismatch) efficiency (η_r) takes into account losses because of mismatch between the antenna and the feeding line (as in equation 2.13) and the conduction and dielectric efficiency (η_{cd}) considers losses in the conductive and dielectric materials within the structure of the antenna. Γ represents the reflection coefficient of the antenna.

$$\eta_0 = \eta_r \cdot \eta_{cd} \tag{2.12}$$

$$\eta_r = 1 - |\Gamma|^2 \tag{2.13}$$

The conduction and dielectric losses of an antenna are very difficult to separate one from another and they are usually combined to form η_{cd}, determined experimentally relating power radiated by the antenna and power supplied to the antenna, as in equation 2.14 where P_r is the antenna radiated power and P_A is the supplied power to the antenna. It is this antenna radiation efficiency (η_{cd}) that is used to relate the gain and directivity as explained in the next section.

$$\eta_{cd} = \frac{P_r}{P_A} \tag{2.14}$$

As the radiated power can be defined as the power delivered to the radiation resistance R_r, and the supplied power can be defined as the power delivered to R_r plus the power delivered to the antenna conduction and dielectric losses R_L, the conduction-dielectric efficiency η_{cd} can also be written as in equation 2.15.

$$\eta_{cd} = \left[\frac{R_r}{R_r + R_L}\right] \tag{2.15}$$

2.1.5 Directivity

In these next sections, the antenna parameters related to radiation are analysed. Directivity (D) is the radiation capability of an antenna in one specific direction. It is expressed using a relation between the antenna under test (AUT) and the isotropic antenna, as shown in equation 2.16, where $\wp$ is the power density of the AUT and P_r is the total power radiated by the AUT [14]. A directivity of 10 dBi indicates the antenna directs 10 times more power in the direction of its main lobe compared to the isotropic antenna.

$$D(\theta, \varphi) = \frac{\wp(\theta, \varphi)}{\frac{P_r}{4\pi r^2}} \tag{2.16}$$

Usually, directivity is referred to the peak figure, which coincides with the direction of the main lobe. Therefore, directivity depends on maximum power density, i.e. power density in the direction of maximum propagation, as shown in equation 2.17.

$$D = \frac{\wp_{max}}{\frac{P_r}{4\pi r^2}} \tag{2.17}$$

An *isotropic antenna* is an antenna which radiates equally in all directions. So, its directivity is equal to 1 (0 dBi) and it is the minimum directivity in the direction of the main lobe another antenna can achieve [14].

Desirable directivity of an antenna depends on the antenna application. If the AUT is used for broadcasting, the antenna should have low directivity, i.e. as close to 0 dBi as possible. On the other hand, if the AUT is used for transmitting in a specific direction like in satellite communications it needs high directivity. For example, the radio telescope at Arecibo Observatory is the second-largest parabolic dish antenna in the world with 305 m diameter it provides a gain of 70 dBi at 2.38 GHz [18]. Some intermediate cases would be, for example, a microstrip patch antenna with directivity around 5 dBi.

2.1.6 Gain

One of the most important properties of an antenna is its ability to direct radiated power at a particular directions while suppressing it in all other directions. The gain (G) is defined as the ratio of radiation intensity in a given direction to the radiation intensity that would be obtained if the power accepted by the AUT was radiated isotropically, i.e. distributed equally in all directions, as shown in equation 2.18 where $\wp(\theta, \varphi)$ is the power density and P_A is the supplied power to the antenna.

$$G(\theta, \varphi) = \frac{\wp(\theta, \varphi)}{\frac{P_A}{4\pi r^2}} \tag{2.18}$$

From equation 2.19 it can be observed the gain is the product of directivity and efficiency, where P_r is the radiated power.

$$G(\theta, \varphi) = \frac{\wp(\theta, \varphi)}{\frac{P_A}{4\pi r^2}} = \frac{P_r}{P_A} \cdot \frac{\wp(\theta, \varphi)}{\frac{P_r}{4\pi r^2}} = \eta_{cd} \cdot D(\theta, \varphi) \tag{2.19}$$

Do not confuse antenna gain with an amplifier's gain. An antenna is a passive element, therefore it does not amplify signals. Its gain describes how much power is radiated in each direction.

Just as directivity, antenna gain is usually referred to the peak figure, that is in the direction of the main lobe, as shown in equation 2.20.

$$G = \frac{\wp max}{\frac{P_A}{4\pi r^2}} \tag{2.20}$$

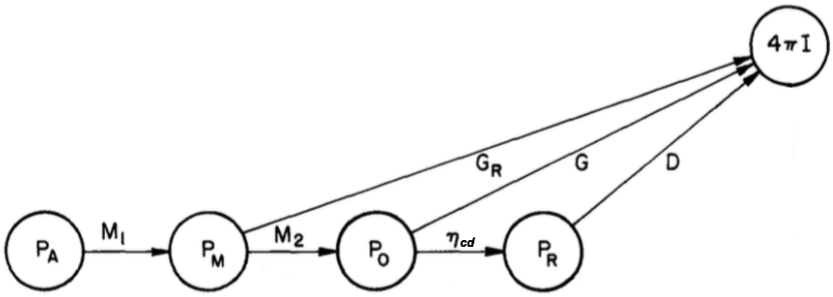

FIGURE 2.3: Flow chart showing the relation between realised gain, gain and directivity with efficiencies, based on [13].

Figure 2.3 represents the interrelationships between power supplied (P_A), power matched to the transmission line (P_M), power accepted by the antenna (P_o) and power radiated (P_r) with impedance mismatches (M_1 and M_2) and antenna efficiency (η_{cd}), obtaining *realised gain* (G_R), *gain* (G) and *directivity* (D) depending on whether efficiency and mismatches are taken into account or not. In the flow chart $4\pi I$ is the radiation intensity of the antenna that the antenna is actually radiating [13].

Although *gain* takes into account the efficiency of an antenna, it does not include losses arising from impedance and polarisation mismatches [14]. The *realised gain* of an antenna is closer to reality because it also takes into account the reflection or mismatch losses. For example, if an antenna presents high efficiency but is not well-matched to its transmission line it will not perform as expected. This is not displayed by the gain figure, whereas it is represented in the realised gain. In this thesis the *realised gain* will be used to indicate the gain of the antennas proposed.

2.1.7 Radiation pattern

The radiation pattern gives information about the intensity and direction of electromagnetic (EM) waves exiting the antenna as a function of space coordinates. It is mostly defined in the far-field region and it represents the spatial variation of the power density along a constant radius with peaks at the regions in space where the antenna is radiating with high intensity. These are called lobes. It also presents nulls or zeros to indicate no radiation in that particular direction [14].

Frequently, the radiation pattern is normalised to its maximum value and usually plotted in dB on a logarithmic scale to highlight the lower values, which refer to the minor lobes.

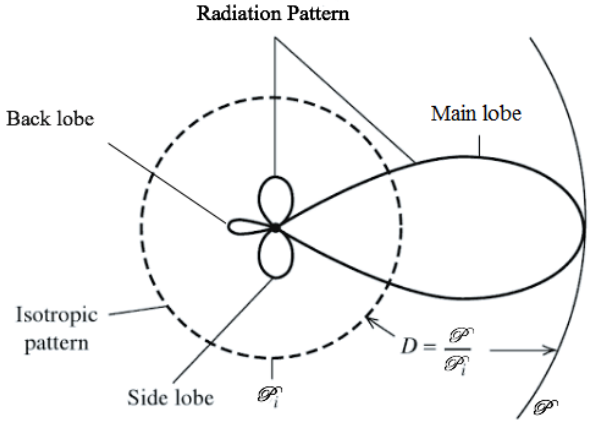

FIGURE 2.4: Representation of the radiation pattern in spherical coordinates and directivity D, based on [19].

The biggest lobe, called the "main lobe", indicates the main direction of radiation, i.e. the direction where most power is radiated to. The "back lobe" is the beam approximately at 180° from the main lobe of the antenna. Other beams in the radiation pattern are called "side lobes". Power radiated to side lobes and back lobe is diverted from the main lobe, which contributes to a loss in the antenna gain. Therefore, these lobes should be minimised. In Figure 2.4 the described beams are represented with the relation between the power density of the antenna ($\wp$) and the power density of the isotropic antenna ($\wp_i$). This parameter defines the directivity of the antenna (D).

The beamwidth of the main lobe is generally defined by half-power beamwidth (HPBW) as the angular separation between two half-power points or when the normalised radiation pattern in dB is radiating at -3 dB value of its maximum in the main lobe, as shown in Figure 2.5. It can also be defined by the angular separation between two nulls

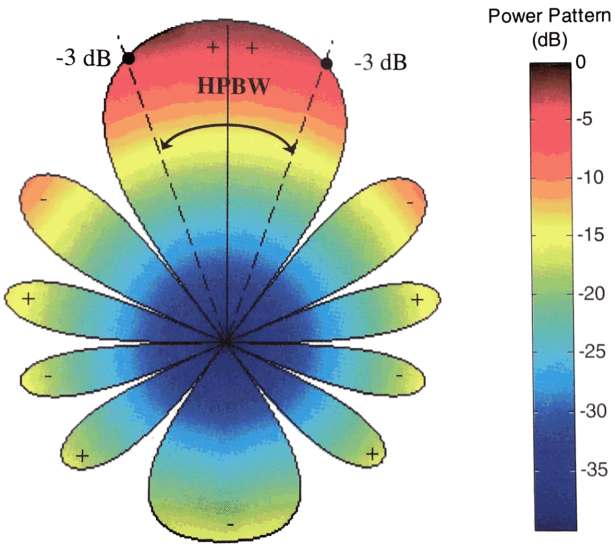

FIGURE 2.5: Two-dimensional normalised example radiation pattern in dB [14].

Types of radiation patterns

ISOTROPIC:	An isotropic radiator is defined by radiating equally in all directions. It is an hypothetical lossless antenna that is used as a reference to express the directive properties of an actual antenna.
DIRECTIONAL:	A directional radiation pattern is able to transmit or receive signals more efficiently in certain directions than in others.
OMNIDIRECTIONAL:	It is a special case of directional pattern. It is defined as "having an essentially non-directional pattern in a given plane and a directional pattern in any orthogonal plane" [14]. A good example is a dipole antenna.

TABLE 2.1: Table describing the different types of radiation patterns.

in the radiation pattern called first-null beamwidth (FNBW), which are sometimes easier to measure than the HPBW. An antenna's beamwidth is important to determine the capability of an antenna to distinguish two adjacent radiating sources [20].

There are three types of radiation patterns as presented in Table 2.1, although only two of them are physically realisable: directional and omnidirectional antennas [21].

For linearly polarised antennas, radiation pattern is usually described in *E-plane* and *H-plane*. The *E-plane* can be defined as "the plane containing the electric-field vector and the direction of maximum radiation" and the *H-plane* as "the plane containing the magnetic-field vector and the direction of maximum radiation" [14]. Figure 2.6 represents a pyramidal horn antenna with its *E-plane* and *H-plane*, in planes *x-z* and *x-y* respectively. Usually the antennas are oriented so that the *E-plane* coincides with one of the geometrical planes of the antenna.

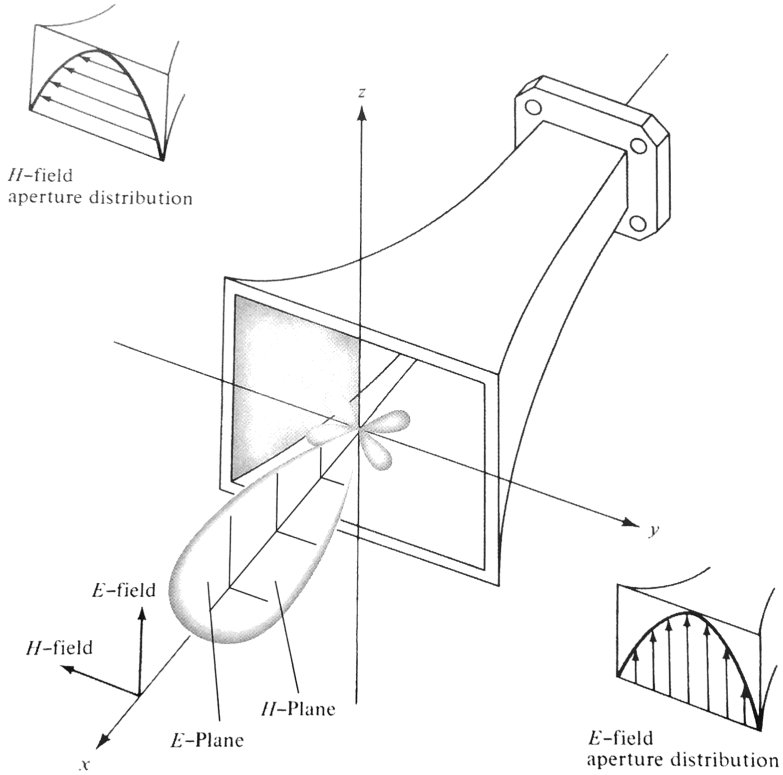

FIGURE 2.6: *E-plane* and *H-plane* radiation patterns for a pyramidal horn antenna with H-field and E-field aperture distributions [14].

2.1.8 Polarisation

Another parameter to take into account when designing antennas is polarisation. Polarisation is defined as the polarisation of the wave transmitted (radiated) by the antenna, that is "the property of an electromagnetic wave describing the time-varying direction and relative magnitude of the E-field vector" [21]. Polarisation varies with the direction, so that different parts of the radiation pattern may have different polarisations. When

direction is not specified, polarisation of an antenna is taken to be in the direction of the main lobe [14].

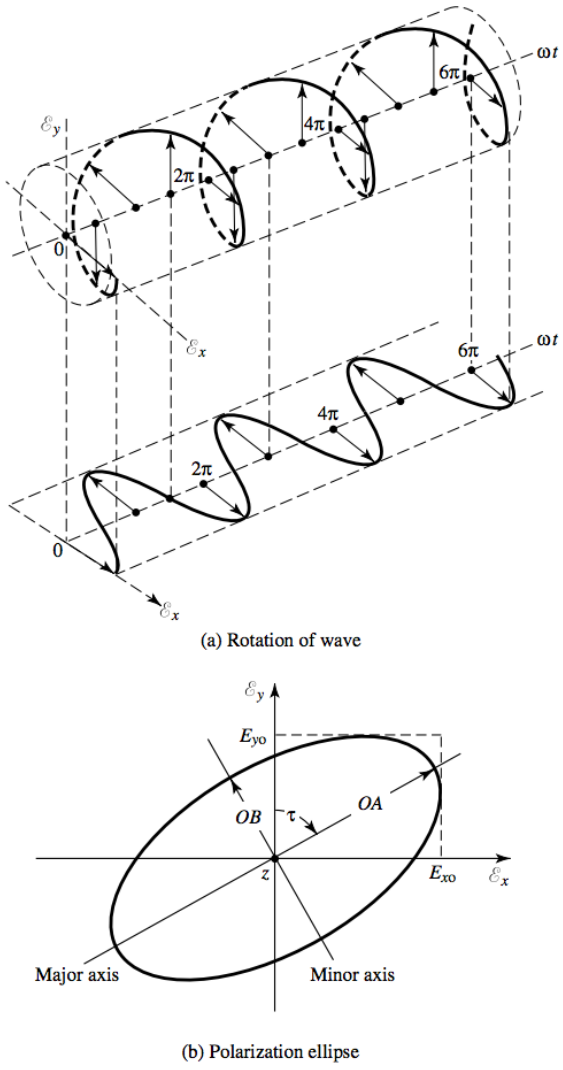

FIGURE 2.7: Rotation of a plane electromagnetic wave and its polarisation ellipse at z = 0 as a function of time [14].

Polarisation of a radiated wave comes from the curve traced by the end point of the vector representing the instantaneous E-field as a function of time, observed along the direction of propagation, as described in equation 2.21 when traveling in the negative z direction (see Figure 2.7). The instantaneous components are related to their complex counterparts by equations 2.22 – 2.23, where E_{xo} and E_{yo} are the maximum magnitudes of the x and y components respectively [14].

In Figure 2.7 (a) the electromagnetic wave is projected from 3D to a plane that shows the field intensity as a function of time. In Figure 2.7 (b) the curve traced by the electromagnetic waves when looking from the wt axis is displayed, that is along the direction of propagation.

$$\varepsilon(z,t) = \hat{a}_x \varepsilon_x(z,t) + \hat{a}_y \varepsilon_y(z,t) \tag{2.21}$$

$$\varepsilon_x(z,t) = E_{xo} cos(\omega t + kz + \phi_x) \tag{2.22}$$

$$\varepsilon_y(z,t) = E_{yo} cos(\omega t + kz + \phi_y) \tag{2.23}$$

Polarisation can be divided in different categories: linear, circular and elliptical, depending on the time-phase difference and the magnitudes of the two components x and y between the ε_x and ε_y components of the E-field [14].

The antenna polarisation characteristics can be represented by its *polarisation pattern*, which is the spatial distribution of the different polarisations over the antenna's radiation sphere. The polarisation of this sphere can be resolved into a pair of orthogonal polarisations: *co-polarisation* and *cross-polarisation*. Co-polarisation is the polarisation the antenna is intended to radiate, while cross-polarisation represents the polarisation orthogonal to the co-polarisation at each point.

In practice, the axis of the main lobe of the antenna should be pointing to the same direction as the polar axis of the radiation sphere. When the polarisations of the transmitting and receiving antennas are not aligned a polarisation mismatch appears. Therefore, antenna polarisation is important because both transmitting and receiving antennas need to have the same polarisation and be aligned so that the receiving antenna can extract the maximum amount of energy [20].

2.1.9 Phase Centre

In antenna theory, a phase centre is the reference point in an antenna from which hypothetical omnidirectional radiation originates. Radiation is spread spherically outward and any radiated fields measured on the surface of a sphere with a centre at that point have the same phase. The *apparent phase centre* is used when the phase centre position presents small variations especially over the main lobe [21]. These parameters are

relevant to travelling wave antennas and antenna arrays, which will be presented in the next sections of this chapter.

There can be a different phase centre for the E-plane and H-plane. The E-plane phase centre of a horn antenna usually coincides with the H-plane, which is why this antenna is useful as a feed antenna for reflectors. This is not the case of the log-periodic arrays and for this reason they are not widely used as feeds. When an antenna, such as a horn antenna, is used as a feed for a reflector its phase centre must be located at the focal point to obtain the maximum gain from the reflector antenna [14].

Mathematically, the far-field radiated component by an antenna can be expressed as in equation 2.24, where $\hat{\mathbf{u}}$ is a unit vector and $E(\theta, \varphi)$ and $\psi(\theta, \varphi)$ represent the (θ, φ) variations of the amplitude and phase, respectively. The phase centre is the reference point where $\psi(\theta, \varphi)$ is independent of θ and φ for a given frequency.

$$\mathbf{E_u} = \hat{\mathbf{u}} \cdot E(\theta, \varphi) e^{j\psi(\theta,\varphi)} \frac{e^{-jkr}}{r} \tag{2.24}$$

This is an important parameter for navigation and tracking systems, as well as other aircraft systems, to define a reference point where at a specific frequency the radiated component does not present phase variations, only amplitude variations. For example, in an aircraft radar that detects ground moving targets (GMTs) a technique called Displaced Phase Centre Antenna (DPCA) is used to compensate the forward movement of the aircraft, that is responsible for the phase centre displacement of the radar antennas. This technique consists of using two alternate transmitting antennas that are displaced in the opposite direction of the movement. Thus, in consecutive pulses the phase centre difference is eliminated [20].

To illustrate the phase centre variations, Figure 2.8 and Figure 2.9 show a Dual-Ridge Horn antenna simulated at frequencies of 2 GHz and 5 GHz respectively, which results in different phase centres. At 2 GHz the phase centre is located at (0,0,15.99) and at 5 GHz the phase centre is located at (0,0,8.60) which is closer to the feed point of the antenna. This type of antenna is ideal to showcase these variations as it can work across a wide range of frequencies. In particular, this antenna can operate from 800 MHz up to 10 GHz.

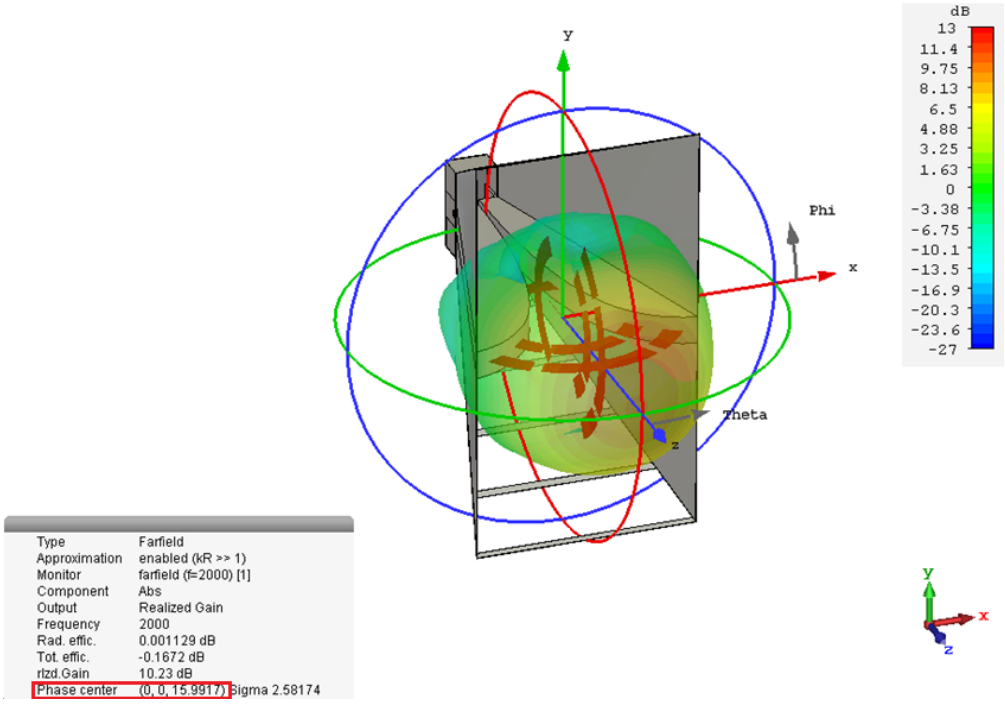

FIGURE 2.8: Phase centre is located at (0,0,15.99) cm for a Dual-Ridge Horn Antenna at 2 GHz. In this case the phase centre is closer to the wide aperture.

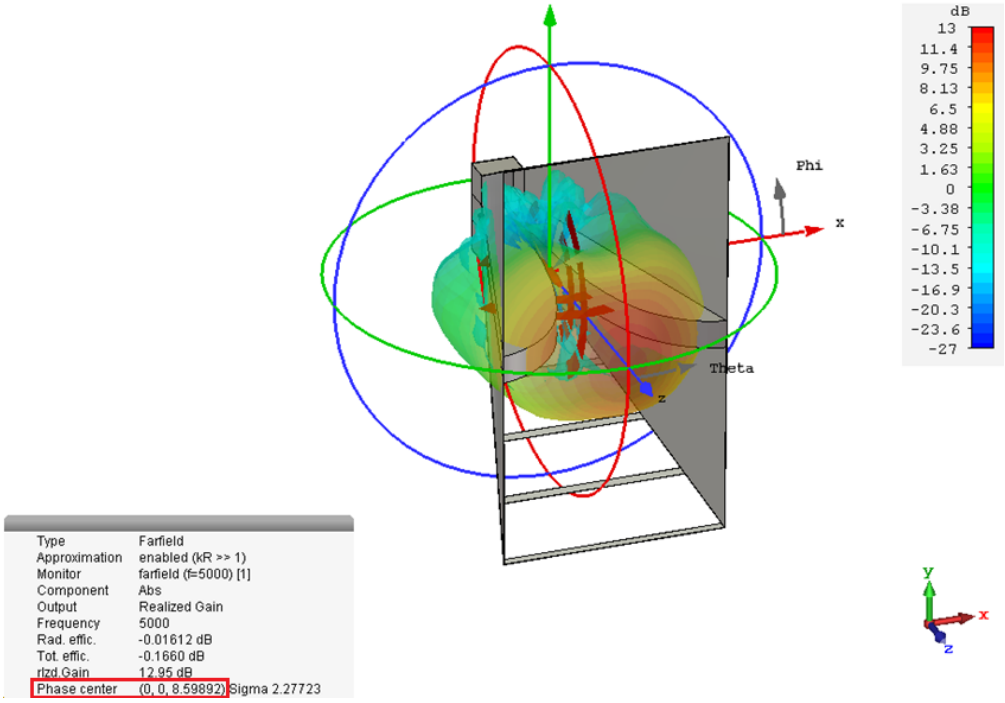

FIGURE 2.9: Phase centre is located at (0,0,8.60) cm for a Dual-Ridge Horn Antenna at 5 GHz. In this case the phase centre is closer to the narrow aperture of the antenna.

2.2 Operating frequency against size

The operating frequency and size of an antenna are two closely related parameters, which makes it important to have them in mind when designing antennas for specific applications. Usually, the size of an antenna depends on the antenna application and the operating frequency band. It is related by the speed of light (c), an approximation of an EM wave propagating velocity in free-space. Frequency (f) and wavelength (λ) are inversely proportional, as shown in equation 2.25.

$$f = \frac{c}{\lambda} \tag{2.25}$$

So, for example, when designing a dipole to operate at 500 MHz, the wavelength is 0.6 m if considering the wave velocity is close to the speed of light in vacuum. Minimising mismatch loss, for the highest antenna efficiency the size of the dipole is determined be around half-wavelength: 0.3 m. That is when the reactance of the antenna is close to zero which makes the dipole resonant. When another dipole is required to operate at 250 MHz, the size of the new half-wave dipole should be 0.6 m, according to equation 2.25.

2.3 Classification by geometry

After defining the main characteristics of an antenna, these next sections are dedicated to briefly describe different types of antenna geometry.

2.3.1 Wire antennas

Wire antennas are the simplest type of antennas and the easiest to calculate the radiated fields. Most wire antennas are resonant antennas. Some examples are as described in Table 2.2.

2.3.2 Aperture antennas

Aperture antennas provide higher directivity compared to wire antennas. They are becoming more popular because of the increasing demand for antennas in higher frequencies. These types of antennas are robust and they can be conveniently mounted in

Types of Wire Antennas	
Monopole antenna:	Is a wire with a ground plane characterised by its omnidirectional radiation pattern, which are commonly used for Wi-Fi routers as such devices must support connections from multiple directions.
Dipole antenna:	Needs double the length of the monopole for the same operating frequency. Dipoles are commonly used as *rabbit ears* for television antennas to receive the VHF terrestrial television bands.
Loop antenna:	Consists of a closed loop of wire and are characterised by low radiation resistance and high reactance, which makes it difficult to match its impedance to a transmitter. They perform better when in contact with the human body compared to other antennas like dipoles, thus are used for hearing aids.
Helical antenna:	Presents higher directivity compared to monopoles and dipoles. These antennas can work in two different modes: *normal* or *axial* mode. In normal mode the antenna acts like an electrically short monopole with linear polarisation, used in mobile and portable communications applications. In axial mode the dimensions of the antenna are comparable to the operating wavelength so that the antenna functions radiating a beam off along the antenna's axis. It radiates circularly polarised waves which can be used for satellite communications.
Yagi-Uda antenna:	Is another type of directional wire antennas with a folded dipole and directors to increase its directivity. Because of its high gain, usually 12 dBi or higher, these antennas are commonly used for long-distance emissions, such as terrestrial television.

Table 2.2: Table describing different types of wire antennas.

a surface and covered with a dielectric material to protect them from the environmental conditions. Some examples of aperture antennas are described in Table 2.3 [14].

Types of Aperture Antennas	
Horn antennas:	Are the most widely used microwave antennas as feed antennas for reflector dishes or satellite tracking and as a universal standard for calibration and gain measurements of other antennas, because of its wideband operation and stable gain.
Reflector Dish antennas:	Are able to transmit and receive signals with very high gain, which makes it useful for very-long distance transmissions such as satellite communications. The aim of these antennas is to focus energy into a specific direction. To avoid radiation in the back and to the sides, a corner-reflector or parabolic shapes are used.
Microstrip Patch antennas:	Consist of a metallic patch, which can have many shapes depending on the application, on top of a grounded substrate. Some of the advantages of these antennas are the ease of fabrication and installation, low cost and small size. Some disadvantages are their low efficiency and low power handling.

Table 2.3: Table describing different types of aperture antennas.

2.4 Resonant antennas and travelling wave antennas

Apart from geometry, antennas can be divided into two groups: resonant antennas and travelling wave antennas. This section describes them.

2.4.1 Resonant antennas

A resonant antenna is an antenna such that it has standing waves of current on it. These elements behave like resonators; therefore the antenna working frequency is dependent on the antenna length. A dipole antenna is the resonant antenna most widely used. It is based on two conductive elements that are connected to the feed line. In Figure 2.10,

there are two fields induced to the dipole antenna: magnetic field and electric field. The dark blue parts are the conductive elements.

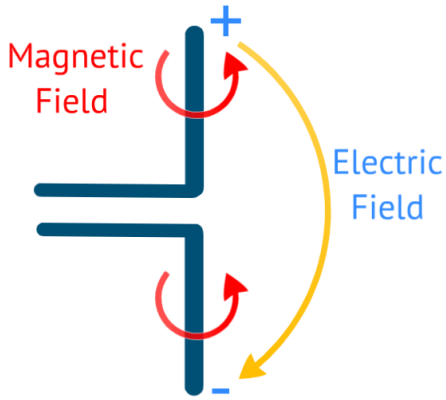

FIGURE 2.10: E-field and H-field for a dipole antenna.

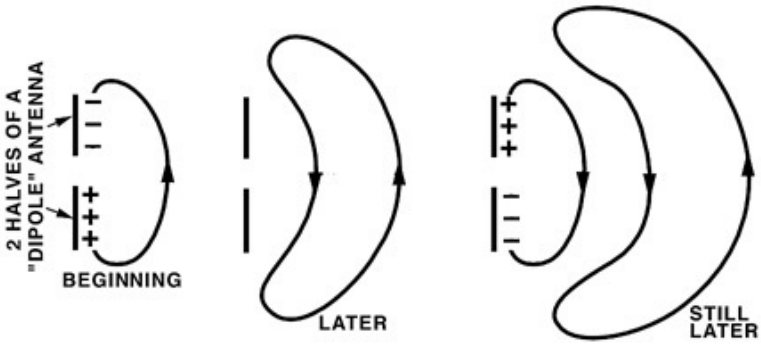

FIGURE 2.11: Magnetic and Electric Fields radiation [22].

Figure 2.11 shows the current changing phase and how electromagnetic waves form loops and are pushed into the air. A more detailed procedure of this process is explained next [21]:

1. At the beginning, the lower conductor is excited using a positive wave, thus there are positives charges in the top half and negative charges in the bottom half. A magnetic field appears surrounding it, as there is some current flowing in the conductor. An electric field is created between the positive and negative poles.

2. This excitation that was increasing in the first quarter of the period, is decreasing on the second quarter of the period, so this can be seen as introducing opposite charges that will neutralise the current generated on the conductors by the end of the second quarter period.

3. Then, as there is no charge or current in the conductors the electric field lines must be detached from the antenna. Consequently, they are united together to form closed loops which are being radiated to free-space.

4. In the second half of the period the same procedure is followed but in the opposite direction. The conductor on the top gets positives charges, so now an electric field line goes in the opposite direction.

5. Then the negative charge decreases, so that a field line will be created to close the loop.

6. Finally, when the current reaches zero again (after 1 period), the electric field line will be closed and an electric wave will be pushed to the air. And this process will continue, starting from the beginning again.

2.4.2 Travelling wave antennas

Travelling wave antennas are defined by minimising reflections in the open-end of the antenna under test (AUT). This way, current and voltage travelling waves appear, thus changing the current and voltage phase distribution as a function of space. There are two types of travelling wave antennas: *slow wave* and *fast wave*.

$$v_p = \frac{\omega}{k} \tag{2.26}$$

- **Slow wave** (also called "surface wave antennas") are those antennas with a phase velocity less than or equal to speed of light c, as shown in equation 2.27, where phase velocity (v_p) is the relation between angular frequency (ω) and phase constant k (equation 2.26). It radiates from discontinuities or curvatures that interrupt a bound wave on the antenna surface [14]. Some example are a long wire, a Vivaldi antenna and an open transmission line which binds the wave by slowing a passing wave and bending it in the direction of the structure. Most of these antennas are end-fire [23].

$$v_p \leq c \tag{2.27}$$

- **Fast wave** (or "leaky-wave antennas") are those antennas that have a phase velocity greater than the speed of light (c) for example transmission lines with a slot, as shown in equation 2.28 [14]. A leaky-wave antenna "couples power in small increments per unit length, either continuously or discretely, from a travelling wave structure to free-space" [13]. This antenna can be regarded as transmission lines

that gradually leak the energy out into free space depending on the phase constant of the leaky wave along the transmission line [24]. Compared to slow-wave antennas, the fast-wave continuously lose energy because of radiation. Only closed structures such as waveguides support fast waves, for example a waveguide with slots.

$$v_p > c \tag{2.28}$$

2.5 UWB antennas

Nonetheless, not all antennas are narrowband. Some antennas are able to operate across a large bandwidth (more than 500 MHz or 25 % of the centre frequency) [13]. These are called ultra-wideband (UWB) antennas. Lately, UWB antennas are more required because of the increasing number of UWB systems and their applications, which are detailed next.

UWB systems differ from other systems in their spread of the necessary energy over a wide frequency range (> 500 MHz) in order to radiate below a limit and share spectrum with other users. For example, unlicensed use of UWB is authorised in the frequency range from 3.1 GHz to 10.6 GHz in United States (FCC) with up to -41.25 dBm/MHz EIRP [25]. These systems are not restricted to a single frequency, but they transmit streams of very short pulses that can be spread over a broad range of frequencies [26].

Some applications of UWB include, but are not limited to [27]: short-range very high-speed broadband access to the Internet, localisation at centimetre-level accuracy, covert communication links, high-resolution ground-penetrating radar, through-wall imaging, precision navigation and asset tracking. Table 2.4 shows different types of UWB antennas [28].

2.5.1 Advantages and disadvantages

The principal advantage of UWB communications is that they allow mobility of wireless devices with high data rate and low power consuming communications. Furthermore, the broad frequency they use makes UWB very resistant to interference. In addition, a huge amount of data can be transmitted within these systems. Besides, security is less of an issue since short pulses are very difficult to intercept.

Nonetheless, as UWB antennas work over a broad range of frequencies they need a sufficient impedance matching bandwidth and a stable gain versus frequency response,

Type of antenna	*Examples of antennas*
Omnidirectional	Discone Bi-conical Roll/thick/planar monopole Roll/thick/planar dipole
Directional	TEM horn Vivaldi Log-periodic Big aperture
Miniaturised	On-PCB Dielectric loading LTCC-based DRA
Arrays	Compact Beam-steering Less-mutual coupling
Special considerations	Spectral-notched Less-dispersion Diversity

TABLE 2.4: Examples of UWB antennas.

as well as constant group delay and high radiation efficiency [29]. This can be a challenge when designing this type of antennas.

2.5.2 UWB antenna parameters

The main UWB antenna parameters for impulse radio are described in this section [30].

- **Time response:** Describes how the antenna responds to the input signal. Time signals can be analysed in simulation. In CST MWS the simulated input signal (i1) and the simulated reflection to the point of excitation from the antenna aperture (o1,1) are presented. A high-efficiency antenna presents low reflection, i.e. o1,1 has lower amplitude compared to i1. Whereas a low-efficiency antenna will present losses within the antenna and/or high reflections because of mismatch, i.e. amplitude of o1,1 close to amplitude of i1.
- **Group delay:** Describes the difference in delay across frequency. Group delay is an important parameter for radar applications. It needs to be constant across all frequencies to ensure no time distortion, because a distortion will render radar range measurements inaccurate [31, 32].

- **Fidelity:** It is a time domain characteristic of UWB antennas that measures the correlation between the radiated waveform and the excitation signal. Typical applications include high precision through-wall radar imaging and PC-peripherals like wireless printers [33]. The antenna fidelity can be defined as in equation 2.29, where a(t) is the excitation signal and the response r(t) is the radiated pulse for a given direction. When the two signals are identical the fidelity reaches its maximum value 1. In general, the fidelity factor is close to 1 for an antenna to be suitable for UWB applications where pulse radiation characteristics are important. As this is not a requirement for this research project, fidelity will not be studied.

$$F = max_\tau \left| \frac{\int_{-\infty}^{\infty} a(t)r(t+\tau)dt}{\sqrt{\left(\int_{-\infty}^{\infty} a(t)^2 dt\right)\left(\int_{-\infty}^{\infty} r(t)^2 dt\right)}} \right|, \; 0 \leq F \leq 1 \tag{2.29}$$

2.5.3 Vivaldi antenna

A Vivaldi antenna is a slow-wave travelling wave antenna introduced by Gibson (1979). It is characterised by an aperiodic continuously scaled structure (or a tapered slot antenna (TSA)), which permits a constant gain within a wide range of frequencies. This antenna has significant constant gain and linear polarisation [12]. Vivaldi antennas can fit into smaller spaces than other ultra-wideband antennas like a ridge horn antenna because they are planar antennas fabricated from a flat laminate. They also offer stable group delay and allow for a narrow pulse width when used for radar applications. The design of these type of antennas is simpler compared to other ultra-wideband antennas such as log periodic and fractal antennas and can be scaled for use at any frequency. It presents the advantage of being fed directly by a microstrip line. The main disadvantage of a Vivaldi antenna is that its phase centre varies depending on the operating frequency. This can be an issue when a Vivaldi antenna is used as a dish feed, but not for the industrial applications of this research project.

As a travelling wave antenna, the power flows parallel to the structure, excited by the narrow slot and progressing to the open end. Figure 2.12 depicts a Vivaldi antenna, where the golden part is conductive and the blue part is a dielectric material. The aperture of the antenna is the open end (on the left hand side). It radiates perpendicular to the aperture of the antenna.

The Vivaldi antenna radiates whenever a wave is not bound anymore to the structure. The antenna is excited from the narrowest slot end (on the right hand side), then a

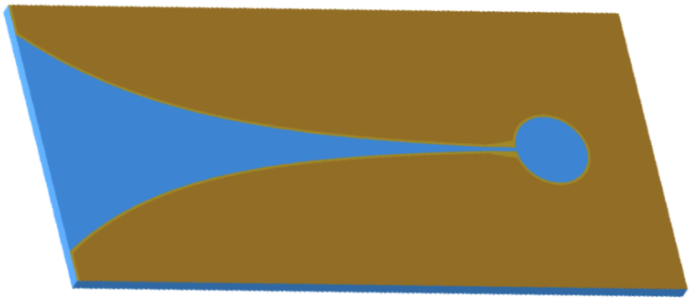

FIGURE 2.12: Vivaldi Antenna [34].

bound is created between the top and bottom side of the Vivaldi antenna. Later, the wave travels to the end of the aperture (from right to left). While the wave is bound, one side cancels the other side and there is no radiation. This is the propagation area. Afterwards, when the slot width is around quarter-wavelength, there is a turning point and the waves are not bound to each other anymore. Here is where the radiating area starts [35, 36].

Hence, having a continuously tapered slot admits a wide operating bandwidth for a Vivaldi antenna, since the start of the radiating part, at around half-wavelength, moves for each operating frequency, making the antenna work across a wide range of operating frequencies. Therefore, the narrow part of the Vivaldi limits the highest frequency in the antenna and the aperture size restricts the lowest frequency, because the waves cannot propagate farther in the antenna for lower operating frequencies.

The feeding is an important part of the Vivaldi antenna. Different feeding methods are a circular cavity and a radial stub, a stripline-to-slotline transition and a stripline stub and a slotline cavity, as described in [37]. Each method provides a certain bandwidth and frequency response to the antenna that can be required depending on the application.

This planar antenna was not being fully studied until the growing developments of multi-mode terminals, where single terminals can have many applications, or cognitive radio was developed. This type of radio requires wideband sensing and reconfigurable narrowband communications.

As stated in the introduction, the industrial requirements for antennas in this research project are:

1. High gain

2. Ability to operate across a wide range of frequencies
3. Stable radiation pattern across all operating frequencies
4. Good isolation between frequency bands
5. Reconfigurable band rejection

For these reasons, as a Vivaldi antenna is inherently wideband, it is a good prospect and it will be the basis of the proposed reconfigurable designs for this research project. Some advantages of a Vivaldi antenna are:

- Broadband characteristics.
- Easily scaled to a wide range of operating frequencies.
- Easy manufacturing process, because it is a planar antenna and can be designed on a PCB.
- Impedance matching using a microstrip line, for the feed line.

A Vivaldi antenna can be reconfigured in the following ways: polarisation, steering the main lobe or tuning the operating frequency.

The polarisation of a Vivaldi antenna is linear, as it is a planar antenna and the E-field is bound across the aperture. To change polarisation more than one Vivaldi antenna would be needed. Therefore this project will not consider polarisation reconfiguration for the Vivaldi antenna.

Reconfiguration of the antenna's radiation pattern can be achieved by varying the shape, length, dielectric thickness or relative permittivity of the substrate of the Vivaldi antenna [38]. This could be done by adding or removing some parts of the Vivaldi or by enabling a larger/shorter path for the current on one side of the Vivaldi antenna.

Finally, changing the operating frequency of the Vivaldi implies to change antenna shape, length or dielectric thickness. These are challenging geometric characteristics to tune, still the feed line is also limiting the antenna's operating frequency. By controlling the feed line some frequencies can be rejected and a preferred band can be selected. As some of the requirements of the project are wide operating range of frequencies and reconfigurable band rejection, a Vivaldi antenna is a good proposal for this research project. Therefore, this research project will study different methods to tune the feed line of a Vivaldi antenna to achieve several highly-isolated narrowbands.

2.6 Reconfigurable antennas

After explaining the antenna radiation characteristics, in this section reconfigurable antennas are considered. Reconfiguration when used in the context of antennas, "is the capacity to change an individual radiator's fundamental operating characteristics through electrical, mechanical, or other means" [15, 39]. These reconfigurable characteristics are:

1. Operating frequency
2. Polarisation
3. Radiation pattern (beamforming or steering)

The main impediment is to tune one of these characteristics without altering other antenna parameters. Reconfigurable antennas are useful for limited space, low cost or low power consumption or to be used in different systems or applications, because they enable the use of one antenna for several systems [21]. Additionally, reconfigurable antennas enable the future mobile communications because they can cope with the increasing demands in mobile communciations and allow the integration of multiple applications into a single platform [24].

2.6.1 Importance of reconfigurable antennas

Because of the rapid proliferation of wireless communications systems, the electromagnetic spectrum has become more and more congested. To address this challenge, new wireless communication systems are required to be cognitive and reconfigurable [24]. Currently, antennas are a critical part of the communication systems. However, a big limitation appears when they are incapable to be adaptive to dynamic environments [15, 40]. Cognitive systems start monitoring a channel to detect unused parts of the spectrum in which to operate. Therefore, reconfigurable antennas with adaptive radiation characteristics which can be dynamically changed to the environment are essential for the higher demand in antenna capabilities for future wireless communications, since these antennas can operate in one frequency band while rejecting other bands. Thus, the system performance is not limited by the antenna characteristics.

Multiband antennas and wideband antennas can operate across a wide frequency range, but only reconfigurable antennas can provide noise rejection in the bands that are not in use so that filter requirements of the front-end circuits can be greatly reduced [24].

Narrowband reconfigurable antennas are even more critical in security applications because of the possibility of jamming signals that can saturate the receiving system. Other relevant security applications may include anti-UAV systems to ensure rogue drones are not interfering in a controlled airspace or committing crimes, like drug smuggling. An appropriate security system to disable rogue drones requires a highly directive antenna capable of tuning to a drone operating frequency without jamming other bands and handling high power.

A system consisting of a wideband antenna plus a filter can be argued to be used in this type of applications. As demonstrated later in Chapter 4, a filter may provide difficulties such as non-linearity, gain loss, higher complexity and power consumption, it is bulky and requires a matching circuit. On the other hand, a reconfigurable antenna can accommodate adjustable capabilities required for the project while preserving high performance and low cost.

2.6.2 Applications of reconfigurable antennas

Although some applications of reconfigurable antennas have been explained in the previous section, this section provides more examples on applications requiring reconfigurable antennas.

The importance of reconfigurable antennas is demonstrated by the wide range of applications they have. Cognitive radio, MIMO channels, wearables, wireless sensing and satellite communications are all possible applications [24]. Their ability to be adaptive on demand allows them to dynamically provide multiple wireless applications without the need of increased space to accommodate multiple antennas.

Cognitive radio is one of the main applications of reconfigurable antennas as explained in the previous section. Cognitive radio systems are based on monitoring the transmission channels and searching for unused frequencies in the spectrum. Therefore, a cognitive radio requires an antenna that can efficiently identify changes in the communications channels and react accordingly [24].

Moreover, reconfigurable antennas provide a great improvement in multiple-input multiple-output (MIMO) systems because not only can they change their radiation patterns, but also polarisation and frequency properties, by morphing their physical structure [40].

Frequency reconfigurable antennas can change operating bands and filter out interfering signals [15], which can be crucial to tackle the saturation of the existing mobile phone systems.

Furthermore, frequency reconfigurable antennas can be applied to wireless sensing applications such as industrial process control, battlefield surveillance and implantable medical telemetries among others [24] since these antennas enable multiple operating bands providing high isolation and stealth capability.

In security applications where stealth is a critical feature, reconfigurable antennas can play a crucial part. A reconfigurable antenna can be designed to only radiate when in excited state by using a fluid as a radiator. When not in use the fluid can be stored elsewhere thereby reducing the system RCS.

More applications can be found on wearables where the allocated space for the antenna system is scarce and on portable wireless devices where reconfigurable antennas bring the possibility to redirect transmitting signal or improve a noisy connection to conserve battery. Moreover, they can change operating bands or switch the standard operation swiftly and filter out interfering signals, which can be crucial to tackle the saturation of the existing mobile phone systems [15, 24]. For example, to reject the WLAN band (5.15–5.825 GHz) to avoid interference in ultra-wideband antennas.

2.7 Summary of chapter

This chapter has presented the background theory necessary for this research project. Starting with antenna parameters, such as antenna field regions, reflection coefficient, bandwidth, efficiency, gain, directivity, radiation pattern, polarisation and phase centre. Next, a classification by geometry and a classification by resonance or travelling wave antennas is presented. Then, reconfigurable antennas and wideband antennas are described, while presenting the Vivaldi antenna and its characteristics, which will be the basis of the proposed reconfigurable designs for this research project. The importance of reconfigurable antennas for wireless communications systems is presented and the applications of reconfigurable antennas explained.

Chapter 3

Literature review

In this chapter reconfigurable antennas that have been proposed are classified and discussed depending on the characteristic that can be reconfigured: operating frequency, polarisation and radiation pattern. In each section, antennas are categorised by how they are reconfigured, either using RF switches or other methods that can mechanically change the radiation behaviours of the antennas. Later, considering these methods suffer from some disadvantages, new design techniques are proposed to overcome the disadvantages by electronic components to reconfigure the antennas. The proposed designs are then analysed.

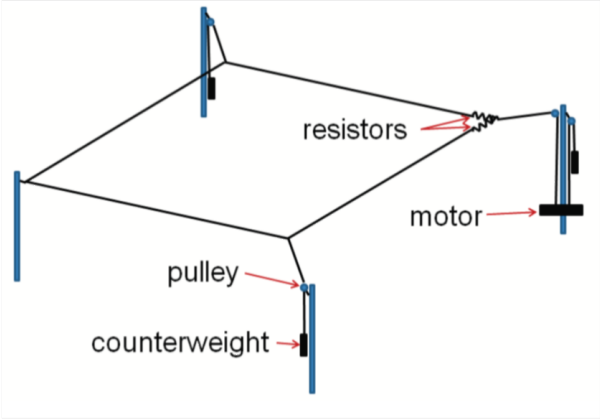

FIGURE 3.1: Reconfigurable rhombic antenna designed by Bruce and Beck [41].

The first reconfigurable antenna is believed to have been reported in 1935, when Bruce and Beck changed the size of a rhombic antenna by stretching the wires with a motor and counter weights [41]. Figure 3.1 shows a diagram of the reconfigurable antenna proposed by Bruce and Beck. This antenna needs to be terminated by resistors (usually 600-800 Ω) to reduce reflections. This kind of antenna is excited from the other end

where the resistors are placed. A single main lobe radiation pattern is acquired when radiation beams 2, 3, 6 and 7 from each wire are aligned, as shown in Figure 3.2. Reconfiguring this antenna consists of changing the length of the major axis of the rhombic wire antenna to steer the beam in azimuth. However, as the antenna operates in the short-wave radio frequency spectrum (HF), the axis needed to change by more than 100 m to only steer 17.5 ° the main lobe. This method is rudimentary and it has a size constraint, but it is believed to be the first reconfigurable antenna.

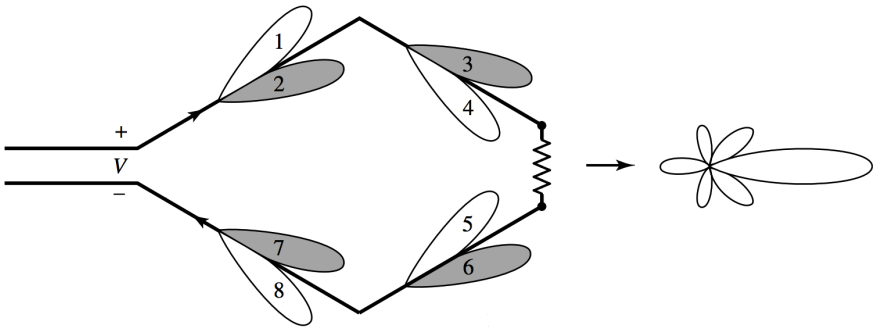

FIGURE 3.2: Schematic of a rhombic antenna's operation and its radiation pattern [14].

Since 1935 other designs have been proposed. Some other new designs are presented and analysed next, and they are classified by their reconfigurable antenna parameters. An antenna can be reconfigured in three different parameters: operating frequency, polarisation or radiation pattern. Different reconfiguration techniques can be implemented to satisfy the imposed constraints and fulfil the antenna function. Most of these techniques can be classified as in Table 3.1 [24]. In the next sections each reconfiguration technique is explained and some examples are presented.

Switches	**Actuators**	**Material change**
Electrical	Motors	Plasmonics
Optical	Linear Actuators	Liquid Crystals
Thermal		

TABLE 3.1: Antenna reconfiguration techniques.

3.1 Frequency reconfigurable antennas

Frequency is closely related to the size of the antenna. Introducing elements that can enable or disable radiating shapes of the antenna will change the operating frequency.

Frequency reconfiguration can be divided in: discrete tuning and continuous tuning, depending on whether the changing of frequency is continuous or discrete.

3.1.1 Discrete tuning

Discrete tuning occurs when the operating frequency change is discrete, i.e. the operating frequency is fixed and can only change between a certain number of bands which are finite, as shown in Figure 3.3. The operating frequency of the antenna is changed by adding or removing shapes of the radiating area through electronic, optical or mechanical actuators, among others. Some examples of discrete adjustment are detailed next.

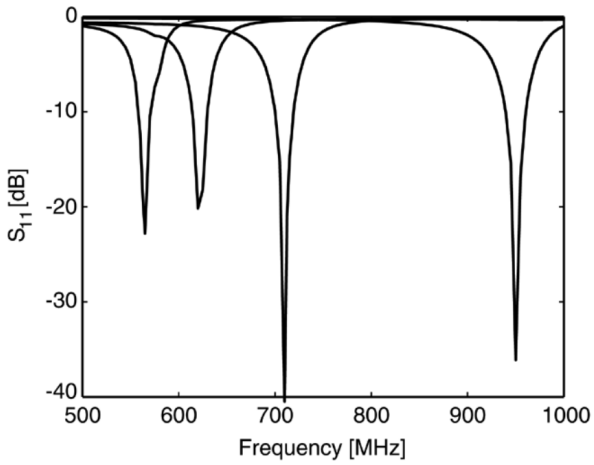

FIGURE 3.3: S_{11} parameter of a switched antenna that works at 4 different bands: 560 MHz, 625 MHz, 710 MHz and 950 MHz [3].

In [42] Radio Frequency Micro-Electro-Mechanical-Systems (RF-MEMS) switches are used to change the effective length of a printed dipole. Figure 3.4 shows the diagram of a dipole in grey and two RF-MEMS switches in red (1 and 2), positioned in the middle of the dipole arm, to stop or allow the current into the outer part of the dipole. When changing the effective size of the dipole, the operating frequency is changed. Some advantages of these switches are: high isolation, linearity and they can be used across multiple frequency bands [43]. A drawback is that they are slower than other techniques. So, in the end, this is a trade-off. The geometry of the antenna is fairly simple to build, in spite of the poor match at the low band mode, where the S_{11} parameter is only -10.2 dB, and the radiation performance measured is quite close to the radiation of an ideal dipole with radiation efficiencies close to 90 %.

A Field-Effect Transistor (FET) switch can be used to switch on or off some parts of an antenna by allowing or stopping current from flowing in those parts. The switch

FIGURE 3.4: Printed dipole using RF-MEMS switches to switch on/off a part of it.

controls the current distribution, therefore controls the radiation pattern, operating frequency or polarisation. Some characteristics of FET switches are: high insertion loss, higher switching speed compared to RF-MEMS switches, low power handling and low electrostatic-discharge (ESD) immunity. In [44] the authors suggested using FET switches and a voltage control to build a reconfigurable aperture antenna. Figure 3.5 shows a small part of this antenna, formed by conductive patches attached to each other using FET switches. This system allows the antenna to control the exact aperture and its shape. But, because of high insertion loss of these switches the radiation efficiency is low. This design enables a high degree-of-freedom which is not necessary. After all, there are a certain amount of shapes to radiate and it would be more efficient to just introduce a significant lower amount of switches and choose between some predefined shapes designed for each particular application the antenna is built for. For example, a dipole, U-shape dipole, bow-tie antenna, circular and square patch antenna, or any combination of the required designs.

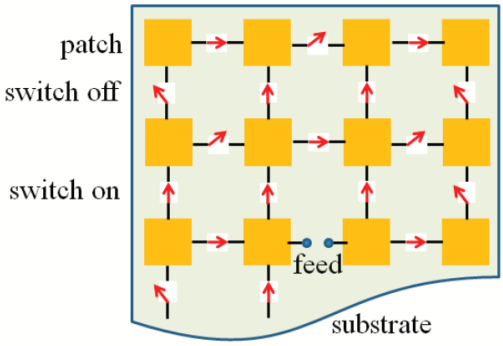

FIGURE 3.5: Reconfigurable aperture antenna based on switched links between electrically small metalllic patches [44].

Another kind of electronic device that can be used as a switch in reconfigurable antennas is PIN diodes. PIN diodes consist of "a silicon wafer containing nearly equal p-type and n-type impurities, with additional p-type impurities diffused from one side and additional n-type impurities from the other side"; this leaves a lightly doped intrinsic layer in the middle, to act as a dielectric barrier between the n-type and p-type regions [45]. A PIN diode presents the two heavily doped p-type (P) and n-type (N) regions where the

ohmic contacts are formed. These two regions are separated by a wide, lightly-doped intrinsic region.

Some characteristics of PIN diodes are detailed next:

- High insertion loss
- Higher switching speed compared to RF-MEMS switches
- Less susceptible to ESD
- Higher upper frequency limit compared to FET switches and RF-MEMS switches

In [3] Peroulis et al. suggested to use four PIN diodes to change the effective length of an S-shaped slot to operate in one of four selectable frequency bands. Figure 3.6 shows a diagram of the slot antenna indicating the position of the four switches. Although PIN diodes can work at higher frequencies compared to other switches already presented, the antenna gain is deteriorated by more than 2.5 dBi at those frequencies which is too high specially for some applications, such as frequency spectrum monitoring. Furthermore, PIN diodes need a reverse voltage of -20 V to maintain the switches in OFF position with a well designed matching network, which makes them less suitable for low power applications. And, finally, although the radiation pattern is barely maintained, the polarisation is not and it degrades the received signal.

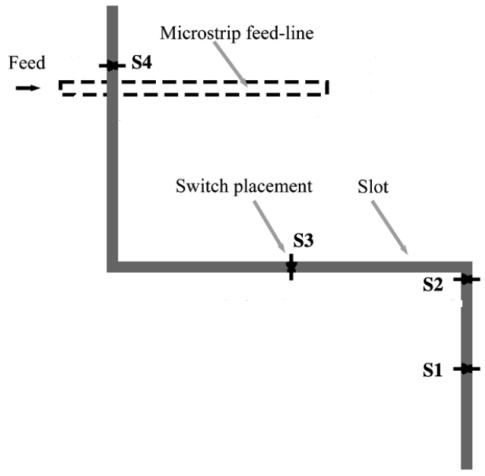

FIGURE 3.6: Slot antenna using four PIN diodes [3].

3.1.1.1 Bias lines

One of the major challenges when designing reconfigurable antennas are the bias lines. Bias lines effectively control the RF switches state that are introduced in reconfigurable designs in order to tune an antenna parameter. For many reconfigurable designs a DC voltage must be directly applied to activate the RF switch and this introduces a new metallic connection that is subject to both DC and RF signals. Therefore, bias lines can severely affect the antenna RF performance by altering the RF current or voltage distribution within the antenna [46].

In [46] the S_{11} is drastically altered once metallic bias lines are placed within the antenna near-field. Thus, the authors propose to use highly resistive lines to deliver the DC activation voltage. The RF is highly attenuated along the line and in their example design negligible effects are observed on the antenna performance. The main drawback of this technique is the high costs of fabrication which may not be suitable for a prototyping stage.

Current designs for bias lines include quarter-wave transformers for narrowband designs [47] and radial open stubs for wideband antenna designs [48]. Spiral RF filters and interdigitated capacitors can be used for wideband applications as well [49]. For those wideband designs the main challenge is the space required for these passive microwave circuits as it may be too large for a given antenna topology.

Previously, some advantages and disadvantages of different RF switches (RF-MEMS switches, FET switches and PIN diodes) are presented, but the main disadvantage are the bias lines. As the bias lines in the surroundings of an antenna may change the antenna RF performance, an optical switch is a good alternative because it eliminates the bias line effects by being controlled using an LED, for example. Freeman et al. used an optical switch to change the effective length of a monopole antenna in [50], a similar idea to [42]. In [51] Panagamuwa et al. presented two silicon photoconductive switches introduced in the middle of a balanced dipole, controlled by infrared laser diodes guided with fibre-optic cables. Figure 3.7 presents a picture of the printed dipole. If the switches are on, the operating frequency is 2.16 GHz and it is tuned up to 3.15 GHz when the switches are off. When the switches are off, it usually means there is no connection. If there is no connection, the physical length of the dipole antenna is shorter, i.e. the antenna operates at a higher frequency.

These designs solve the problem of bias lines structures. Although optical switches need to be controlled with their controlling circuitry as well, which will integrate the optical

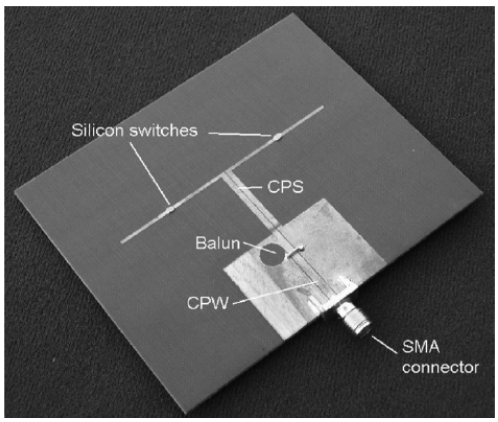

FIGURE 3.7: Printed dipole with silicon photoconductive switches [51].

emitting part. This part is then adjacent to the antenna, making the design bulky, less robust and subject to vibrations and misalignment of the optical controlling part.

3.1.2 Continuous tuning

Switches are commonly used for discrete frequency tuning, thus other devices can be utilised to reconfigure antennas in a continuous way. A continuous frequency tuning means the operating frequency can have any value from within a set with a specific resolution, as shown in Figure 3.8, where the operating frequency can move from 270 MHz to 470 MHz. This is usually achieved by changing the effective antenna length. To change the length of the antenna continuously the use of devices with a continuous range of values is considered. Some examples are: varactor diodes and materials such as liquid crystal. This type of reconfiguration needs a device able to change smoothly a characteristic that influences the antenna performance. In the following, there are some examples on what kind of components can be used and how.

A varactor diode is a diode with a very thin depletion layer, thus it can act like a capacitor. Typically, varying a reverse bias voltage between 0 V and 30 V, varactor diodes change their capacitance between 2.4 pF and 0.4 pF. In [53] Bhartia et al. connected two varactor diodes at the radiating edges to continuously tune a microstrip patch antenna. Manipulating the value of the varactor diode, the effective length of the patch antenna can be changed. Figure 3.9 depicts the schematic of the antenna with the two varactor diodes. From the results observed, this design can only achieve a 20 % – 30 % tuning, which may not be sufficient for wide frequency range applications. Furthermore varactor diodes are non-linear, hence they are not easy to reconfigure to specific values.

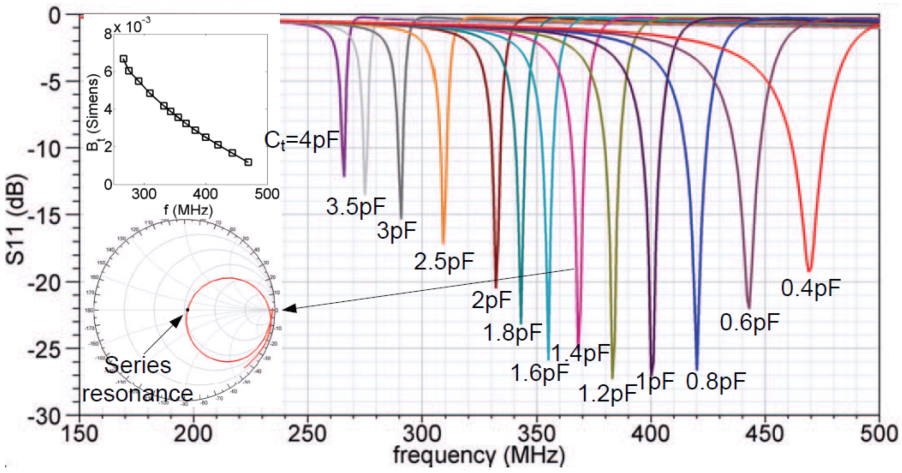

FIGURE 3.8: S_{11} parameter of a continuous tuning antenna that operates between 270 MHz and 470 MHz [52].

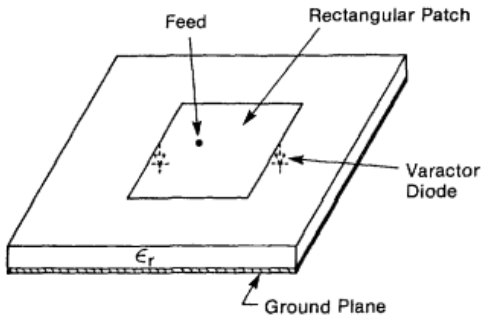

FIGURE 3.9: A microstrip patch antenna that uses two varactor diodes for continuous tuning [53].

Other methods to reconfigure frequency can be used, such as physical changes. Langer et al. presented in [54] a microstrip antenna covered with a thin layer of magnetic material that changed the operating frequency by altering the elevation angle controlled by a magnetic field (see Figure 3.10). This method uses mechanical actuators, which come with some disadvantages: the maintenance of other antenna characteristics susceptible to physical shape changes, low versatility because each design is specific for each antenna or actuation mechanism and it cannot be used with most types of antennas.

Another technique used to reconfigure antennas is presented in [55], when applying a DC voltage in a microstrip patch antenna that has a thin layer of Liquid Crystal (LC) a variation in the alignment angle with the electric field can be obtained. Depending on the LC alignment angle, a different relative permittivity will appear in the direction along the electric field. Given that antenna frequency depends on the relative permittivity, a dielectric tuning will change the antenna's operating frequency. Material changes are

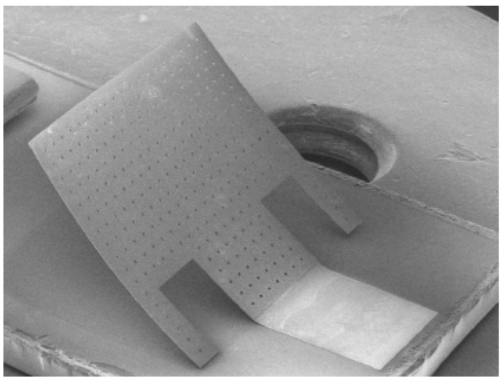

FIGURE 3.10: Reconfigurable out-of-plane microstrip patch antenna [54].

those alterations in the relative permittivity or relative permeability, when applying an electric or magnetic fields, which result in a change of the effective electrical length of the AUT. Figure 3.11 illustrates the antenna with LC layer and how the angle changes for different input voltages. This reconfiguration only gives 4 % range tuning with high losses because of the LC material. Radiation efficiency for this design varies between 7 %, when the LC is in the unbiased state, and 25 % otherwise, which is too low for a high-gain application. Moreover, this method is slow, the LC takes time to align with the electric field and sometimes not all LC is well aligned. The biasing voltage is high as well.

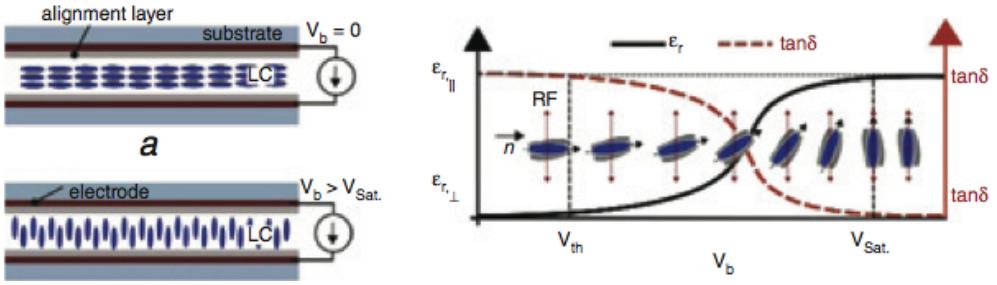

FIGURE 3.11: Thin layer of LC in a microstrip patch antenna [55, 56].

3.1.3 Reconfiguration combining switching and continuous tuning

As discussed before, one disadvantage of continuous tuning is that it cannot change the frequency in a wide range of bands. In the case of the switching antennas, too many switches to get a continuous adjustment would mean higher insertion loss, as in [44]. Therefore, a combination of switching and reactive tuning can also be used like in [57]. Jung et al. presented a monopole structure that uses a PIN diode to provide tuning

between two operating frequency bands: 2 GHz and 5 GHz. Furthermore, a varactor diode is used for fine tuning within each band. The combination of both technologies is a good alternative to overcome the difficulties of finding a suitable component for frequency and the required isolation and linearity. Figure 3.12 shows a diagram of the antenna and its components. This is a good alternative because it can provide the advantages of both techniques. On the other hand, this means more switches, which means higher insertion loss and lower overall gain. As a consequence, in this design there is a trade-off between degrees of reconfiguration and antenna performance.

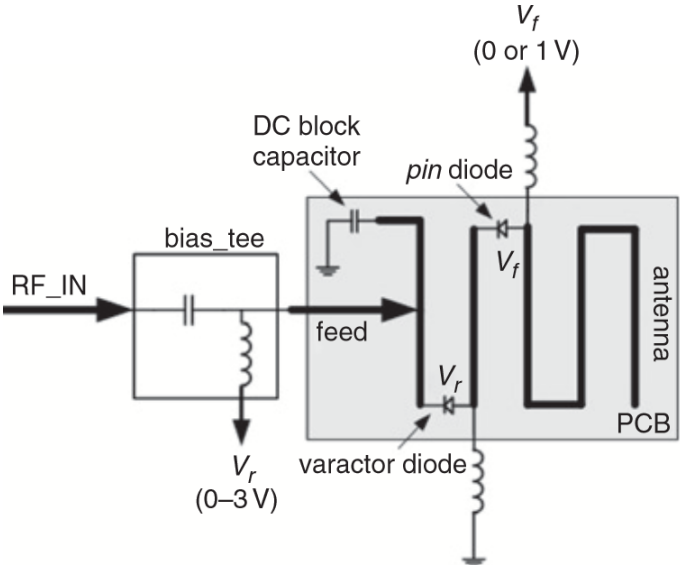

FIGURE 3.12: Macro-micro frequency tuning antenna for reconfigurable wireless communication systems [57].

3.2 Antennas with reconfigurable polarisation

Apart from frequency, other parameters such as polarisation can be reconfigured. The direction of the current flow is what determines the polarisation of an antenna. Finding a way of changing this direction or forcing new paths for the antenna current are some methods to reconfigure polarisation in the AUT. Some examples are explained below.

Switches can be useful to enable new paths for the current or change the present paths. In [58] Wang et al. presented a microstrip patch antenna where they placed RF-MEMS switches in the feed line to switch from one linear polarisation to the orthogonal linear polarisation or to circular polarisation (see Figure 3.13). RF-MEMS switches have some advantages, but the drawbacks, such as switching speed and insertion loss in high frequencies, compared to other technologies are significant.

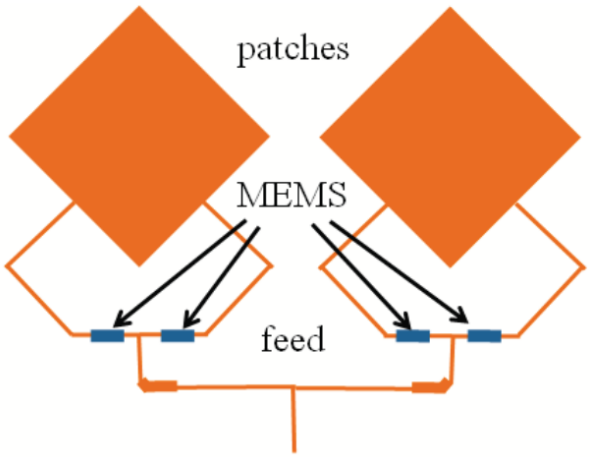

FIGURE 3.13: RF-MEMS switches tuning polarisation in a microstrip patch antenna [58].

PIN diodes can be useful in reconfiguring polarisation as well. For example, in [59] a reconfigurable patch antenna using switchable slots for circular polarisation diversity is proposed. Switches are used to change between Right Hand Circular Polarisation (RHCP) and Left Hand Circular Polarisation (LHCP). They use phase differences in the centre frequency of the propagating modes to switch between polarisations. Figure 3.14 illustrates a diagram of the antenna using switches to short-circuit the slots. These methods are good but they cannot be extended to other designs because they are very specific of these square patches and the way they are fed.

Material changes can also be used to achieve reconfiguration of the polarisation. Rainville and Harackiewicz suggested a magnetic tuning of a microstrip patch antenna fabricated on a ferrite film in [60]. It is based on a static magnetic biasing of the ferrite film; when a static field is applied it tunes the frequency of the cross polarised field and creates a range of elliptical polarisations. Optimising the feeding point and the ferrite film properties, circular and linear polarisations can be obtained.

Coupled feeding is another example for changing from RHCP to LHCP in a microstrip ring antenna. In [61] a U-shaped microstrip feed line is proposed to excite a circularly polarised ring antenna with an operating frequency of 2.7 GHz. Figure 3.15 presents a diagram of the suggested antenna. When feeding excites the antenna from port 1 and port 2 is left open-circuited, RHCP is achieved. Whenever port 2 is excited and port 1 left in open-circuit, LHCP is configured (see Figure 3.16). The main drawback of these methods is that they are very specific for each antenna, shape, etc. and they cannot be extrapolated.

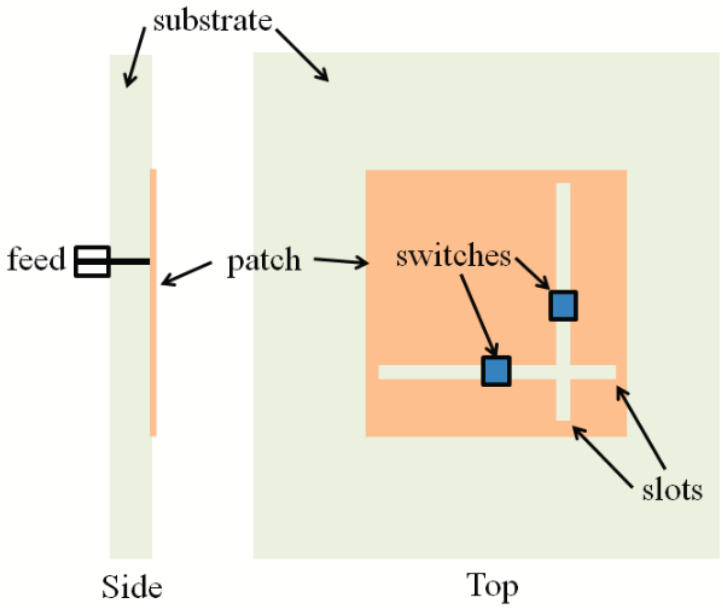

FIGURE 3.14: Microstrip slotted-patch antenna with PIN diodes to tune antenna polarisation [59].

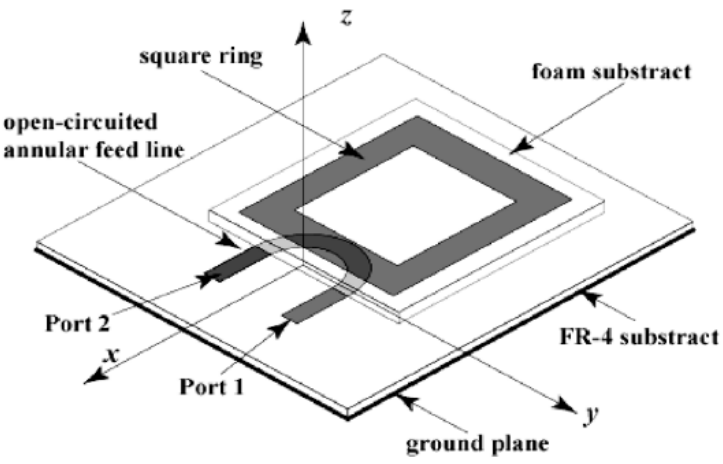

FIGURE 3.15: U-shaped microstrip feed line in a ring antenna [61].

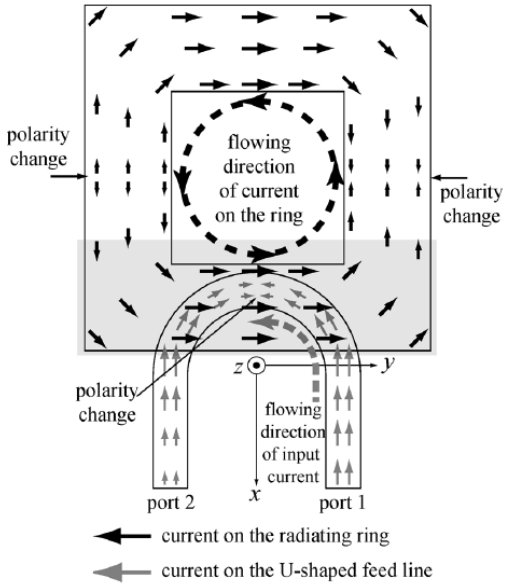

FIGURE 3.16: Current flowing in a circularly polarised ring antenna [61].

3.3 Radiation pattern reconfigurable antennas

The third parameter that can be reconfigured is radiation pattern. The radiation pattern of an antenna is determined by the arrangement of electric and magnetic currents on the antenna structure. Hence, by controlling the way in which the currents flow in the structure or change the physical structure of the antenna its radiation pattern can be adjusted. The main problem, in this case, is to change the radiation pattern without changing the operating frequency or the polarisation, which depend on physical structure and current flow too. Below there are some examples on how to accomplish this.

In [62] Clarricoats and Zhou designed a radiation-reconfigurable reflector antenna by changing the structure of a mesh reflector. Although this type of mechanical change does not affect the operating frequency of the antenna, it is very difficult to achieve and build.

A planar "V" antenna with a coplanar transmission line feed is suggested in [63]. MEMS actuators are used to physically move the arms of the antenna to steer the main lobe and reconfigure the radiation pattern. Figure 3.17 shows a diagram of the design. As stated before, although this design does not change the frequency response, it is not versatile and it is only specific of this type of antenna. This design will also present multiple mechanical problems in the long run, such as misalignment and actuators durability.

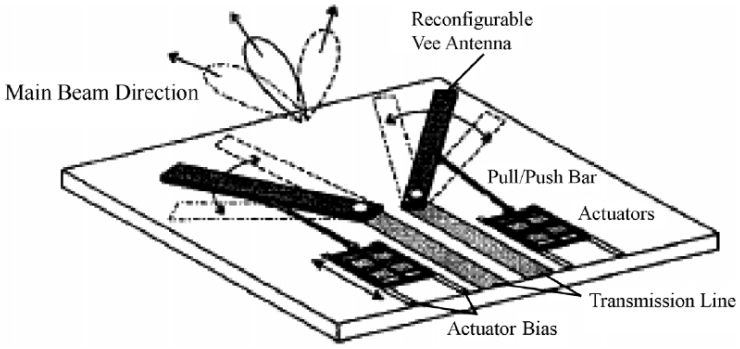

FIGURE 3.17: Vee antenna using MEMS to steer the main lobe [63].

Radiation pattern can also be adjusted by other means, for example electrical or electronic tunings. Electrical changes in the radiating structure result in changes in the radiation characteristics. Nikolaou et al. presented a slot antenna with two diodes placed at locations around the slot to control the direction of a pattern null [64]. Figure 3.18 depicts the antenna and Figure 3.19 shows the different radiation patterns that can be achieved while reconfiguring the AUT. When activating the left PIN diode a null is forced in this direction, so that the radiation pattern is the dashed one. A similar thing happens with the right diode (dotted line). When activating both diodes, the radiation pattern result is the continuous line. This design presents a steer in the radiation pattern depending on the diode location in the antenna. To make the main lobe continuously steerable the design would be challenging because a lot of diodes need to be introduced close together, along with the small but finite shift in frequency when a diode is biased, which is around 3 % deviation.

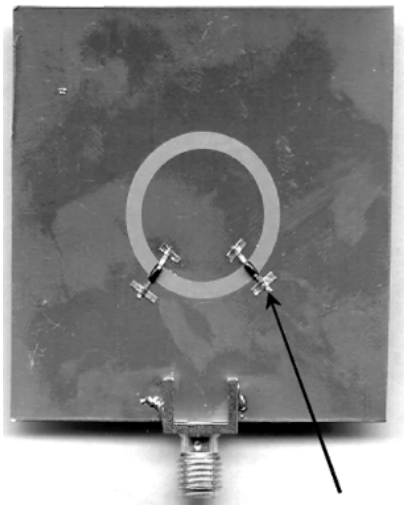

FIGURE 3.18: Reconfigurable annular slot antenna using PIN diodes [64].

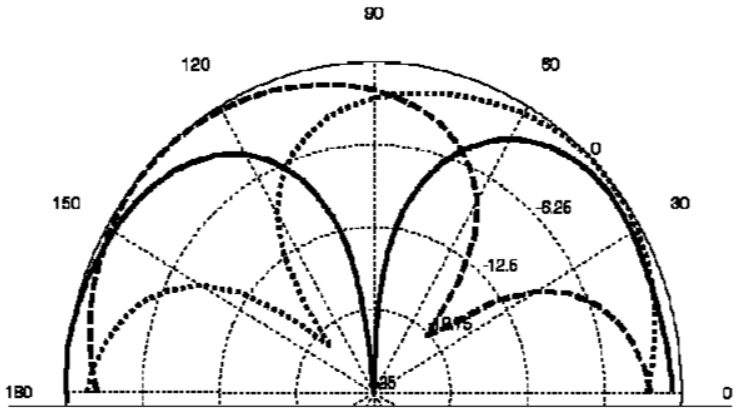

FIGURE 3.19: Radiation patterns of the reconfigurable annular slot antenna [64].

On the other hand, electronically tuned antennas rely on the mutual coupling between closely spaced driven and parasitic elements. This is one of the most effective methods to change radiation pattern independently from frequency. It has wide frequency bandwidth and a range of available topologies and functionalities. For example, Zhang et al. presented in [65] a linear element with two spaced parasitic elements positioned parallel to the driven element (see Figure 3.20). The length of the parasitic elements is changed with electronic switches, which alter the magnitude and phase of the currents on the parasitic elements relative to the driven element.

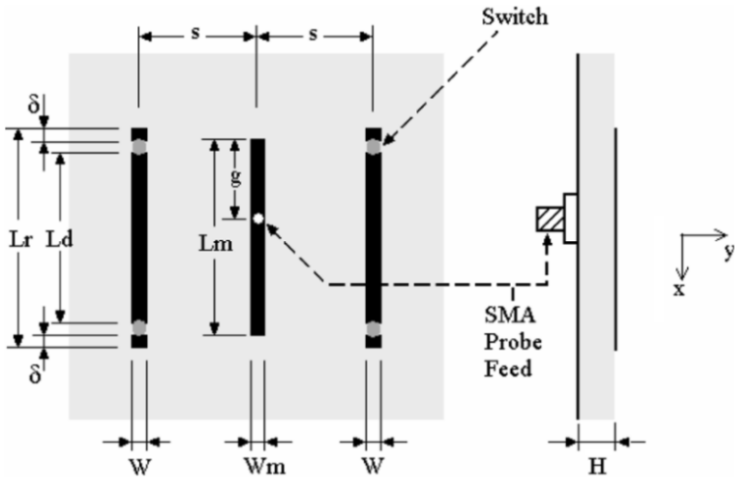

FIGURE 3.20: Diagram of the driven element with the two parasitic elements [65].

The different radiation patterns achievable are presented in Figure 3.21, where the main lobe in the H-plane has been steered in different directions, when activating each parasitic element. But the main variation is in the increased back lobe of the antenna.

The parasitic element forces the radiated energy to one side but leaves the direction of maximum gain almost in the same direction.

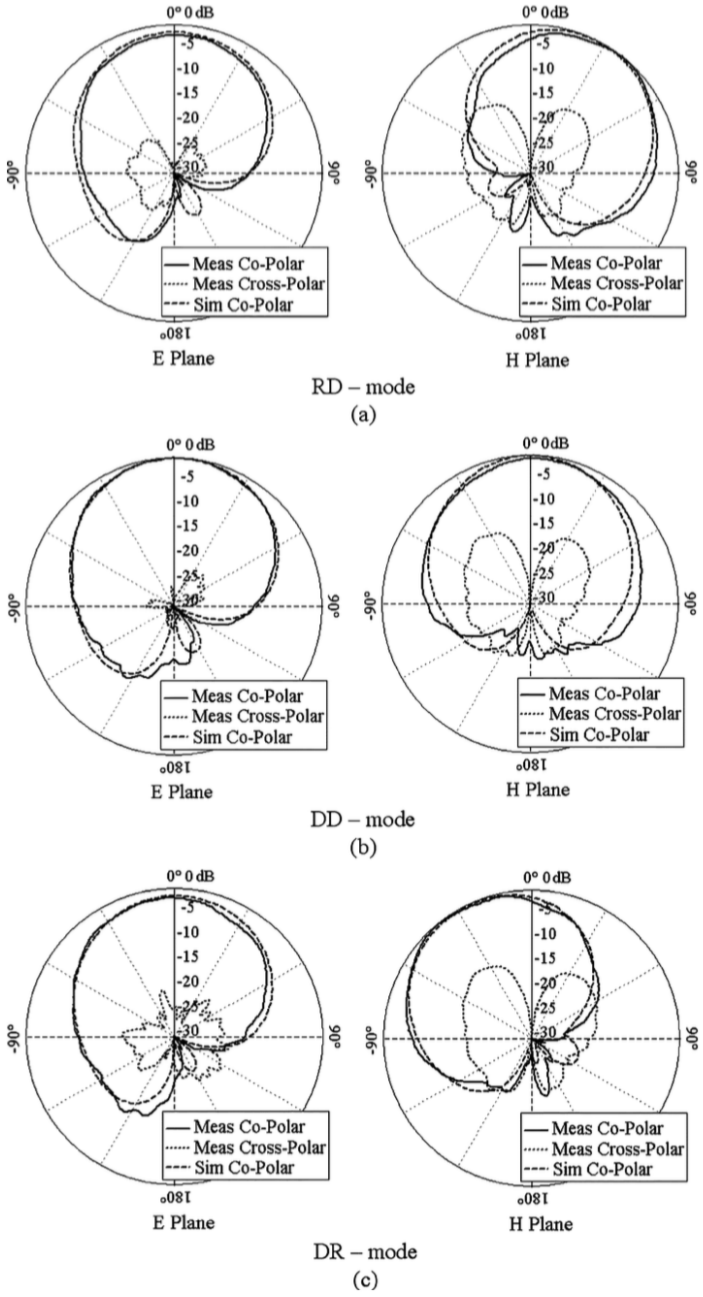

FIGURE 3.21: Radiation patterns depending on parasitic elements length [65].

3.4 RF switches comparison summary

Table 3.2 provides a summary comparison for the main switching techniques identified for use in reconfigurable antennas, based on the proposed designs explained before. As it can be seen, RF-MEMS switches have the highest bandwidth and the lowest insertion loss at 1 GHz, but they also demand a high actuation voltage [66]. Although in terms of switching speed the PIN diode is the best switch, of the order of nanoseconds, but then this switch requires a high biasing current [67], which the GaAs MMIC switches do not require [68]. The FET switches are fast and have good isolation but the insertion loss is high [69]. Finally, GaAs MMIC switches have an acceptable insertion loss and bandwidth, one of the fastest switching speeds and low actuation voltage and bias current. Despite their lower isolation, which is close to the PIN diodes isolation, it is a good candidate for reconfigurable antennas along with RF-MEMS switches.

	PIN diode [67]	*FET [69]*	*RF-MEMS [66]*	*GaAs MMIC [68]*
Insertion loss at 1 GHz (dB)	0.6	1.0	< 0.16	0.7
Isolation at 1 GHz (dB)	15	60	> 24	25
Switching speed (s)	$650 \cdot 10^{-9}$	$5{\cdot}10^{-9}$	10^{-6}	$40{\cdot}10^{-9}$
Bandwidth (MHz)	20-2000	100-6000	DC-12000	DC - 6000
Actuation voltage (V)	40	5	0-90	1.2-5
Bias current (μA)	10^4	5	< 10	0.2
Price per unit (£)	0.98	5.8	12	5.44

Table 3.2: Switching techniques parameters comparison.

3.5 Reconfigurable Vivaldi antennas

As analysed up to this point, many different techniques to reconfigure antennas have been presented, but most of them operate in a narrow range of frequencies. In order to maintain the radiation characteristics of an antenna across a wide frequency range, one can base a reconfigurable design on frequency-independent antennas. The Vivaldi antenna is a wideband antenna that provides high constant gain across a wide range of frequencies. In this section, some proposed designs for reconfigurable Vivaldi antennas are described and analysed.

In [70] several rings are introduced in a Vivaldi antenna to resonate at different frequencies. As it resonates in specific frequency bands, some energy is accumulated in the rings stopping it to be radiated from the antenna. Figure 3.22 shows the Vivaldi antenna with ring resonators. As accumulated current is in the rings, it diminishes the overall gain of

the antenna down to 3.27 dBi from the usual 10 dBi. Because of its low gain it is not suitable for spectrum monitoring [71], because the higher the antenna gain the better the SNR will be.

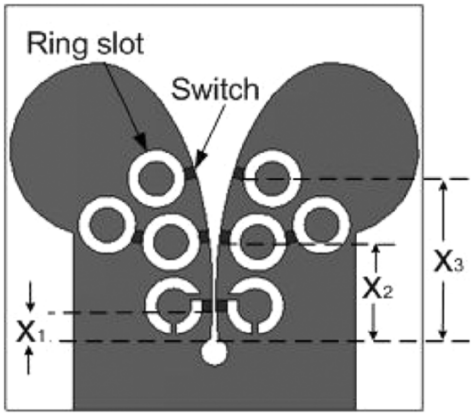

FIGURE 3.22: Four-band reconfigurable antenna with ring resonators [70].

A tuneable stop band in a Vivaldi antenna is proposed in [72]. Three varactor diodes are distributed on a microstrip line resonator which couples to the tapered slot, as shown in Figure 3.23. The varactor diodes change the electrical length of the resonator, achieving several reconfigurable stop bands. But the maximum gain obtained is 7 dBi, which is still low for a travelling wave antenna such as the Vivaldi antenna. As stated before, by introducing elements that resonate at certain frequencies the overall gain of the antenna is diminished. And as a Vivaldi antenna is a travelling wave antenna, which means the current flows from the exciting port to the radiating aperture, when a part that resonates is introduced it disturbs the whole response and deteriorates the overall performance of the antenna.

Apart from switches, varactor diodes are also used in Vivaldi reconfiguration. In [73] a halved Vivaldi antenna is proposed working with a ground plane to reconfigure a band rejection of 20 dB with a frequency tuning range of 4 GHz. It uses a rejection filter consisting of two microstrip resonators and two varactor diodes coupled to the slot of the Vivaldi. Figure 3.24 shows a diagram of the antenna. This design presents higher gain compared to the tunable stop band in [72], but it requires a ground plane big enough, so that it makes the design suitable for vehicular communications but not for portable devices.

In [74] a reflectarray is shown to perform beam steering by using RF-MEMS switches inserted in the coplanar strip transmission line of a Vivaldi antenna. Several switches are introduced along the transmission line behind the flared-notch of the Vivaldi. Figure 3.25

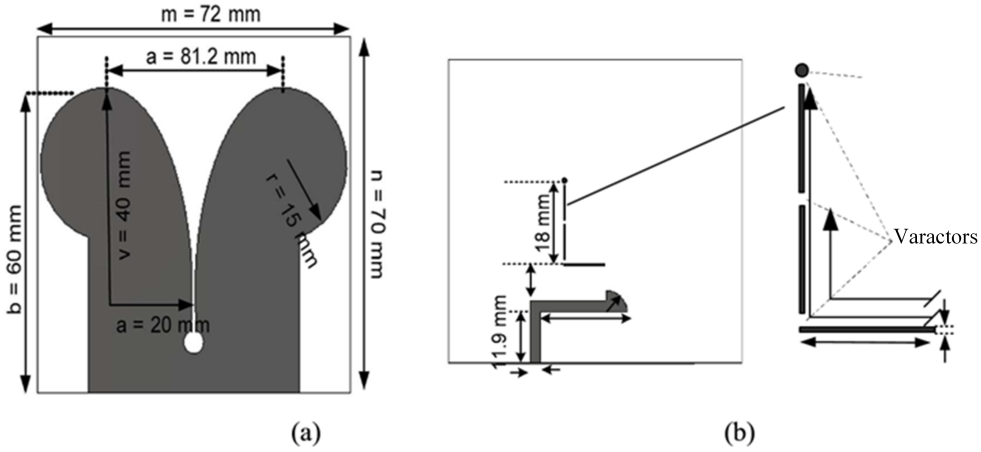

FIGURE 3.23: Tunable stop band Vivaldi antenna, (a) front view, (b) rear view with zoom in the resonator [72].

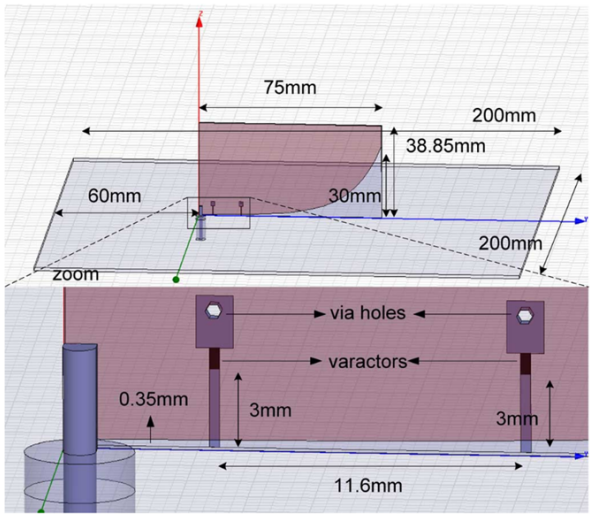

FIGURE 3.24: Halved Vivaldi antenna with tunable stop band [73].

shows the design. Using an array of these elements and by switching the RF-MEMS switches the signal is reflected along the line beyond which all the remaining switches are in reflecting mode. So, the radiated signal time delay is twice the time of travel between the first closed switch and the antenna phase centre. A similar idea is presented in [75]. RF-MEMS switches are used to short-circuit the slot of a Vivaldi antenna in a reflectarray application. By choosing which switches are short-circuiting the slots in the array a beam steering is performed. But in those cases more than one reflector-element is needed to steer the main lobe.

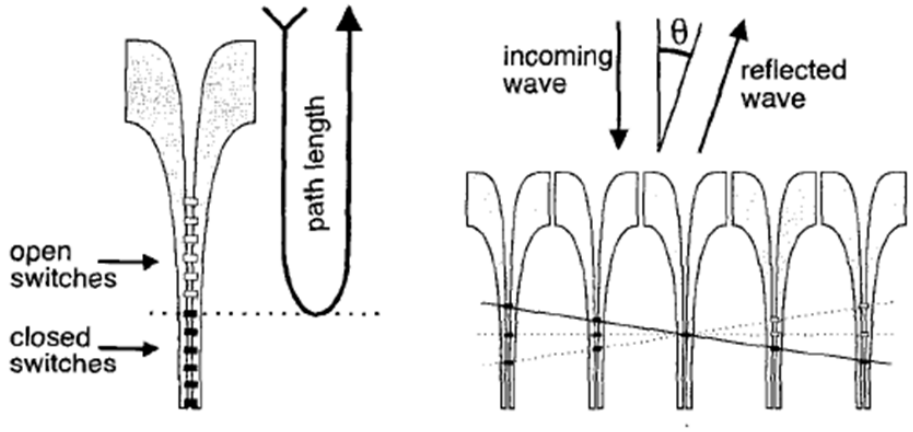

FIGURE 3.25: Reflectarray using RF-MEMS switches to perform beam steering [74].

An antipodal Vivaldi antenna is proposed for cognitive radio applications in [76]. The antenna works from 1.5 GHz up to 10 GHz. It provides a reconfigurable band notch by using three nested complementary split-ring resonators (SRR) in the ground plane, close to the feed point as shown in Figure 3.26. This avoids degradation to the performance of the antenna. The SRR are controlled by three electronic switches. Although the gain is preserved over the lower bands, at high frequency it is degraded, which could be because of the similarity between the wavelength at these frequencies and the size of the furthest aperture. However, this paper only shows the radiation pattern at the frequency of one reconfigurable notch that in this case is omnidirectional. It does not facilitate any other radiation pattern or gain of the antenna in other situations. The stability of the radiation characteristics in other modes is questionable.

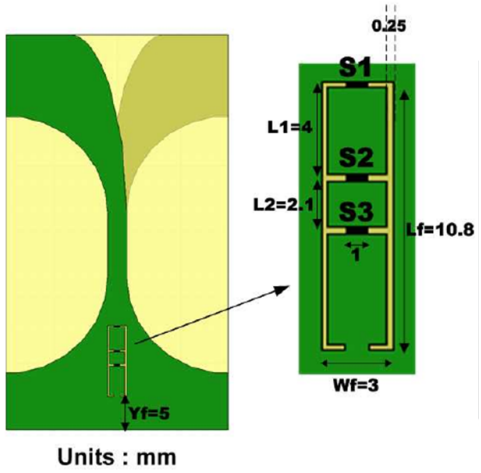

FIGURE 3.26: Antipodal Vivaldi antenna with a reconfigurable band notch [76].

In [77] another Antipodal Vivaldi with two SRR is proposed. It uses the SRR and switches to couple a certain frequency whose quarter-wavelength corresponds to the SRR electrical length as shown in Figure 3.27. By varying the capacitive load in the SRR, the electrical length of the SRR is changed and the antenna is tuned in frequency. The authors propose to use varactor diodes to vary the capacitive load in the SRR and, thus, achieve 30 narrrowbands using the two SRR, one SRR for the lower frequencies and the other one for the higher operating frequencies. They show partial experimental results, only showing the Antipodal Vivaldi in UWB mode, that is with one wideband from 3.3 GHz up to 10.6 GHz, and two narrowband modes by soldering two different capacitor values in the SRR. Gain is not measured, but only calculated and the realised gain is very low: from 2 dBi to only 5 dBi. Because of the nonlinearity of the varactor diodes they would become a major challenge in the implementation of this design.

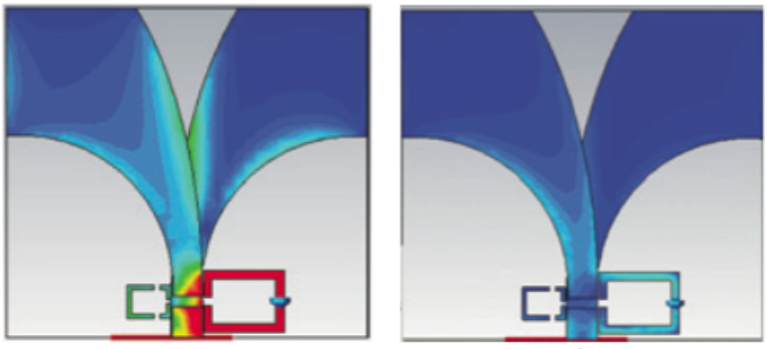

FIGURE 3.27: Current distribution for in-band (left) and out-of-band (right) operation of an Antipodal Vivaldi antenna with SRR and switches [77].

Conclusively, reconfigurable Vivaldi antennas proposed up until now present low gain in case of frequency reconfiguration of several frequency bands and introduce a resonating part to filter out a specific frequency band, which makes the overall gain of the antenna very low.

3.6 New technologies on reconfigurable antennas

Reconfigurable antennas presented before are based on designs that introduce an element which changes or adds some parts to the antenna. Novel technologies give a new perspective to reconfigurable antennas by introducing new materials that can be used as radiators, such as fluid metals. New developments show that fluid antennas can have radiation efficiencies up to 90 % [78].

Lately, numerous implantable RF devices use liquid antennas since these systems must be compact, wearable, biocompatible and reliable. While metallic antennas are effective in the air, when in contact with human tissue they become inefficient and unmatched. In addition, mechanical changes are difficult because of the risk of defects, unwanted resonances and altered impedance [79]. The use of liquid metal solves these problems and grants mechanical reconfiguration. Flexible plastic can also be used to encapsulate the liquid antennas to make them versatile and more rugged. In this section, several proposed designs for fluid antennas are described and analysed.

A liquid dipole can have similar radiation efficiency compared to a solid metallic element, as So et al. show in [78]. They took advantage of flexible or bendable materials to make antennas durable and deformable. The fluid antenna can flow in response to deformation of the elastomer, which is used to encapsulate the liquid and as a dielectric, and thus change the antenna's operating frequency. The elastomer utilised as the antenna substrate is polydimethylsiloxane (PDMS), to which they have introduced two microfluidic channels. The conductive element of the antenna is eutectic gallium indium (EGaIn), which is a low-viscosity liquid at room temperature and possesses a thin oxide skin that provides mechanical stability to the fluid within the elastomeric channels. Its conductivity ($\sigma = 3.4 \cdot 10^6\ S \cdot m^{-1}$) is higher compared to other metal liquids but still below conductivity of copper at room temperature ($\sigma = 5.96 \cdot 10^7\ S \cdot m^{-1}$). Figure 3.28 shows the fluid dipole prototype being stretched. The resonant frequency varied from 1.85 GHz down to 1.6 GHz, when stretched from 54 to 66 mm, maintaining its electrical continuity. This proposed design is a good start, but the materials used are still expensive and difficult to build.

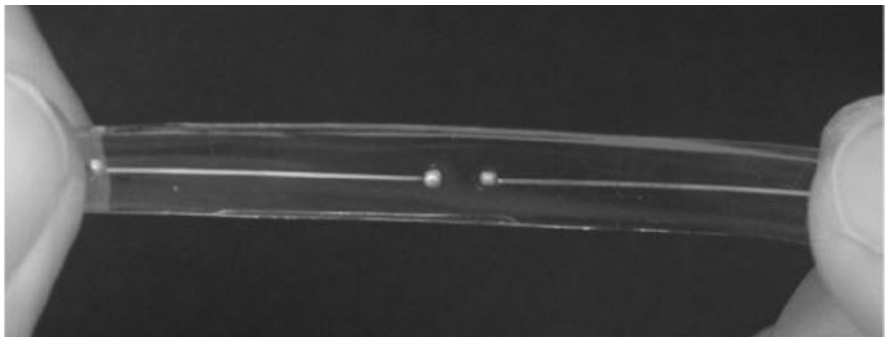

FIGURE 3.28: Liquid dipole encased using an elastomer and being stretched [78].

Similarly, a microstrip patch antenna is presented in [80]. It uses PDMS as the flexible elastomer which encases a series of multilayer microfluidic serpentine channels to form a microstrip patch. EGaIn is the liquid metal alloy used as the radiator material. It is very flexible and its tenacity is tested by measuring the antenna response when flexed.

It is shown that the operating frequency of the antenna does not change. The radiation efficiency is around 60 % which is lower compared to conventional patch antenna (typically 72 % – 91 %). Figure 3.29 shows the multilayer antenna and its flexibility. Although they are trying to build a microstrip patch antenna the performance is not comparable to a metal patch, so some advances have to be made in this field to be able to produce a microstrip patch fluid antenna.

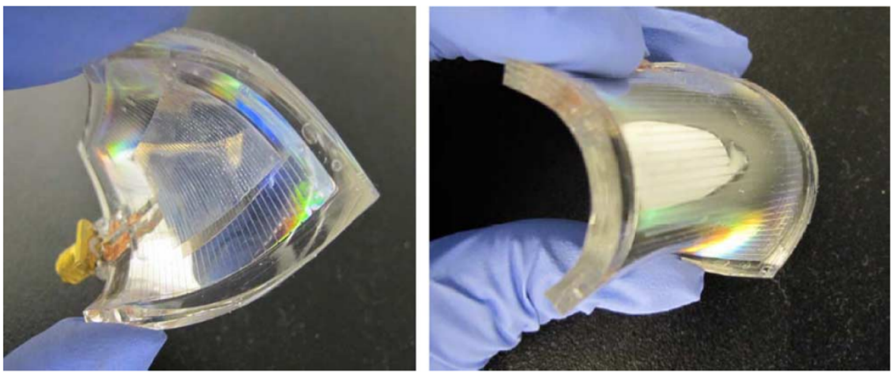

FIGURE 3.29: Microstrip patch antenna using a multilayer microfluidic serpentine channels [80].

While in RF fluid research the most popular fluid systems use metal fluids like EGaIn, in [81] Galinstan is used to tune a dual-band slot antenna. Galinstan is a non-toxic eutectic alloy of Gallium, Indium and Tin with an electric conductivity of $\sigma = 3.5 \cdot 10^6\ S \cdot m^{-1}$ [10]. However, to avoid Galinstan from sticking to channel walls, a Teflon solution needs to be used as a lubricant. This alloy is introduced in two separated PDMS structures, each containing two micro channels on top of each slot antenna. The tuning method is based on using different configurations of filled and empty channels, which changes the loaded capacitance and thus the resonant frequency.

In [10] a new material is proposed to avoid the Aluminum oxidation when in contact with the Galinstan surface. Galinstan is known to dissolve Aluminum, Nickel and Platinum leading to the formation of oxides on their surface at room temperature [82]. These surface oxides result in a very high contact resistance and make their use impractical. Ahlberg et. al. used graphene to create an effective diffusion barrier for preventing aluminum oxide in the interaction between the aluminum and Galinstan in electronic devices to interconnect in stretchable electronics.

Furthermore, a CPW folded slot antenna is loaded with two fluid metal channels on top of the slot to reconfigure the resonant frequency in [83]. It uses Galinstan as the fluid metal and PDMS microfluidic structures bonded to the circuit board to enclose the fluid. This design gives more than an octave switching ratio which is higher compared to other

designs. Figure 3.30 shows a fabricated prototype of the antenna. The main drawbacks of this design are the fluid channels control system currently cannot be electronically controlled and only discrete tuning can be achieved.

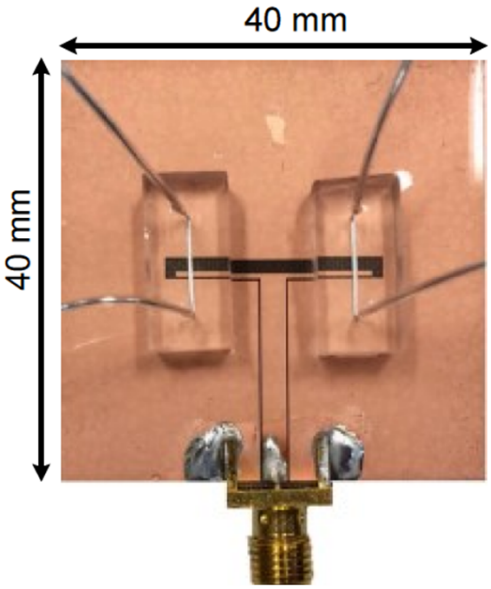

FIGURE 3.30: CPW folded slot antenna with fluid metal channels on top to reconfigure the resonant frequency [83].

3D printing technologies have also been used to fabricate flexible antennas for wearable applications with liquid metals as in [84]. The proposed antenna uses Galinstan to form an Inverted F Antenna (IFA) with a flexible thin plate of copper ground plane. The IFA is designed at 900 MHz and the frequency response is measured for different radius of curvature, where the antenna presents a shift of the antenna resonance of around 2 %. The main drawback of this design is the low efficiency (about 40 %), which the authors attribute to resistive, dielectric and Galinstan's conductivity losses.

An improved design is presented in [85], where the efficiency issues are resolved and the antenna achieves a maximum efficiency of 70 % at the resonant frequency of 885 MHz. The improved design includes a flexible foam in order to keep the antenna radiating arm at a constant distance from the ground plane. The authors also validated the antenna performance with the influence of the human body as the antenna is intended for wearable applications, achieving similar results compared to the measured performance of the antenna without influence of a human body.

In [86] the authors present a 3D printed reconfigurable helical antenna. A liquid metal alloy is used to vary the number of turns of the helix by controlling the volume of the EGaIn and thus tuning the gain of the antenna, when the antenna is radiating in axial

mode. At the operating frequency of 5 GHz they can achieve a 4 dB improvement in the antenna's gain by changing from 2 turns to 8 turns of the helix. The gain tuning is significant but it is important to highlight that there is a frequency deviation of around 300 MHz when reconfiguring the antenna that could become a serious issue for narrow-band applications.

Although EGaIn and Galinstan are widely used in fluid antennas because of their high electrical conductivity, they are expensive. Alternatives are: aqueous NaCl solutions, NaOH solutions, H_2SO_4 solutions or KCl solutions. These solutions have electric conductivities from 14 S/m to 85.2 S/m, which are much lower compared to EGaIn or Galinstan but these ionised solutions are cheaper and easier to produce. In [87] a range of different ionised solutions are presented and analysed, concluding that materials with certain amount of conductivity can be used as antennas and need not be essentially solid.

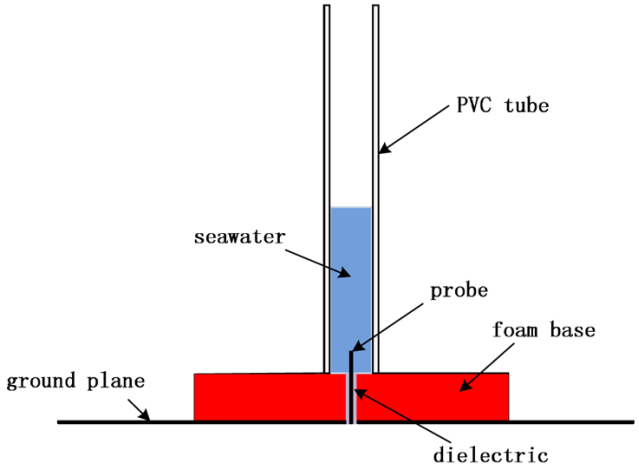

FIGURE 3.31: Seawater monopole antenna [88].

In the same manner, in [88] seawater is used to design a monopole antenna. Figure 3.31 shows a diagram with the PVC tube encasing the seawater. Although the efficiency is only 32 %, seawater is easy to get, non-toxic and eco-friendly. The efficiency can be improved up to 80 % by increasing the concentration of sodium chloride in water. By analysing and experimenting with different easy-to-get materials, like KCl solutions, a fairly good-conductive antenna can be achieved with performances good enough to be competitive with the solid-metal conventional antennas, as fluid antennas can be easily reconfigured.

3.7 Summary of chapter

Antennas can be reconfigured in polarisation, radiation pattern or operating frequency. Frequency reconfiguration is a feasible solution to the higher demand in antenna capabilities, since these antennas can operate in one frequency band while rejecting other bands, thereby increasing signal-to-noise ratio (SNR) [2].

Frequency reconfiguration can be classified in two categories: discrete tuning using RF switches and continuous tuning using other methods. For the discrete method several designs have been presented using RF-MEMS switches, FET switches, PIN diodes and photoconductive switches. The latter ones are proposed to avoid interference from bias lines to control the switches, although some other disadvantages appear, like fragility. In the case of PIN diodes and FET switches, these switches have high insertion loss at higher frequencies unsuitable for the industrial requirements of this research project. Therefore, RF-MEMS switches are a good candidate to start. For the continuous tuning, other components are proposed: varactor diodes, mechanical changes and LC. However these methods present low efficiency and low range tuning. Consequently a combination of discrete and continuous tuning is presented. These designs present a trade-off between degrees of reconfiguration and antenna performance.

For polarisation diversity, the proposed designs are very specific for each antenna design and they cannot be extrapolated to other antennas.

In the radiation pattern reconfiguration three main designs are analysed. A reconfigurable reflector antenna and a planar "V" antenna that use mechanical changes, which are not easy to extrapolate to other designs. And a design with two reconfigurable parasitic elements in parallel to a driven element that claim to steer the main lobe, although they increase the back lobe considerably and the gain in the main direction is mostly unaffected. Reconfigurable polarisation designs and reconfigurable radiation pattern designs are not a requirement of this project, therefore will not be further analysed.

Although some work has been done in the field of frequency reconfigurable antennas, most of the designs can only operate in a narrow frequency range. The use of the so-called frequency-independent antenna, such as a Vivaldi antenna, allows the design to operate across a wide frequency range while maintaining the radiation characteristics. Different designs using a Vivaldi antenna have been presented, but none of them maintain high gain and consistent radiation pattern across a wide frequency range, as they introduce resonant elements that compromise the antenna gain. Therefore, in this project the nature how the electrical surface current flows in the travelling-wave Vivaldi antenna will be determined and then, with that understanding, an RF switch will be introduced

to tune the operating frequency of the wideband antenna without sacrificing antenna gain.

Moreover, new technologies currently reveal that other materials can be used as antennas, like fluid metal alloys. Several examples have been presented using different types of fluids. EGaIn is the most commonly used with high conductivity, but it is expensive. The same applies to Galinstan. But seawater or ionised solutions such as NaCl, NaOH or KCl solutions show good characteristics to be implemented in a low-cost reconfigurable antenna design.

Chapter 4

Frequency-reconfigurable switched Vivaldi antennas

4.1 Introduction

This chapter aims to explain several reconfigurable antenna designs that have been proposed to fulfil the requirements of this research project. The frequency reconfiguration is based on a wideband antenna because it will maintain the radiation characteristics in all the bands. A planar Vivaldi antenna is considered because of its directional radiation pattern and ease of manufacturing within the departmental workshop. The procedure to design a planar Vivaldi antenna is explained first and some improvements on the design are proposed and implemented next.

Once a basic Vivaldi antenna is simulated and analysed, a reconfigurable design is proposed based on the understanding acquired and the literature review. The first design studied is a switched dual-band antenna that can be shifted between two frequency bands centered at 2.7 GHz and 3.9 GHz. In order to improve the SNR of the antenna, a quarter-wave microstrip stub and a three-quarter wave slot are introduced to control the operating frequency. Given the Vivaldi antenna is frequency-independent, the radiation characteristics such as polarisation, radiation pattern and direction of the main lobe, are going to be maintained in all operating bands. The antenna is electronically reconfigured by using two Radant RMSW100 RF-MEMS switches which adjust the length of the current path for each band. These switches were selected because they present very low insertion loss and they can operate across a wide frequency range, although they will need a driver to operate them as they require an actuation voltage of 90 V.

The same idea of adjusting the current path is applied to a tri-band design, by using 4 RF switches. And, finally, a quad-band antenna with 6 RF switches is presented to reconfigure the operating frequency between any band from 1.5 GHz up to 6 GHz.

A prototype of the two-band design is fabricated and tested. Several problems arise related to the electronic switches and to the fabrication procedure in the departmental workshop. Therefore, a new dual-band design is proposed using only one GaAs MMIC RF switch. A low insertion loss GaAs MMIC switch is selected because of its lower actuation voltage and higher switching speed compared to the Radant RF-MEMS switch. The proposed design is fabricated and successfully verified in the university anechoic chamber achieving switched tuning and good isolation.

Moreover, a model with calculation formulae is then extracted from transmission line theory and empirical experience. This model is applied to design a dual-band Vivaldi antenna prototype optimised to overcome the limitations of fabrication in the departmental workshop.

4.2 Design of a Vivaldi antenna

To start, a model of a basic Vivaldi antenna is designed and simulated to get a benchmark for comparison. The basic Vivaldi is designed following equations reported in [12, 89]. The basic Vivaldi antenna defined here presents an exponential flare with a circular stub in the bottom layer and a microstrip line that is connected to a 50 Ω port terminated with a radial stub. The radial stub and circular stub have a wideband operation to match a wide frequency range. This antenna is used in the reconfigurable design as the basis antenna by replacing the wide matching stubs by narrow-band stubs but maintaining the same exponential flare.

Next sections describe the initial design of a basic Vivaldi antenna as well as the study and simulation of the proposed antenna as it is the basis of the reconfigurable designs.

4.2.1 Basic Vivaldi antenna

The geometry of the Vivaldi antenna is characterised by an aperiodic continuously scaled structure (or a tapered slot antenna (TSA)), which permits a constant gain within a wide frequency range. This antenna has high constant gain and linear polarisation inside its operating frequency range [12].

An exponential flare suits best the structure of a tapered slot antenna as the gradient of the flare must be proportional to wavelength to achieve a constant beamwidth [12, 36]. The exponential flare is designed to match the 50 Ω antenna input impedance to the free-space impedance (377 Ω), following equation 4.1, where $Z_0 = 50\ \Omega$, $Z_L = 377\ \Omega$ and α is calculated as in equation 4.2 [89, 90].

$$Z(x) = Z_0 \cdot e^{\alpha x} \tag{4.1}$$

$$\alpha = \frac{1}{L_{flare}} ln\left(\frac{Z_L}{Z_0}\right) \tag{4.2}$$

Therefore, the flare of the Vivaldi antenna can be calculated as in equation 4.3, where $A = \frac{W_{LB}}{2}$, $B = \frac{W_{slot}}{2}$ and $L_{flare} = 200$ mm. Figure 4.1 and Figure 4.2 represent the antenna and its parameters used in the equations.

$$x\ (mm) = Ae^{\alpha y} + B \tag{4.3}$$

The top layer presents a 50 Ω microstrip feed line that is terminated with an open-circuit stub, as shown in Figure 4.1. The stub matches the impedance of the input port to the impedance in the bottom-layer slot. The bottom layer accommodates the exponentially tapered Vivaldi antenna as shown in Figure 4.2. The antenna is designed on a substrate of Taconic RF-43 with a thickness of 0.762 mm and relative permittivity (ε_r) of 4.3, which is a low-loss alternative to FR-4 [91, 92]. The antenna is excited from the microstrip line in the top layer. The intersection from stub to slot line is formed by two stubs: a quarter-wave stub (L_{stub}) and a three-quarter wavelengths slot line (L_{slot}). The length of these stubs limits the operating band of the Vivaldi antenna, as quarter-wave stubs are inherently narrowband.

The maximum and minimum operating frequency of a Vivaldi antenna are defined by the width of the narrow part of the aperture (W_{HB}) and the width of the widest part of the aperture (W_{LB}) of the antenna, shown in Figure 4.2. The length of the antenna needs to be long enough to be able to accommodate the slot length and tapered slot length. This length needs to be greater than one wavelength at the centre frequency [93]. In this design, $L_{antenna}$ is 250 mm.

As the width in the narrow part of the slot limits the highest frequency in the antenna and the aperture size restricts the lowest frequency, in equation 4.4 the dimensions of the antenna are defined to operate between 1 GHz and 6 GHz.

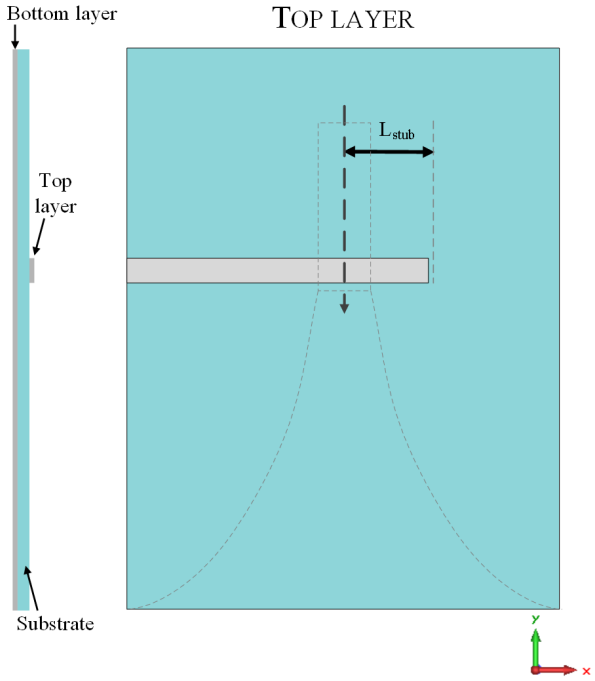

FIGURE 4.1: Diagram of the top layer of a Vivaldi antenna.

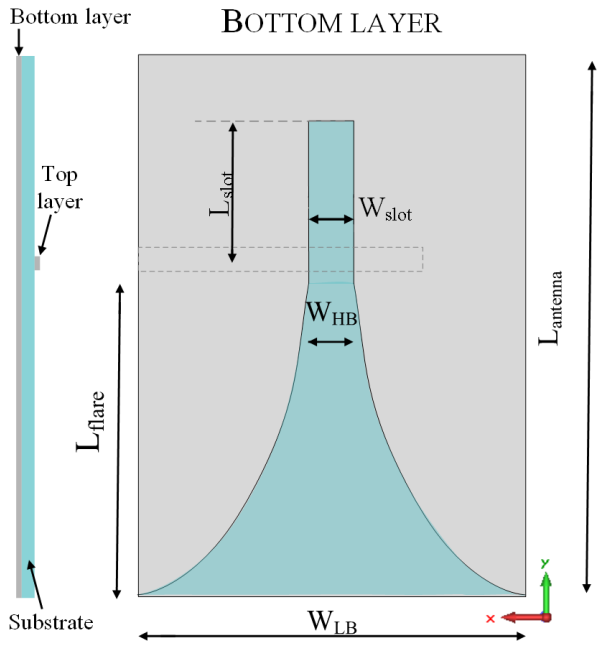

FIGURE 4.2: Diagram of the bottom layer of a Vivaldi antenna.

$$W_{LB} = \frac{\lambda_{low\ frequency}}{2} = \frac{3 \cdot 10^8 / 1 \cdot 10^9}{2} = 0.15\ m = 150\ mm$$
$$W_{HB} = \frac{\lambda_{high\ frequency}}{2} = \frac{3 \cdot 10^8 / 6 \cdot 10^9}{2} = 0.025\ m = 25\ mm \tag{4.4}$$

The position, length and width of the stub and the slot have been optimised for maximising the signal coupling in terms of impedance matching.

As stated before, the quarter-wave stubs are inherently narrowband. To avoid limiting the operating band of the Vivaldi antenna, a circular stub is introduced in the bottom layer at the end of the slot, as shown in Figure 4.3. The circular stub (16 mm diameter) expands the frequency bands by two times. In the top layer the feed line is terminated with an open-circuit radial stub to widen the matched band as shown in Figure 4.4. The radial stub (12.5 mm length and radial angle of 92°) operates as a quarter-wave stub across a wide frequency range allowing a wider band to be well matched.

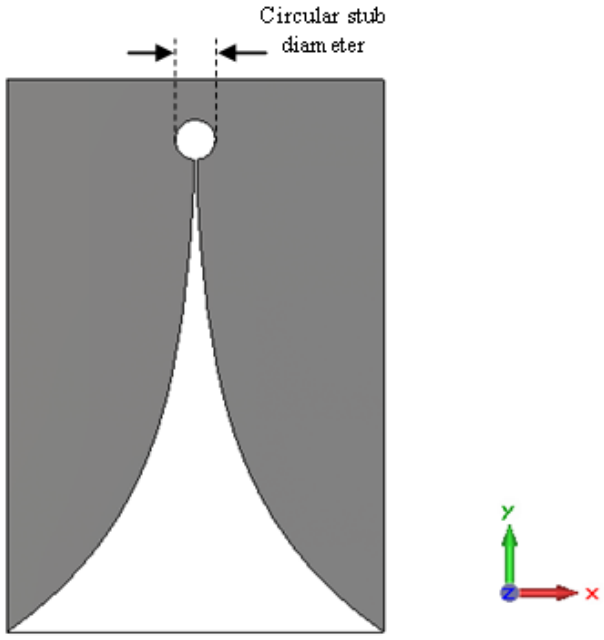

FIGURE 4.3: Bottom view of the simulated basic Vivaldi antenna with circular stub.

The simulated operating band of this design can be extracted from the S_{11} parameter in Figure 4.5. The S_{11} falls below -10 dB ± 0.5 dB (green dashed line) at 900 MHz up to 5.6 GHz.

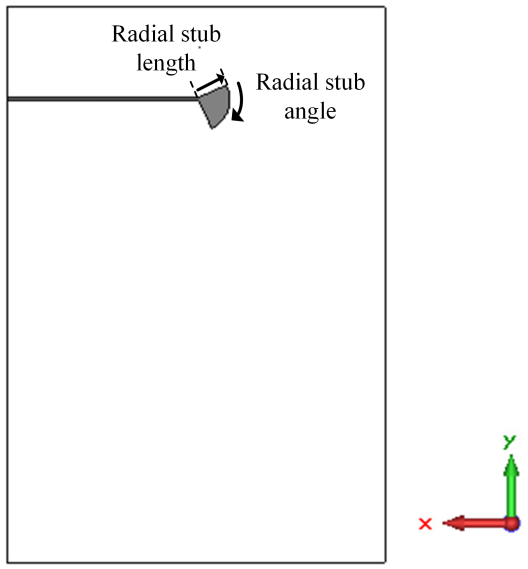

FIGURE 4.4: Top view of the simulated basic Vivaldi antenna with radial stub.

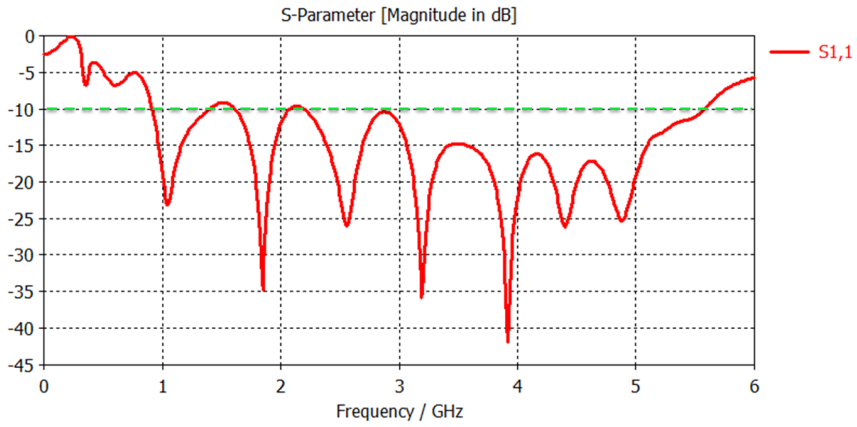

FIGURE 4.5: Simulated S_{11} for basic Vivaldi antenna.

Figure 4.6 presents the gain against frequency of the basic Vivaldi antenna. Gain is constant within the operating band of the antenna with a value of 10.2 dBi.

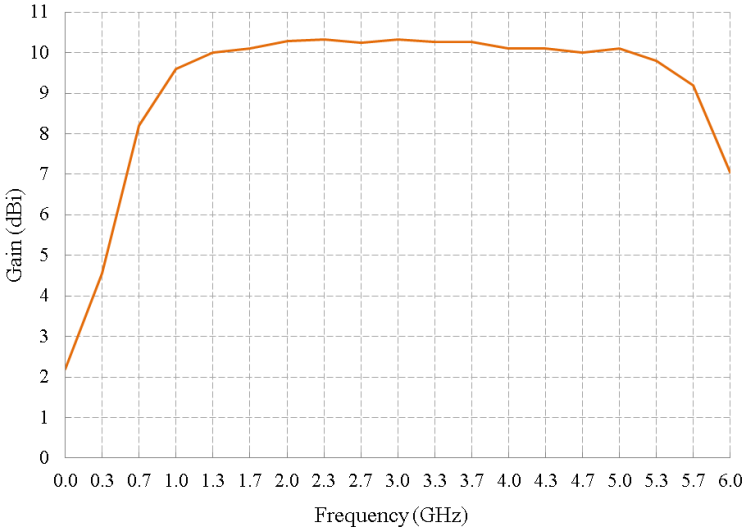

FIGURE 4.6: Simulated gain against frequency for basic Vivaldi antenna.

Figure 4.7 presents the surface current distribution in the basic Vivaldi antenna for various operating frequencies: 2 GHz, 3 GHz, 4 GHz and 5 GHz. The antenna is clearly radiating in all frequencies as the current is propagated to the open end of the Vivaldi antenna (bottom part of the pictures). The radial stub is operating as a quarter-wave stub across all frequencies and the circular slot matches the impedance in all bands achieving a flat gain as shown in Figure 4.6.

A 3D view of the radiation pattern at mid-band (3 GHz) is shown in Figure 4.8. As analysed before, this antenna has a directional beam perpendicular to the aperture. In Figure 4.9 the E-plane (red line) and the H-plane (green line) of the Vivaldi antenna are presented. E-plane has a 3 dB beamwidth of 44° and H-plane displays a 3 dB beamwidth of 58°. The main lobe is wider in the H-plane, which is because of the planar design and the curve defined by the antenna tapering. As the frequency increases the 3 dB beamwidth in the H-plane and E-plane decrease.

Figure 4.10 and Figure 4.11 show the time response and group delay of the antenna, respectively. The time signals results show a high-efficiency antenna as it presents low reflection. And group delay is constant in all bands with a peak of 2 ns at 3.36 GHz. These results are suitable for spectrum monitoring and cognitive radio applications.

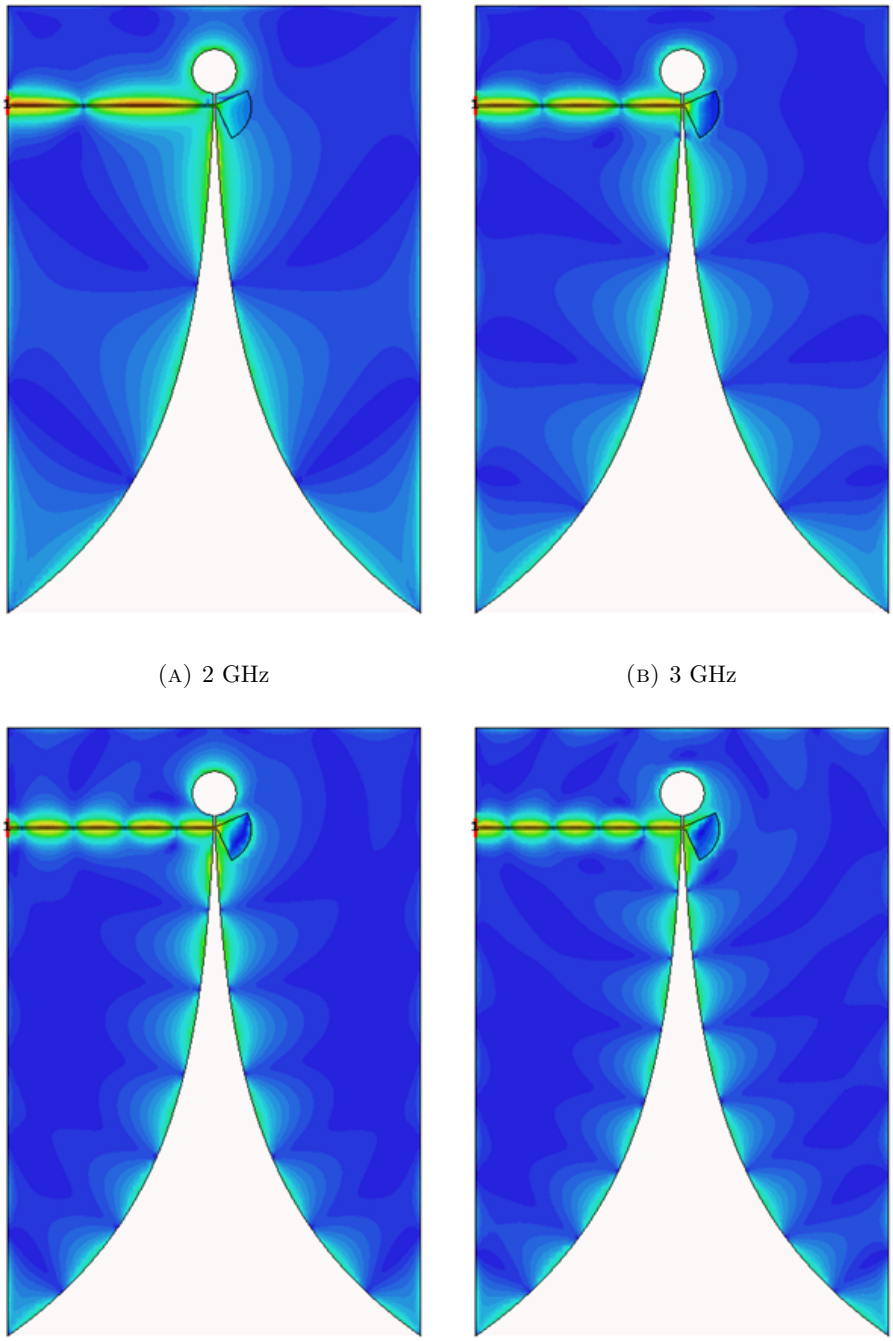

(A) 2 GHz (B) 3 GHz

(C) 4 GHz (D) 5 GHz

FIGURE 4.7: Surface current distribution for the basic Vivaldi antenna.

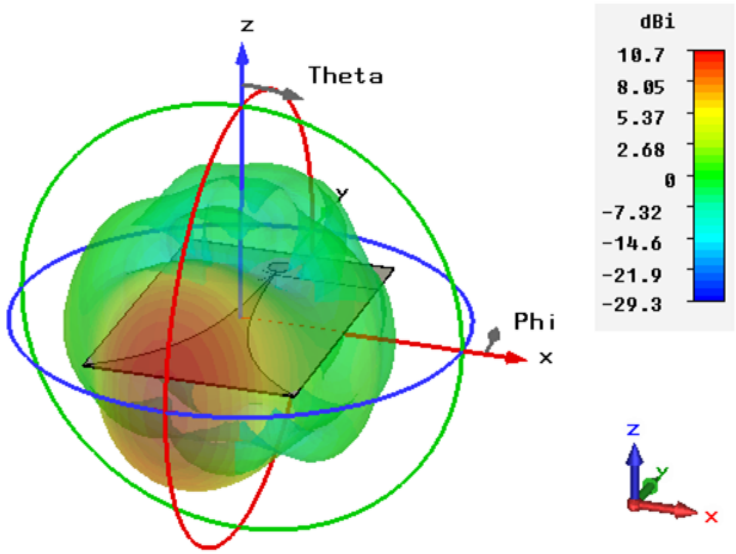

FIGURE 4.8: 3D view radiation pattern of the basic Vivaldi antenna at 3 GHz.

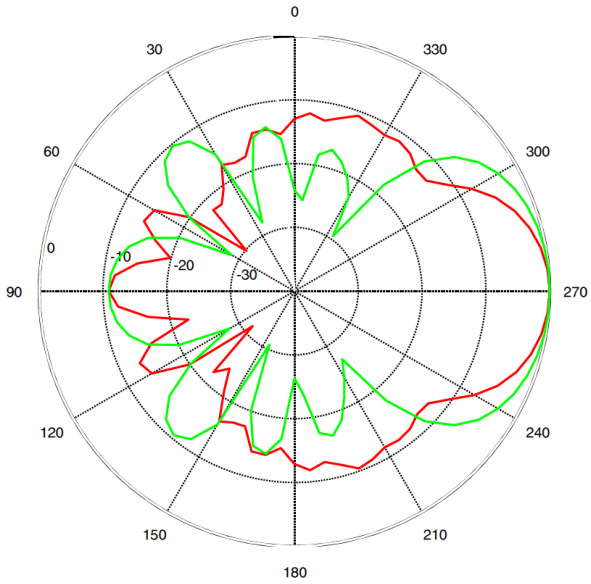

FIGURE 4.9: E-plane (red) and H-plane (green) radiation patterns of the basic Vivaldi antenna at 3 GHz.

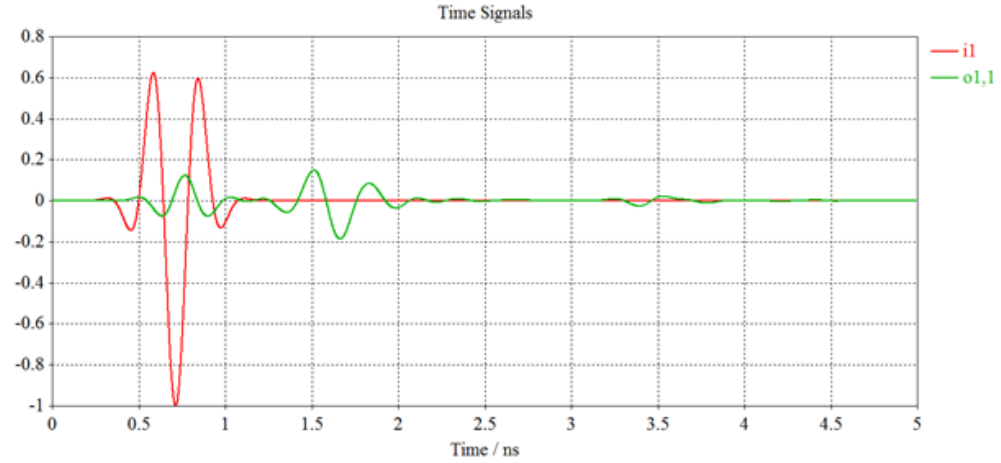

FIGURE 4.10: Simulated time signals, i1 (input signal) o1,1 (output signal) of the basic Vivaldi antenna.

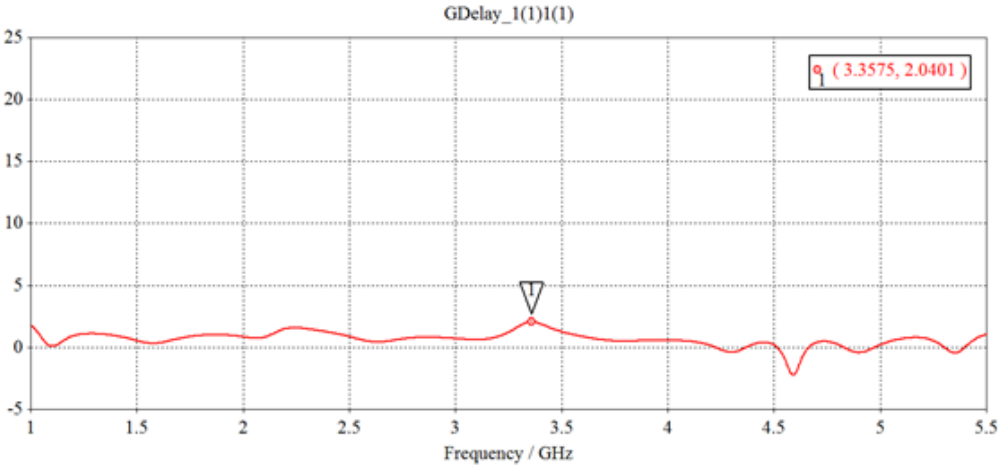

FIGURE 4.11: Simulated group delay of the basic Vivaldi antenna with a peak of 2 ns at 3.36 GHz.

4.2.2 Improvements on the basic Vivaldi antenna

While studying the basic Vivaldi antenna some ideas were implemented to improve its performance. One of these ideas is the dielectric extension. It consists of extending the substrate material at the aperture in a semi-circular shape, as shown in Figure 4.12. This extension of 72 mm enables a better matching of the radiated waves to the air minimising discontinuities.

The simulated realised gain is shown in Figure 4.13. The antenna operating frequency is not affected by the dielectric extension. On the other hand, the gain has increased by

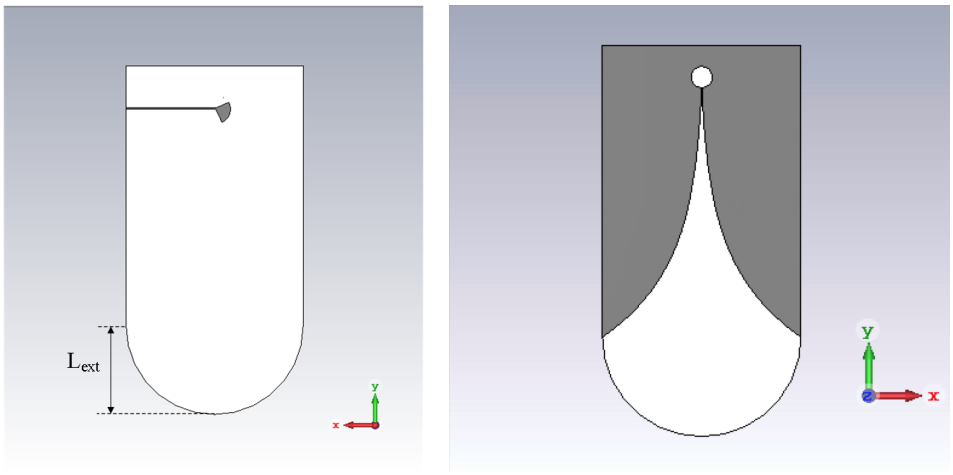

(A) Top view (B) Bottom view

FIGURE 4.12: Vivaldi antenna with dielectric extension.

up to 2 dB. Although there is a slightly increasing tendency, it can be said the gain is still stable across all operating band.

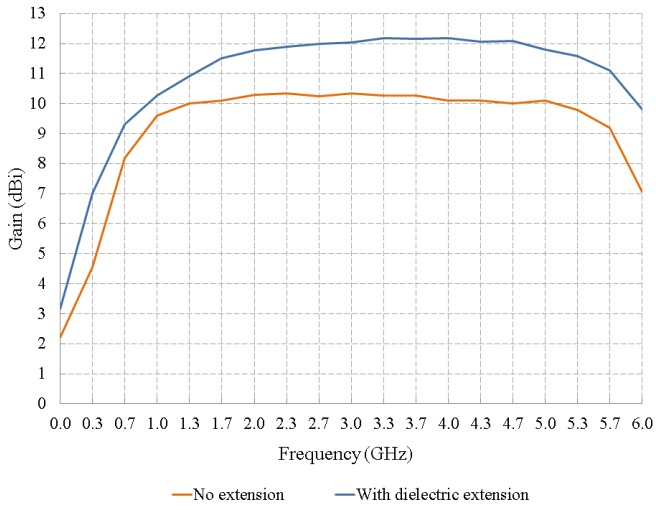

FIGURE 4.13: Simulated gain comparison of the basic Vivaldi with no extension and the basic Vivaldi with dielectric extension.

In the previous section a basic Vivaldi antenna was designed and simulated to create a benchmark for comparison. The wideband antenna operates from 1 GHz up to 5.5 GHz with stable gain of 10.2 dBi. A dielectric extension (L_{ext}) is implemented, which improves the gain by up to 2 dB. This improved antenna is used in the next sections as the basis

of the reconfigurable designs by replacing the circular and radial stubs by narrow-band stubs but maintaining the same exponential flare.

4.3 RF switch to tune a reconfigurable antenna

In order to reconfigure the proposed reconfigurable Vivaldi antenna RF switches are required. Radant RMSW100 RF-MEMS switches were chosen because they present low insertion loss, good isolation, high switching speed, low bias current and operate up to 12 GHz. Table 4.1 displays a summary of the Radant RMSW100 switch characteristics obtained from the manufacturer's datasheet [66].

Parameter	**Value**
Operating frequency	< 12 GHz
Insertion loss	0.16 dB
Isolation	24 dB
Actuation voltage	90 V
Switching speed	10^{-6} s
Bias current	10 μA

TABLE 4.1: Radant RMSW100 RF-MEMS switch characteristics [66].

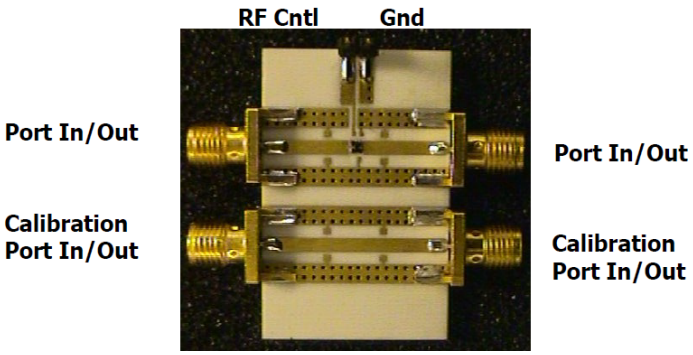

FIGURE 4.14: Radant RMSW100 RF-MEMS switches evaluation board.

An experiment was set up to measure the switch characteristics using the Agilent E5071C VNA [94] and then import the S-parameters measurements into CST MWS. The RMSW101 evaluation board provided by the manufacturer was used to measure the switch parameters (see Figure 4.14).

Figure 4.15 and Figure 4.16 show the measured reflection coefficient (S_{11}) and transmission coefficient (S_{21}) for the switch OFF mode and ON mode, respectively. The plots show an insertion loss of 0.17 dB, isolation of 23 dB and a return loss of 30 dB at 3 GHz,

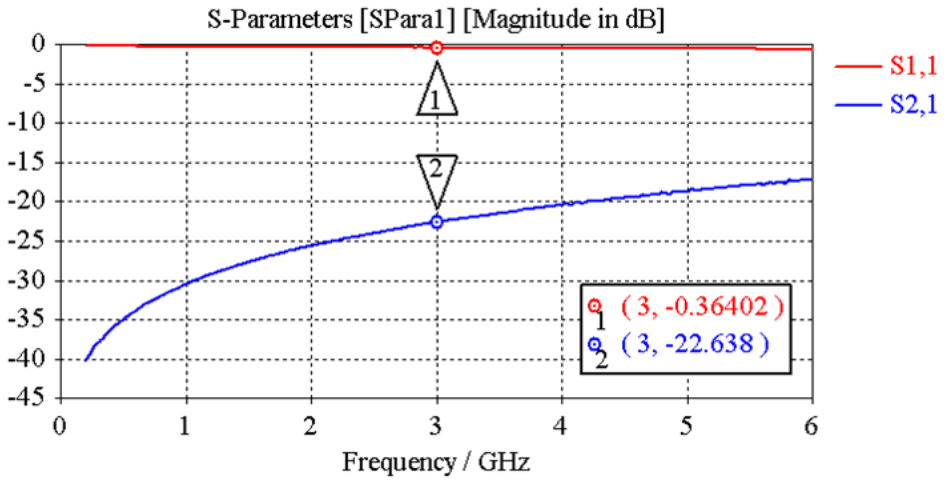

FIGURE 4.15: S-parameters for Radant RMSW100 RF-MEMS switches in OFF mode.

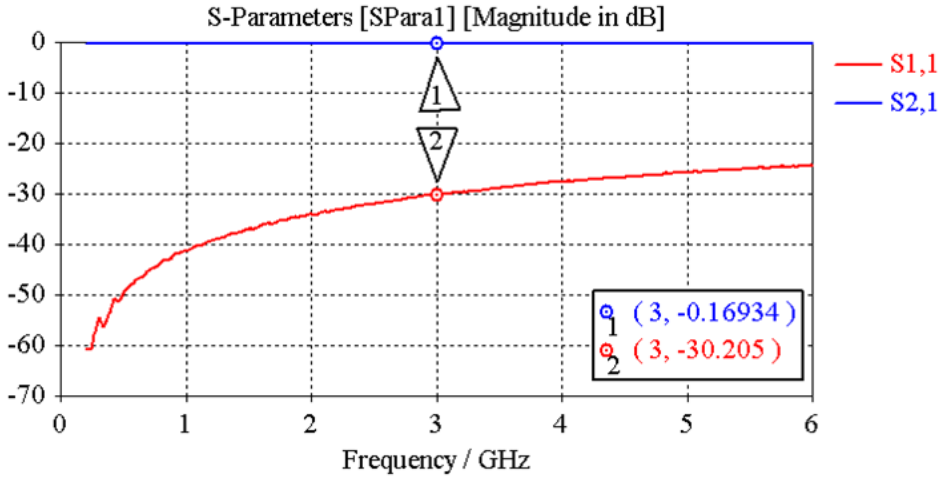

FIGURE 4.16: S-parameters for Radant RMSW100 RF-MEMS switches in ON mode.

which is in close agreement with the data provided by the manufacturer. Therefore, the Radant MEMS RMSW100 switches are good candidates to be used for frequency reconfigurable antennas.

The recommended actuation voltage is 90 V. Therefore, these switches require a driver. The Radant RMDR1000 driver provided by the manufacturer is used. The driver board has a microcontroller that needs to be programmed in advance as shown in Figure 4.17.

All these characteristics and requirements are taken into account to design the reconfigurable Vivaldi antenna as discussed in the next section. The measured reflection and transmission coefficients are imported into CST MWS to get more accurate results.

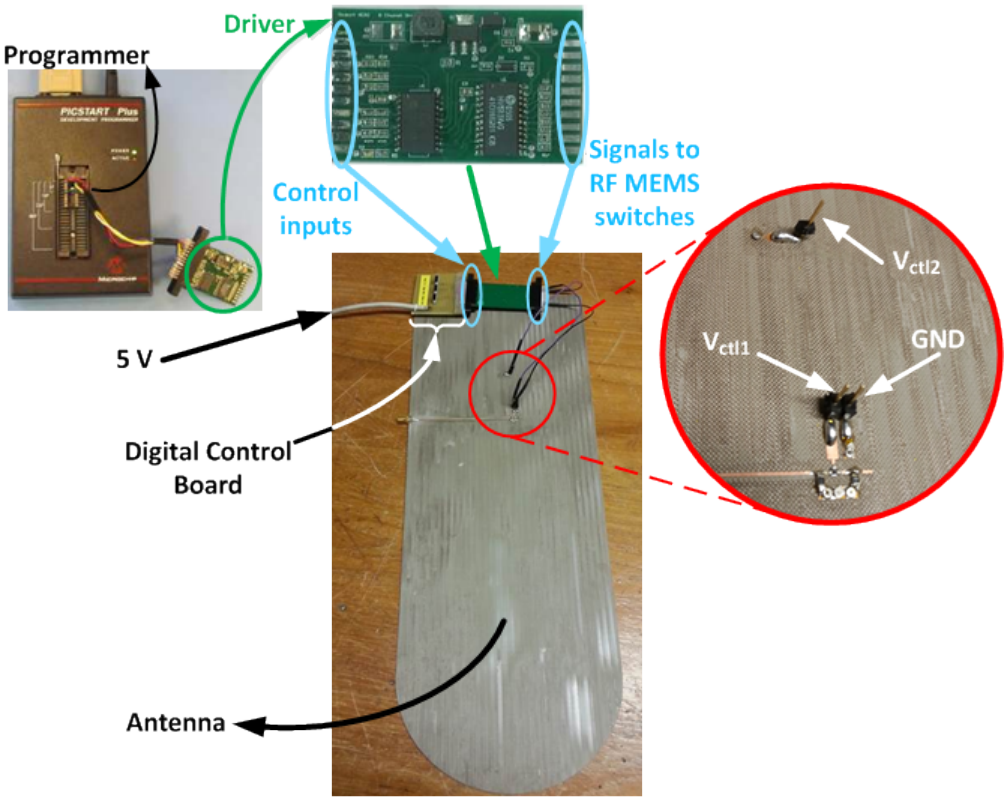

FIGURE 4.17: Experiment setup for Design A.

Figure 4.17 presents a block diagram of the experiment setup for Design A with the RF MEMS switches, RF MEMS driver, programmer and digital control board. The driver, which provides the voltage required to actuate the RF MEMS switches, is programmed using the PIC programmer. The digital control board provides the user interface with SPDT switches to change the switches states. The digital control board is connected to the driver. The driver reads the signals from the digital control board and sends the required signals to the RF MEMS switches with V_{ctl1} and V_{ctl2} to operate at the low band or at the high band. RF Ground (GND) is also connected to the antenna.

4.4 Frequency-reconfigurable Vivaldi antenna

As seen in the basic Vivaldi antenna previously presented, the quarter-wave stubs cause the antenna to operate in a narrower band. This is the reason why in the basic Vivaldi a circular stub and a radial stub are introduced. Nevertheless, to design a frequency-reconfigurable Vivaldi antenna a narrower band compared to the basic Vivaldi antenna

is required. This narrower band is achieved by the quarter-wave stubs introduced at the beginning of this chapter.

4.4.1 Technical Analysis

In this new reconfigurable design, frequency reconfiguration is accomplished by RF switches introduced in the stub of the feed line (Sw 1) and the slot line (Sw 2), as shown in Figure 4.18. The positions of these switches determine the effective length of the slot and the stub based on the required operating frequency. The RF switches control the current path while setting a maximum in the stub-to-slot intersection to produce a higher operating band. To operate in the lower band, the switches allow the current path to use the full length of the stub and the slot.

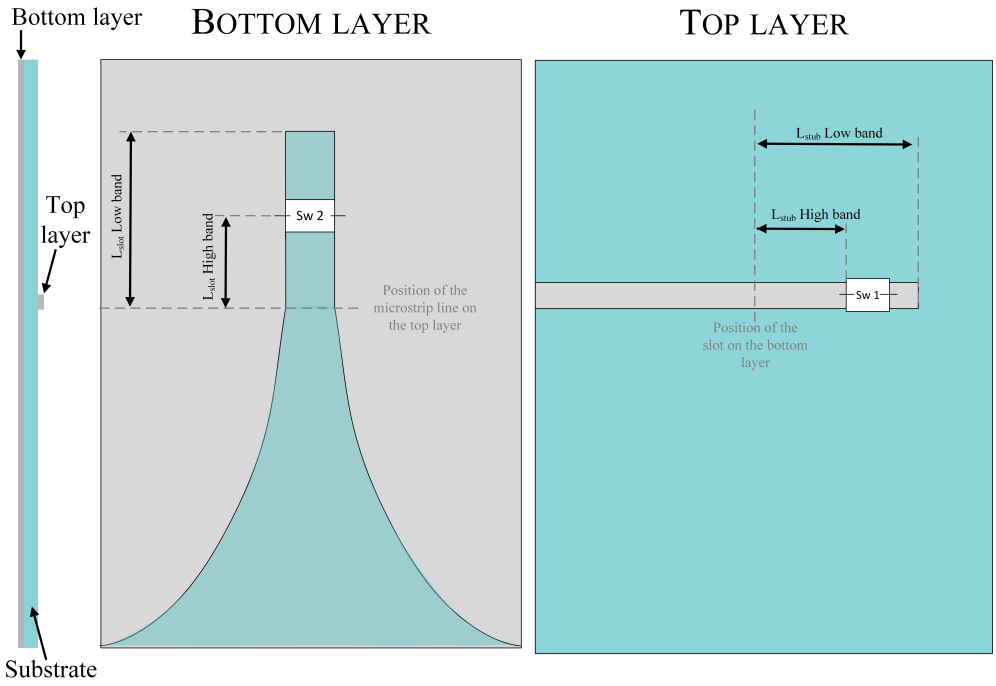

FIGURE 4.18: Geometry of the dual-band switched design with two RF switches, indicating the lengths of the stub and the slot.

$$\lambda_g = \frac{\lambda_0}{\sqrt{\varepsilon_{eff}}} \tag{4.5}$$

The effective length of the stub and the slot follow equation 4.6, where λ_g is the guided wavelength in the stub (approximated as in equation 4.5) and λ_0 is the free-space wavelength that propagates through the slot at the centre frequency of the band. For the

low-band mode the current path is using the full length of both the stub and the slot and for the high-band mode the stub and the slot lengths are shortened at the RF switches positions.

$$\begin{aligned} L_{stub} &= \frac{\lambda_g}{4} \\ L_{slot} &= \frac{3}{4} \cdot \lambda_0 \end{aligned} \tag{4.6}$$

To understand how the reconfiguration works the current distribution in the stub and slot is analysed. The stub terminates with an open-circuit, which means the current is zero at the end of the microstrip line. To get the maximum current propagated from the stub to the slot, the current at the stub-to-slot intersection needs to be maximum. Therefore, the distance between the end of the stub and the intersection to the slot should be $\lambda/4$ at the centre frequency of the band. This method maintains a well matched stub-to-slot intersection only in a narrow frequency range.

The slot line terminates with a short circuit, which causes a maximum in the current path at that point. Therefore, the distance to the stub-to-slot intersection should be $3/4 \cdot \lambda$ to force a zero just above the intersection. As a consequence, the current is propagated in phase to the aperture of the Vivaldi. For out-of-band frequencies, the current is resonating in the stub or the slot, thus the antenna does not radiate as no current is propagated to the exponentially tapered aperture.

Therefore, the procedure to design a frequency-reconfigurable Vivaldi antenna goes as follows: the Vivaldi antenna is designed first for the required low band and then the RF switches are introduced in the stub and slot at the calculated distances to enable a high band. When calculating the length of the stub and slot and the position of the RF switches, some bands can also be rejected by forcing a minimum of current propagated to the slot. Taking this into account, a reconfigurable Vivaldi antenna with high isolation can be designed by rejecting the operating high-band in low-band mode and vice versa.

Next, the current distribution for each mode of configuration is presented for a better understanding of the operation. Figure 4.19 shows the current for the low-band mode. In this mode the current uses the full length of the stub and the slot. Number 2 and number 3 indicate the position of the RF switches in the antenna. When the antenna is in in-band operation (left image) there is a maximum in the stub-to-slot intersection and the current is propagating to the aperture of the Vivaldi antenna. But, when the antenna is in out-of-band operation (right image) the small amount of current that is

transmitted to the slot is resonating in the slot and is not propagating to the antenna aperture, thus the antenna does not radiate.

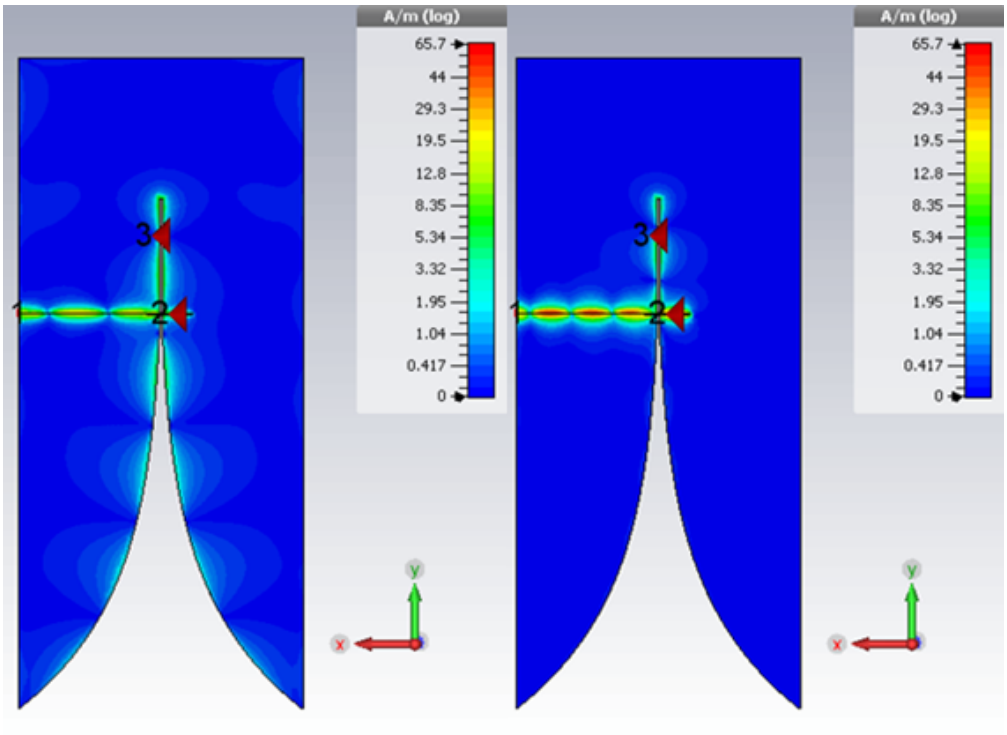

FIGURE 4.19: Current distribution for low-band mode. Left image is in-band operation, right image is out-band operation.

Figure 4.20 presents the current distribution for the high-band mode. In this case, the RF switches force the current to have a shorter path so that the maximum coupling to the slot happens at a higher frequency. The left image shows the antenna in in-band operation and the right image shows the antenna in out-of-band operation, where the current is resonating in the slot line instead of propagated to the antenna aperture.

These rejected bands in out-of-band operation contribute to the high isolation of this reconfigurable design. Furthermore, the high-isolated bands can be tuned easily by adjusting the lengths of the stub and slot line and the position of the RF switches.

4.4.2 Dual-band switched design

The dual-band switched Vivaldi design is produced on a single microwave substrate, as shown in Figure 4.18. The bottom layer is composed of a slot inserted in an exponentially tapered aperture, making the beamwidth stable from 1 GHz to 6 GHz. In the top layer,

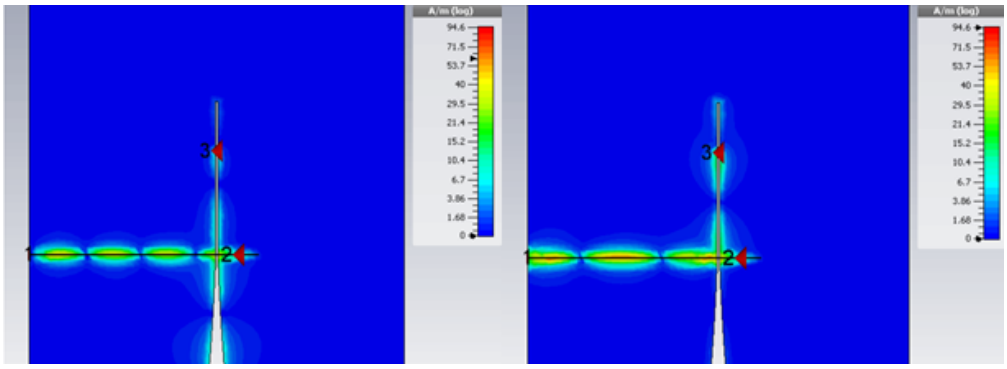

FIGURE 4.20: Current distribution for high-band mode. Left image is in-band operation, right image is out-band operation.

a microstrip line terminated with a stub is used to excite the antenna. The position and length of the stub and the widths of the stub and slot have been optimised for maximising signal coupling.

Two RF switches are introduced, one in the stub and one in the slot, as shown in Figure 4.18. The frequency response of the switches has been analysed and considered in the antenna simulation using CST Microwave Studio. The location of the switches has been optimised for switching between a higher band and a lower band. The distance to the stub-to-slot intersection is calculated as shown in equations 4.7, where $\lambda_{g,HB}$ is the guided wavelength in the stub and $\lambda_{0,HB}$ is the free-space wavelength, at the centre frequency of the high band (HB). LB indicates the low band. Table 4.2 describes the operation of the RF switches for each mode.

$$\begin{aligned} L_{stub,\,High\ band} &= \frac{\lambda_{g,\,HB}}{4} \qquad L_{slot,\,High\ band} = \frac{3}{4}\cdot\lambda_{0,\,HB} \\ L_{stub,\,Low\ band} &= \frac{\lambda_{g,\,LB}}{4} \qquad L_{slot,\,Low\ band} = \frac{3}{4}\cdot\lambda_{0,\,LB} \end{aligned} \tag{4.7}$$

	Switch	**Low band**	**High band**
Stub switch	Switch 1	ON	OFF
Slot switch	Switch 2	OFF	ON

TABLE 4.2: Operation of the switches for low-band mode and high-band mode.

4.4.3 Tri-band switched design

For the tri-band switched Vivaldi design two RF switches are introduced in the stub and two more in the slot, four in total. These switches allow the antenna to operate in three different operating bands: a low band, a mid band and a high band. The position of these switches determine the effective length of the stub and the slot, as shown in equations 4.8, where HB indicates the high band, MB indicates the mid band and LB, the low band. Figure 4.21 shows the geometry of the antenna with the four RF switches. Table 4.3 presents the operation of the RF switches for each of the three bands.

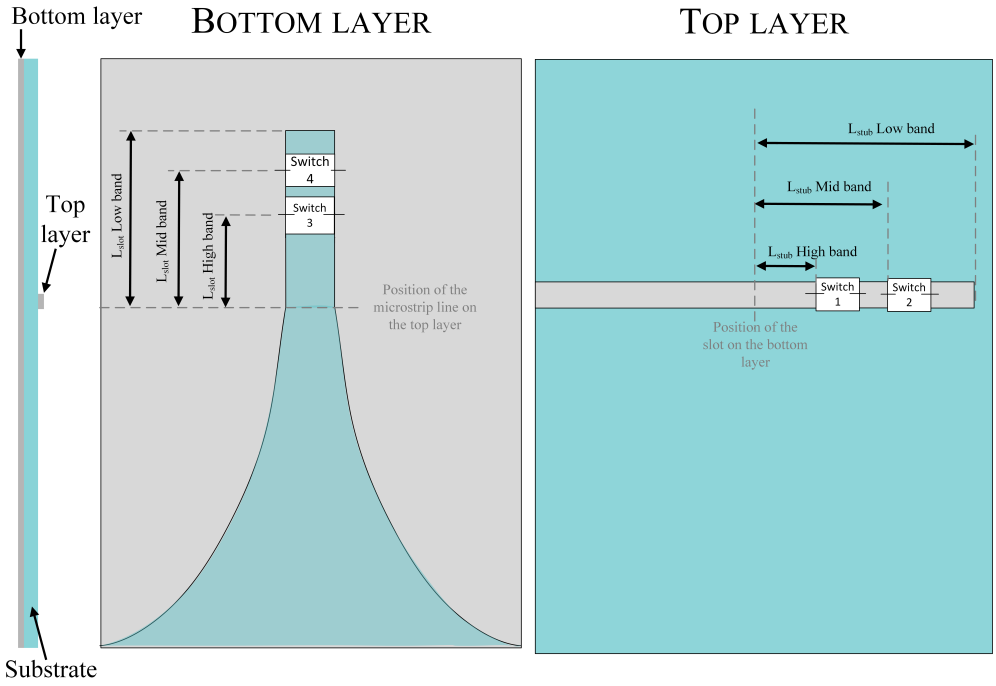

FIGURE 4.21: Geometry of the tri-band switched design using four switches, indicating the position in the stub and the slot.

$$
\begin{aligned}
L_{stub,\,High\ band} &= \frac{\lambda_{g,HB}}{4} \qquad L_{slot,\,High\ band} = \frac{3}{4}\cdot\lambda_{0,HB} \\
L_{stub,\,Mid\ band} &= \frac{\lambda_{g,MB}}{4} \qquad L_{slot,\,Mid\ band} = \frac{3}{4}\cdot\lambda_{0,MB} \\
L_{stub,\,Low\ band} &= \frac{\lambda_{g,LB}}{4} \qquad L_{slot,\,Low\ band} = \frac{3}{4}\cdot\lambda_{0,LB}
\end{aligned}
\tag{4.8}
$$

	Switch	Low band	Mid band	High band
Stub	Switch 1	ON	ON	OFF
Switches	Switch 2	ON	OFF	OFF
Slot	Switch 3	OFF	OFF	ON
Switches	Switch 4	OFF	ON	OFF

TABLE 4.3: Operation of the switches for low-band mode, mid-band mode and high-band mode.

4.4.4 Quad-band switched design

The quad-band switched Vivaldi design inserts three RF switches in the stub and three RF switches in the slot. These switches allow the antenna to work in four different frequency bands to cover all bands from 1.5 GHz up to 6 GHz: a low band, two mid bands and a high band. The position of these switches determine the effective length of the stubs, as shown in equations 4.9, where HB indicates the high band, MB2 indicates the highest mid band, MB1 indicates the lowest mid band and LB indicates the low band. Figure 4.22 presents the geometry of the antenna with the RF switches. Table 4.4 displays the switch configuration for each band.

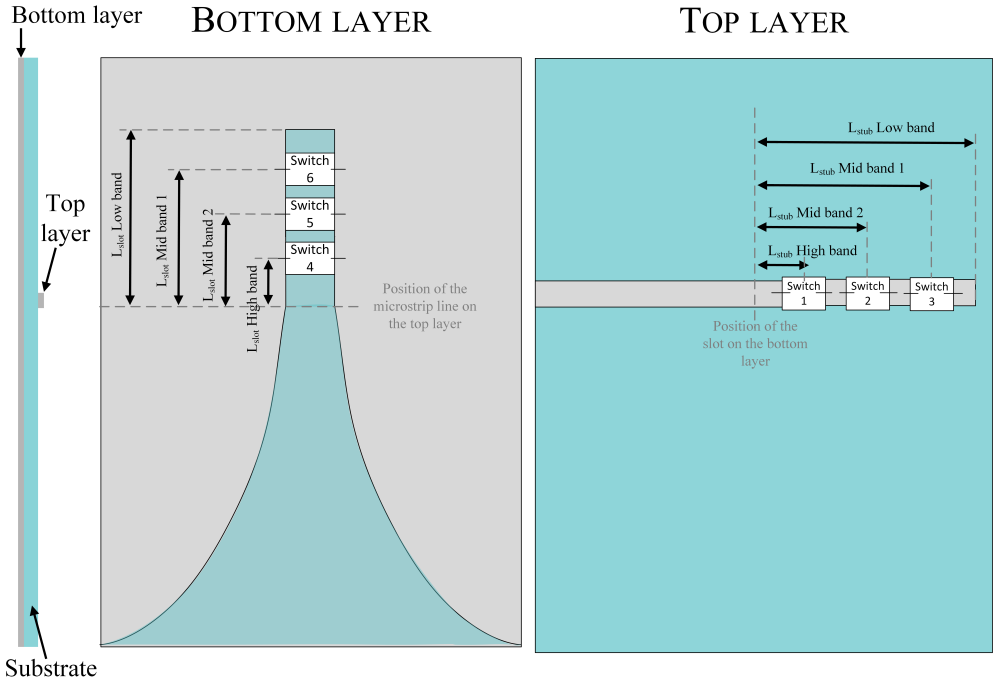

FIGURE 4.22: Geometry of the quad-band switched design using six switches and indicating the position of the switches in the stub and the slot.

$$
\begin{aligned}
L_{stub,\,High\ band} &= \frac{\lambda_{g,HB}}{4} & L_{slot,\,High\ band} &= \frac{3}{4}\cdot\lambda_{0,HB} \\
L_{stub,\,Mid\ band2} &= \frac{\lambda_{g,MB2}}{4} & L_{slot,\,Mid\ band2} &= \frac{3}{4}\cdot\lambda_{0,MB2} \\
L_{stub,\,Mid\ band1} &= \frac{\lambda_{g,MB1}}{4} & L_{slot,\,Mid\ band1} &= \frac{3}{4}\cdot\lambda_{0,MB1} \\
L_{stub,\,Low\ band} &= \frac{\lambda_{g,LB}}{4} & L_{slot,\,Low\ band} &= \frac{3}{4}\cdot\lambda_{0,LB}
\end{aligned}
\tag{4.9}
$$

	Switch	**Low band**	**Mid band 1**	**Mid band 2**	**High band**
Stub	Switch 1	ON	ON	ON	OFF
	Switch 2	ON	ON	OFF	OFF
Switches	Switch 3	ON	OFF	OFF	OFF
Slot	Switch 4	OFF	OFF	OFF	ON
	Switch 5	OFF	OFF	ON	OFF
Switches	Switch 6	OFF	ON	OFF	OFF

TABLE 4.4: Switch configuration for the quad-band switched Vivaldi antenna.

4.5 Simulation results

Once the geometry of the three reconfigurable Vivaldi designs is presented, the obtained CST simulation results are discussed.

4.5.1 Dual-band switched design

The simulated S_{11} parameter and realised gain for the dual-band switched Vivaldi antenna are shown in Figure 4.23. The realised gain is calculated at $(\theta, \phi) = (90°,\ -90°)$, which is the direction of the main lobe, perpendicular to the aperture. Red lines indicate the low band and blue lines present the high band.

Analysing the results, the in-band gain for each band is stable and drops outside the band, presenting high isolation between bands making it suitable for security applications such as spectrum monitoring. The obtained operating bands and gain in each mode of the antenna are presented in Table 4.5. High isolation between bands is achieved. In low-band mode the isolation is up to 23 dB and in high-band mode the isolation goes up to 28.5 dB.

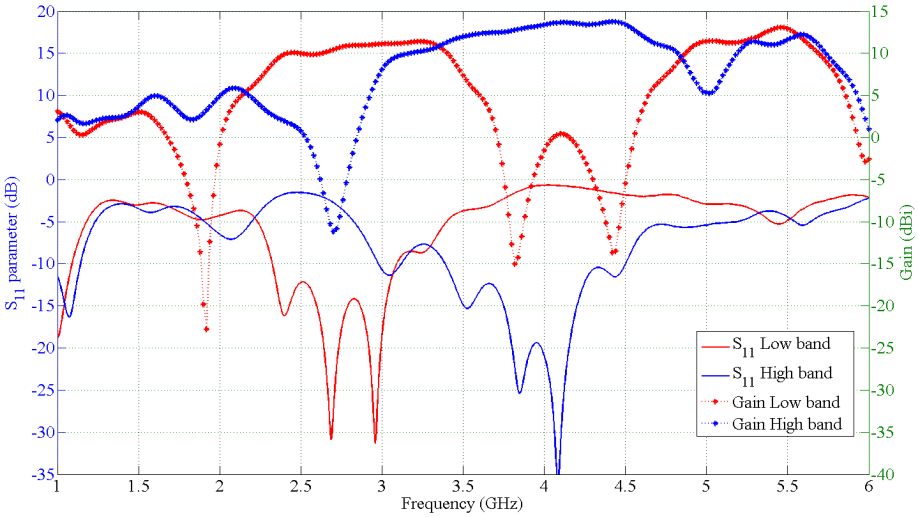

FIGURE 4.23: Simulated S_{11} parameter and realised gain of the dual-band switched Vivaldi antenna.

	Frequency range (centre)	*Bandwidth*	*Gain*
Low band	2.33-3.02 GHz (2.7 GHz)	0.69 GHz	10.00-11.78 dBi
High band	3.29-4.58 GHz (3.9 GHz)	1.29 GHz	11.32-13.65 dBi

TABLE 4.5: Simulated frequency and gain results for the dual-band switched Vivaldi antenna.

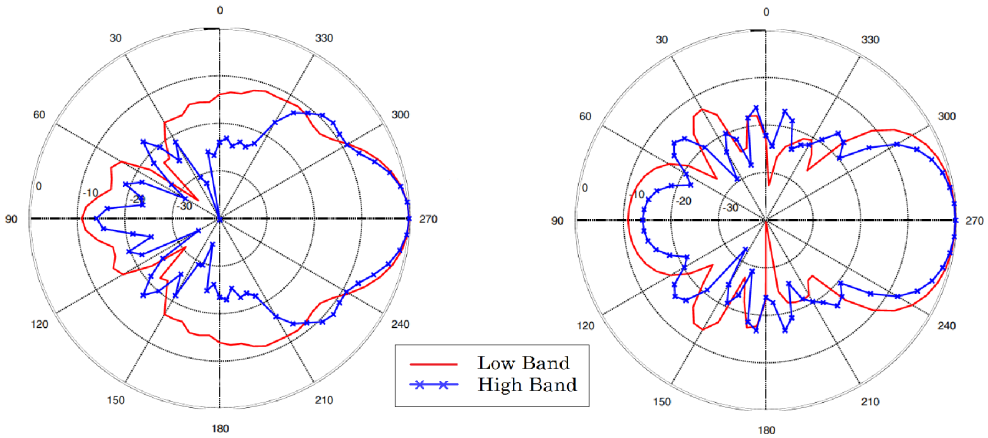

FIGURE 4.24: Simulated E-plane radiation pattern (left) and H-plane radiation pattern (right) of the dual-band switched Vivaldi antenna at 2.7 GHz for the low band and at 3.9 GHz for the high band.

The normalised radiation patterns of the dual-band switched antenna are shown in Figure 4.24. Half-Power Beamwidth (HPBW) of the E-plane is 33.9° for the low band and 29.9° for the high band. HPBW of the H-plane for the low band is 52.3° and for the high band 41.4°. Therefore, the radiation pattern for both bands is similar in E-plane and H-plane, with the biggest difference in the H-plane. This is because of the planar design of the Vivaldi antenna.

4.5.2 Tri-band switched design

The simulated S_{11} parameter and gain for the tri-band switched design of the Vivaldi antenna at different operating bands are shown in Figure 4.25. The realised in-band gain is stable and drops rapidly in the immediate proximity of the edges of the operating band. As the electrical size of the radiating aperture varies with operating frequency, the maximum gain variation is 2.2 dB within a band. The gain tends to increase in frequency with a linear trend. Table 4.6 summarises the obtained results on operating bands and realised gain and Table 4.7 shows the HPBW for the E-plane and H-plane of each band.

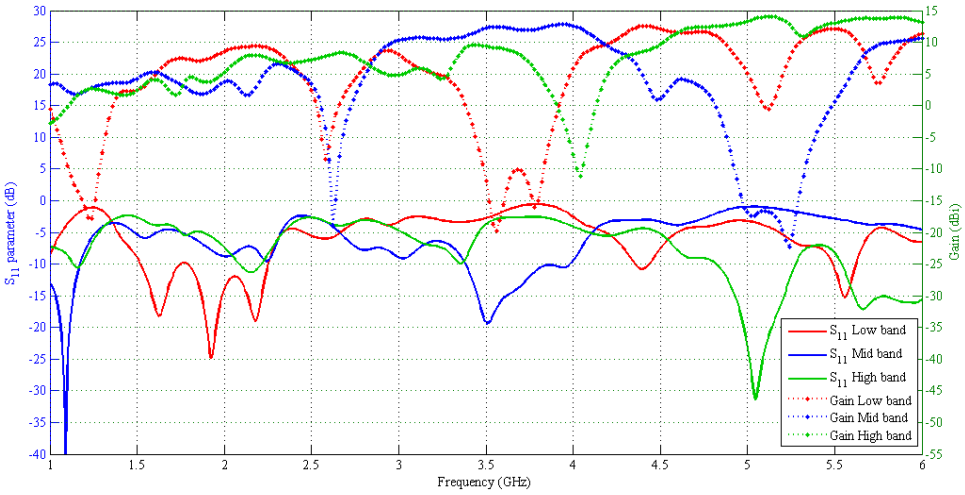

FIGURE 4.25: Simulated S_{11} parameter and realised gain of the tri-band reconfigurable Vivaldi antenna for low-band, mid-band and high-band modes.

In Figure 4.26 the radiation pattern for the E-plane and H-plane are presented. The direction of the main lobe is constant in all bands at $(\theta, \phi) = (90°, \ -90°)$. H-plane HPBW is decreasing significantly, but it is stable in E-plane. Overall the radiation pattern is maintained for all bands. There is a bigger difference in the H-plane of this design compared to the dual-band because the frequency bands are further apart.

	Frequency range (centre)	*Bandwidth*	*Gain*
Low band	1.5-2.25 GHz (1.88 GHz)	750 MHz	8.7-9.8 dBi
Mid band	3.4-4.0 GHz (3.7 GHz)	600 MHz	12.5-13.7 dBi
High band	4.8-5.25 GHz (5.03 GHz)	450 MHz	13.8-14.9 dBi

TABLE 4.6: Simulated frequency and gain results for the tri-band switched Vivaldi antenna.

		3 dB beamwidth	
	Centre freq.	*E-plane*	*H-plane*
Low band	2.0 GHz	63.6°	77.5°
Mid band	3.75 GHz	28.3°	41.2°
High band	5.2 GHz	25.1°	22.6°

TABLE 4.7: Simulated radiation pattern results for the tri-band switched design.

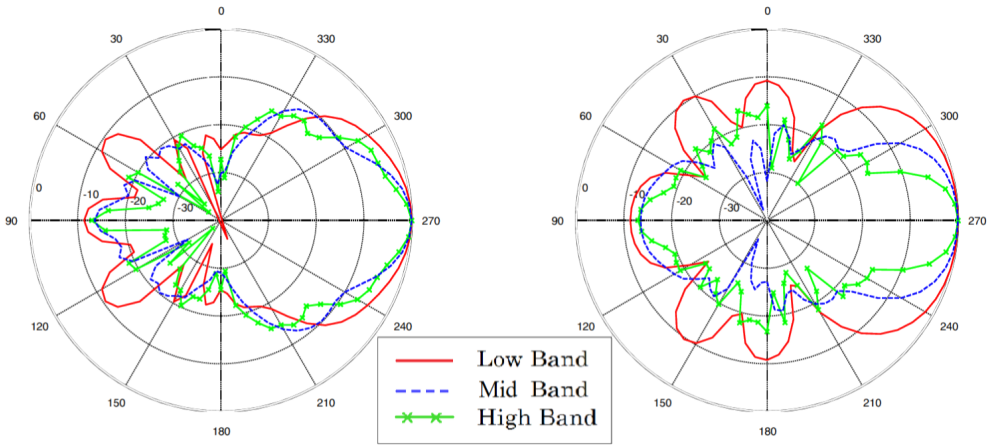

FIGURE 4.26: Simulated E-plane radiation pattern (left) and H-plane radiation pattern (right) of the tri-band design at 2 GHz for the low band, at 3.75 GHz for the mid band and at 5.2 GHz for the high band.

4.5.3 Quad-band switched design

For the quad-band switched design, all frequencies from 1.5 GHz to 6 GHz are covered divided in 4 bands. Figure 4.27 shows the S_{11} response on the left axis and the realised gain in the direction of maximum radiation $(\theta, \phi) = (90°, -90°)$ on the right axis where LB is low band, MB1 and MB2 are mid band 1 and mid band 2 respectively, and HB is high band. The gain is stable within each band and drops outside the band, providing high isolation between bands of up to 30 dB. It also tends to increase with frequency in a linear trend. A good isolation between bands combined with wide operating bandwidth

can be very useful for spectrum monitoring in case there is a jamming signal that needs to be suppressed to be able to receive communications without saturating the receiver. Table 4.8 summarises the results of frequency and realised gain obtained.

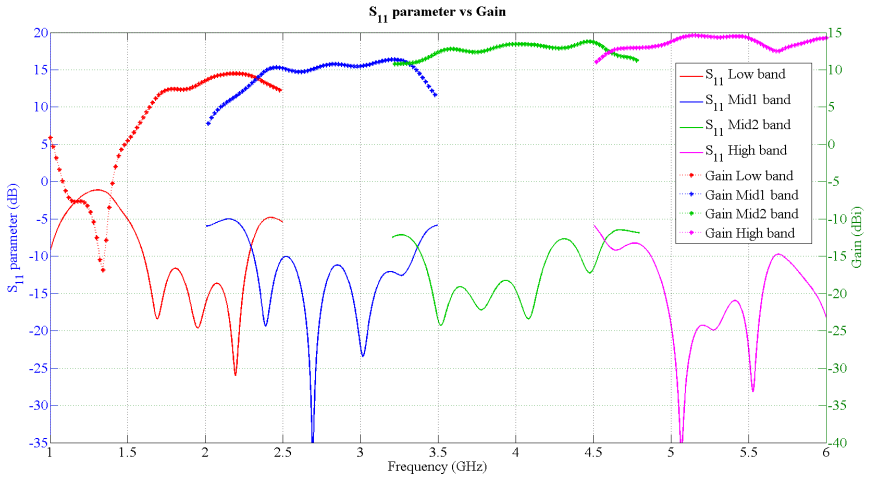

FIGURE 4.27: Simulated S_{11} parameter and realised gain of the quad-band switched Vivaldi antenna.

	Frequency range (centre)	*Bandwidth*	*Gain*
Low band	1.65-2.35 GHz (2 GHz)	700 MHz	8.5-10.0 dBi
Mid band 1	2.3-3.3 GHz (2.8 GHz)	1000 MHz	10.2-11.3 dBi
Mid band 2	3.4-4.4 GHz (3.9 GHz)	1000 MHz	11.2-13.2 dBi
High band	4.55-6.0 GHz (5.3 GHz)	1500 MHz	13.4-15.0 dBi

TABLE 4.8: Simulated frequency and gain results for the quad-band switched Vivaldi antenna.

In Figure 4.28 the 3D radiation patterns of the four bands are presented. Direction of the main lobe is maintained in all four bands. HPBW is stable in the E-plane and decreases in frequency when looking at the H-plane, from 70° at the lowest frequency to 20° at the highest frequency. This is because the high frequencies are being affected by the big aperture needed for the radiation at the lowest frequency.

Figure 4.29 shows the polar plot of the radiation patterns for the E-plane on the left image and H-plane on the right image. In the E-plane, the HPBW is 63° for the low band and down to 28° for the high band and 32° for the mid bands. In the H-plane, the low band HPBW is 70°, in the mid band 1 is 56°, in the mid band 2 is 41° and in the high band is 25°. The direction of the main lobe is $(\theta, \phi) = (90°, \ -90°)$ in each band

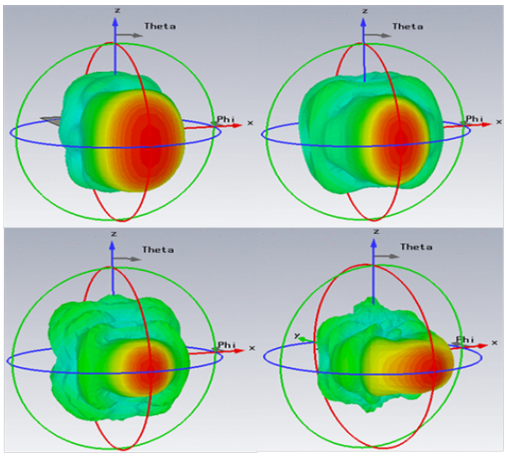

FIGURE 4.28: Radiation pattern of quad-band design at 2 GHz (Top-left), 3 GHz (Top-right), 4 GHz (Bottom-left) and 5 GHz (Bottom-right).

and the HPBW has a big change only in the H-plane because of the planar antenna design.

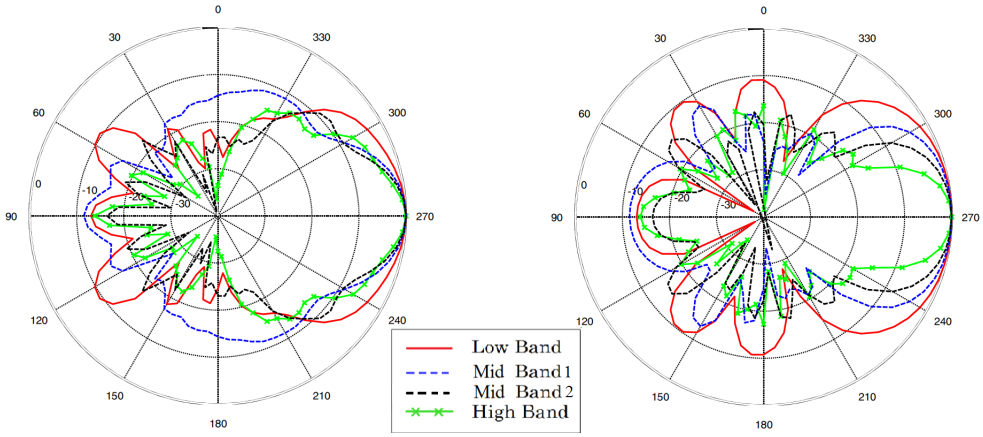

FIGURE 4.29: Simulated E-plane radiation patterns (left) and H-plane radiation patterns (right) of the quad-band switched design at 2 GHz for the low band, at 2.8 GHz for the mid band 1, at 3.9 GHz for the mid band 2 and at 5.3 GHz for the high band.

4.6 Measurements for design A: dual-band reconfigurable Vivaldi antenna using RF-MEMS switches

Once good simulation results were achieved, a dual-band prototype was fabricated and tested. The prototype was fabricated in the departmental workshop using a milling machine. The milling machine removes the copper line by line, but the etching machine

cannot be used as the antenna design is too big. Figure 4.30 and Figure 4.31 present the fabricated prototype top layer and bottom layer respectively. RF-MEMS switches are soldered manually. The datasheet requests a wire bonding machine to be used for soldering, but this machine was inaccessible. This made soldering very difficult because the pads of the switch are very small and the switch is ESD sensitive. Figure 4.32 and Figure 4.33 show a zoom in the switch positions that were soldered manually to the antenna. In the stub, two capacitors are required for the switch to operate properly.

FIGURE 4.30: Top layer connected to the Radant driver to control the switches of the prototype for design A.

FIGURE 4.31: Bottom layer of the prototype for design A.

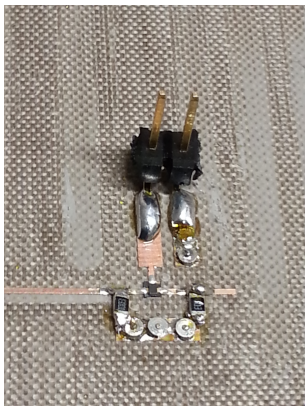

FIGURE 4.32: Zoom in the microstrip line stub for prototype of design A.

FIGURE 4.33: Zoom in the slot switch for prototype of design A.

The antenna reflection coefficient results are shown in Figure 4.34. Solid lines are the measured results and dashed lines are the simulated results for comparison. The measurements differ from the simulation results in terms of bandwidth, operating frequencies and level of matching. As reflection coefficient results did not present good matching, gain was not measured for design A as results would be inconclusive.

The Radant RF-MEMS switches theoretically seemed to be a good candidate for reconfigurable antennas, but in practice they proved to be very difficult to integrate in an antenna design, lossy and the biasing was complicated. Furthermore, they demanded a 90 V actuation voltage which requires an expensive driver circuit with high voltages affecting the antenna performance, making it not suitable for low-cost designs. In addition, they are ESD sensitive which made device handling difficult. Also the performance of these switches degrades with time. They may present good parameters theoretically but when applied to antennas they do not offer good results.

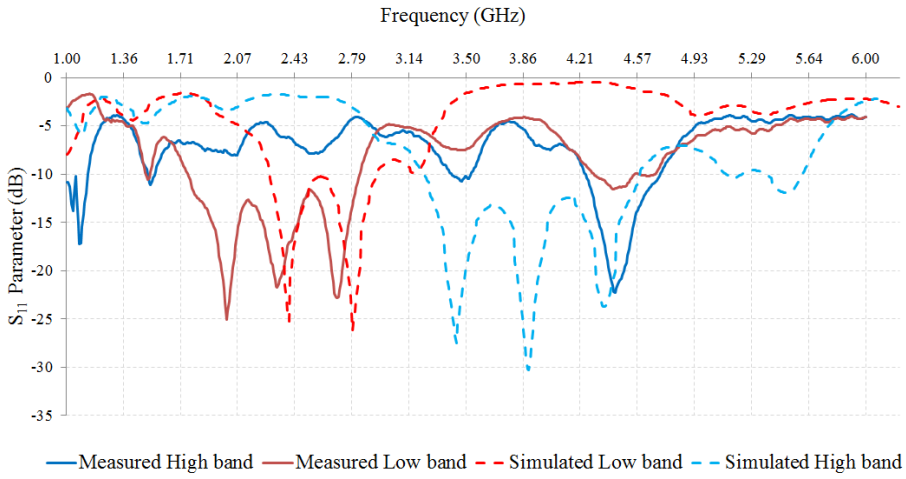

FIGURE 4.34: Measured and simulated reflection coefficient for design A.

In the next section of this chapter a low insertion loss GaAs MMIC RF switch is considered for design B. Moreover, as the fabricated prototype of design A is bigger than an A4 it had to be milled because it did not fit into the workshop's etching machine. For next design the Vivaldi antenna is adapted so that it can fit in the etching tank. The etching technique provides higher resolution (up to 50 μm) for small parts and removes the copper with higher accuracy compared to the milling technique.

4.7 Design B: dual-band reconfigurable Vivaldi antenna using a GaAs MMIC switch

Since design A measurements did not agree well with simulation and the proposed RF-MEMS switches are not suitable for manual soldering, a new design is proposed: a dual-band reconfigurable Vivaldi antenna using a GaAs Monolithic Microwave Integrated Circuit (MMIC) switch (Hittite HMC550AE [68]).

These switches are low cost, do not require a driver as their control voltage is 5 V and are easy to solder as they are provided in a SOT26 SMT package. As discussed in the literature review, the GaAs MMIC switches provide some advantages over the other technologies for the purpose of this project, such as low insertion loss, fast switching, low actuation voltage and low cost.

Despite the limited isolation it is a good candidate for this project. The RF switches used in this research project are Hittite HMC550AE SPST which operate from DC to 6 GHz [68].

In order to test the dual-band switched design of the Vivaldi antenna, first the design is adapted to be fabricated in the departmental workshop for fast prototyping. The design requirements of the HMC550AE are taken into account as well. Despite the improvements on gain this design B does not implement the dielectric extension because it has been optimised to the dimensions of the departmental workshop.

4.7.1 Antenna geometry

For design B the reconfiguration is performed using only one switch to simplify the fabrication and measurement processes. The switch is introduced into the slot to control the operating bands, as presented in Figure 4.35. Therefore, the length of the stub is the same for both bands which needs to be a compromise between the 2 modes of operation. This constraint can reduce the isolation between bands.

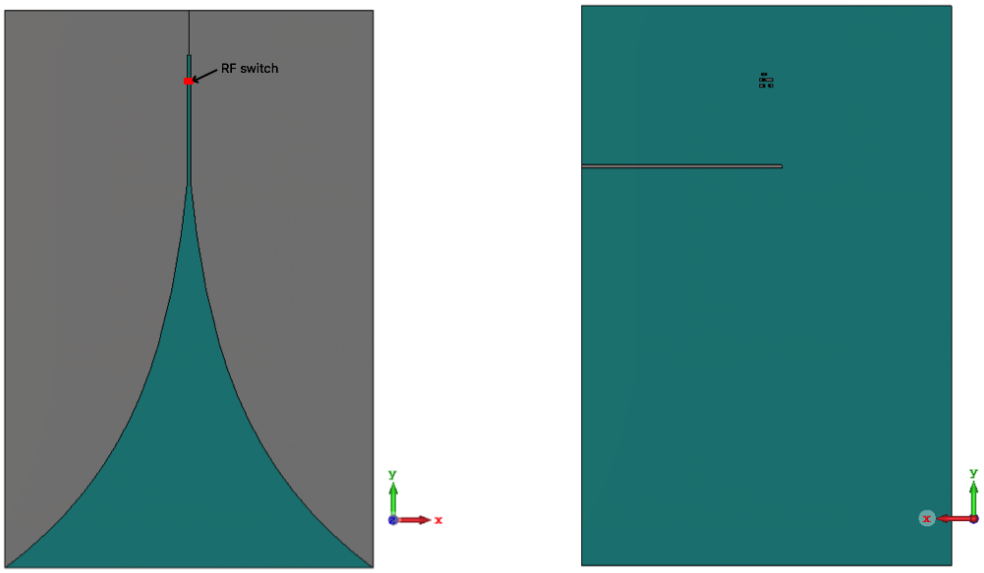

FIGURE 4.35: Bottom layer (left) and top layer (right) of CST model of design B.

The design parameters and their values are indicated in Table 4.9 and Figure 4.36. The stub-to-slot intersection is highlighted in red in the Top Layer.

The requirements of the RF switch are first considered. For the switch biasing to operate properly a cut is necessary to separate the RF ground plane from the DC ground plane.

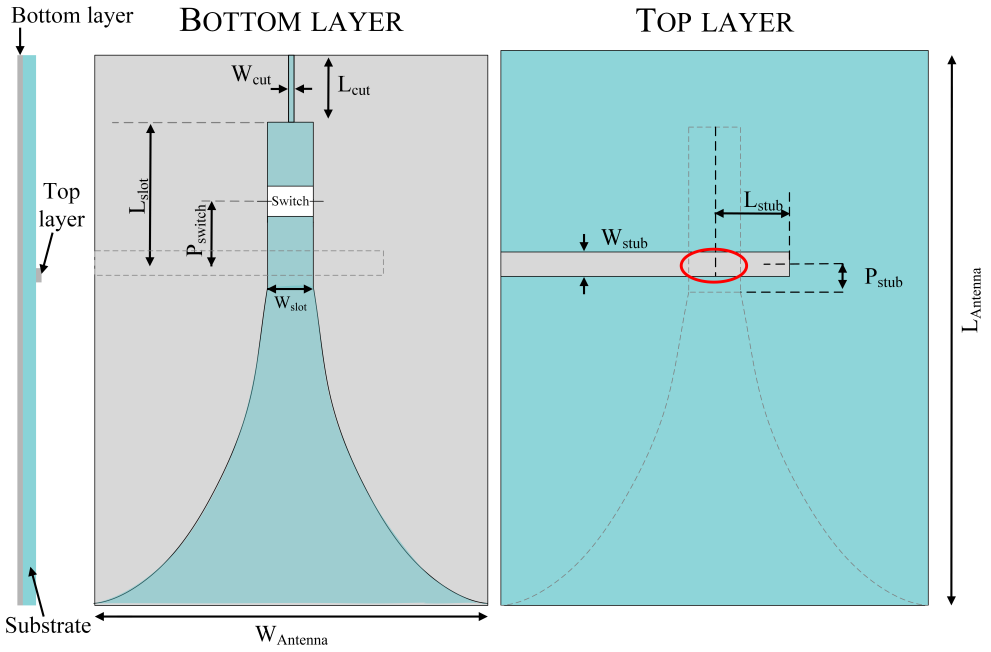

FIGURE 4.36: Bottom layer (left) and top layer (right) of design B.

Design parameters	*Dimensions (mm)*
$\mathbf{L}_{antenna}$	250.0
$\mathbf{W}_{antenna}$	150.0
$\mathbf{L}_{slot}$	60.0
$\mathbf{W}_{slot}$	1.22
$\mathbf{Pos}_{switch}$	40.0
$\mathbf{L}_{stub}$	7.98
$\mathbf{W}_{stub}$	1.5
$\mathbf{Pos}_{stub}$	15.8
$\mathbf{L}_{cut}$	20.0
$\mathbf{W}_{cut}$	0.2

TABLE 4.9: Design parameters for design B.

This cut separates the antenna in two halves for proper biasing of the RF switch as the DC ground and RF ground need to be separated, as shown in Figure 4.37.

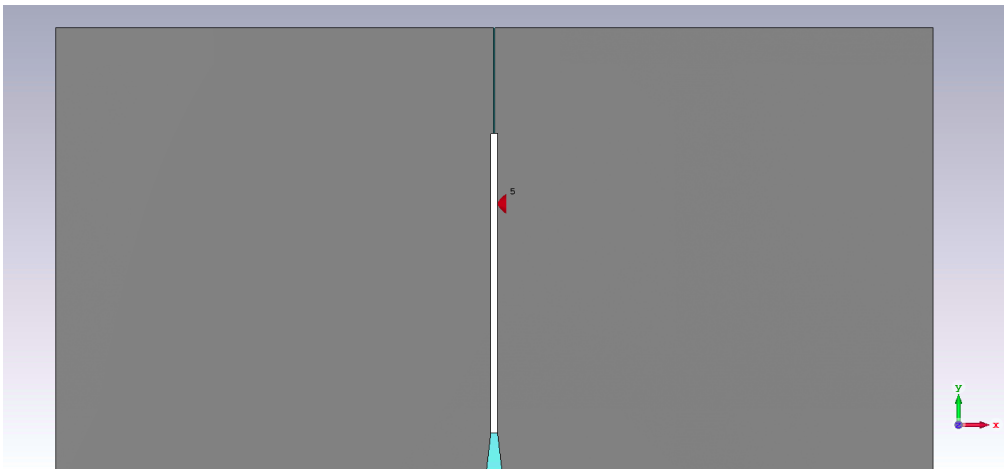

FIGURE 4.37: Quarter-wave cut to separate the ground plane in design B.

The width of the gap or cut is 0.2 mm, significantly small compared to the wavelength of the operating frequencies so that it does not affect the operation of the antenna. The length is a quarter-wavelength at the low frequency band, because that is when the end of the slot is critical. Thus, as it is an open-circuit at the edge of the antenna by using transmission line theory it can be determined it will operate as a short circuit at the end of the slot. This is a quarter-wave transformer, consequently the operating frequencies of the transformer are very narrow-band. Therefore, this needs to be taken into account if the antenna low band and high band are widely separated. In this case, at some frequencies the short circuit may appear as an open circuit and have current coupled resonating.

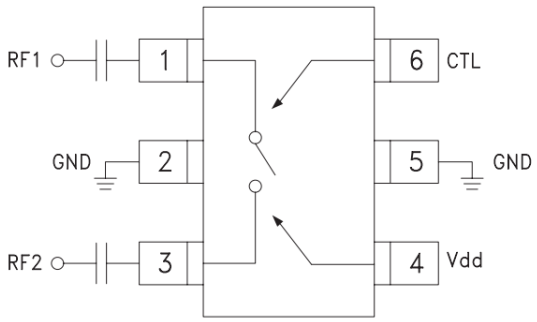

FIGURE 4.38: Typical application circuit of the HMC550AE RF switch [68].

Next, the layout to properly connect the HMC550AE RF switch to the antenna is considered. A schematic of the HMC550AE switch from the datasheet is presented in Figure 4.38. This switch requirements are: DC blocking capacitors for each RF port, two ports connected to ground (GND), a control voltage and a supply voltage (V_{dd}) of 5 V. The value of the capacitors determine the lowest frequency of operation. It is calculated as in equation 4.10, where the reactance at the operating frequency should be as low as possible [95]. For our application, a frequency of 1 GHz is low enough. Therefore, if $\chi_c < 2\ \Omega$ is acceptable, a capacitance of C = 100 pF can be used.

$$\chi_c = \frac{1}{2\pi f \cdot C} \tag{4.10}$$

The implementation simulated in CST Microwave Studio is shown in Figure 4.39. The blue elements represent the 100 pF DC blocking capacitors. The RF switch is superposed on the image to show where the switch will be soldered. The RF ports are 1 and 3, where the DC blocks are located. The pads are connected using vias that interconnect the pads from this side to the wings on the other side of the Vivaldi antenna. These vias (shown as circles in the figure) are located at the point which the slot is short-circuited when operating in high-band mode. In CST a "S-parameter discrete port" can be introduced between pins 1 and 3 to reproduce the measured switch modes. Then, the measured S-parameters for ON and OFF modes are imported to run the simulation and get more accurate results.

4.7.2 Simulation results

The simulation results are detailed and analysed next. First, the simulated operating frequency and gain are presented. Second, the radiation patterns for the different operating modes are displayed to show the direction of the main lobe and beamwidth are maintained. Finally, the current distributions for the different modes are reported to provide better understanding of each mode.

4.7.2.1 Operating frequency and gain

Figure 4.40 shows the simulated S_{11} and gain for design B. The S_{11} parameter for each mode is represented in solid lines, where the low band is shown with red lines and the blue lines represent the high band. The simulated gain at the direction of the main lobe $(\theta, \phi) = (90°,\ -90°)$ is shown in dashed lines.

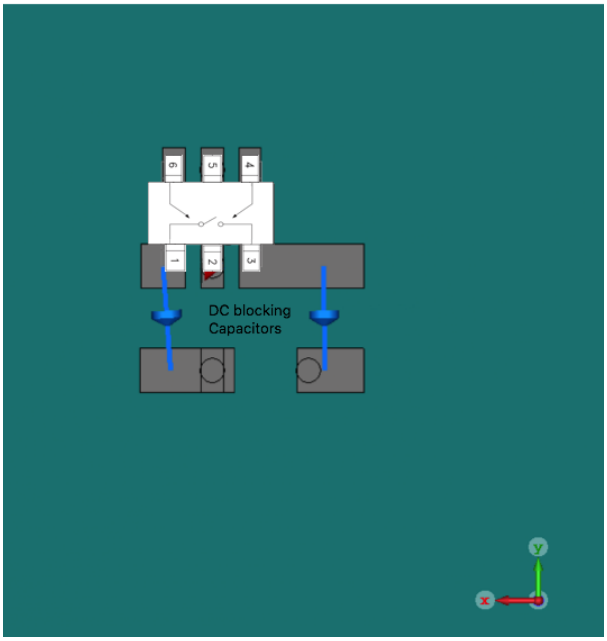

FIGURE 4.39: Top layer of design B. Zoomed in at the RF switch layout to connect the HMC550AE switch to the slot on the bottom layer.

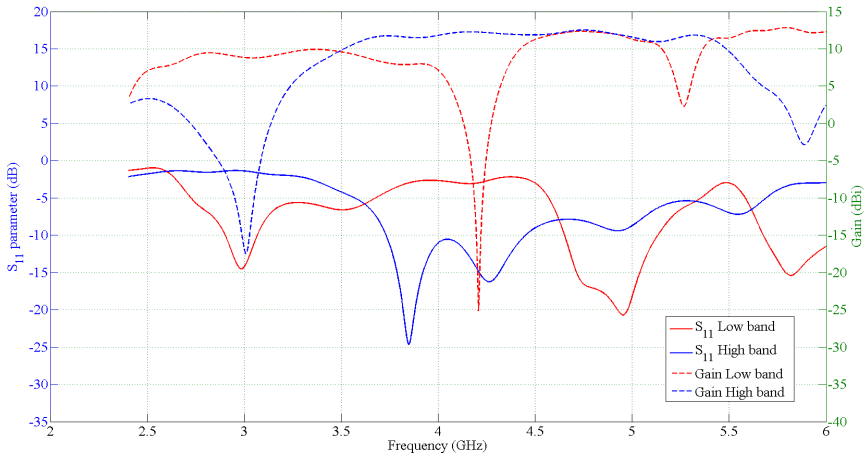

FIGURE 4.40: Simulated S_{11} parameter and realised gain of design B.

Analysing the results, in low-band mode there is a band at 3 GHz, and two other bands at 4.7 GHz and 5.8 GHz. These higher bands appear because of the design being well matched for this mode of operation too as the stub is not tuned in this design. More components are required to suppress these higher bands, for example another RF switch in the stub. As it is acceptable for the industry requirements of this project the suppression will not be necessary. Therefore the low band is considered at 3 GHz.

In high-band mode, there is a band centered at 4.1 GHz. The in-band gain for each band is stable and drops outside the band, which makes this design suitable for rejecting jamming signals for example.

The isolation between bands is greater than 25 dB. As the higher rejection between bands happens at 4.2 GHz, which is in-band in the high-band mode, this frequency of operation is used in the high-band mode. The frequency bands and gain of each configuration of the antenna are presented in Table 4.10.

	Frequency range (centre)	*Gain*	*Isolation*
Low band	2.9-3.1 GHz (3.0 GHz)	8.8-9.1 dBi	26 dB
High band	3.8-4.4 GHz (4.1 GHz)	11.1-12.5 dBi	37.5 dB

TABLE 4.10: Simulated performance for design B.

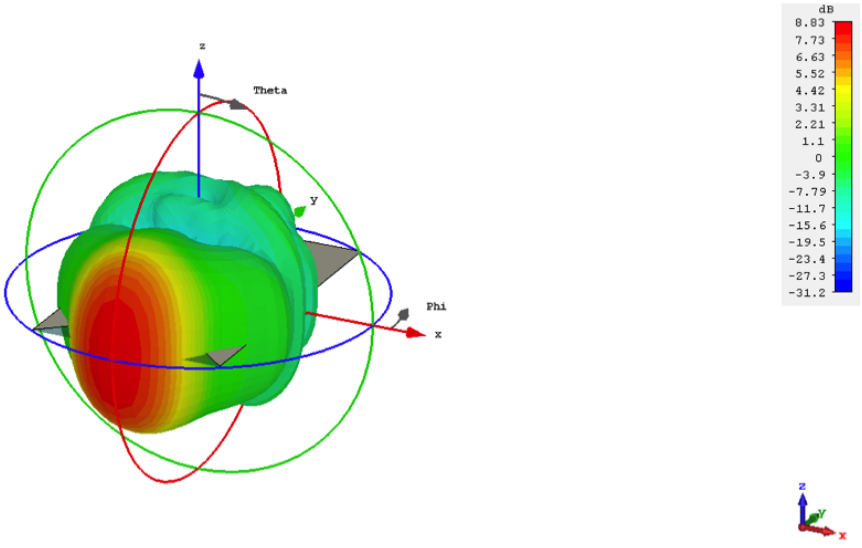

FIGURE 4.41: 3D radiation pattern at 3 GHz (selected band) for low-band mode.

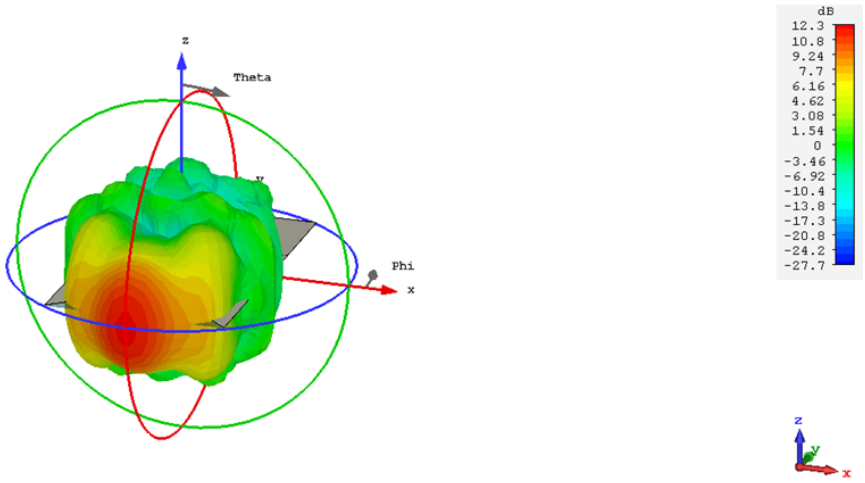

FIGURE 4.42: 3D radiation pattern at 4.7 GHz (higher band) for low-band mode.

4.7.2.2 Radiation pattern

The antenna radiation patterns are analysed here for the different operation modes. Figure 4.41 represents the simulated 3D radiation pattern at 3 GHz for low-band mode. Realised gain is 8.83 dBi. The direction of maximum radiation is to the open end of the Vivaldi antenna as expected. E-plane (blue circle) coincides with the XY plane. H-plane (red circle) is orthogonal to E-plane and it includes the direction of maximum radiation, so it coincides with ZY plane. HPBW on the E-plane is narrower than on the H-plane. As explained before, this is because of the antenna planar geometry, where EM waves are bound in E-plane between the tapered slot but not in the H-plane.

Figure 4.42 displays the radiation pattern at 4.7 GHz in low-band mode. As shown in Figure 4.40 the antenna is well matched in this mode and presents high gain. The E-plane starts to widen as the big aperture for lower frequencies affects the radiation pattern at higher frequencies.

Figure 4.43 represents the simulated 3D radiation pattern at 4.2 GHz for high-band operation. Realised gain is 12.2 dBi. In this operating mode the beamwidths on both planes are narrower compared to low-band mode at 3 GHz because the operating frequency is higher. In both operation modes the antenna has high constant gain and the direction of maximum radiation is stable.

To demonstrate the high isolation between bands, Figure 4.44 displays the 3D radiation pattern in high-band mode (the RF switch is ON) at 3 GHz. As presented the gain

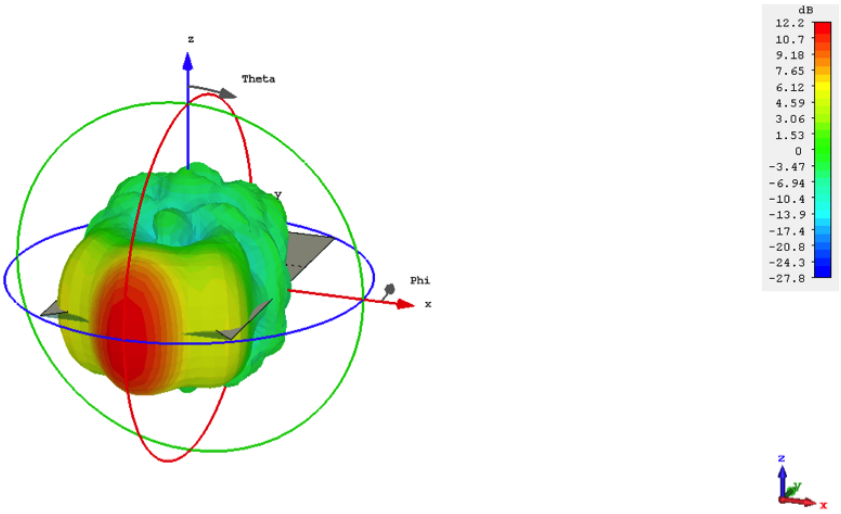

FIGURE 4.43: 3D radiation pattern at 4.2 GHz for high-band mode.

is very low (-12.6 dBi maximum), but it is even lower in the broadside direction. It is crucial to highlight the null in the direction of maximum radiation, that is to the negatives Y axis in the figure. Later, the current distributions are analysed to show the origin of this high isolation.

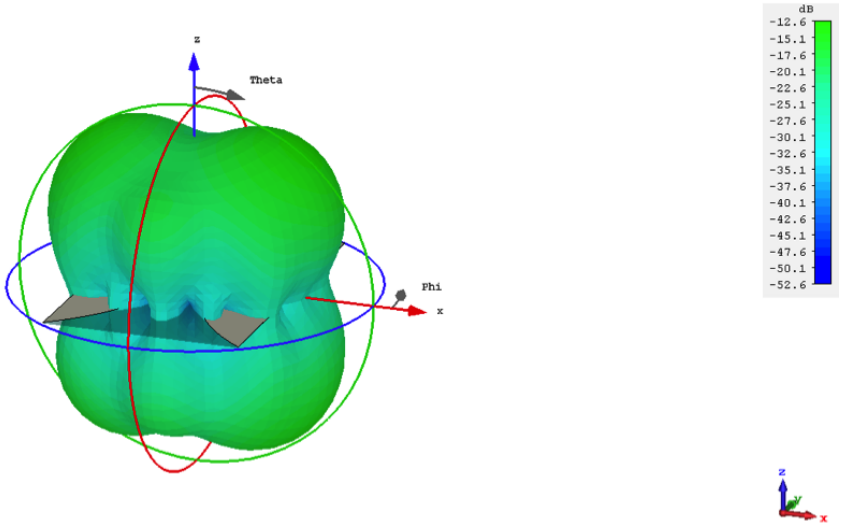

FIGURE 4.44: 3D radiation pattern at 3 GHz for high-band mode.

Figure 4.45 presents the radiation pattern at 4.7 GHz in high-band mode. This radiation pattern is closely related to the radiation pattern in low-band mode as shown in

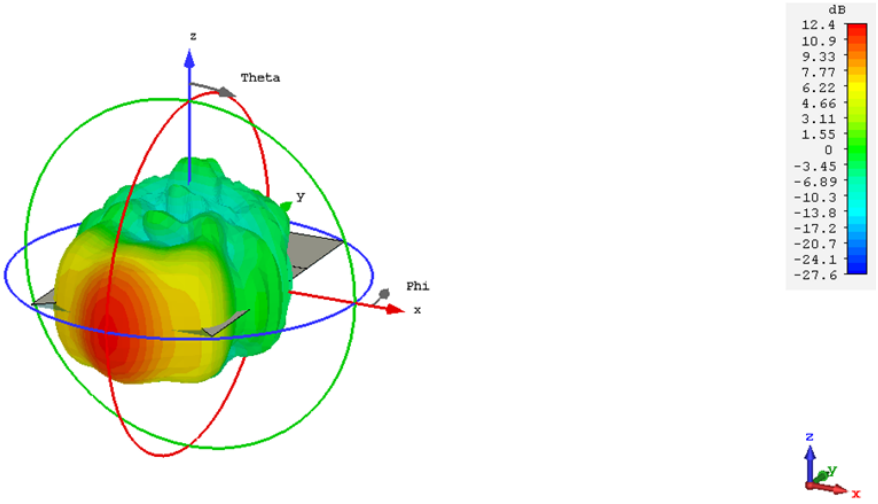

FIGURE 4.45: 3D radiation pattern at 4.7 GHz for high-band mode.

Figure 4.42. Therefore, the antenna is well matched and operating properly for both low-band and high-band modes at 4.7 GHz.

Furthermore, in Figure 4.46 the out-of-band operation of the low-band mode (RF switch is OFF) is presented. Although there are some peaks in several directions, the radiation pattern presents a null in the direction of the maximum radiation in this operation mode. Therefore, a high isolation can be expected in this case too.

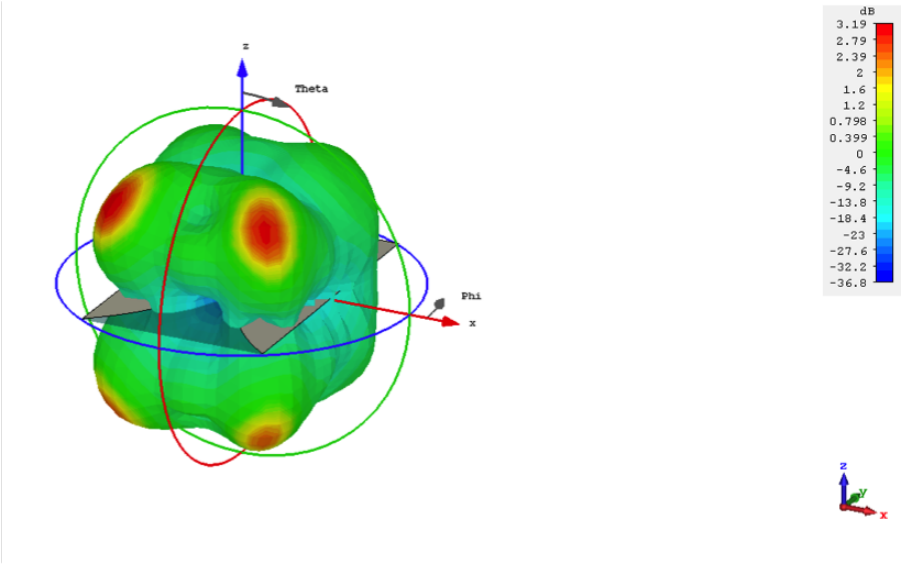

FIGURE 4.46: 3D radiation pattern at 4.2 GHz for low-band mode.

The normalised polar plots of the radiation patterns for the dual-band antenna are analysed next. Half-power beamwidth of the E-plane is 35.0° for the low band and 24.3° for the high band. HPBW of the H-plane for the low band is 61.3° and for the high band 44.2°, as summarised in Table 4.11. Therefore, the radiation pattern for both bands is similar in E-plane and H-plane, with the biggest difference in the H-plane. This is because of the planar design of the Vivaldi antenna.

		3 dB beamwidth	
	Frequency	*E-plane*	*H-plane*
Low band	3.0 GHz	35.0°	61.3°
High band	4.2 GHz	24.3°	44.2°

TABLE 4.11: Simulated HPBW for the different modes of design B.

In Figure 4.47 the polar plots of the normalised radiation patterns for the two modes are presented. Green lines represent E-plane and H-plane for the low-band mode at 3 GHz and red lines present E-plane and H-plane for the high-band mode at 4.2 GHz. These are normalised considering the gain for these modes is different and the purpose of these plots is to show the difference in radiation pattern and HPBW for the different modes. The radiation pattern are closely related, maintaining the direction of the main lobe.

Figure 4.48 presents the E-plane and H-plane polar plots comparing the different operating modes (switch ON and OFF) at the frequency of 3 GHz. At the direction of maximum radiation (-90° in the plots) there is more than 25.7 dB isolation in both E-plane and H-plane. This is because of the current being confined in the stub and the slot at the back of the antenna when operating in high-band mode.

Figure 4.49 presents the E-plane and H-plane polar plots comparing the different operating modes (switch ON and OFF) at the frequency of 4.2 GHz. At the direction of maximum radiation (-90° in the plots) there is 37.5 dB isolation in both E-plane and H-plane. In this case the cut to separate the ground plane in the Vivaldi antenna is contributing to the radiation, although the out-of-band operation is acceptable because the out-of-band back lobe is still lower than the in-band back lobe.

4.7.2.3 Current distributions

The current distributions for different operating modes are analysed next. For low-band mode, i.e. when the RF switch is OFF, the current is not short-circuited by the RF switch but instead uses the full length of the slot. This way the current travels the

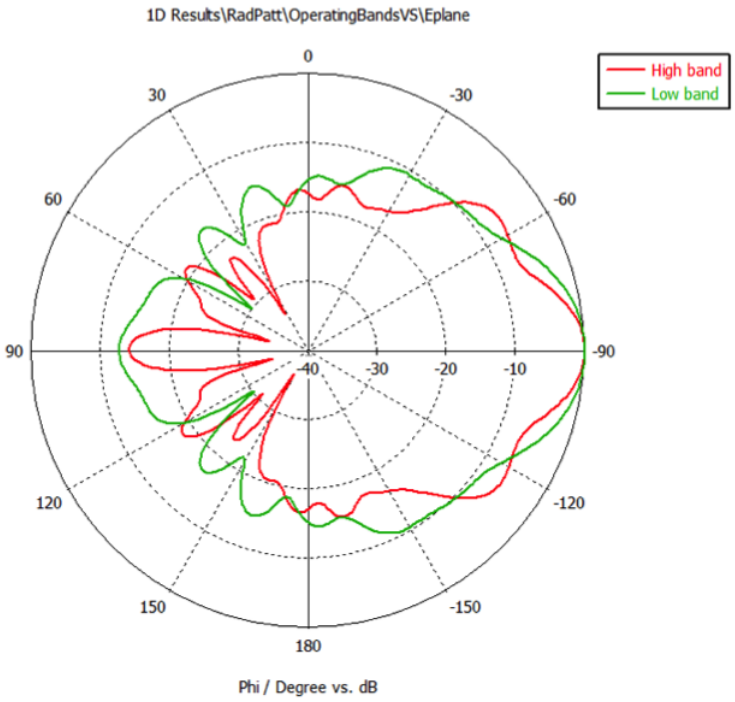

(A) E-plane

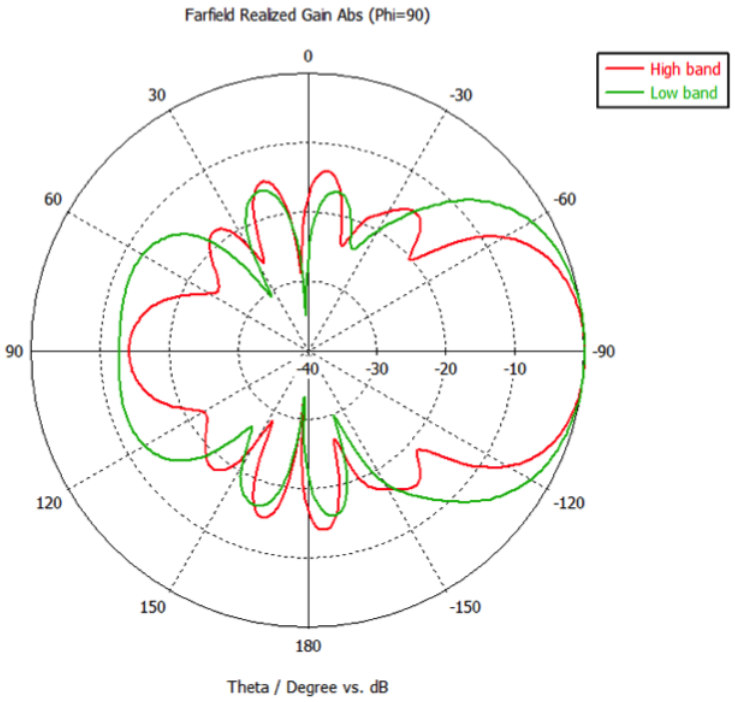

(B) H-plane

FIGURE 4.47: Polar plot of E-plane and H-plane normalised radiation patterns for low-band mode at 3 GHz (green line) and high-band mode at 4.2 GHz (red line) of design B.

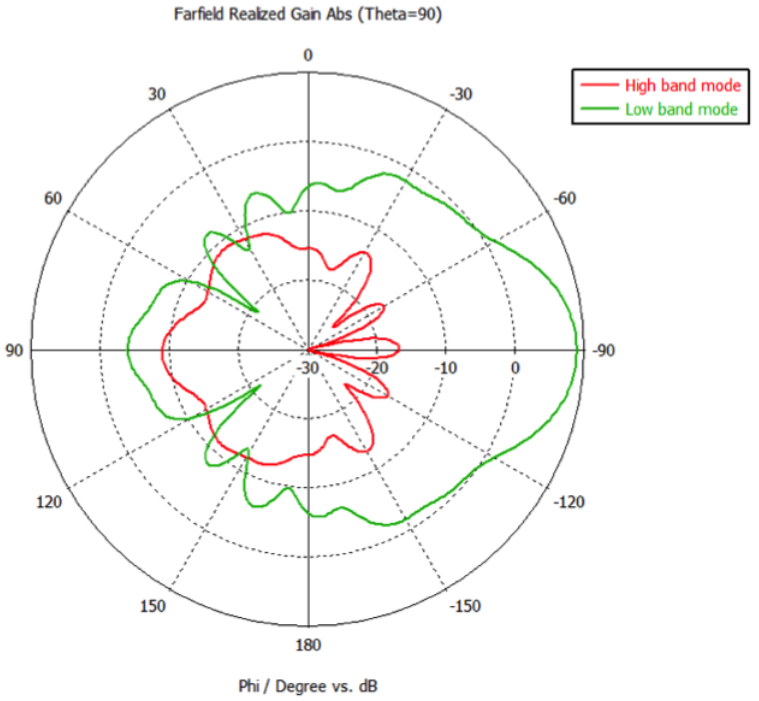

(A) E-plane

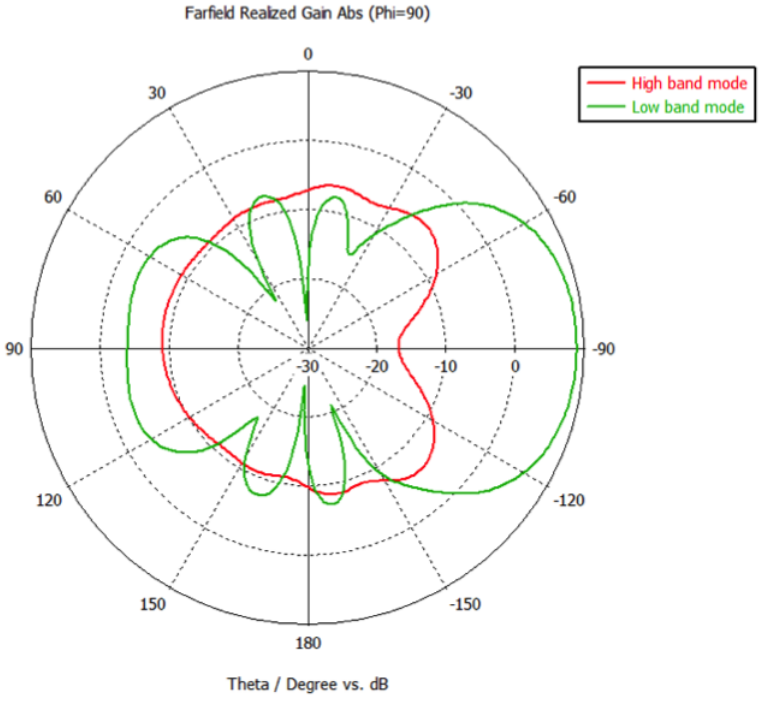

(B) H-plane

FIGURE 4.48: Polar plot of E-plane and H-plane radiation patterns for low-band mode (green line) and high-band mode (red line) at 3 GHz of design B .

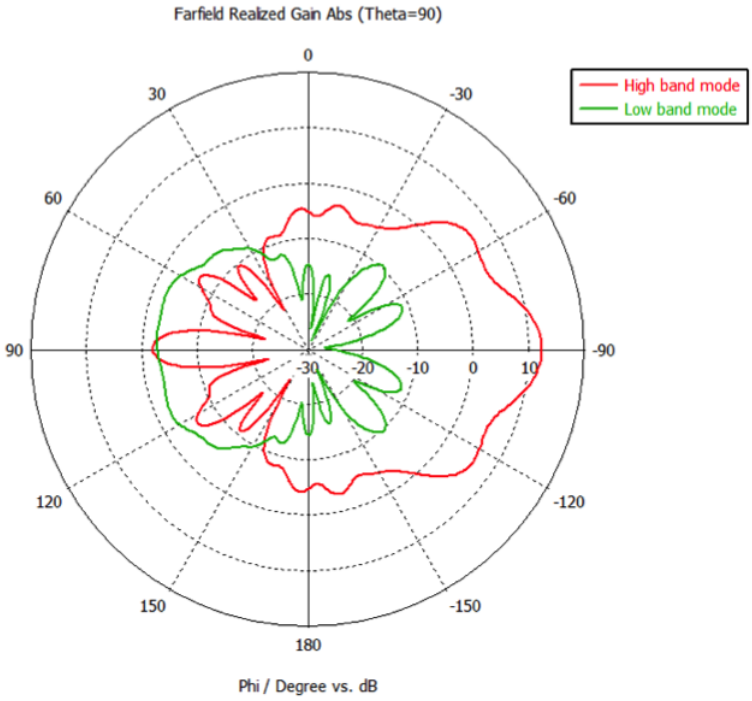

(A) E-plane

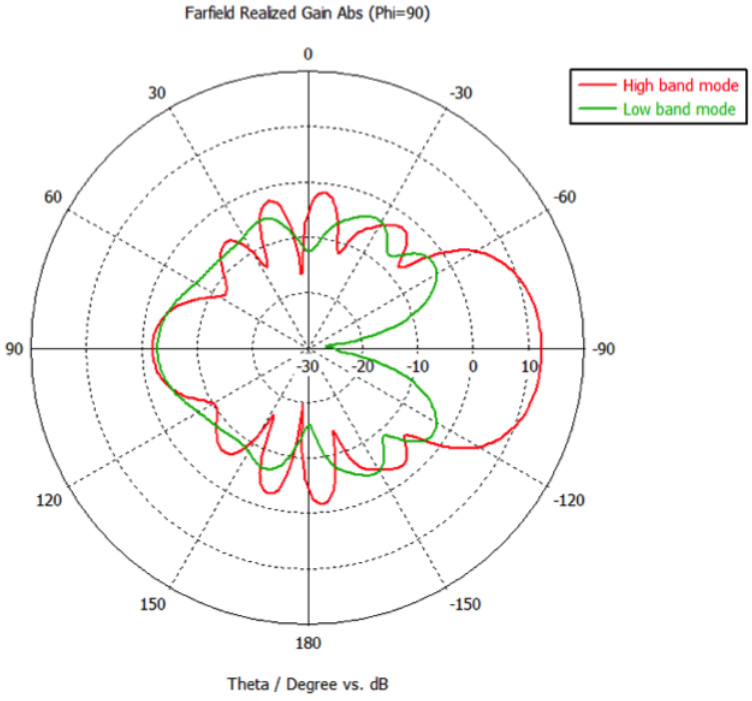

(B) H-plane

FIGURE 4.49: Polar plot of E-plane and H-plane radiation patterns for low-band mode (green line) and high-band mode (red line) at 4.2 GHz of design B.

maximum length of the reconfigurable slot. The antenna in low-band mode operates at around 3 GHz, that is when the slot length is equal to 3/4 of the wavelength, as shown in Figure 4.50. The current is well matched at the stub-to-slot intersection and thus, it is propagated to the open end of the Vivaldi and then radiated.

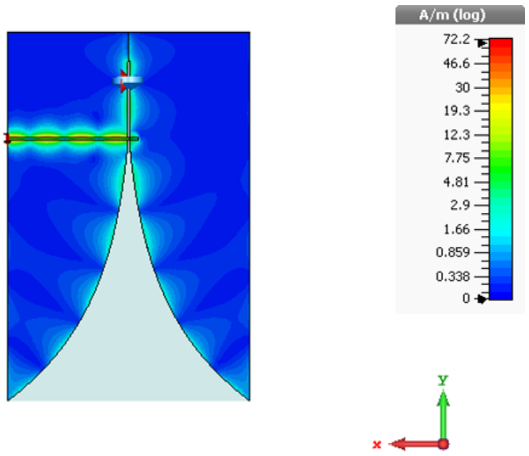

FIGURE 4.50: Current distribution for low-band mode at 3 GHz of design B.

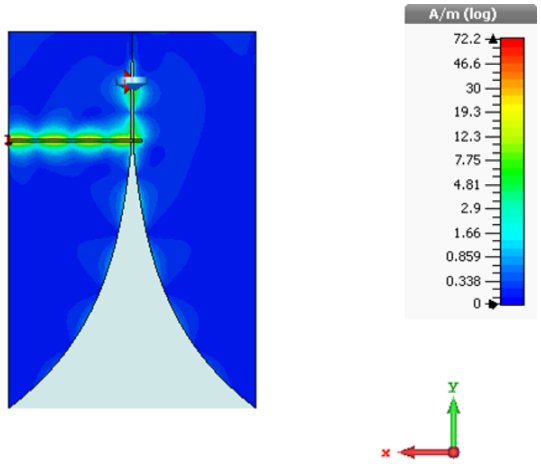

FIGURE 4.51: Current distribution for high-band mode at 3 GHz of design B.

When the RF switch is ON, that is in high-band mode, the current is short-circuited at the switch. At 3 GHz the length of the slot is calculated so that the current does not add in phase to propagate to the antenna open end. At that frequency the length from the RF switch to the stub-to-slot intersection is half-wavelength. Therefore, in

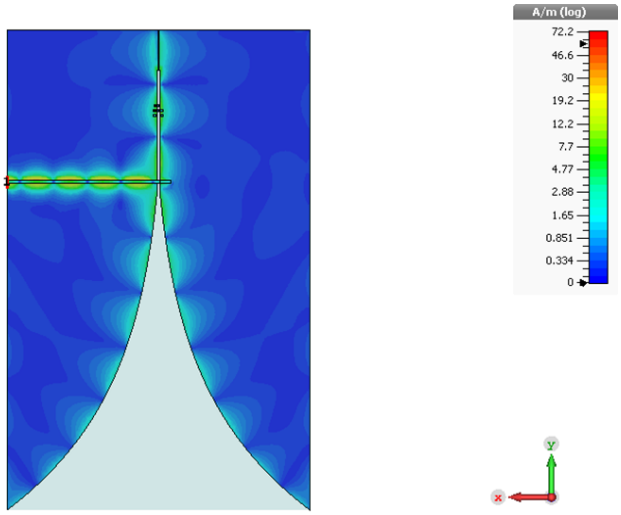

FIGURE 4.52: Current distribution for low-band mode at 4.7 GHz of design B.

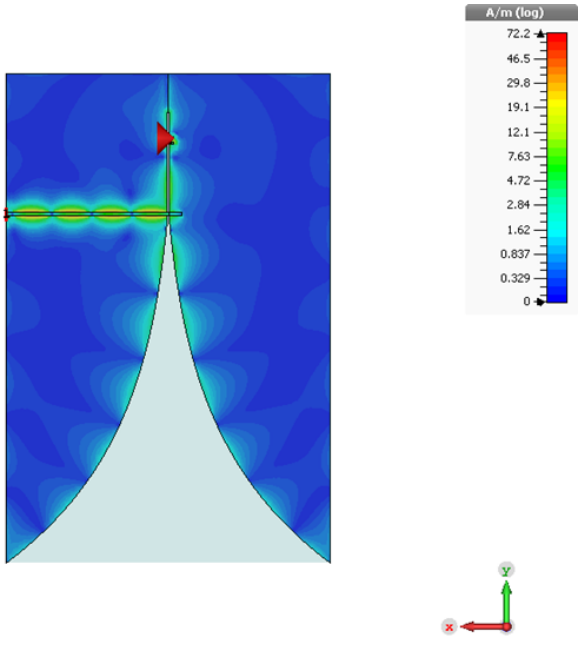

FIGURE 4.53: Current distribution for high-band mode at 4.2 GHz of design B.

Figure 4.51 all current is resonating in the stub and the slot. Consequently, no current is propagated to the exponentially tapered end of the Vivaldi antenna.

Figure 4.52 displays the current distribution for low-band mode at 4.7 GHz. The antenna radiates because most of the current is propagated to the open end of the antenna. Using the current distribution helps understand the reason why the antenna is well matched at 4.7 GHz in both low-band mode and high-band mode. The current is coupled to the separation cut because the L_{cut} is equal to half-wavelength at 4.7 GHz regardless of the state of the RF switch. This length combined with the slot length provides a null just over the stub-to-slot intersection which couples all current in phase to the open end of the antenna.

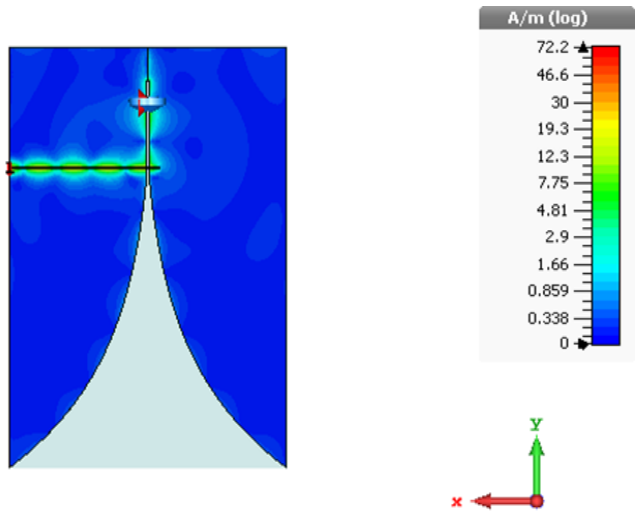

FIGURE 4.54: Current distribution for low-band mode at 4.2 GHz of design B.

In high-band mode the RF switch creates a short circuit at a specific point of the slot to create a current maximum at that point. Although some current is passing through and resonates at the end of the slot, it does not affect the operation of the high-band mode. Figure 4.53 presents the current distribution at 4.2 GHz in high-band mode. The new effective length of the slot is 3/4 of the wavelength at the high-band operating frequency. Thus, most of the current is propagated to the exponentially tapered end of the Vivaldi antenna and then radiated.

Finally, in low-band mode at 4.2 GHz the distance from the slot termination to the intersection is calculated so that the current does not add in phase to propagate to the

antenna tapered end. Thus, there is no current radiating from the exponentially tapered end of the Vivaldi antenna, as shown in Figure 4.54.

4.8 Antenna verification

When good simulation results are obtained a prototype is fabricated to be tested. This section explains the prototype that was built to test design B with the measurement procedure and verified with measured results.

The dual-band prototype had to be modified to overcome the limitations in the workshop. Design A was bigger than an A4 sheet of paper, which is the maximum size that can be used for the etching machine. Therefore, a smaller dual-band switched antenna was designed, called design B, and simulated, although its performance is degraded compared to the original design. Pictures of the top and bottom layers of the prototype constructed are shown in Figure 4.55. The small board on the top-right corner is connected to the RF switch in the top layer to change the operating band of the antenna. This board can easily be replaced for a microcontroller that reconfigures the bands automatically to suit cognitive radio applications for example.

Figure 4.56 presents a block diagram of the experiment setup for Design B with a GaAs MMIC switch and a digital control board to operate the switch. The digital control board supply voltage is 5 V. The user can change the operating mode between low band and high band using this board. Three cables are connected to the switch: V_{ctl} (the control voltage) in blue, V_{dd} (the supplied voltage) in green and GND (DC ground) in yellow, as shown in the figure.

4.8.1 RF switch measurements

Initially, the S-parameters of the RF switch given by the manufacturer are imported into CST Microwave Studio. Next, to verify the data from the manufacturer datasheet an experiment is set up to measure the S-parameters of the HMC550AE switch. Before beginning any other tests, a control board was designed to measure the real S-parameters of the RF switch using a VNA. Figure 4.57 shows a picture of the setup with an Agilent E5071C VNA. The blue cable (V_{ctl}), orange cable (V_{dd}) and black cable (GND) are connected to the control board to change the state of the RF switch. A picture of the control board is shown in Figure 4.58. To control the RF switch a slide switch connects the output either to ground or to V_{dd}. This board also gives the switch the control

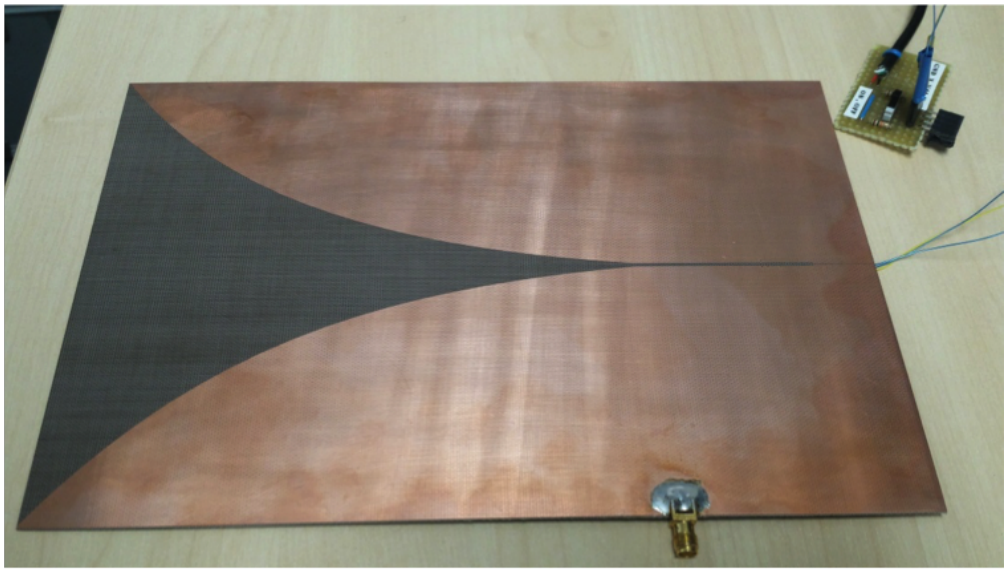

(A) Bottom layer

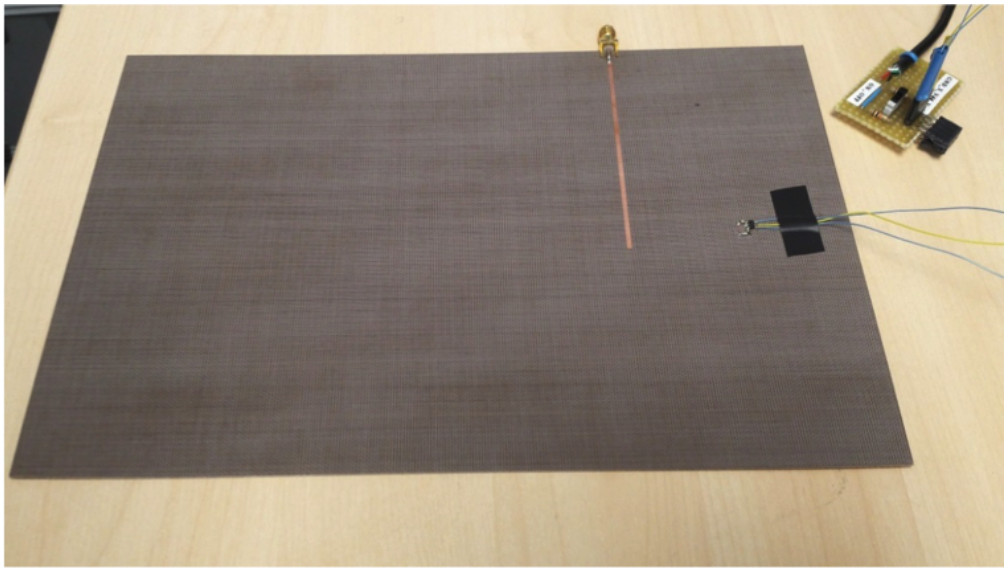

(B) Top layer

FIGURE 4.55: Prototype fabricated for design B.

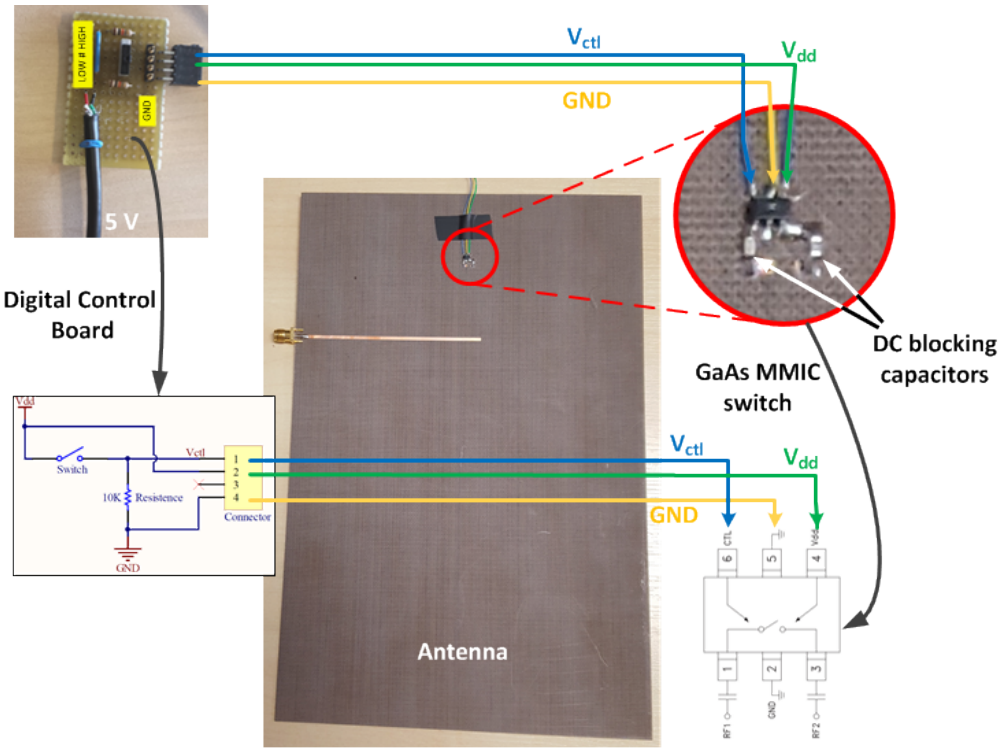

FIGURE 4.56: Experiment setup for Design B.

voltage it needs to operate. When the LOW mode is selected, the RF switch is OFF and when HIGH mode is selected, the switch changes its state to ON.

The S-parameters measured are presented in Figure 4.59 for the ON mode and in Figure 4.60 for the OFF mode. They were slightly different from the manufacturer parameters, specially above 4 GHz. As the reconfigurable design would be considerably affected, these measured parameters were imported into CST and the antenna design was consequently adapted.

4.8.2 Measurement procedure

In this section, the techniques used to measure the operating bands, gain and radiation patterns of the antenna are described. The measurements was performed in an anechoic chamber at University College London. The setup in the chamber is shown in Figure 4.61, with the antenna under test (AUT) on the left hand side of the picture and the rotating structure with the source antenna on the right.

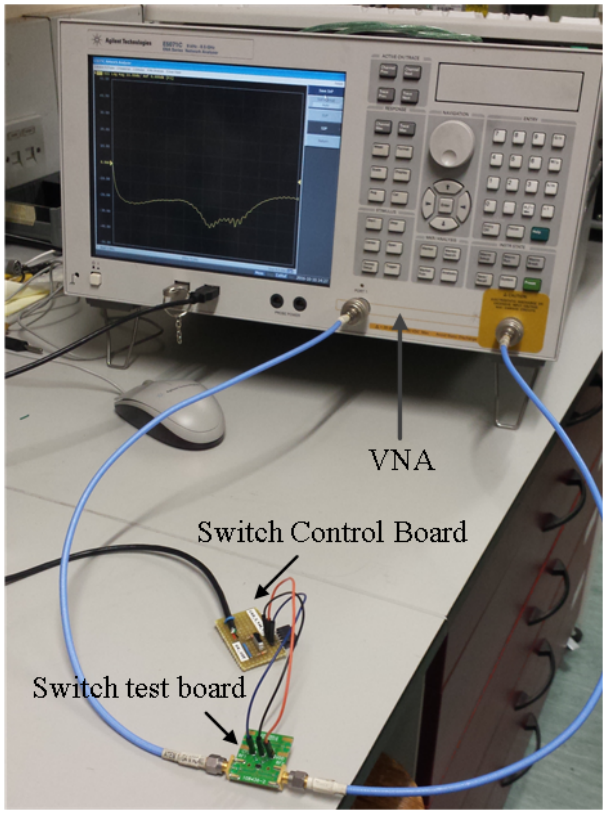

FIGURE 4.57: Measurement of the S-parameters for the RF switch HMC550AE.

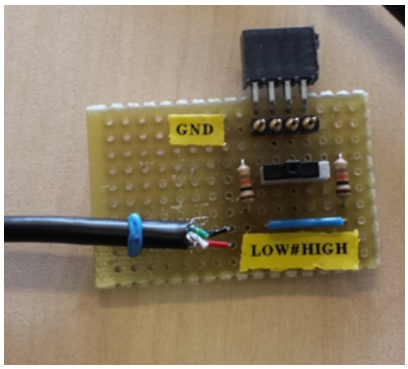

FIGURE 4.58: Control board of the RF switch.

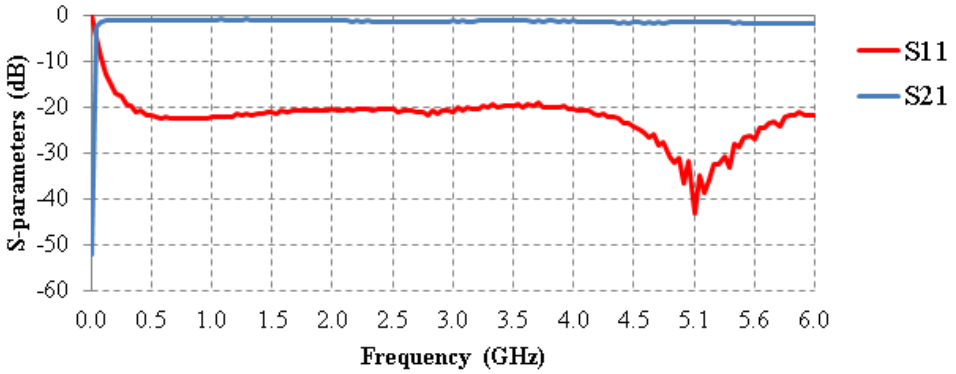

FIGURE 4.59: Measured S-parameters for HMC550AE switch in ON mode.

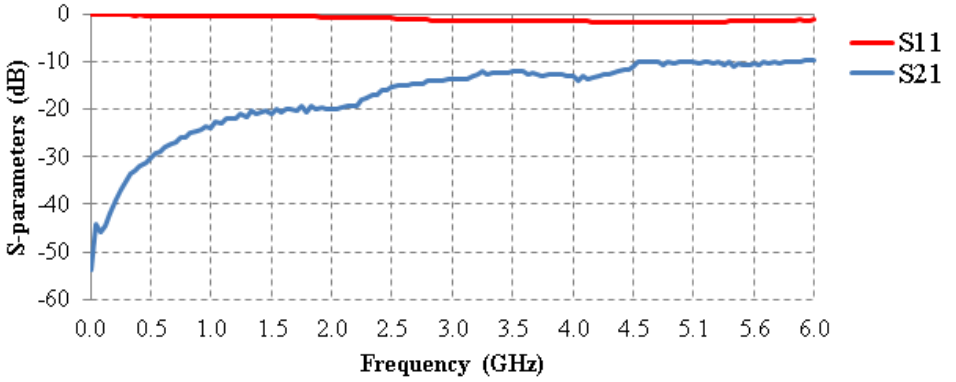

FIGURE 4.60: Measured S-parameters for HMC550AE switch in OFF mode.

The procedure consists of transmitting using a known source antenna to the AUT which is located at a specific distance. Ideally, only one direct signal path should exist between the source antenna and the AUT. To ensure best results this procedure can be done in a low-reflection environment like an anechoic chamber or in a suitable outdoor environment, since there will be a better approximation to a plane wave.

Another factor to take into account in an antenna measurement is the measurement in near-field or far-field. The conventional setup for most applications requires the antenna to be in far-field, which offers several advantages [96]:

- The measured field pattern is valid for any distance within the far-field region.
- The result is not sensitive to the changes in the location of the phase of the antennas.
- Coupling and multiple reflections between antennas are reduced.

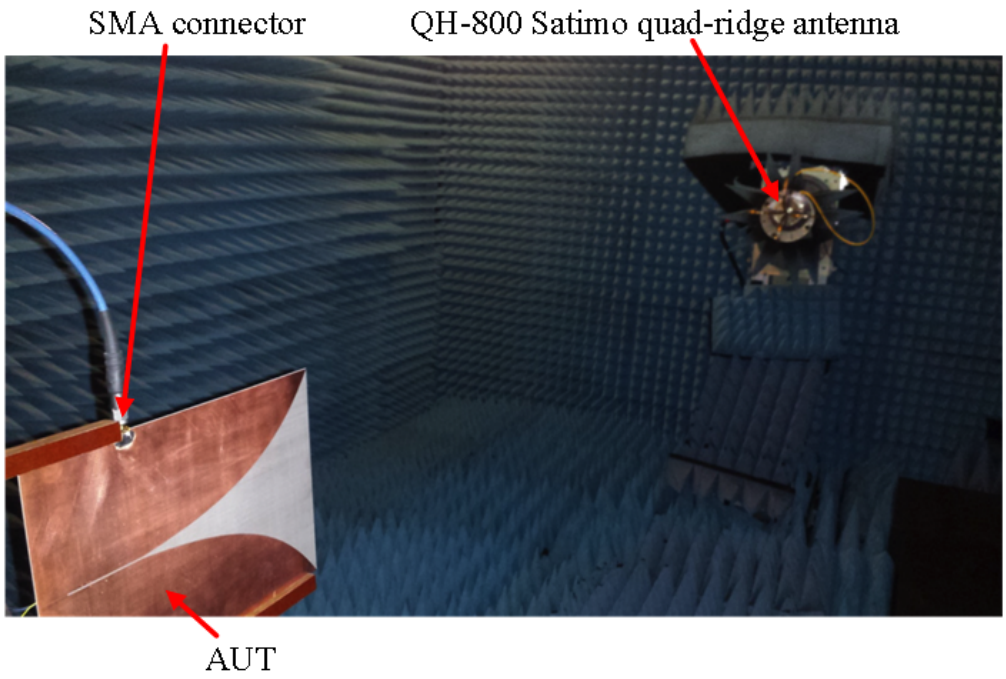

FIGURE 4.61: Measuring the prototype of design B in the anechoic chamber.

Considering equation 2.3 the minimum distance at which the source and AUT antennas can be placed is calculated. The dimension of the aperture of the antenna is 0.15 m. Therefore to satisfy the far-field conditions, the distance between antennas needs to be a minimum of 0.3 m at 2 GHz and 0.9 m at 6 GHz as shown in equations 4.11 – 4.13. Since the transmitting antenna and the receiving antenna in the anechoic chamber are separated by more than 2 m this requirement is satisfied for all operating bands.

$$R \geq \frac{2(0.15)^2}{\lambda} \tag{4.11}$$

$$R(at\ 2\ GHz) \geq \frac{2(0.15)^2}{0.15} = 0.3\ m \tag{4.12}$$

$$R(at\ 6\ GHz) \geq \frac{2(0.15)^2}{0.05} = 0.9\ m \tag{4.13}$$

Several antenna characteristics are measured: reflection coefficient, realised gain at the direction of the main lobe against frequency and radiation patterns at the frequencies of interest.

The source antenna used is the QH-800 Satimo quad-ridge antenna which operates from 800 MHz to 12 GHz. It can be excited either vertically or horizontally to measure E-plane, H-plane and cross-polarisation as well. The realised gain from the antenna datasheet increases with frequency from 7.8 dBi at 2 GHz up to 12.5 dBi at 6 GHz.

To measure the reflection coefficient, a R&S ZNB40 Vector Network Analyzer is used. The AUT is set up with a support that holds the antenna straight and aligned with the source antenna and attaches it to the turntable from the mounting structure as shown in Figure 4.62. The turntable rotates to situate the AUT in vertical or horizontal positions to measure both E-plane and H-plane. The mounting structure turns to measure the radiation pattern from -90° to +90° in azimuth. Before the measurement, a 1-port open-short-match (OSM) standard calibration is performed at the receiving port using 85033D calibration kit, which is required for the reflection coefficient measurement. The S_{11} parameter is measured to verify the proper antenna operation as calculated by the simulation and will be analysed later in this chapter.

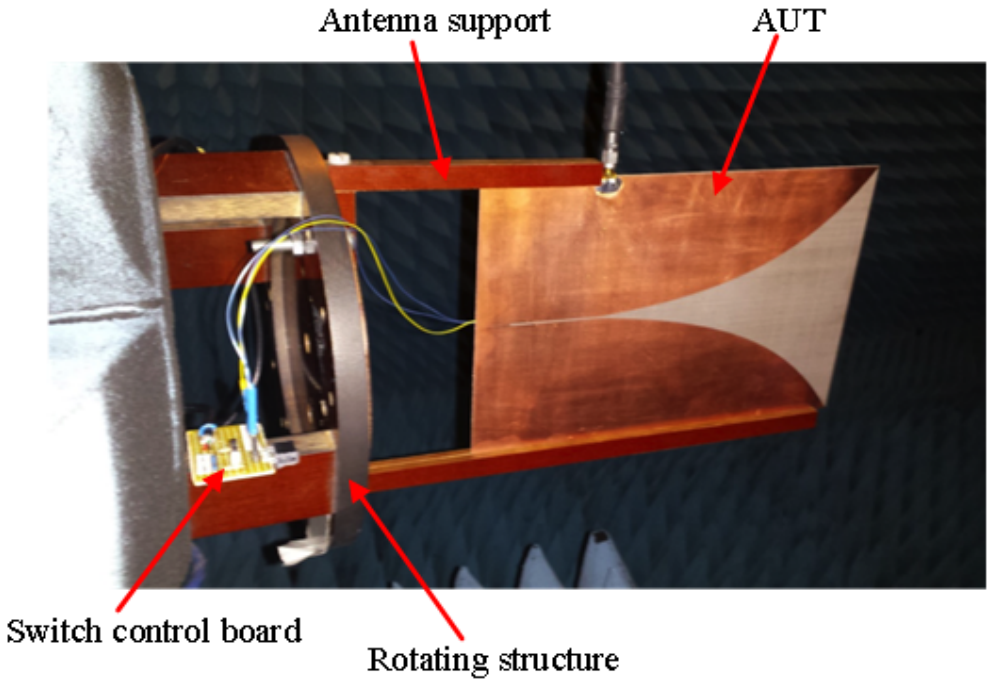

FIGURE 4.62: The AUT with the switch-controlling board in the turntable of the anechoic chamber.

The source antenna and AUT need to be aligned properly before commencing any measurements. This includes the main lobe peaks aligned with the line of measurement but also it is critical that the polarisation of the two antennas is aligned as well.

The radiation pattern is measured in 2D patterns at the frequencies of interest. A 3D pattern is not feasible to produce because of the limitations in the turning table and mounting structure in the chamber. Radiation pattern was measured from -90° to +90° at 1 degree increment in azimuth. However the back lobe cannot be measured in the setup of this anechoic chamber, because of the metallic structure of the turntable where the AUT was mounted. The mount rotates in azimuth in a forward direction and the data is recorded in a computer.

For the gain measurement a comparison method is used. First, a reference measurement with a known reference antenna is set. The reference antenna used is SH-800 Satimo dual ridge horn. Ideally it should be the same model as the source antenna, but this is the closest one available in the chamber at the time. This reference antenna also operates from 800 MHz to 12 GHz and it delivers stable gain across the operating band. The boresight gain from the datasheet of the SH-800 goes from 11 dBi at 2 GHz up to 12.5 dBi at 6 GHz.

$$P_{out1} = P_{in} + G_{source} + G_{ref} - Pathloss \tag{4.14}$$

$$P_{out2} = P_{in} + G_{source} + G_{AUT} - Pathloss \tag{4.15}$$

$$P_{out1} - P_{out2} = G_{ref} - G_{AUT} \tag{4.16}$$

Firstly, the received power at the reference antenna (SH-800) is recorded following Friis transmission principle in dB. Equation 4.14 presents the received power for the first experiment where P_{out1} is the received power of experiment 1, P_{in} is the input power of experiment 1 and 2, G_{source} is the gain of the source antenna, G_{ref} is the gain of the reference antenna and $Pathloss$ are the losses because of ground reflections and multipath in the measurement environment. Then, the reference antenna is replaced by the AUT and the received power recorded again as in equation 4.15, where P_{out2} is the received power of experiment 2 and G_{AUT} is the gain of the AUT. The other parameters remain the same. Finally, using the already known antenna gain of the reference antenna, equation 4.15 is subtracted from equation 4.14 and equation 4.16 obtained. The measured gain of the AUT can be determined by isolating G_{AUT} on that equation.

4.8.3 Measured reflection coefficient and gain results for design B

The prototype operates at two different bands, when switched between the two operating modes using the control board. Table 4.12 summarises the characteristics of the two bands. As expected from the simulation results, in low-band mode the antenna operates simultaneously in two bands: at 3.1 GHz and at 4.7 GHz. In high-band mode it operates at 4.2 GHz. A rejection between bands of 20 dB in the low-band mode at 3.1 GHz and of 15 dB in the high-band mode can be achieved. For the band at 4.7 GHz in low-band mode the isolation is not as high because another switch is required in the stub to reject these frequencies.

	Centre frequency	*Bandwidth*	*Gain*	*Isolation*
Low Band	3.06 GHz	0.2 GHz	10.5 dBi	20 dB
High Band	4.19 GHz	0.7 GHz	12 dBi	15 dB

TABLE 4.12: Measured results for design B.

4.8.4 Comparison test and simulation results

Figure 4.63 shows a comparison between measured (solid lines) and simulated (dashed lines) reflection coefficient. The low band is displayed in red and the high band is displayed in blue. The measured results are in good agreement with the simulated results, although there are some discrepancies at higher frequencies which can be because of parasitic elements of the components, the limitations of the anechoic chamber and fabrication tolerances.

The measured gain is compared to the simulated gain in Figure 4.64. The maximum gain is stable inside the band and the measured rejected bands are close to the simulated bands. The measured rejected frequency in the low band mode at 4.1 GHz is 17 dB higher compared to the simulated result. This can be because of poor switch isolation between ON and OFF states. The in-band gain in high-band mode is up to 1.5 dB lower than the simulated gain, although at 4.1 GHz the measured gain is the highest achieved and it is similar as the simulated gain: 12 dBi.

Figure 4.65 compares the measured and simulated radiation patterns for E-plane (4.65a) and H-plane (4.65b) in the low-band mode. Figure 4.66 compares the measured and simulated radiation patterns for E-plane (4.66a) and H-plane (4.66b) in the high-band mode. In both modes measured results agree with simulated results. The biggest difference is found in the H-plane when measuring close to 0° and 180°. In high-band mode the side

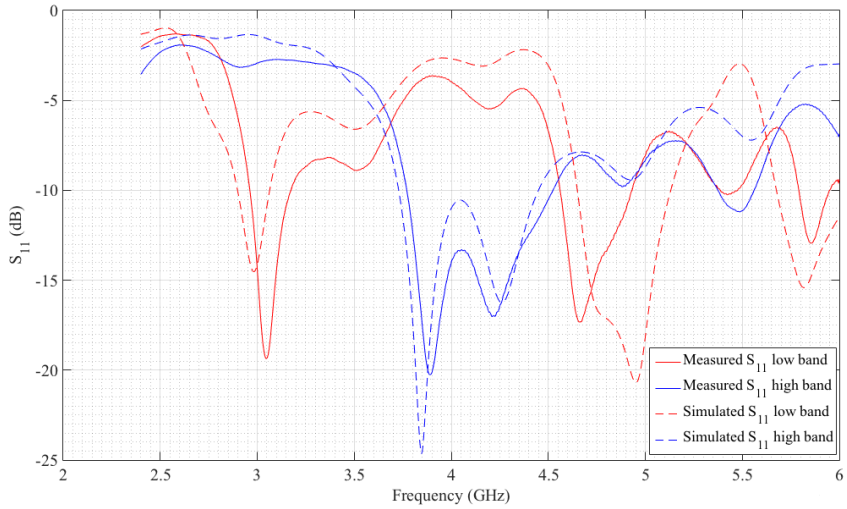

FIGURE 4.63: Measured (solid lines) and simulated (dashed lines) S_{11} for design B.

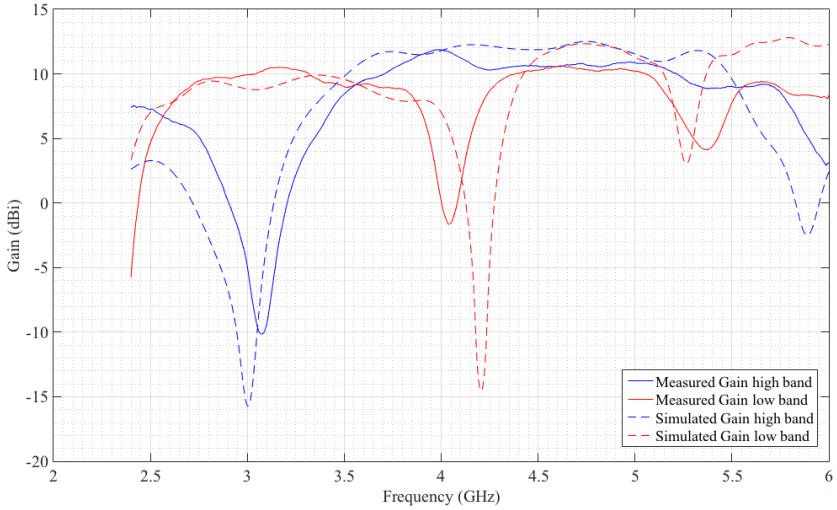

FIGURE 4.64: Measured (solid lines) and simulated (dashed lines) gain for design B.

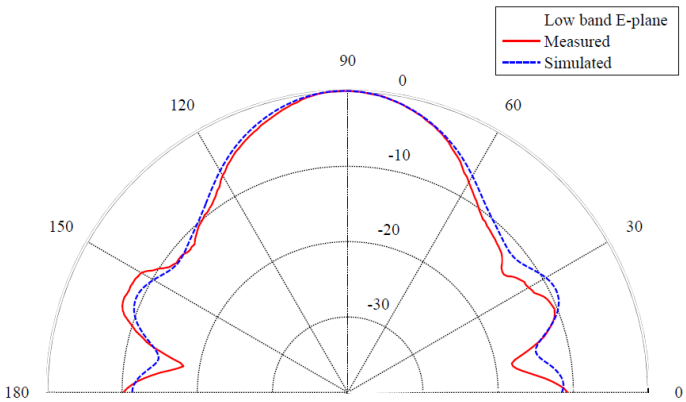

(A) E-plane

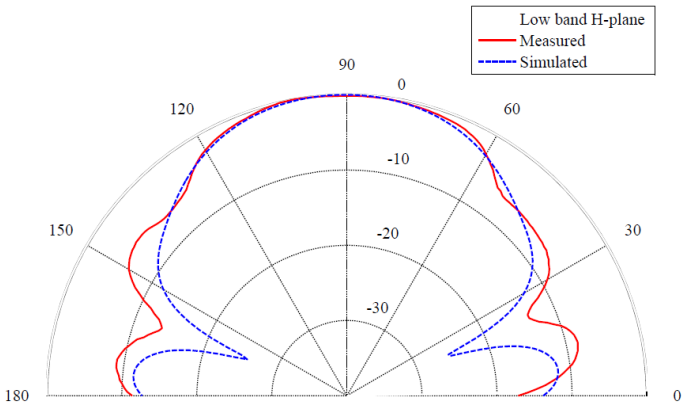

(B) H-plane

FIGURE 4.65: Measured (red solid line) and simulated (blue dashed line) E-plane and H-plane radiation pattern for low-band mode of design B.

lobes at these angles are 5 dB higher. This can be because of the switch-control board, as it was located behind the antenna and could be affecting the radiation pattern when driving the RF switch in ON state.

4.9 Analytical modelling for antenna parameters

For better understanding of how these reconfigurable antennas operate and to generalise the concepts used for designs A and B, a method to calculate the design parameters using a series of formulae in terms of frequency (in GHz) is proposed here. To extract these formulae both transmission line theory and empirical experience are applied. The obtained formulae are presented in equation 4.17, equation 4.18 and equation 4.19, based

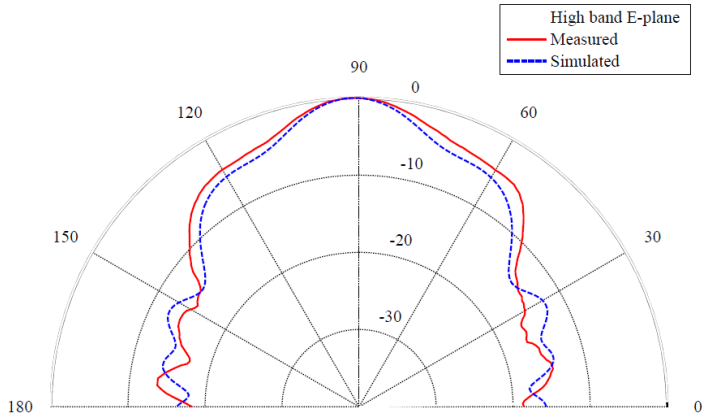

(A) E-plane

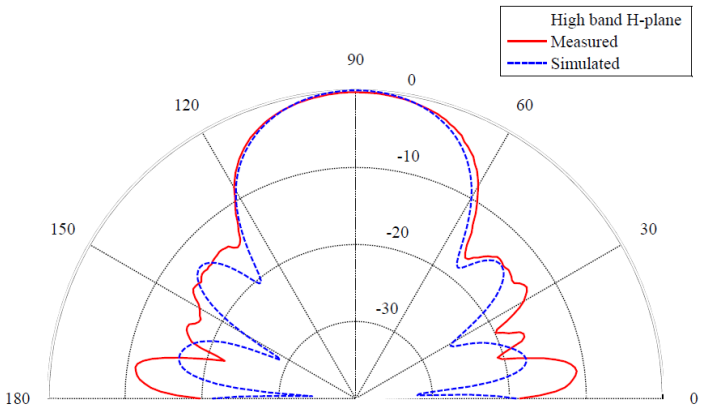

(B) H-plane

FIGURE 4.66: Measured (red solid line) and simulated (blue dashed line) E-plane and H-plane radiation pattern for the high-band mode of design B.

on the design parameters shown in Figure 4.67 and Figure 4.68. This method assumes a basic Vivaldi antenna is already designed and it covers the whole operating frequency bands of interest.

$$Slot\ length\ (L_{slot}) = \frac{0.75}{4 \cdot f(GHz)} \tag{4.17}$$

$$Stub\ length\ (L_{stub}) = \frac{0.15}{4 \cdot f(GHz)} \tag{4.18}$$

$$Stub\ position\ (Pos_{stub}) = \frac{0.25}{4 \cdot f(GHz)} \tag{4.19}$$

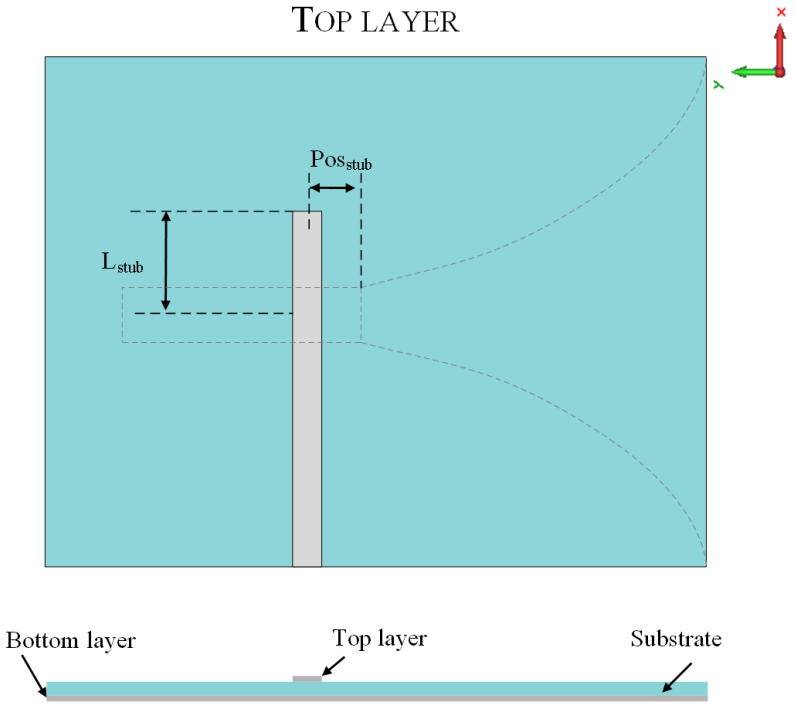

FIGURE 4.67: Top view of the reconfigurable Vivaldi antenna with design parameters.

The slot length depends on the wavelength that propagates in the slot line of the antenna, which is close to the free-space wavelength. For the antenna to be well match at a specific frequency the slot needs to be three-quarters of the wavelength at the operating frequency. Thus, the current will be added in phase at the stub-to-slot intersection and then propagated to the open end of the Vivaldi antenna.

The stub length depends on the guided wavelength ($\lambda_g = \lambda_0/\sqrt{\varepsilon_r}$) that propagates in the stub or the feedline of the antenna. For the antenna to be match at a specific frequency the stub needs to be a quarter of the guided wavelength at the operating frequency. Thus, the current will be added in phase at the stub-to-slot intersection and later propagated to the open end of the Vivaldi antenna.

The stub position depends on the wavelength that propagates in the slot line. The best match is when the position of the stub is at a quarter-wavelength to the beginning of the tapering at the operating frequency.

These formulae are used to calculate the low-band mode and the high-band mode. In high-band mode, the results are used to determine the slot RF-switch position. For the stub position and length a trade-off must be made between the low-band and the

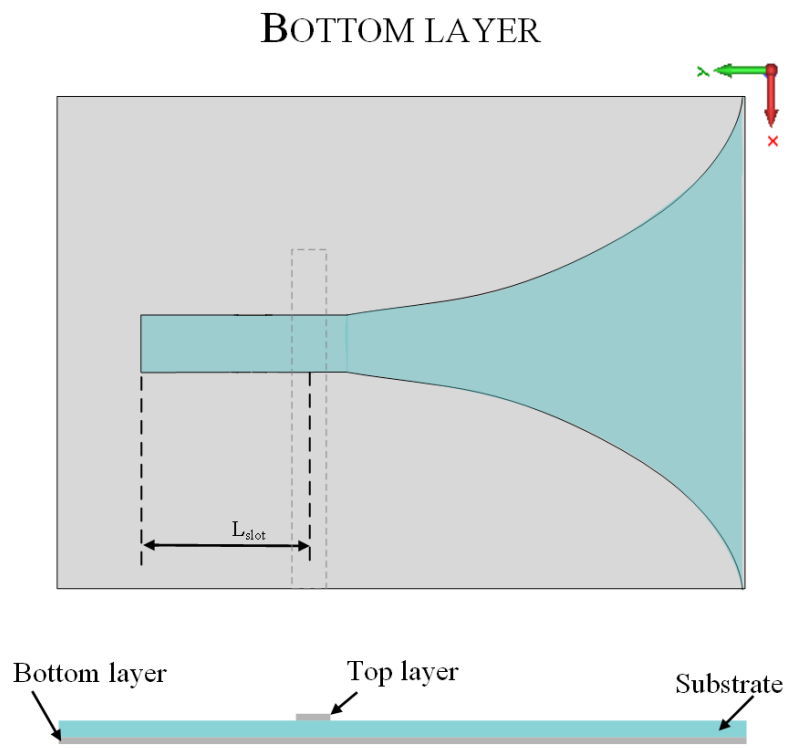

FIGURE 4.68: Bottom view of the reconfigurable Vivaldi antenna with design parameters.

high-band modes. In Appendix B the relation between L_{slot} against frequency, L_{stub} against frequency and Pos_{stub} against frequency is presented in Figures B.2 – B.4.

These formulae are used to calculate the design of different Vivaldi antennas which operate at these given frequencies: 2 GHz, 3 GHz, 4 GHz and 5 GHz. Figure 4.69 presents the simulated results for the S_{11} parameter of each band. The results show good agreement with the given calculated operating frequency, although as the frequency increases the bandwidth increases as well. This is because of the stub length of the design being matched at higher frequencies.

The rejected or blocked frequencies can also be calculated depending on the length of the slot and the stub for each design. When the slot length is equal to a half-wavelength (see Figure 4.70a), a full-wavelength (see Figure 4.70b) or multiples of these (see Figure 4.70c) for a particular frequency the resulting gain of the Vivaldi drops, as all current is resonating in the slot. Half-wavelength and full-wavelength in the slot are two of the first rejected frequencies, as presented in equation 4.20 and equation 4.21. The stub length also determines rejected frequencies, as shown in equation 4.22 and equation 4.23. This occurs when the stub is a multiple of the guided half-wavelength (see

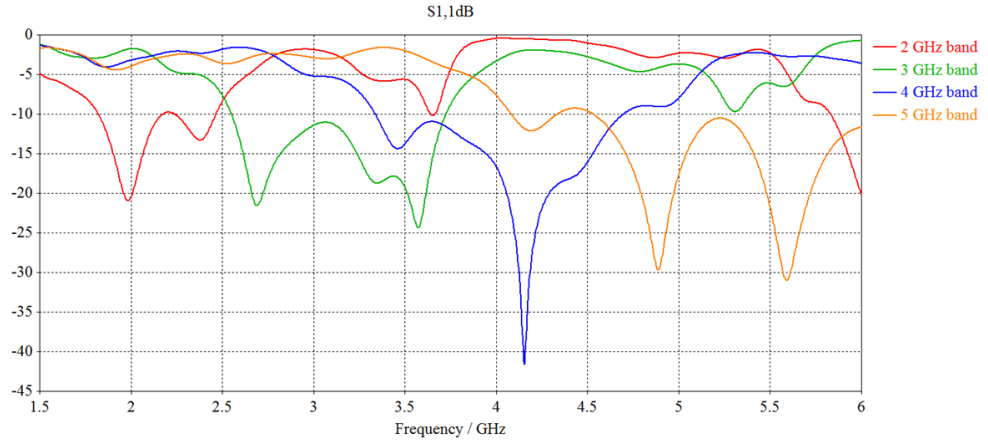

FIGURE 4.69: S_{11} parameter for the different operating bands of the reconfigurable Vivaldi antenna.

Figure 4.70d). A reconfigurable Vivaldi antenna can be designed using equations 4.17 – 4.23 to operate at the desired frequencies and reject the other bands so as to have higher isolation. One can also use these equations to design a Vivaldi antenna that rejects specific undesired frequencies.

$$Rejected\ frequency\ _1\ (in\ GHz) = \frac{0.26}{2 \cdot L_{slot}} \tag{4.20}$$

$$Rejected\ frequency\ _2\ (in\ GHz) = \frac{0.26}{L_{slot}} \tag{4.21}$$

$$Rejected\ frequency\ _3\ (in\ GHz) = \frac{0.157}{2 \cdot L_{stub}} \tag{4.22}$$

$$Rejected\ frequency\ _4\ (in\ GHz) = \frac{0.157}{L_{stub}} \tag{4.23}$$

Figure 4.71 represents the gain in the direction of maximum radiation for each band: 2 GHz in red, 3 GHz in green, 4 GHz in blue and 5 GHz in orange. For each band there are several drops in gain, the frequencies of this drops can be calculated using equations 4.20 – 4.23, with a minimum accuracy of 96.6 % compared to the simulated results.

The technical analysis presented here, demonstrates a reproducible method to calculate the dimensions of a reconfigurable Vivaldi antenna. It can be used to determine the slot

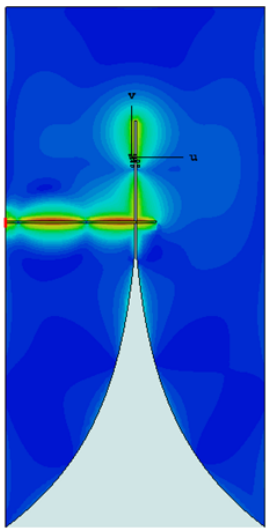

(A) Slot length is equal to half-wavelength.

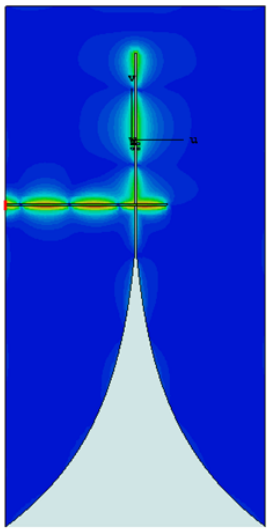

(B) Slot length is equal to 1 wavelength.

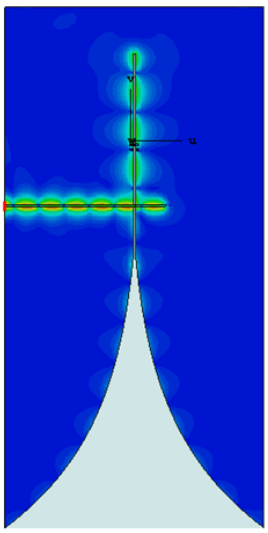

(C) Slot length is equal to 2 wavelengths.

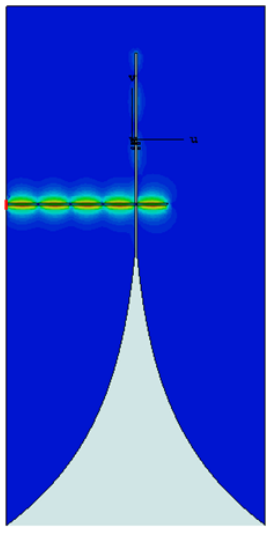

(D) Stub length is equal to half-wavelength.

FIGURE 4.70: Current distributions for different rejected frequencies in the reconfigurable Vivaldi antenna design.

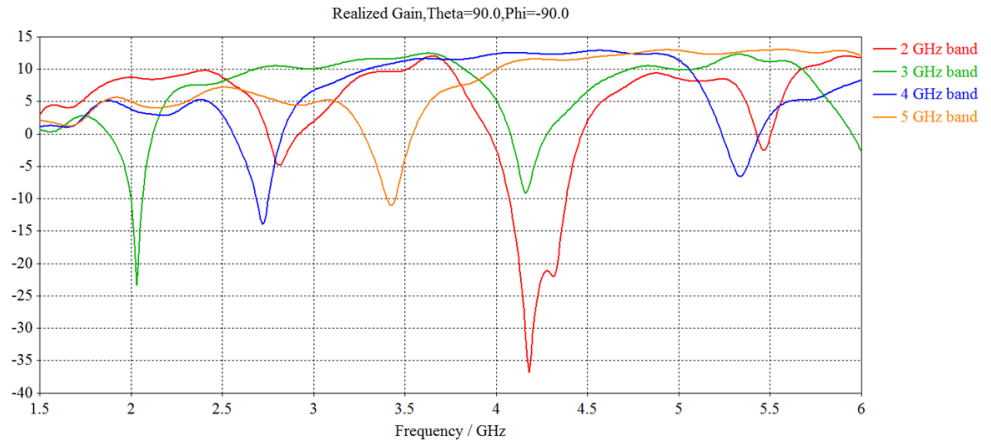

FIGURE 4.71: Realised gain for the different operating bands of the reconfigurable Vivaldi antenna.

length, stub length and stub position for the low-band mode and the RF-switch position in the slot and the stub in high-band mode. These RF switches can be introduced at any point of the slot or the stub and so the desired operating band inside the frequency range of the Vivaldi can be obtained.

4.10 A reconfigurable antenna versus a combination of antenna and filter system

As the necessity of a reconfigurable antenna design can be challenged arguing that an antenna + filter system can be implemented instead, this section addresses the requirements of such a filter that is able to achieve similar parameters as a reconfigurable antenna.

First, a non-tunable RLC filter is designed in CST MWS. Obtained results are analysed, but since ideal components are used, a commercially available non-tunable filter is proposed next. The specifications of tunable filters are not widely available as they are usually designed for specific requirements of each project. Therefore, in this section only non-tunable filters are compared. To fully compare an antenna + filter system with the reconfigurable Vivaldi antennas proposed in this research project a tunable filter would need to be designed and this is out of the scope of this project.

An RLC band-pass filter is designed in CST to operate at 3.3 GHz with 500 MHz bandwidth. Figure 4.72 presents the model. RLC filters are the simplest resonator structure, consisting of parallel or series inductors and capacitors.

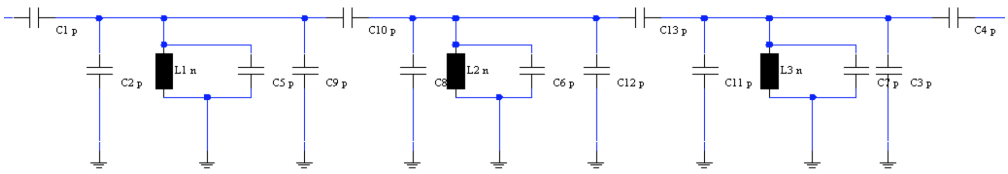

FIGURE 4.72: RLC band-pass filter of order 3 generated using CST MWS.

The designed filter is connected to the input port of the basic Vivaldi antenna and the combined frequency response is shown in Figure 4.73. In red, the Vivaldi antenna presents a wideband from 1 GHz up to 5.6 GHz. When the filter is applied, the bandwidth presents two bands: band 1 at 3 GHz and band 2 from 3.4 GHz up to 4 GHz as the green line shows. Other bands are rejected by the filter. Figure 4.74 presents the realised gain comparing the Vivaldi antenna (in red) and the Vivaldi antenna + RLC system (in green). The realised gain of the filter system is close to the realised gain of the basic Vivaldi antenna. At 3.3 GHz the gain is 0.4 dB lower. As frequencies outside the band are rejected by the filter, the out-of-band gain drops rapidly.

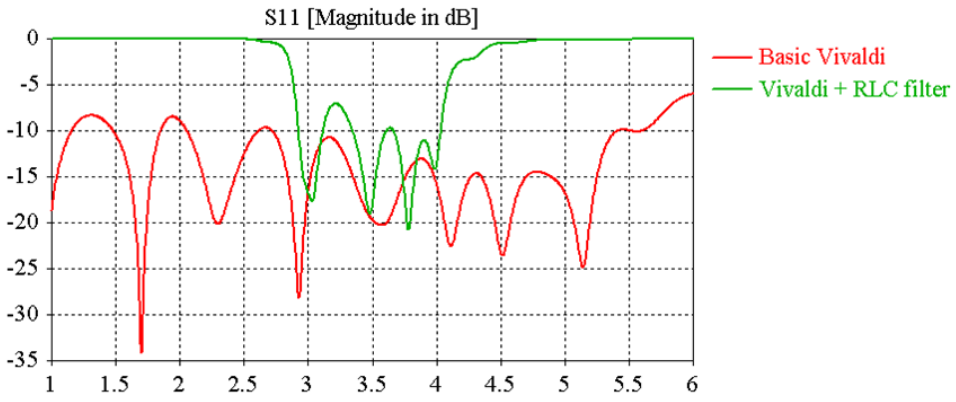

FIGURE 4.73: Simulated reflection coefficient for a Vivaldi + RLC filter system.

The main advantage of this design is its compactness, but it has poor performance. The lumped-element RLC filter in CST is designed using ideal capacitors and inductors. When operating at high frequencies, from 600 MHz, the inductor values become too small to be practical. For example, an inductor of 1 nH at 600 MHz is not even one full turn of wire. A distributed filter, usually used at the microwave band to overcome the issues aroused from the lumped-element RLC filter, offers a better compromise in terms of size and performance. The main drawbacks are the large space required to

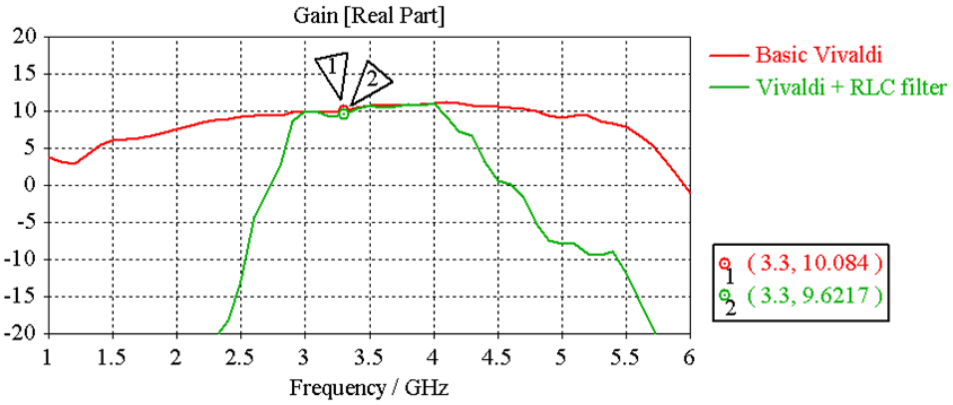

FIGURE 4.74: Simulated gain for a Vivaldi + RLC filter system.

implement the filter and, for a band-pass filter, the multiple band-pass replicas of the lumped-element filter because of the harmonics.

In practice a commercially available band-pass filter would be used. After a market research, the Dilabs B033ND5S band-pass filter is a reasonable choice as it operates at 3.3 GHz with 400 MHz bandwidth and it provides a small solution to be integrated with a portable system as it is designed with high-relative permittivity materials to reduce the overall size of the filter [97]. Table 4.13 presents a summary of this commercially available band-pass filter. The Dielectric Laboratories B033ND5S is available at a price of £206 per unit. The manufacturer also provides the S-parameters files which are introduced in CST MWS for simulation.

Parameter	**Value**
Operating band	3.1 to 3.5 GHz
Insertion loss	2.5 dB
Out-of-band attenuation	25 dB
Size	9.98 x 8.97 x 3.5 mm

TABLE 4.13: Dielectric Laboratories B033ND5S band-pass filter characteristics [97].

The filter frequency response using the manufacturer touchstone files is shown in Figure 4.75. The matching of the filter system is not as good as the matching of the basic Vivaldi antenna. The simulated realised gain is presented in Figure 4.76. At the operating frequency (3.3 GHz) the basic Vivaldi antenna has 1.9 dB higher gain compared to the antenna + filter system. This is because of the high insertion loss the filter introduces.

Furthermore, the filter system may require a matching circuit to match the antenna input port impedance. In the simulated model no matching was performed.

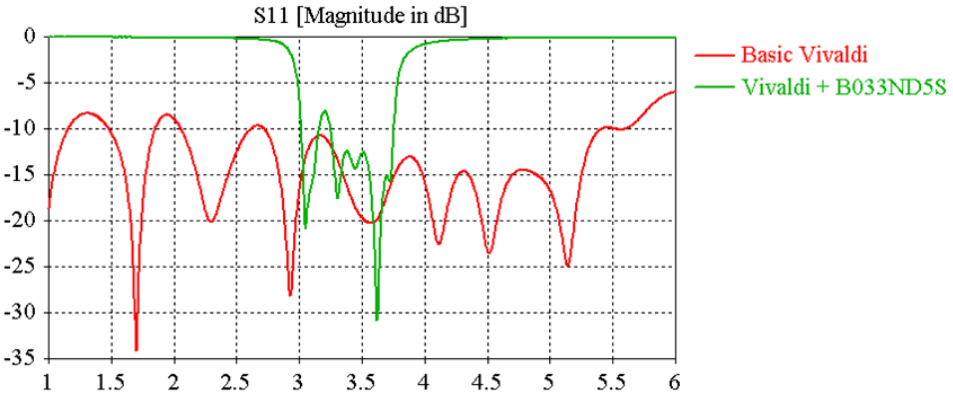

FIGURE 4.75: Simulated reflection coefficient for a Vivaldi + B033ND5S filter system.

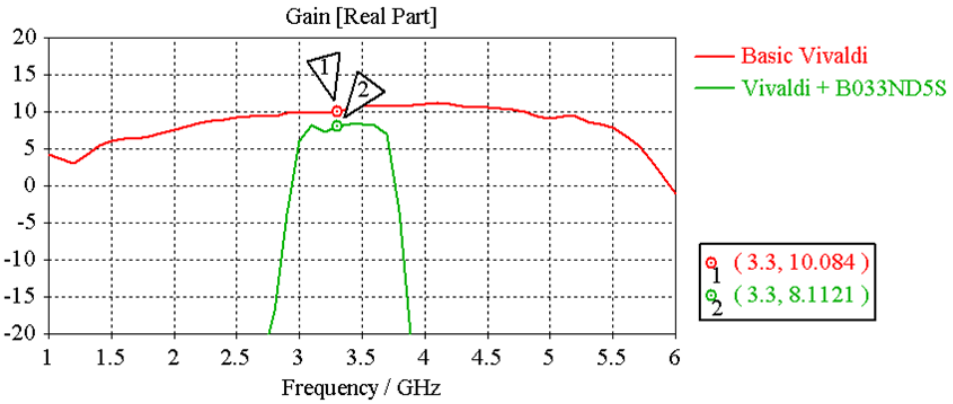

FIGURE 4.76: Simulated gain for a Vivaldi + B033ND5S filter system.

Another important issue to point out is that the filter model used in these simulations is fixed and non-reconfigurable. To have the same adaptability as a reconfigurable antenna in an antenna + filter system a reconfigurable filter is needed which will increase the cost, complexity, power consumption and occupied space of the design. Furthermore, a reconfigurable filter may not have the ideal performance as shown in the simulated results and it may degrade significantly the gain and even introduce undesirable bands to the design.

A frequency reconfigurable Vivaldi antenna can be electronically controlled to change the operating band without degrading the antenna performance or without the need of a bulky reconfigurable filter. Furthermore, frequency reconfigurable antennas can relax the filter requirements or even suppress the need of a filter [98].

In conclusion, introducing a filter may be a solution for some applications but for most portable devices with requirements on low cost, low power consumption and low complexity and restricted space a reconfigurable antenna may be a better answer.

4.11 Conclusion

A novel method for frequency reconfigurable antenna design was presented in this chapter. This low-cost method based its design in a directional wideband antenna, such as a Vivaldi antenna, because it can provide stable radiation pattern in all its bands. RF switches are introduced into the frequency-tuning stubs to reconfigure the band matched in the feed line of the Vivaldi antenna. These RF switches adjust the current path, thus tuning the operating frequencies the antenna become well matched.

First, a basic Vivaldi antenna was designed in CST operating from 900 MHz to 5.6 GHz. This antenna was optimised with a substrate extension which contributes to a 2 dB gain increase in the whole band.

The reconfiguration using RF switches was studied next. Several designs provide two, three and four reconfigurable frequency bands. Stable high gain was achieved, between 10 dBi and 14 dBi, with a maximum difference of 2 dB inside each band. The gain dropped rapidly outside the band and each band provided up to 30 dB of rejection to the closest band, which can be advantageous for spectrum surveillance. A good isolation between bands combined with wide bandwidth can be very useful for spectrum monitoring in case there is a jamming signal that needs to be suppressed to be able to receive communications without saturating the receiver. The position of the switches in the slot and the stub can be modified to adjust the operating bands. All the proposed designs accomplished in-band stable high gain and several rejected frequencies which can be adjusted to block certain bands.

Design A was proposed using Radant RMSW100 RF-MEMS switches. These switches present low insertion loss, good isolation and low bias current while operating up to 12 GHz. They require a driver to operate because the actuation voltage of the switches is 90 V. The fabricated prototype presented several challenges. The fabrication in the departmental workshop was performed using a milling machine which removed some of the dielectric substrate when removing the copper in some sections. The etching machine could not be used because the antenna needs to fit in an A4. This was taken into account for the following designs. Another challenge was the RF-MEMS switches integration in the antenna. This was made by manually soldering the switches although

a wire bonding machine was required to do the job which was unavailable. Furthermore, these switches are ESD sensitive, making the task even more complicated. The measured results for design A were not satisfactory. Several discrepancies appeared for the reflection coefficient and the gain was not measured as the results would be inconclusive.

The Radant RMSW100 RF-MEMS switches seemed a good candidate for reconfigurable antennas but they were very difficult to integrate in the design, the biasing demanded an expensive driver with driving voltages affecting the antenna performance. All these reasons proved these RF-MEMS switches were not suitable for the security applications of this project.

A low insertion loss GaAs MMIC RF switch was considered for design B. HMC550AE RF switches are low cost, do not require a driver and are easily integrated in the design as they are provided in a SOT26 SMT package. Surface mounted HMC550AE RF switches were used to reconfigure the current paths in the antenna. Yet they have some drawbacks, for example, poor isolation. For this design one RF switch was used for reconfiguration to simplify the fabrication and measurement process. First, a cut was introduced to separate the RF ground plane from the DC ground plane to properly bias the RF switch. This cut separates the two wings of the antenna. The antenna was designed to have two bands with high isolation, although only one switch was used. Even with only one RF switch in the design, the isolation between bands was more than 25 dB. The antenna high isolation can relax the requirements of the filter in the receiver or even suppress the need for a filter.

The measured results of design B showed good agreement with the simulated results, both for reflection coefficient and gain. Good isolation for the low band in high-band mode was obtained but in the low-band mode the high-band isolation differs by more than 10 dB compared to simulation. It can be caused by fabrication inaccuracies, the coupling of the bias lines to the control board, measurement misalignment or other limitations in the setting of the university anechoic chamber.

Moreover, a model for the technical analysis of the reconfigurable Vivaldi antenna was introduced. A reproducible method was proposed to calculate the dimensions and switch positions of a reconfigurable Vivaldi antenna. It can be used to determine the slot length, stub length and stub position for a low-band mode and to calculate the RF-switch positions in the slot and the stub for other higher bands. These RF switches can be introduced at any point of the slot or the stub and so the desired operating band inside the frequency range of the Vivaldi can be obtained. The model also calculates the rejected frequencies of each band with a minimum accuracy of 96.6 % compared to simulation.

Finally, as the need of a reconfigurable antenna can be challenged arguing that a system including an antenna plus a filter is more viable a comparison study was performed. Two filters are proposed: an RLC filter because of its simplicity and a commercially available filter (Dilabs B033ND5S). The RLC filter is not feasible for frequencies over 600 MHz as the capacitors and inductors are too small to be practical. The Dilabs filter achieves similar bandwidth but with 2 dB lower gain. The main drawback was that this filter was fixed and was not tunable. A tunable filter will increase the cost, complexity, power consumption while degrading significantly the gain and even introducing undesirable bands. Depending on the application requirements a reconfigurable antenna may present preferable characteristics because of its low cost, low power consumption, low complexity and small space used.

In conclusion, although design B presented satisfactory measured results, it is not a highly flexible design as the technology used does not allow continuous frequency tuning. Furthermore, the RF switches introduced losses, added an extra cost to the system and were not easily integrated in a design with the required bias lines. Consequently, as the RF switches are problematic for low-cost and compact-size designs, new technologies will be studied for frequency reconfigurable antennas in the next chapter.

Chapter 5

Reconfigurable antennas using ionised solutions

5.1 Introduction

Frequency reconfigurable antennas using RF switches can only provide limited capability in frequency tuning. Most of the RF switches are lossy and biasing circuits could be complicated and affect antenna performance significantly, as discussed in section 3.1.1.1, while only achieving discrete tuning. Fluid antennas have no defined shape; therefore theoretically it is possible to create the desirable shape of a fluid antenna for different frequency bands. Continuous tuning can easily be achieved by fluid antennas. Fluid antennas using an ionised solution, such as KCl solution, could be lossy, and the containers of fluid must be leak-free but they can provide highly dynamic low-cost results. Therefore, creative designs are required. Stereolithography (SLA) based 3D printing technology can support creative designs to solve the problem of encasing the fluid and attaching it to an antenna.

In this chapter an ionised solution monopole is considered as an initial design to study the application of ionised solution in antennas. Additionally, further methods for band-tuning in a Vivaldi antenna are studied.

As explained in the conclusion of Chapter 4, RF switches introduce undesirable losses for a high gain antenna design and reconfiguration is limited by bias lines for the applications of this project. Moreover, the use of capacitors, varactor diodes or RF switches for antenna frequency tuning relies on some parts of the antenna resonating at certain frequencies which may deteriorate the overall performance of the antenna. Introducing

fluid control methods can be beneficial because of their durability, ease to conform into desired shapes, reduced biasing effects and high-power handling capability when compared to other RF switches technology [99].

Therefore, the first part of this chapter focuses on a new approach for reconfigurable antennas that can give us satisfactory results, which are fluid antennas. New developments show that fluid antennas have radiation efficiencies close to solid conductor antennas, up to 90 % [78]. A seawater antenna can be treated as a normal conducting antenna when the conductivity value is over 10^2 S/m since antenna efficiency is well over 80 %, as reported in [88]. Some of the advantages that fluid antennas provide are more flexibility when changing the shape of the antenna, no bias lines that will affect radiation and the use of flexible casing materials without cracking.

State-of-the-art designs on fluid antennas were presented in the literature review. Generally they use an expensive liquid conductor material, such as Galinstan [81] or EGaIn [80], because these materials provide high conductivity and efficiency. However a low-cost system requires a low-cost material. Liquid conductors such as mercury are toxic and its high surface energy tends to minimise surface area which prevents it from forming mechanically stable structures [78, 100]. Seawater is a cheap alternative, eco-friendly and easy to get, but it can evaporate and the conductivity is relatively low compared to other liquid conductors. Ionised solutions such as NaCl and KCl, have higher conductivity compared to seawater and are cheap and easy to produce. The aim of the first part of this chapter is to unveil the potential of fluid antennas and then propose a hybrid design for a high-gain reconfigurable antenna.

The second part of this chapter focuses on the insertion of liquid-controlled parts into the reconfigurable Vivaldi antenna. As shown in the previous chapter, RF switches can be introduced at different points of the slot changing the operating frequency of the high band. The same can be implemented using ionised solutions to short-circuit a point of the slot. Introducing a conductive ionised solution reconfiguration instead of RF switches in the Vivaldi design proposed in the previous chapter can be a significant improvement in maintaining high performance while providing continuous tuning within a band.

5.2 Fluid antennas

5.2.1 Introduction to fluid antennas

Fluid antennas can be categorised as dielectric resonator antenna (DRA), because of its low-loss microwave dielectric constant. Their resonant frequencies are predominantly a function of size, shape, material and permittivity [101]. Different materials within a wide range of permittivity can be used to fabricate DRA, thus different sizes can be employed for the same frequency. As a special type of DRA, fluid antennas have some advantages compared to conventional copper antennas [102, 103]:

- Fluid antennas can be reversibly deformed. The casing defines the mechanical properties of the antenna so that the fluid metal flows inside it. When an elastomer casing is used the fluid can adapt to ensure electrical continuity.
- Fluid antennas adopt the mechanical properties of the encasing material.
- These antennas provide flexibility to the design because they are mechanically tunable and sensitive to strain.
- Fluid antennas are durable.
- These antennas are easily conformed into the desired shape.
- The ionised solution can form a contact at room temperature without the need of soldering.
- These antennas can self-heal in response to sharp cuts or cracks.
- The antenna can have small RCS by draining the liquid when not in use for radar or warfare applications.
- The fabrication of the antenna is simple by soft lithography [80, 104].

Furthermore, fluid antennas can be used for medical applications. Portable systems for continuous health monitoring must be wearable, soft, compact, bio-compatible and reliable. Bio-sensors that need to be placed in different parts of the body and then connected using wires suffer from limited performance and usability. Furthermore, current systems that provide wireless connectivity are not designed for continuously transmitting other than to a portable unit worn by the individual and are subject to inaccuracy of GPS indoors [79]. Ionised solutions or liquid conductors are a good alternative for

health monitoring devices as they can overcome limited performance of solid metals in contact with human tissue [105]. Moreover, the use of a flexible plastic casing makes the antenna corrosion-resistant as well as comfortable to wear for real-time bio-monitoring.

Other suitable applications are found in security applications because of the stealth capability of the liquid when not in use. For example, in [106] seawater is radiating under controlled electric and magnetic fields. These fields ionise water so that water molecules oscillate and contribute to radiating energy. This is suitable for stealth capability in security applications as it only radiates in excited state, but also for monitoring health in biomedical applications because of its flexible properties and radiation capability when in contact with human tissue.

5.2.2 New concept: Antennas-on-demand

Recently, a new technology for touchable keyboards has been developed that can be of interest for this research project. In [107] a deformable physical tactile layer that when triggered creates buttons or shapes of a specific size is proposed. An elastomer is used on the topmost part of the multi-layer stacks to allow deformation. Several micro channels feed a transparent liquid into the elastomer layer to create buttons. This enables an array of physical buttons to rise out of the surface of the display.

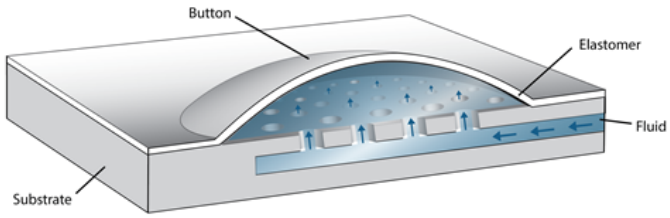

FIGURE 5.1: Deformable fluid button when activated [107].

The deformable button works as follows. The top layer is an elastomer that allows deformation to create buttons when and where needed. In the current design a fixed pattern is used, i.e. a keyboard, but it may create any shape. Each button is connected to a pool of fluid through channels. The substrate contains channels where the fluid can arrive to the buttons and go back. When the keyboard is triggered, a fluid is pushed through the channels to the button dedicated space. As the pressure is maintained the button stays on until the fluid is pushed back and the touchable keyboard becomes flat

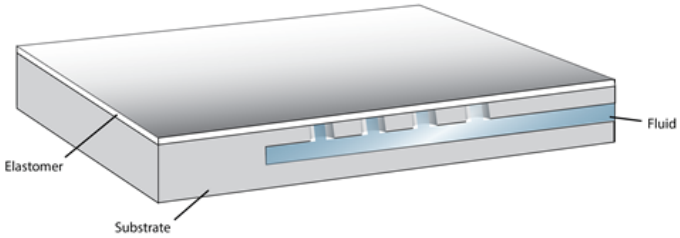

FIGURE 5.2: Deformable button when deactivated [107].

[108]. Figure 5.1 shows a diagram of an emerging button in the surface and Figure 5.2 shows a flat surface with no deformation when the fluid is not pressured.

FIGURE 5.3: Touchable tactile display with deformable buttons [107].

Currently, its application is in tactile displays, where it can materialise buttons for a keyboard. The idea is that when the keyboard is triggered by software, an automatic process makes the touchable keys appear on the screen. Alternatively, when the keyboard is not required it is removed from the screen leaving a flat surface. In Figure 5.3 a tablet is shown with deformable keyboard when activated. Figure 5.4 presents an example of touchable screen in a laptop that a keyboard can appear when needed, but it remains flat when the keyboard is not required.

However, another application in antenna systems is also possible. This could easily apply to reconfigurable antennas by substituting the liquid by a conductive fluid. The resulting reconfigurable antenna has great potential and could form any pattern achievable on a surface allowing a high degree of reconfiguration. Furthermore it could drain all

FIGURE 5.4: Example of application of the deformable keyboard in a laptop [107].

conductive liquid when it is not in use, thus presenting stealth capabilities. It would reduce RCS as well as mutual coupling to other antennas nearby. This new antenna opens up a whole world of possibilities and could be easily integrated in portable devices for biomedical applications, either in a touch screen or at the back of the device.

The novel concept developed in this research project is called "antennas-on-demand". It means the antennas can be made available or non-radiating when necessary, thus eliminating detection and interferences with other systems. Antennas-on-demand can be advantageous to security applications as well as other communications systems where more than one antenna is required.

Moreover, as these fluids have high permittivity, the antenna size can be reduced by $\sqrt{\varepsilon_r}$ [88]. The fluid permittivity depends on the type of conducting liquid and its relative permittivity [106]. This means the antenna can be smaller compared to a solid metal antenna.

5.2.3 Fabrication

The fabrication process for fluid antennas can be implemented using different processes. In this section the two main processes to assemble the encasing for the liquid metal are described. One material used is PDMS (polydimethylsiloxane), which is a flexible and deformable elastomer that is commercially available. The first process is lithography

which is used to create microchannels in the PDMS encasing and then inject the fluid with a syringe to create the radiating elements. Another option is to use a 3D printer to fabricate a 3D model of the desired shape using resin provided by the manufacturer. 3D printers are highly flexible to create the required shape which cannot be easily fabricated using conventional techniques. These printers are becoming cheaper and more available for different types of materials, which makes them a good candidate for fabricating prototype designs in antennas. Several designs using 3D printing for rapid prototyping have already been presented in the literature review [84–86].

Soft-lithographic process is explained in [80] where they fabricate microchannels that define the shape of a radiating element. First, a negative pattern, defined as "master pattern", is created using photolithography. This pattern is used to cure the PDMS pre-polymer and to create a reverse replica of the master. Then, sealing this layer against another thin, flat sheet of PDMS called the "spacer layer" produces microfluidic channels (see Figure 5.5) [78]. A syringe is used to inject liquid metal into the microchannels. These microchannels determine the shape of the fluid in the antenna.

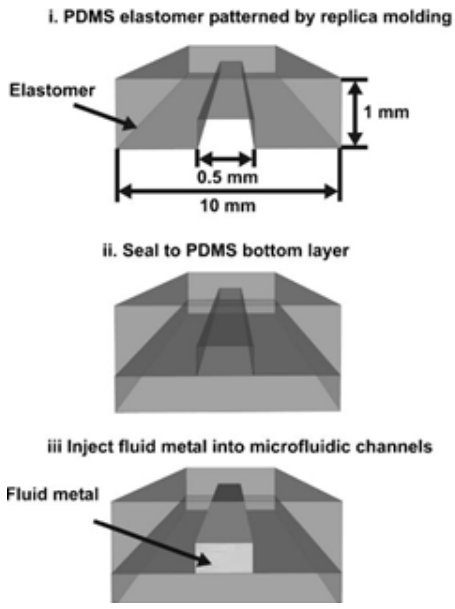

FIGURE 5.5: Microchannel fabrication process using soft lithography [78].

On the other hand, 3D printing uses a resin photopolymer to form numerous shapes. Form1+ is a low-cost 3D printer from Formlabs with high resolution of 25 microns [109]. It uses stereolithography (SLA) to achieve high accuracy and high resolution. Stereolithography consists of dividing the model into different layers of defined thickness and then use ultraviolet radiation to define the selected model. A liquid photopolymer is exposed to an ultraviolet laser that solidifies the polymer when it is sufficiently exposed.

When a layer is completed, the platform supporting the design pulls the model upwards out of the tank to illuminate the next layer. The model is finished by repeating this process layer by layer for each cross-section [110]. The minimum achievable feature size with Form1+ is 300 microns and the layer thickness is between 25 microns and 100 microns. Figure 5.6 shows the Form 1+ 3D printer with an example part that has been 3D-printed. The dimensions of this printer are 30 x 28 x 45 cm and it can print components up to 12.5 x 12.5 x 16.5 cm using different resins depending on the final application [111].

FIGURE 5.6: Form 1+ high-resolution 3D printer [109].

5.2.4 Study of different ionised solutions and concentrations

The main salt ions in seawater that make up 99.3 % of the salinity are [112]: chloride (55 %), sodium (30.6 %), sulfate (7.7 %), magnesium (3.7 %), calcium (1.2 %) and potassium (1.1 %). Sodium chloride (NaCl) and potassium chloride (KCl) are chosen because they are non-toxic, non-corrosive, soluble in water and their solutions in water can be more conductive compared to water. NaCl is sodium chloride also known as common salt. KCl is a metal halide salt composed of potassium and chloride which is only toxic in excess. NaCl and KCl provide some of the ions most responsible for the salinity in seawater.

An experiment was set up to measure the permittivity for different ionised solutions as shown in Figure 5.7. Agilent 85070E Dielectric Probe Kit [113] is used to measure the permittivity properties of the ionised solutions using Agilent E5071C VNA as presented in [114].

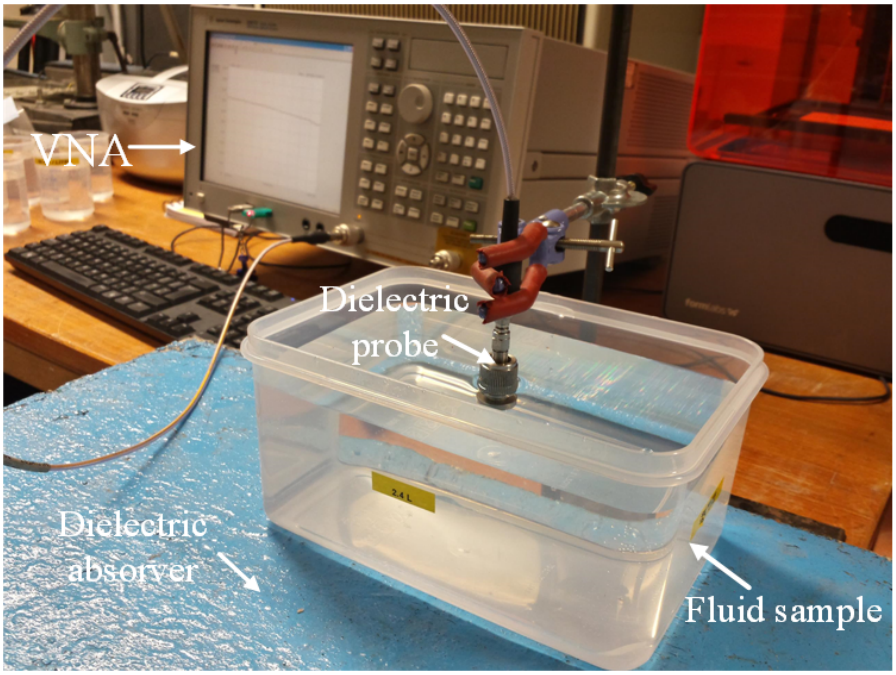

FIGURE 5.7: Experiment setup for permittivity measurements of ionised solutions.

First, deionised water is measured to obtain a reference (as shown in yellow in the results). Then, 0.1 mol, 0.5 mol, 1 mol and 2 mol of NaCl and KCl are dissolved with water. The molecular weight of NaCl and KCl is used to determine the weight of salt per litre that is needed to produce each ionised solution, as calculated in Table 5.1. The ionised solutions are measured at a temperature of 20° C. Permittivity properties are measured from 500 MHz to 8.5 GHz because that is the maximum range given by the VNA.

	0.1 mol	**0.5 mol**	**1 mol**	**2 mol**
NaCl	5.844 g	29.221 g	58.443 g	116.886 g
KCl	7.455 g	37.276 g	74.551 g	149.103 g

TABLE 5.1: Concentration of grams per litre for each measured ionised solution.

The real part of the measured relative permittivity ($\varepsilon_r^{'}$) against frequency is presented in Figure 5.8. The highest relative permittivity is presented by deionised water in yellow. It is close to 80 which is the theoretical value of deionised water.

The tendency of decreasing in frequency is normal, as at low frequencies all types of polarisation may be effective. However, as frequency increases the material net polarisation drops as some polarisation mechanisms cease to contribute. When analysing the

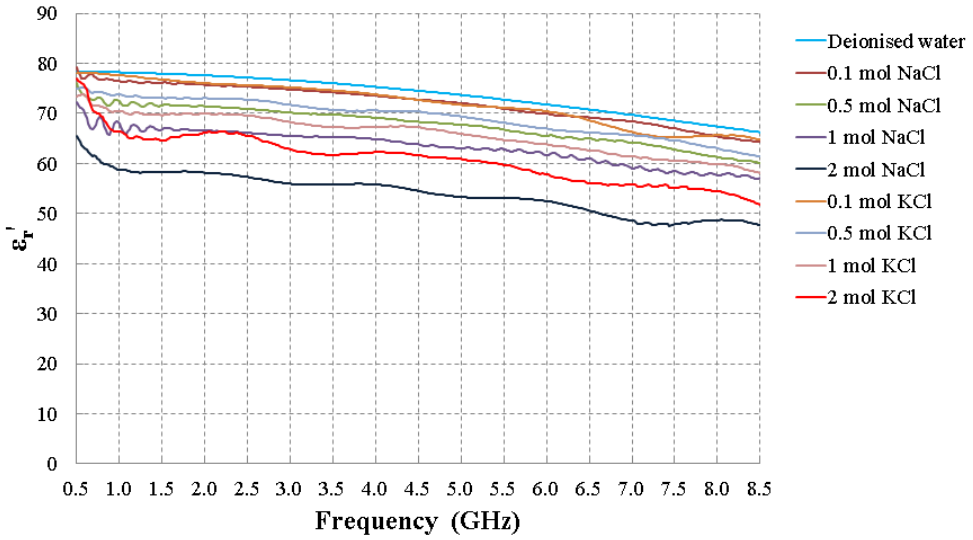

FIGURE 5.8: Measured relative permittivity for different concentrations of NaCl and KCl solutions.

results it can be affirmed that as concentration increases relative permittivity decreases.

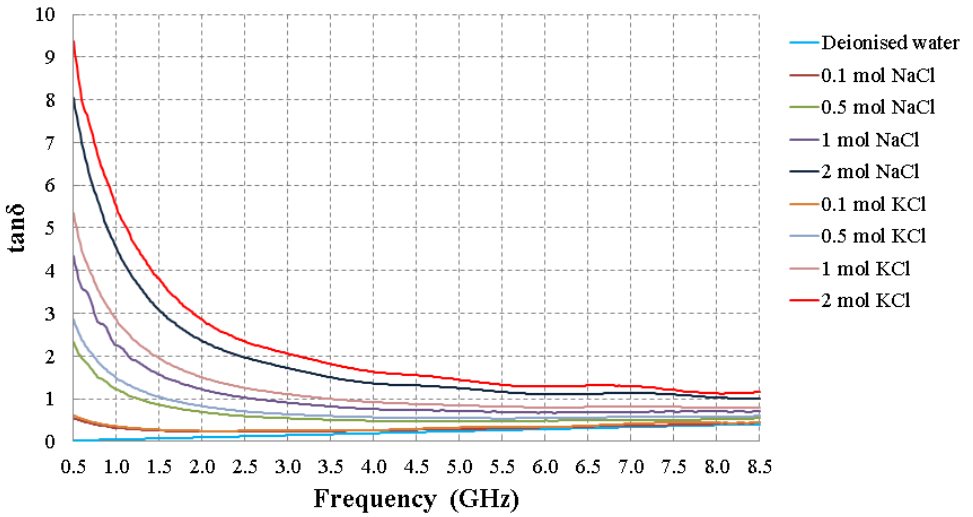

FIGURE 5.9: Measured loss tangent for different concentrations of NaCl and KCl.

To calculate loss tangent ($tan\delta$) equation 5.1 is used, where ε_r'' is the imaginary part and ε_r' is the real part of the complex relative permittivity (ε_r). Loss tangent is a material property that indicates the time it takes to polarise the dielectric material when an alternating field is incident on the material. It depends on frequency, as shown

in Figure 5.9. The higher the loss tangent is and the slower it is to decay the higher the losses in the material.

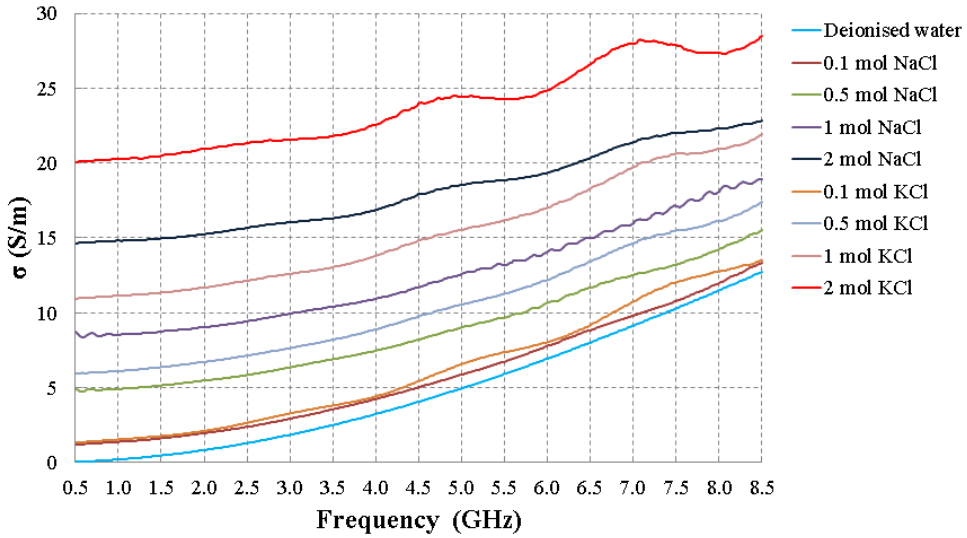

FIGURE 5.10: Measured conductivity for different concentrations of NaCl and KCl.

$$tan\delta = \frac{\varepsilon_r''}{\varepsilon_r'} \tag{5.1}$$

From the relative permittivity and the loss tangent the conductivity of each ionised solution against frequency can be calculated, as presented in Figure 5.10. Conductivity is calculated as in equation 5.2. As expected, deionised water has the lowest conductivity. When increasing the concentrations in both, NaCl and KCl, conductivity increases. Comparing the two ionised solutions, NaCl and KCl, KCl always presents higher conductivity for the same concentration compared to NaCl.

$$\sigma = \omega \cdot \varepsilon_r'' \cdot \varepsilon_0 \tag{5.2}$$

As potassium chloride is one of the main components of seawater, 2 mol KCl solution is chosen as the ionised solution because it presents the best conductivity properties. Its permittivity properties are imported into CST to get more accurate simulation results. CST also uses equation 5.2 to calculate conductivity from permittivity and loss tangent.

5.2.5 Initial designs

In this section, several initial designs using fluid conductors on antennas are presented and their simulation results analysed. To understand the behaviour of fluid antennas a monopole design is chosen for its simplicity.

5.2.5.1 Copper monopole

A monopole with a PDMS encasing is simulated in CST Microwave Studio. The geometry of the design is shown in Figure 5.11. The length of the monopole is 32 mm with a diameter of 1 mm and the ground plane area is 5x5 mm^2.

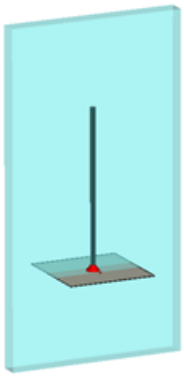

FIGURE 5.11: A monopole design with PDMS encasing.

To encase the fluid a 2 mm thick silicon-based elastomer is used: PDMS (polydimethylsiloxane). A model can easily be fabricated using a 3D printer. The material characteristics of PDMS have been introduced in CST Microwave Studio to obtain realistic results. PDMS has a relative permittivity of $\varepsilon_r = 3.0$ and $tan\delta = 0.05$ at 3.45 GHz [80].

First, a copper monopole antenna encased in a PDMS is simulated. The copper conductivity is $5.96 \cdot 10^7$ S/m. The simulated S_{11} parameter is shown in Figure 5.12. It resonates at 2.4 GHz with a 10-dB bandwidth of 270 MHz, hence it could be used for Wi-Fi or Bluetooth applications. The bandwidth can be tuned by changing the radius of the conductor of the monopole.

The radiation pattern of a copper antenna presents a typical omnidirectional monopole antenna radiation pattern. The radiation efficiency calculated by CST is 86 %.

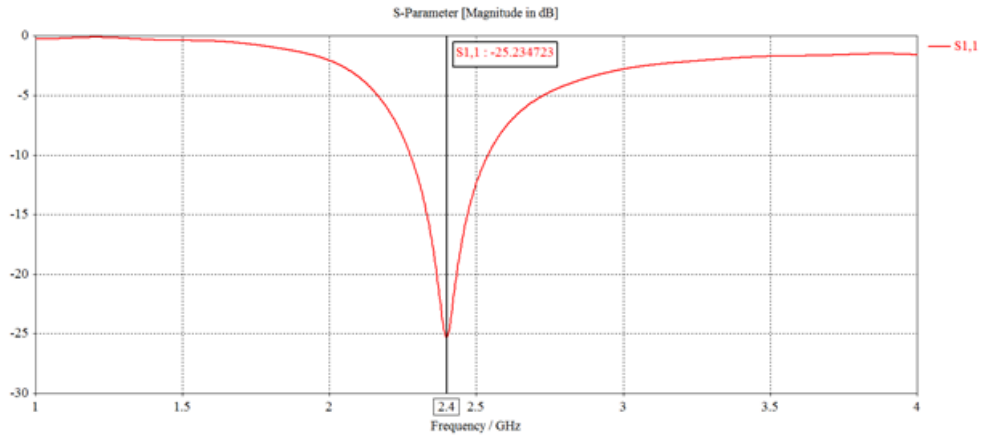

FIGURE 5.12: Simulated S_{11} parameter of copper monopole.

5.2.5.2 EGaIn monopole

Next, a EGaIn monopole is designed using the same dimensions as the copper monopole. The properties of this liquid conductor are introduced in CST Microwave Studio and the simulation results analysed. The simulation operating frequency changes only by 20 MHz, as displayed in Figure 5.13, although the radiation efficiency drops down to 70 %. This is because of the EGaIn conductivity being lower ($\sigma = 3.4 \cdot 10^6$ S/m) compared to the copper conductivity ($\sigma = 5.96 \cdot 10^7$ S/m). The bandwidth is maintained at around 300 MHz.

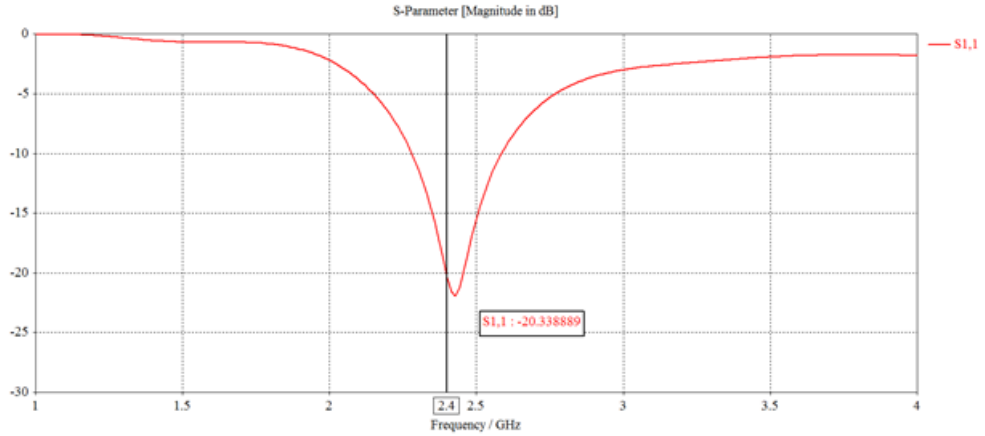

FIGURE 5.13: S_{11} parameter for EGaIn monopole.

Figure 5.14 shows the 3D-view of the radiation pattern. Again, it is maintained compared to the copper monopole with a gain of 2 dBi and 3 dB beamwidth of 85.3°. Figure 5.15

compares both E-planes of copper and EGaIn monopoles and it can be concluded the difference is insignificant.

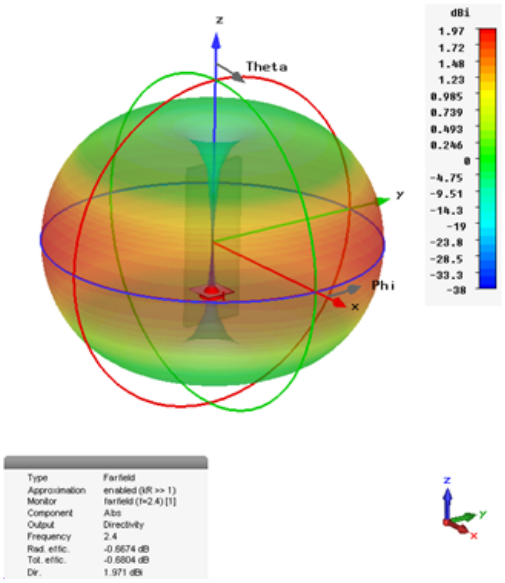

FIGURE 5.14: Radiation pattern of EGaIn monopole.

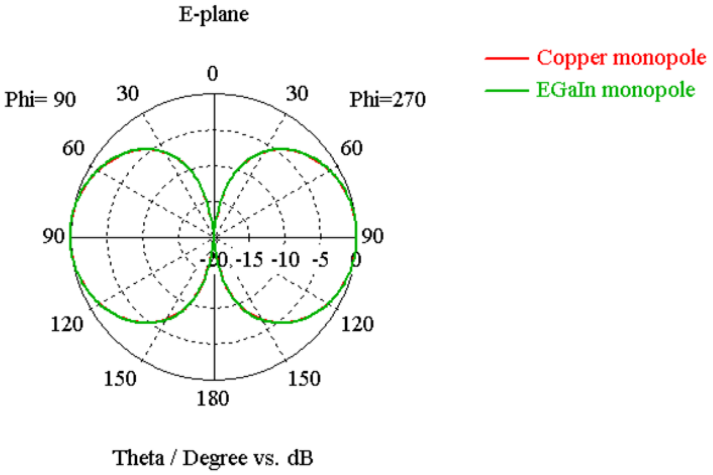

FIGURE 5.15: E-plane comparison between copper monopole and EGaIn monopole.

The surface current distribution of the EGaIn monopole is presented in Figure 5.16. As in the copper monopole, there is a maximum in current at the excitation point and the current diminishes until it gets at the open end of the monopole. This is a typical current distribution for a quarter-wave monopole. This proves it is a resonant antenna because it always presents the maximum and minimum current at the same positions.

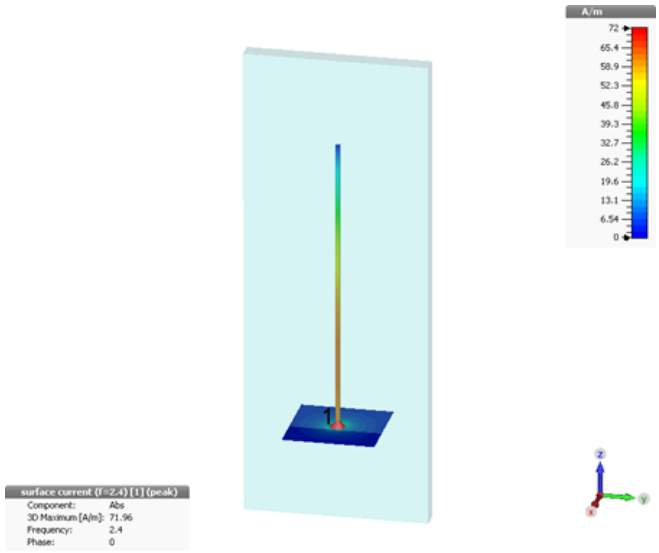

FIGURE 5.16: Surface current distribution for EGaIn monopole.

5.2.5.3 Reconfigurable EGaIn monopoles

The EGaIn monopole results are very close to the copper monopole, so it can easily replace the copper monopole. As a fluid, EGaIn can be pumped in or out of a monopole antenna, achieving frequency reconfiguration.

In Figure 5.17 the EGaIn monopole is simulated with different EGaIn heights. The result is a change in its operating frequency. By changing the height from 25 mm to 35 mm, the operating frequency decreases from 2.9 GHz to 2.25 GHz. Another advantage of this design is it can tune continuously any frequency within a range, by pumping or draining the liquid conductor. Figure 5.18 shows the E-plane radiation pattern for all four frequencies with a minimal difference.

Moreover, the initial design can be extended to a multiple reconfigurable design by introducing more input ports and adding other monopoles in different directions. This technique can be used as in Figure 5.19 with 3 input ports and 3 monopoles. Several monopoles provide polarisation diversity to the design. Additionally, as the fluid antennas allow draining of the fluid, each monopole can be reconfigured to different frequencies as in [88] or even disabled to avoid mutual coupling. Therefore, creating a new concept of "antennas on demand".

For example, in the proposed design when horizontal polarisation is needed the fluid is pumped to the horizontal monopole leaving others with no fluid and only port 1 is excited. The same idea applies to other polarisations. Besides, a combined polarisation

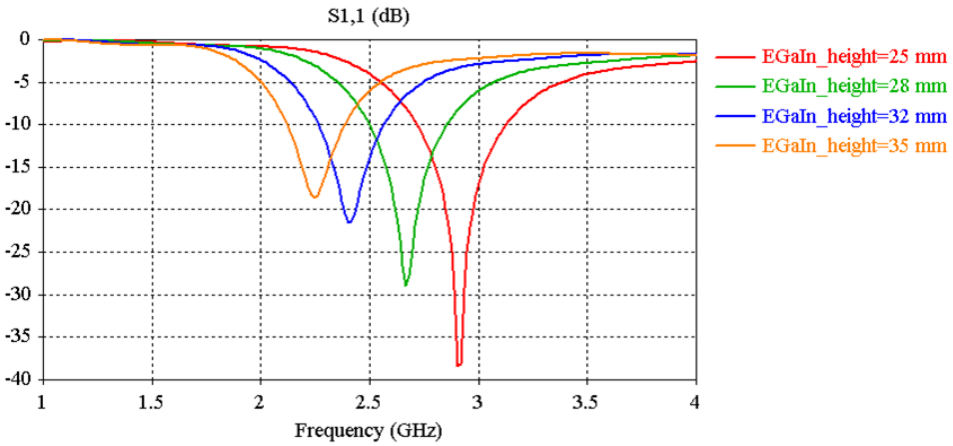

FIGURE 5.17: S_{11} parameter for different heights of EGaIn monopole.

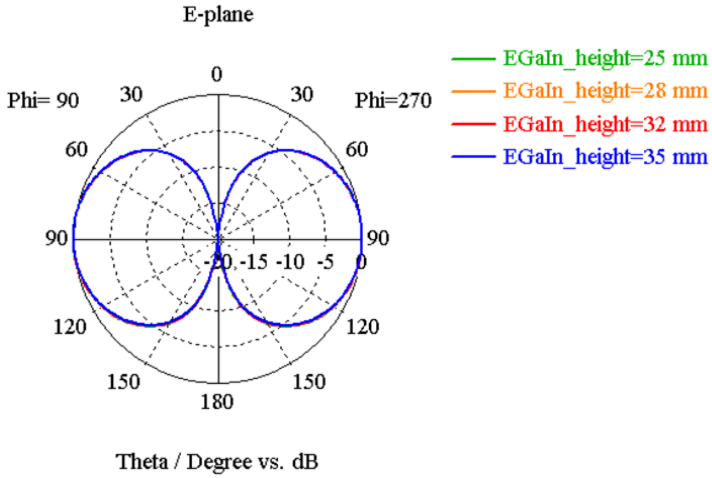

FIGURE 5.18: E-plane radiation pattern for different heights of EGaIn monopole.

(dual polarisation) is also possible. When the antenna is no longer necessary, the fluid is drained to a storage tank where it does not present any coupling effect.

In the simulation an excitation port is introduced, but in practice a different kind of feeding would need to be implemented. An SMA connector would mean a fissure in the sealed encasing material that can result in a leakage of fluid. Therefore, a proximity coupled feed line can be a good alternative for these designs. Different proposed methods need to be studied and adapted to achieve maximum power transmission and lower disturbance to the design.

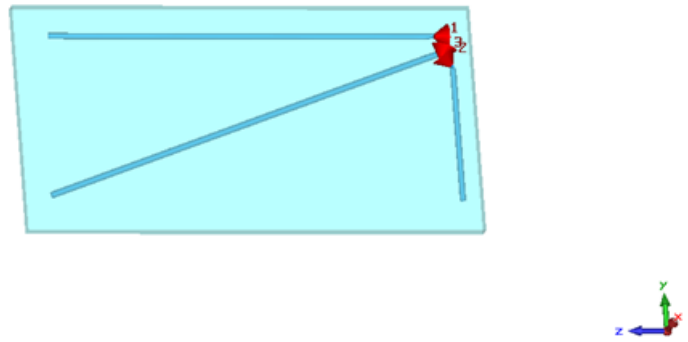

FIGURE 5.19: Reconfigurable design using multiple fluid monopole antennas.

5.2.6 KCl solution monopole

A KCl solution monopole is designed in order to test an ionised solution monopole prototype. The geometry is shown in Figure 5.20. It consists of a 1-mm thick 3D-printed tube on top of a copper ground plane. Figure 5.21 shows a cut view of the geometry. A panel mount SMA connector is modelled to excite the antenna. The tube is 50 mm long, 1 mm thick and has an inner radius of 2.5 mm. The ground plane is 15 x 15 mm^2.

An experiment was set up to measure the dielectric properties of the resin used to 3D-print the tube. Agilent 85070E Dielectric Probe Kit is used to measure the permittivity properties of a 7x7x7 cm^3 3D-printed cube at the frequencies of interest. The resin used is provided by Formlabs, the 3D printer company. Formlabs "clear resin" is measured and a relative permittivity of 2.0 and a loss tangent of 0.1 at 3.0 GHz are obtained. These results are imported into CST to obtain more accurate results when simulating the KCl solution monopole.

The reflection coefficient against frequency is presented in Figure 5.22. This simulation is obtained by varying the height of ionised solution in the monopole. When the ionised solution height increases, the frequency decreases as it is expected. The KCl solution operates as the radiating part of the monopole, if the monopole height increases the operating frequency decreases.

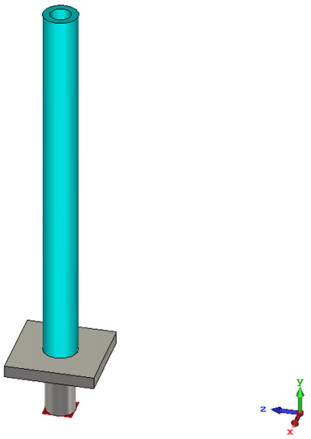

FIGURE 5.20: Ionised solution monopole antenna design.

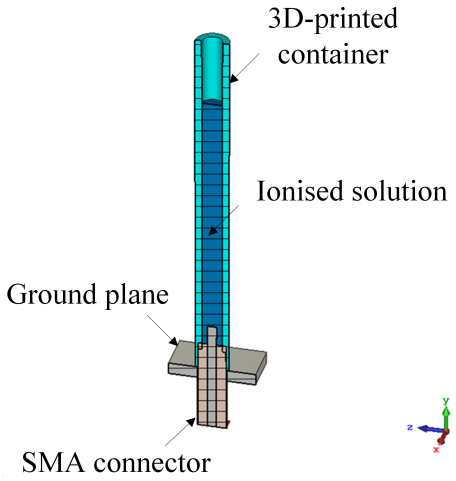

FIGURE 5.21: Cut view of the ionised solution monopole antenna design.

The passband for each configuration is given for the second resonance of the monopole considering this resonance presented better efficiency. Limited matching is implemented as the goal is to prove the concept. Later in this chapter other resonances of the KCl solution monopole are presented and analysed.

Figure 5.23 shows the simulated gain of the KCl solution monopole for different ionised solution heights. Realised gain is around 3 dBi when the solution is 30 mm and 40 mm high, but it goes down to 2 dBi when the ionised solution height is 10 mm and 20 mm high. This is because of the radiation efficiency of the antenna.

Next, the monopole is analysed for different container/tube inner radius at an ionised

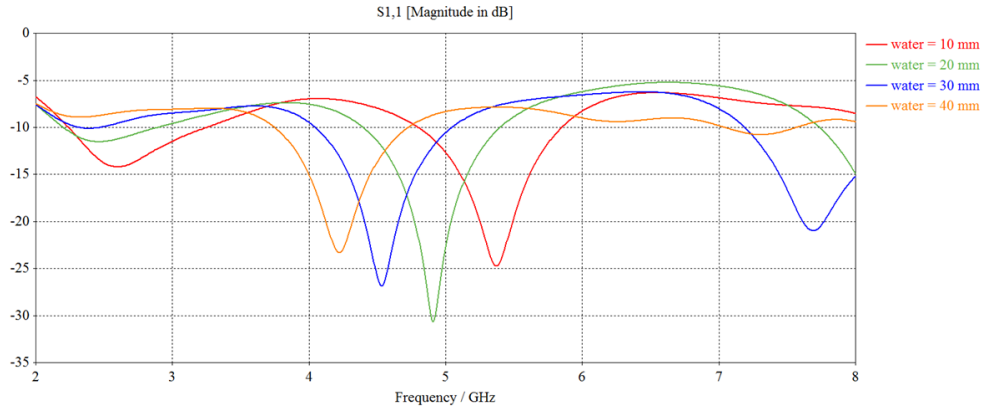

FIGURE 5.22: S_{11} parameter for different KCl solution heights in an ionised solution monopole.

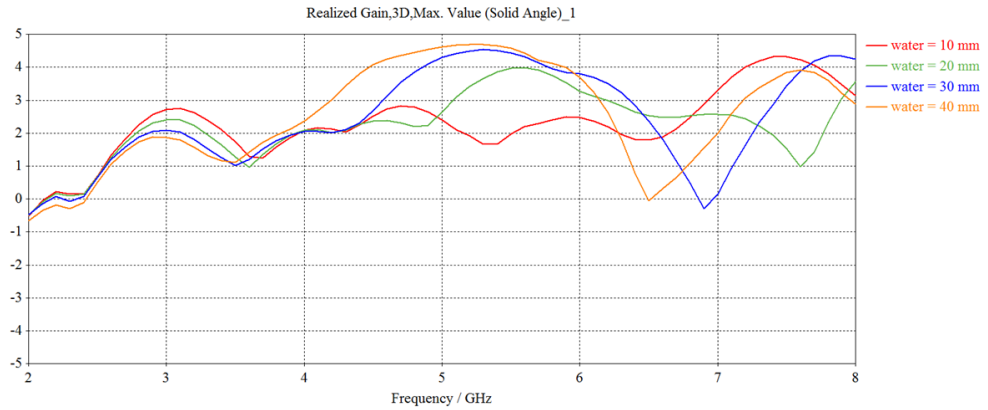

FIGURE 5.23: Simulated realised gain for different KCl solution heights in an ionised solution monopole.

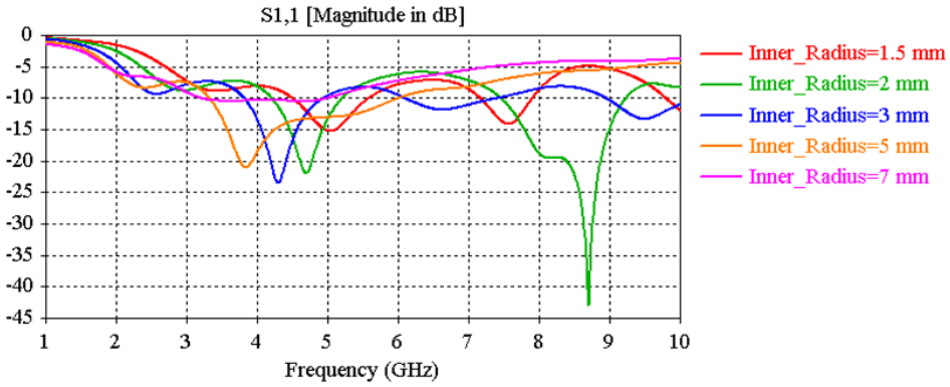

FIGURE 5.24: S_{11} parameter for different container inner radius in an ionised solution monopole.

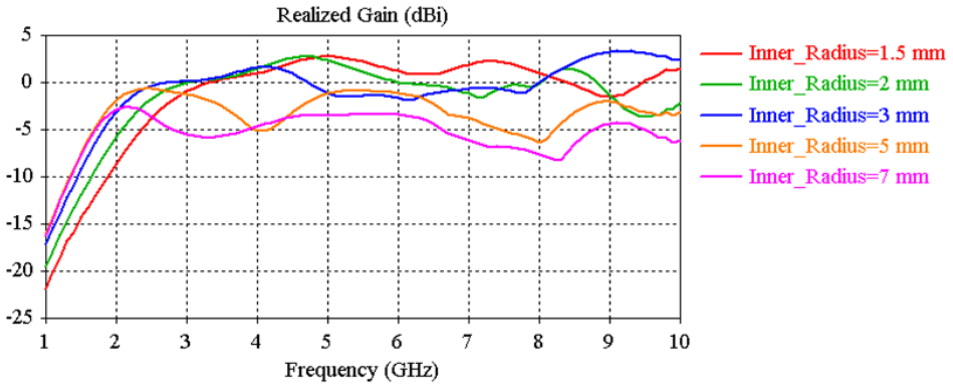

FIGURE 5.25: Simulated realised gain for different container inner radius in an ionised solution monopole.

water height of 40 mm. Figure 5.24 presents the simulated reflection coefficient for different container inner radius. From 1.5 mm up to 5 mm the monopole presents different operating bands. When the radius becomes too big, as in 7 mm, the ionised water becomes too lossy and the antenna efficiency drops. Moreover, when container radius is 2 mm there are two operating frequency, one at 4.6 GHz and another at 8.8 GHz, because this particular antenna is well matched at both frequencies. The ionised water monopole presents different resonances at multiples of the fundamental resonance, but the impedance may not be matched.

Figure 5.25 presents the realised gain for different container radius. Gain for 1.5 mm and 2 mm is 3 dBi and it diminishes to 2 dBi for a radius of 3 mm. As expected, the gain for container radius = 7 mm is very low. Although gain for radius 5 mm is below 0 dBi too. This can be understood by looking at the simulated efficiency in Figure 5.26. Efficiency for radius 5 mm and 7 mm is below 40 % at the matched band. While efficiency for radius = 3 mm is only 45 % at the operating frequency, which causes a 1 dB loss in gain compared to smaller radius. On the other hand, both 2 mm and 1.5 mm radius have an efficiency close to 75 %. In conclusion, antenna efficiency decreases as container radius increases, having the best results at radius = 1.5 mm.

Different resonances are analysed next for an ionised water monopole with a 1.5 mm radius. An antenna with zero imaginary part is said to be resonant, as the imaginary part of the impedance represents power that is stored in the near-field of the antenna. There are basically two types of resonances: parallel type or “antiresonance” and series type. The parallel type usually presents a high peak in the real part of Z and the imaginary part usually goes from inductive to capacitive. When the imaginary part is positive it is called inductive and when it has negative values it is called capacitive. In

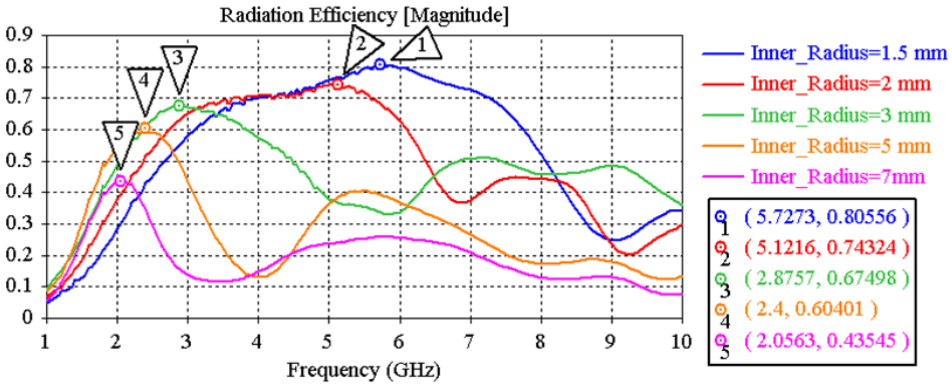

FIGURE 5.26: Simulated efficiency for different container radius in an ionised solution monopole.

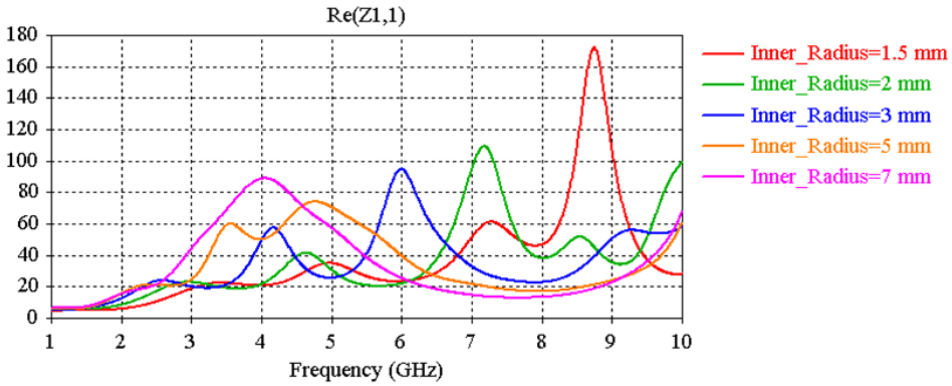

(A) Real part

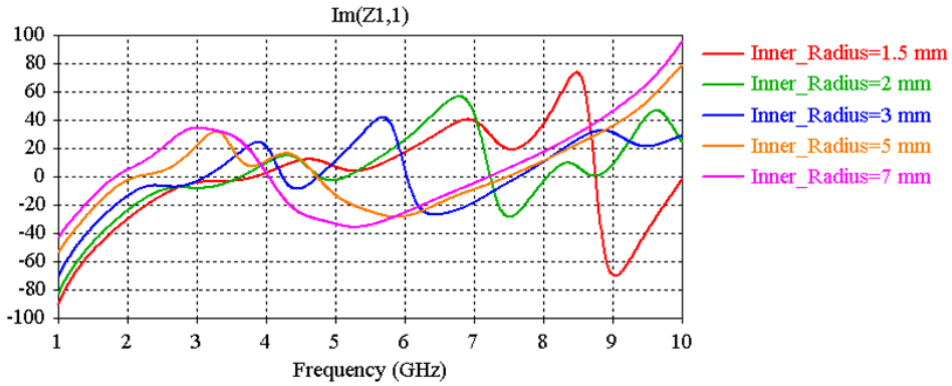

(B) Imaginary part

FIGURE 5.27: Real and imaginary part of Z_{11} for different container radius in an ionised solution monopole.

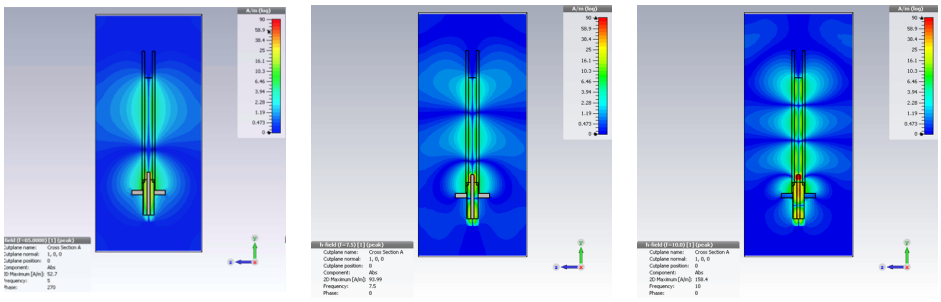

(A) First resonance (B) Second resonance (C) Third resonance

FIGURE 5.28: Surface current distribution for three resonances of an ionised solution monopole.

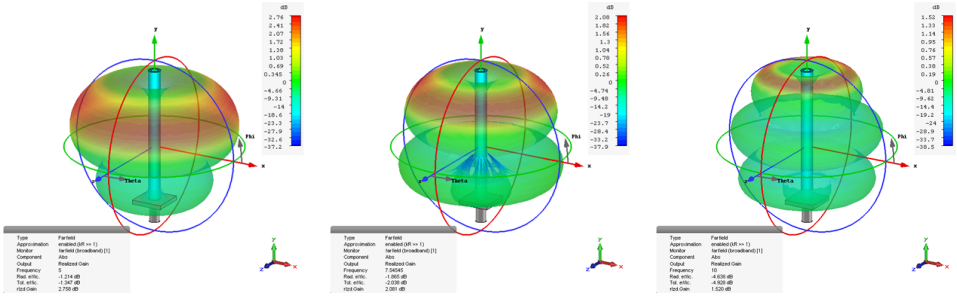

(A) First resonance (B) Second resonance (C) Third resonance

FIGURE 5.29: Radiation pattern for three resonances of an ionised solution monopole.

the series type the impedance is varying slowly in frequency. The imaginary part goes from capacitive to inductive and it is the most desirable for practical implementation. As shown in Figure 5.27 the 1.5 mm radius monopole has 3 resonances at around 5 GHz, 7.5 GHz and 10 GHz. Of these resonances only the 10 GHz is a series resonance.

Figure 5.28 presents the surface current distributions for 5 GHz, 7.5 GHz and 10 GHz. The resonance at 5 GHz occurs when the monopole length is equal to three quarters of a wavelength ($\frac{3}{4} \cdot \lambda$). The resonance at 7.5 GHz occurs when the monopole length is $\frac{5}{4} \cdot \lambda$. And the resonance at 10 GHz occurs when the length is $\frac{7}{4} \cdot \lambda$. More resonances occur in multiples of $\left(n + \frac{1}{4}\right) \cdot \lambda$, where n is an integer.

Figure 5.29 shows the radiation pattern for the first, second and third resonances of the ionised water monopole. As the resonant frequency increases, electric and magnetic fields are added in phase farther from the ground plane. Also, at 10 GHz some of the current is resonating at the pin of the RF connector as its length is half-wavelength at 10 GHz, which may be the cause for the diminishing gain.

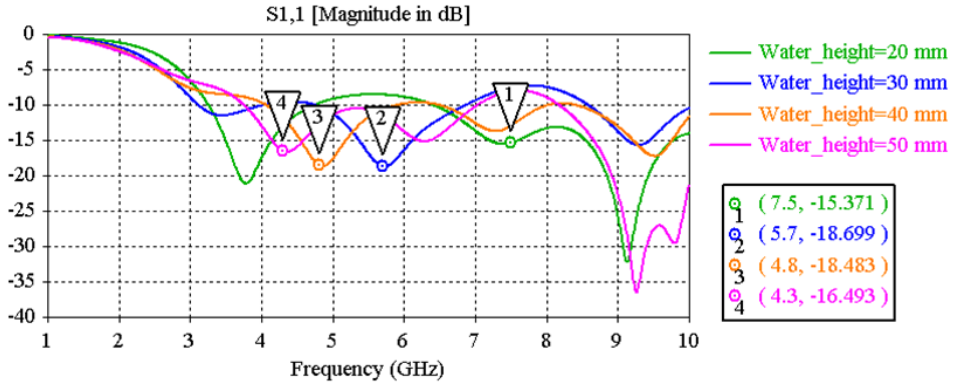

FIGURE 5.30: Simulated S_{11} for different water heights in the simulated ionised solution monopole.

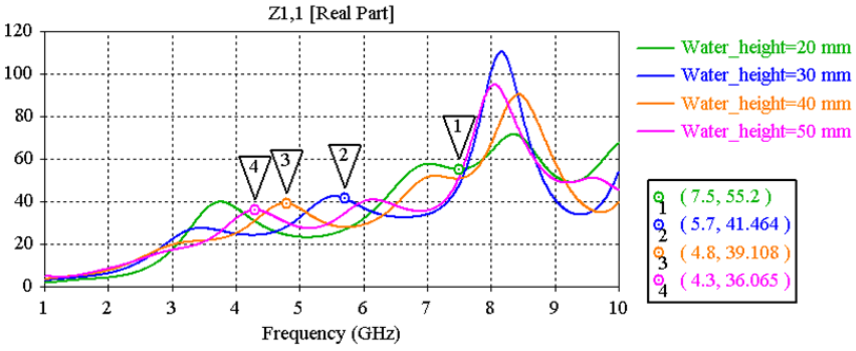

(A) Real part

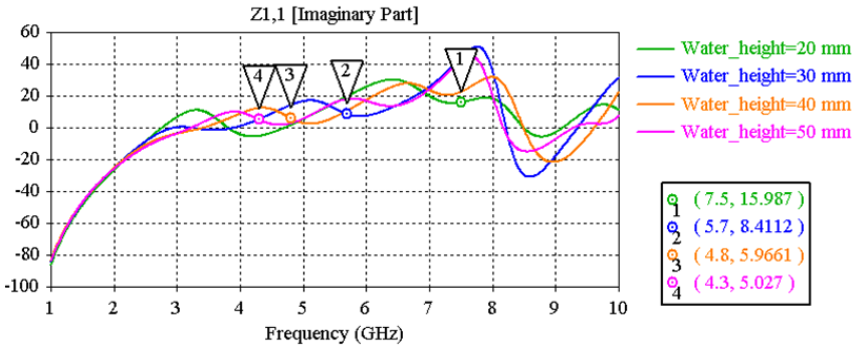

(B) Imaginary part

FIGURE 5.31: Real and imaginary part of Z_{11} for different container inner radius in the simulated ionised solution monopole.

From this study, a 2 mm radius monopole is selected for a prototype with a tube 60 mm long as shown in Figure 5.32, because it is more feasible to fabricate than the 1.5 mm radius. The simulated S_{11} results for this design are shown in Figure 5.30. Operating frequency for each water height goes from 7.5 GHz down to 4.3 GHz when the water height increases, as expected. For a water height of 20 mm the monopole presents two operating frequency: 3.8 GHz and 7.5 GHz, for the second and third resonance. The real part and imaginary part of Z_{11} for each water height are shown in Figure 5.31a and Figure 5.31b respectively. When the water height is 20 mm, there is another resonance at 3.8 GHz. At this frequency the height of the water is $\frac{\lambda}{4}$. Antenna impedance is matched at 50 Ω at this frequency and that is the reason why there is a null in the simulated S_{11}.

FIGURE 5.32: Fabricated KCl solution monopole measurements.

The measured reflection coefficient is presented in Figure 5.33. A 2 mol KCl solution was used. Solid lines are the measured S_{11} and dotted lines represent the simulated S_{11}. A 10 mm water height could not be measured because of the surface tension of the ionised solution. The ionised solution was manually injected using a syringe from the top of the monopole. It was a difficult procedure as the air had to come out to allow the liquid to fill all the tube. The measurements and simulations roughly agree. Nevertheless, the operating band changes from 7.0 GHz to 5.7 GHz and down to 5.0 GHz for 20 mm, 30 mm and 40 mm, respectively. For 50 mm the band at 6.3 GHz is matched instead of

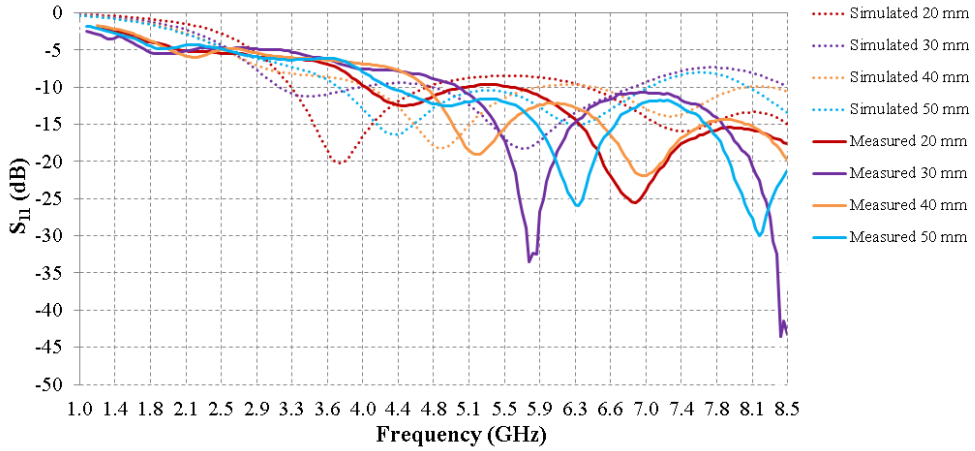

FIGURE 5.33: Measured S_{11} for different water heights in the KCl solution monopole.

the band at 4.4 GHz. 6.3 GHz is the second resonance for 50 mm. Further experimental verification is required to achieve a better matching.

This experiment demonstrates that an ionised water monopole can be used as a reconfigurable antenna enabling continuous frequency tuning. The switching mechanism uses a pump or a pushing system that controls the height of liquid inside the container. This technique eliminates the coupling of bias lines and control systems that deteriorate the antenna performance, providing higher flexibility and dynamic adjustment compared to solid metal designs.

5.3 Design C: Liquid-controlled reconfigurable Vivaldi antenna

The previous section proves an ionised solution can be used instead of copper to radiate as an antenna with efficiency up to 75 %. This section investigates the implementation of a liquid switch to replace the conventional RF switches in design B proposed in Chapter 4.

5.3.1 Antenna geometry

A liquid-controlled or hybrid reconfigurable Vivaldi antenna is proposed here (design C). The aim is to replace the RF switch at the slot in design B for an encased conductive

ionised solution. When there is no liquid inside the case, the antenna operates at the low band. However when liquid is introduced into the case, it creates a short circuit as an ON switch. Thus, the reconfigurable Vivaldi antenna operates at a higher band. By adjusting the position of the case the higher band can be tuned.

Figure 5.34a and Figure 5.34b present the bottom and top layer, respectively. The top layer consists of the feedline ended with a stub and the bottom layer includes the exponential flare, slot and a 3D-printed case to hold the fluid. Dimensions of the design antenna are specified in Table 5.2.

Figure 5.35 is a zoom at the slot where the encased fluid is located. The case is transparent so that the blue liquid inside is visible. A summary of the dimensions of the case is presented in Table 5.3 (see Figure 5.36 and Figure 5.37). A circular hole fitting a syringe is designed on top to inject the fluid using a syringe because this is an initial design to prove the concept. In an electronically controlled antenna, a small hole can be designed at the side of the case to connect a pump to automatically control the fluid.

Design parameters	*Dimensions (mm)*
$\mathbf{L}_{antenna}$	250.0
$\mathbf{W}_{antenna}$	150.0
$\mathbf{L}_{slot}$	60.0
$\mathbf{W}_{slot}$	1.22
$\mathbf{Pos}_{fluid}$	40.0
$\mathbf{L}_{stub}$	7.98
$\mathbf{W}_{stub}$	1.5
$\mathbf{Pos}_{stub}$	15.8

TABLE 5.2: Value for the design parameters for design C.

Design parameters	*Dimensions (mm)*
$\mathbf{L}_{case}$	10.0
$\mathbf{W}_{case}$	30.0
$\mathbf{H}_{case}$	8.0
$\mathbf{W}_{pipe}$	6.2
$\mathbf{H}_{pipe}$	4.0
$\mathbf{W}_{pipe_{wall}}$	1.0
$\mathbf{L}_{cavity}$	5.0
$\mathbf{W}_{cavity}$	10.0
$\mathbf{H}_{cavity}$	4.0

TABLE 5.3: Design parameters for the case in design C.

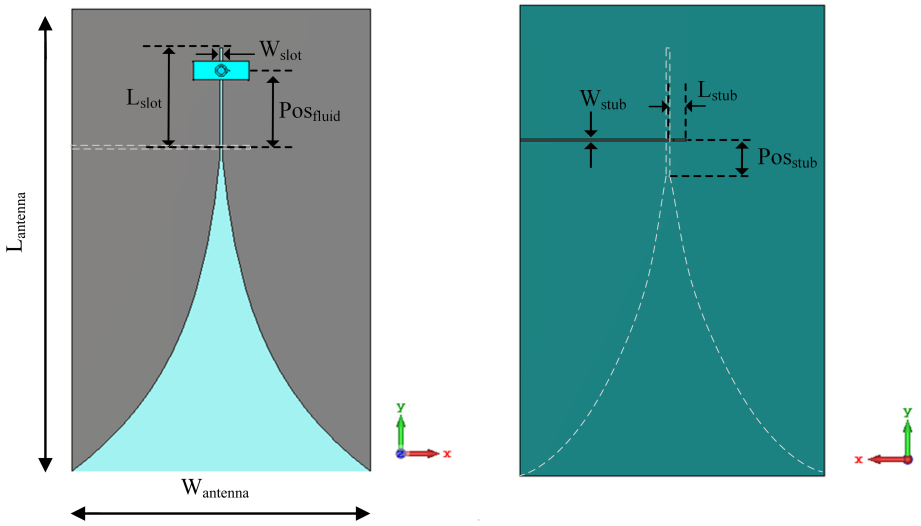

(A) Bottom layer (B) Top layer

FIGURE 5.34: Bottom and top layers of design C with conductive encased fluid as a switch.

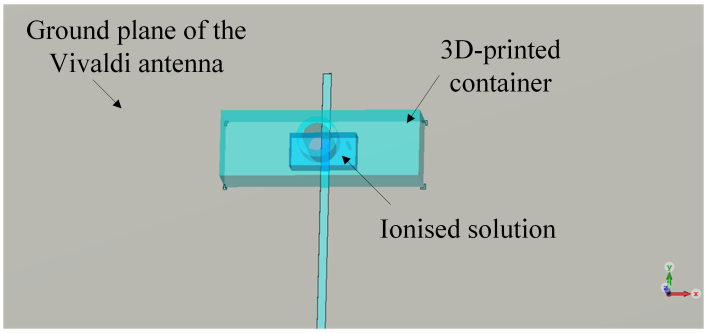

FIGURE 5.35: Conductive encased fluid in the slot of design C.

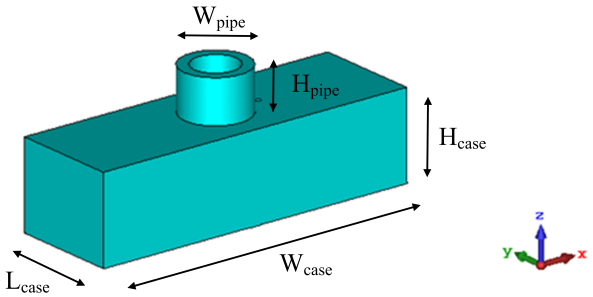

FIGURE 5.36: Case with dimensions.

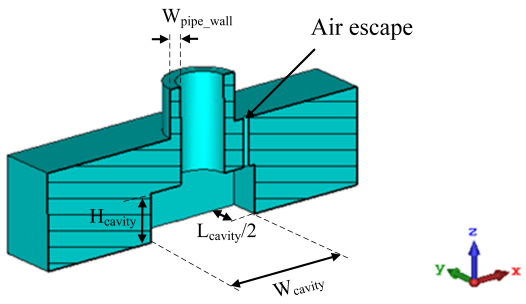

FIGURE 5.37: Cut view of case with dimensions.

5.3.2 Simulated results

The simulated results for design C are shown in Figure 5.38. There are clearly two operating bands: a low band from 2.55 GHz to 3.35 GHz and a high band from 3.4 GHz to 5.1 GHz. As the best band rejection occurs at the higher frequencies of the band, the two operating bands are defined at 3.2 GHz and 4.5 GHz.

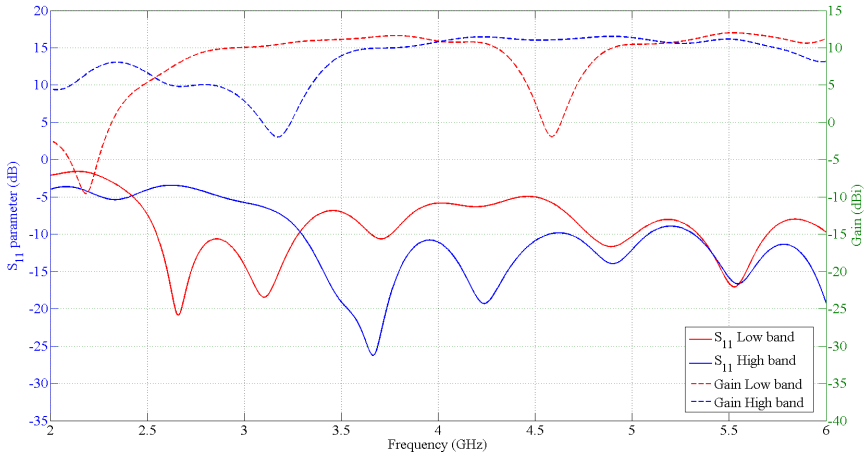

FIGURE 5.38: Simulated reflection coefficient and gain for design C.

Surface current distributions are presented next. Figure 5.39 displays design C in low-band mode, that is without any liquid in the slot case. Figure 5.40 shows design C in high-band mode, that is when liquid is pumped into the case to short-circuit the slot.

Figure 5.39a shows the surface current at 3.2 GHz, thus an in-band frequency. Figure 5.40b presents the in-band current at 4.5 GHz in high-band mode. In the in-band modes the current is coupled to the slot and it is propagated to the exponential flare of the hybrid Vivaldi antenna and then radiated to free-space. On the other hand, in the

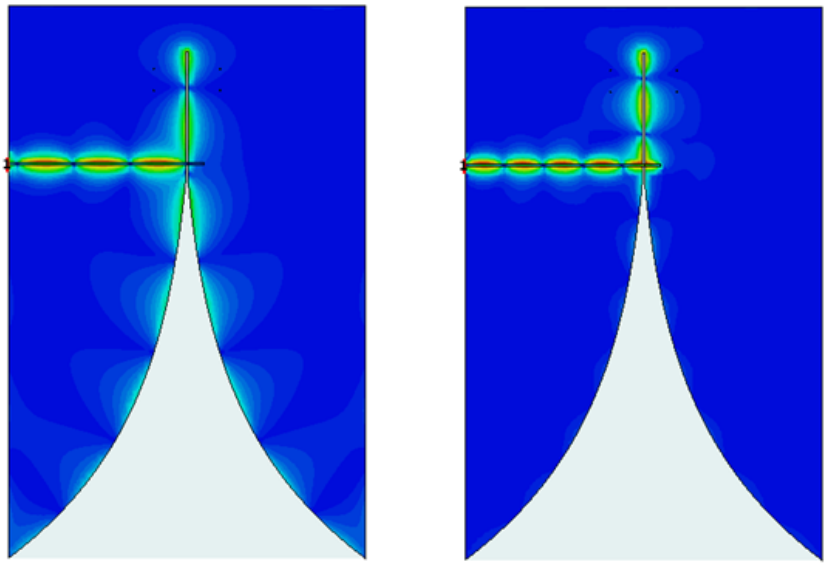

(A) In-band at 3.2 GHz (B) Out-of-band at 4.5 GHz

FIGURE 5.39: Surface current distribution in-band and out-of-band in low-band mode.

out-of-bands, as in Figure 5.39b and Figure 5.40a, the current is resonating in the slot as the stub-to-slot intersection is not matched for these bands.

This antenna presents good isolation between bands because of the small amount of current that is propagated to the exponential flare while operating in a rejected frequency. When there is no current propagated, the gain is at a minimum producing isolation of 14.5 dB based on the simulated results.

Figure 5.41 presents the simulated efficiency for low-band and high-band modes. In low-band mode at 3.2 GHz the efficiency is 93 %, while in high-band mode at 4.5 GHz the efficiency is 80 %. In low-band mode the Vivaldi antenna using electronic switches (design B) has a peak efficiency of 93 %, thus there is no loss in this mode. In high-band mode design B presents a peak efficiency of 83 % at 4.5 GHz. With a 3 % difference, the loss is minimal. Overall high-band mode presents lower efficiency which can be because of the use of a fluid as a switch that absorbs the EM waves instead of creating a short circuit at the slot.

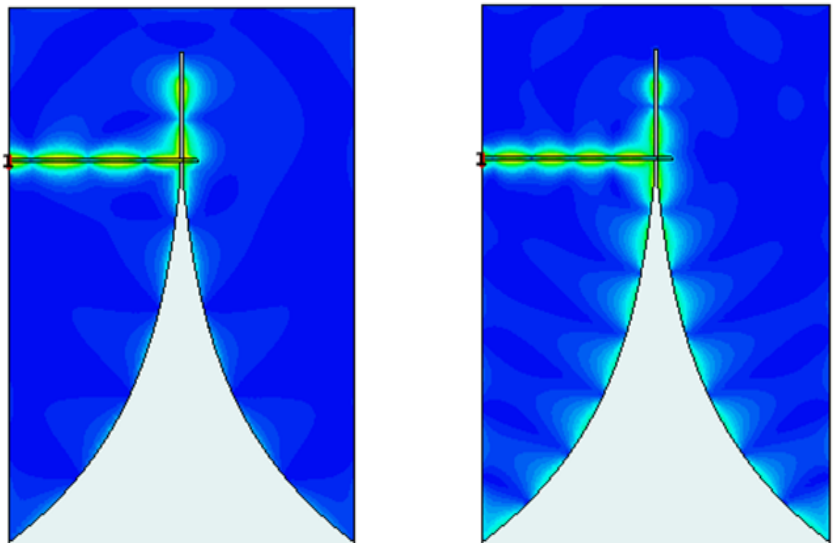

(A) Out-of-band at 3.2 GHz (B) In-band at 4.5 GHz

FIGURE 5.40: Surface current distribution in-band and out-of-band in high-band mode.

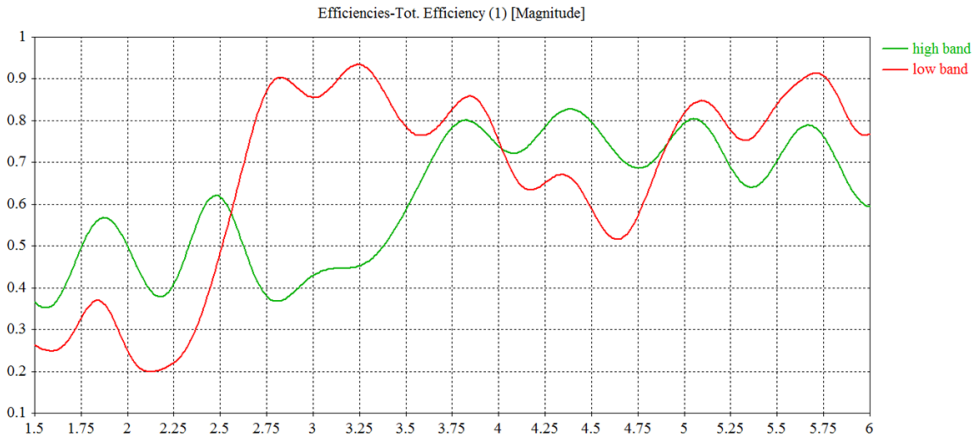

FIGURE 5.41: Simulated efficiency for design C.

5.3.3 Study of different ionised solutions and concentrations

Various concentrations were measured using the dielectric probe. With these measurements the dielectric properties of different concentrations were imported into CST. In this section the design C high-band mode simulation results using different ionised solutions are compared.

0.1 mol KCl, 1 mol NaCl, 2 mol KCl and 2 mol NaCl are selected as a sample of the ionised solutions. 0.1 mol is the minimum measured concentration and it presented the

lowest conductivity. 1 mol NaCl presents a relative permittivity centred between the 0.1 mol KCl and 2 mol KCl permittivities. 2 mol NaCl and 2 mol KCl presented the highest conductivity, lowest relative permittivity but also the highest loss tangent, as shown in Figures 5.8 – 5.10. This high loss tangent can cause losses in the design.

Figure 5.42 presents the simulated antenna total efficiency for 0.1 mol KCl, 1 mol NaCl, 2 mol KCl and 2 mol NaCl. The highest efficiency in the operating band is provided by 2 mol KCl solution with up to 86 % and the lowest efficiency by 0.1 mol KCl solution as expected which is a 5 % lower at 4.5 GHz.

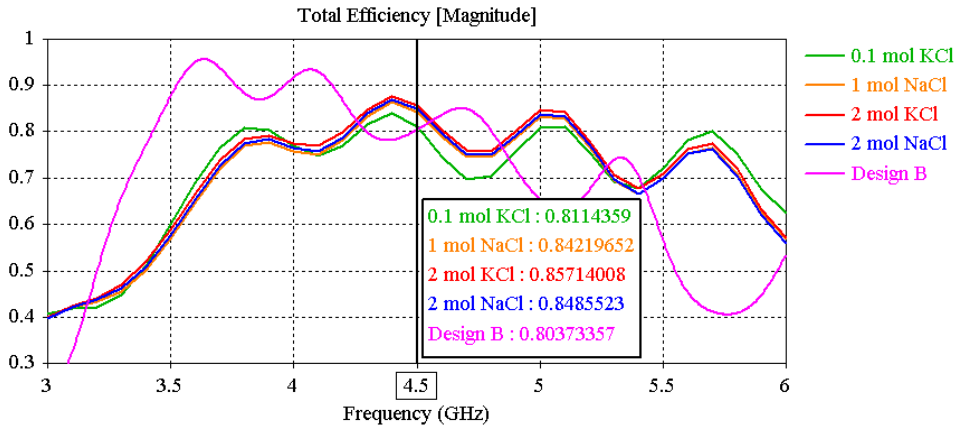

FIGURE 5.42: Simulated total efficiency for different concentrations of NaCl and KCl solutions and compared to the simulated efficiency of design B.

In terms of realised gain, the difference is about 3 % or 0.4 dB lower between 0.1 mol KCl and 2 mol KCl which in simulation. The variation is subtle with the other concentrations because of the small amount of ionised solution used in the design.

The same occurs when looking at the reflection coefficient. For 0.1 mol KCl and 2 mol KCl the variation is of up to 1 dB or 8 %. With a subtle variation for the other concentrations.

Although there is not a significant difference for various concentrations in the geometry of design C, 2 mol KCl solution is used for design C because it presents the highest gain and efficiency. The concentration in the ionised solution is not critical for the geometry proposed in this research project. Other geometries where the ionised solution is used as a radiator may present higher variations. For example in [115] a study is reported for a 2 GHz monopole showing a relation between efficiency and conductivity. The efficiency drops for conductivities between 10^{-3} S/m and 10^{-1} S/m down to 30 %, but rises in a linear trend from 10^{-1} S/m up to 10^{3} S/m. At this point, increasing conductivity does not increase efficiency as it has reached its maximum. Although this is very specific

for the reported monopole it can be used as guidance when using an ionised solution as radiator. In this research project a small amount of ionised solution is used which makes it feasible as the conductivity of the ionised solution does not have a big impact on the antenna efficiency.

5.3.4 Antenna verification

The same procedure explained in the previous chapter for antenna verification in the anechoic chamber is followed to verify design C. The prototype is fabricated in the departmental workshop using an etching technique on a Taconic RF-43 substrate. The initial Vivaldi design was reduced in size to fit an A4 so that it could be produced using the etching machine. The bottom layer and the top layer of the prototype are shown in Figure 5.43. The 3D-printed case for the liquid switch is attached at a point of the slot in the bottom layer.

(A) Bottom layer (B) Top layer

FIGURE 5.43: Prototype fabricated for design C.

Figure 5.44 presents a block diagram of the experiment setup to characterise the fluid-reconfigurable Vivaldi antenna prototype for design C. The fluid switch that is attached to the antenna is connected to a pipe that allows the 2 mol KCl solution to be pumped in and out to reconfigure the operating frequency of the antenna.

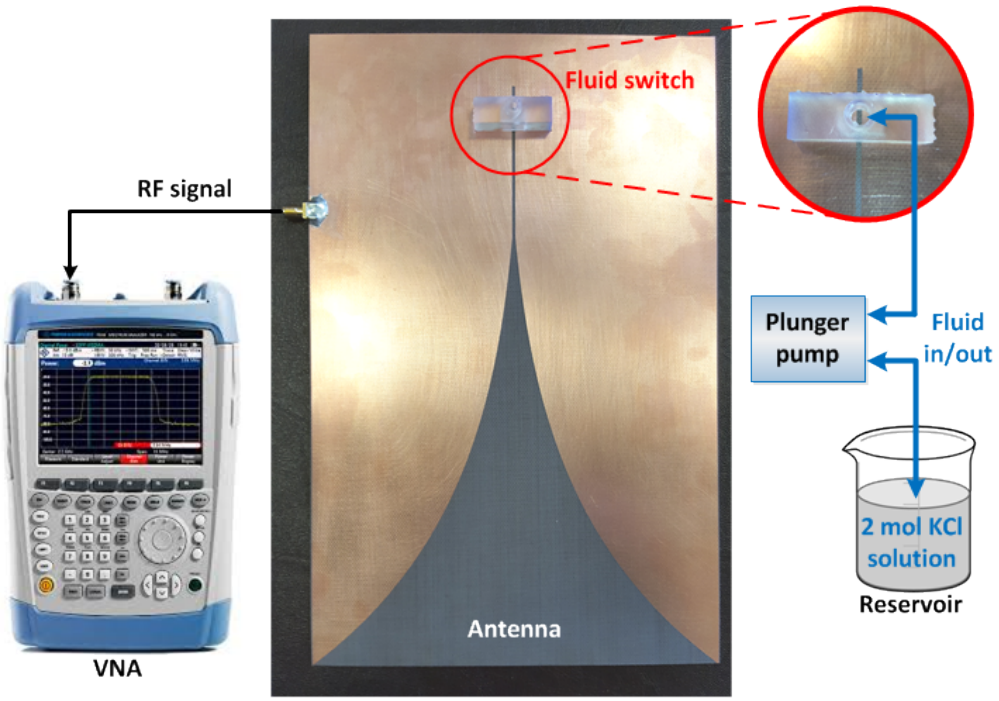

FIGURE 5.44: Experiment setup for Design C.

In the following sections the experiment results are discussed.

5.3.4.1 Test and simulation results comparison

Figure 5.45 shows a comparison between the simulated and measured reflection coefficient for design C. Two operating bands are presented in the test results. Figure 5.46 displays a comparison between the simulated and measured gain for design C. Gain is stable inside the bands and it drops rapidly on the edges of the band. The measured low band (in red) agrees more with the simulated result. In the high band (blue lines) there are some discrepancies for the higher frequencies which can be because of fabrication inaccuracies, the lossy properties of the KCl solution and the low order model used in CST to model the fluid. However the start of the operating band, i.e. below -10 dB, is maintained from 3.4 GHz. Rejected frequencies are in good agreement as well.

Next, the measured radiation pattern is compared to the simulated results. In low-band mode both E-plane and H-plane agree with the simulated results. With a 3 dB beamwidth of 38° in E-plane and 65° in H-plane. In high-band mode measured results have a slight clockwise rotation compared to the simulated results. This can be because of a misalignment in the anechoic chamber setup. 3 dB beamwidth for the high-band

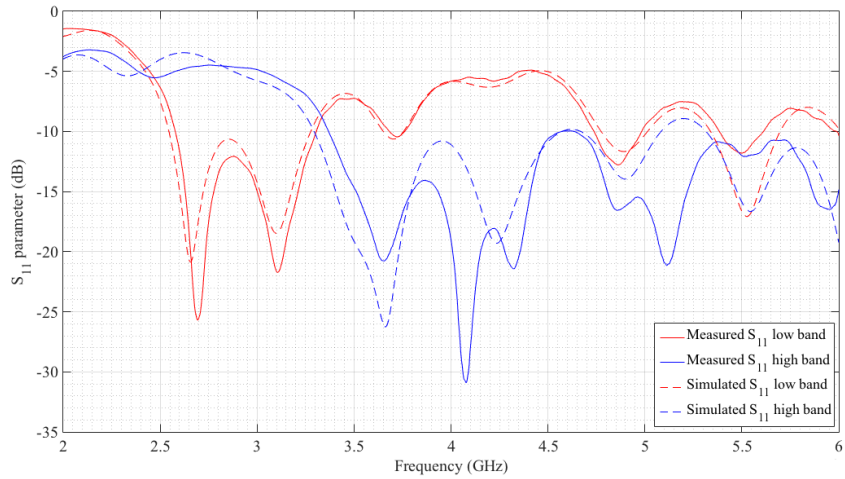

FIGURE 5.45: Simulated and measured reflection coefficient comparison for design C.

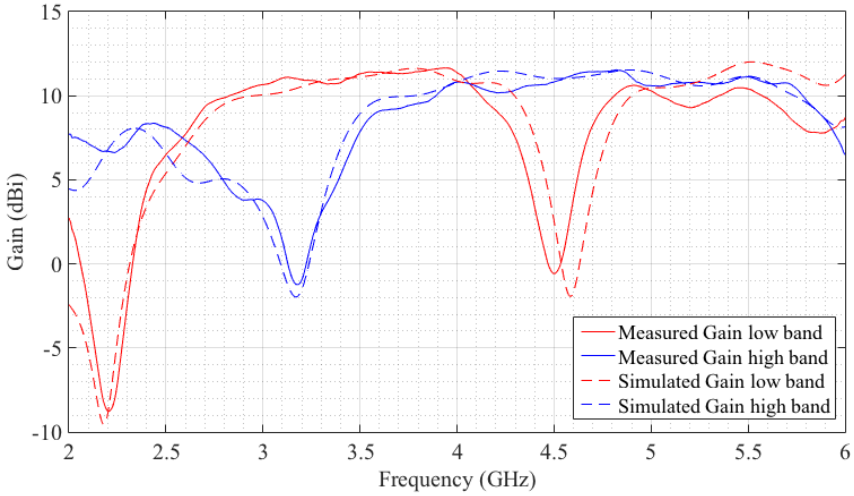

FIGURE 5.46: Simulated and measured gain comparison for design C.

mode in E-plane is 28° with a 2° difference compared to simulation. And 3 dB beamwidth for the high-band mode in H-plane is 49° with a 3° difference compared to simulation.

Several problems arose when fabricating the antenna prototype. The first one was a watertight container was necessary. Leaks were stopped using silicone for this prototype, but for further research a new design is required. The second problem was the KCl solution evaporation and crystallisation. One option is to completely remove the ionised solution from the switch when the antenna is not in use or to design an enclosed area to contain the ionised solution. In addition, the KCl solution dielectric properties

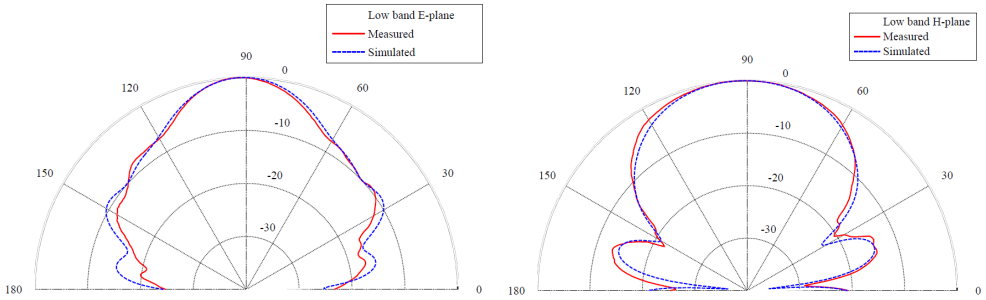

(A) E-plane (B) H-plane

FIGURE 5.47: Measured (red) and simulated (blue) radiation pattern in low-band mode at 3.2 GHz of design C.

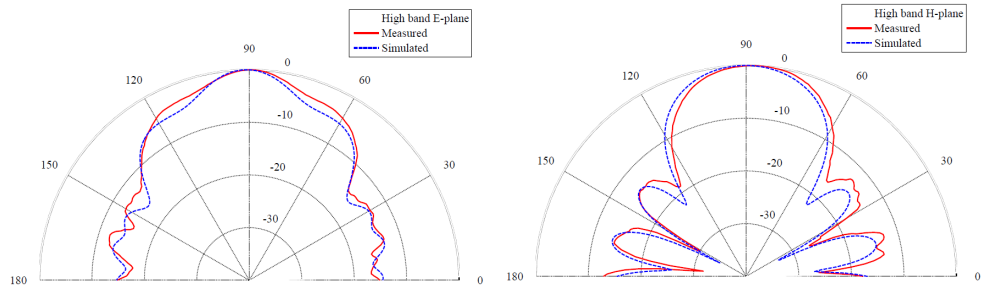

(A) E-plane (B) H-plane

FIGURE 5.48: Measured (red) and simulated (blue) radiation pattern in high-band mode at 4.5 GHz of design C.

change with temperature, which means its performance needs to be studied further in the future. To overcome the temperature problem an enclosed area for the liquid is necessary. Furthermore, the temperature difference can be compensated by a pump as long as the liquid solution remains in a liquid state.

5.3.4.2 Design B and design C measurements comparison

Figure 5.49 compares the measured reflection coefficient and Figure 5.50 compares the gain for design C using a liquid-switch and design B that uses an electronic RF switch to control the operating band. HB indicates high band and LB indicates low band. Looking at the reflection coefficient, there is a frequency shift. Design C is matched 400 MHz lower in frequency than design B. This is because of the effect of the case in the slot and the ionised solution not being as conductive as copper, making the liquid like an absorber and matching it in lower frequencies. However, the gain at 400 MHz is very low compared to the rest of the band. Therefore, this shift is not critical as design C still operates at the frequencies of interest: 3 GHz and 4.5 GHz. From 4.6 GHz and

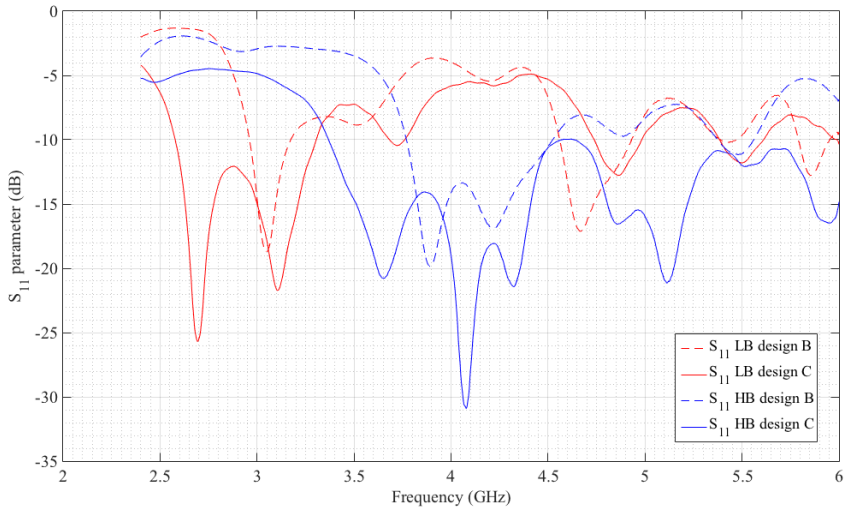

FIGURE 5.49: Measured reflection coefficient compared for design B and design C.

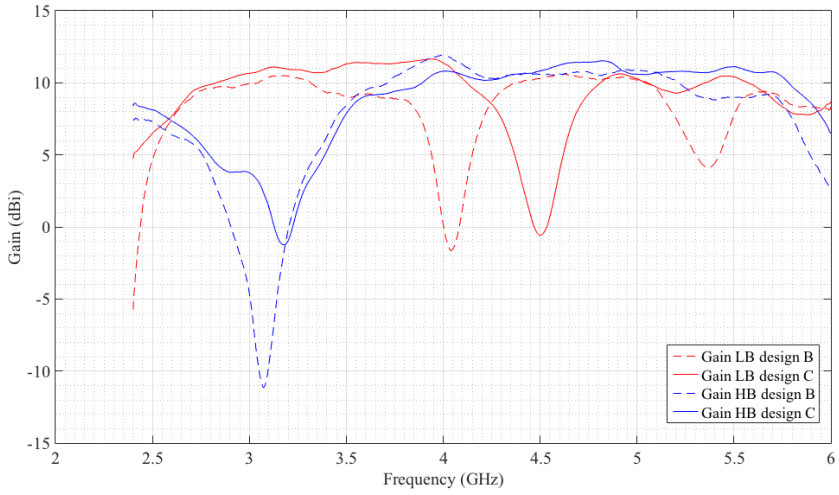

FIGURE 5.50: Measured gain comparing results for design B and design C.

up the high band of design C is again well matched at 5 GHz which design B is not. This can be because of the losses in the liquid material and a poor CST model of the liquid switch which carries the error at higher frequencies. For the gain the main difference is the shift for the rejected frequency in low-band mode. This is because of the liquid case affecting the slot length at these rejected frequencies.

In conclusion, design C using the liquid-switch achieves similar results to design B using an electronic switch. Despite being a slower technique it provides high flexibility to the design, it is cheaper and can easily be adapted to most design geometries using 3D-printing. Moreover, using a different case can provide dynamic continuous tuning to the design.

5.4 Conclusion

This chapter aimed to address the low performance problem of RF switches by using fluid components to tune a reconfigurable antenna. Fluid antennas are a good alternative for reconfigurable antenna designs as they provide the flexibility of adopting the mechanical properties of the encasing material making them flexible and durable, as well as the advantage of suppressing mutual coupling by draining the fluid and disabling the antenna. Ionised solutions such as seawater are inexpensive, easily accessible and eco-friendly, and are a good alternative for low-cost systems.

A new concept was proposed using a 3D-printed flexible resin: "antennas-on-demand". The concept was displayed in a planar antenna using multiple fluid monopoles, but it can be extrapolated to any desirable design. This design provides a high degree of freedom for the geometry of the antenna: it just needs to fit in a surface. It can be introduced on a screen or at the back of a tablet for example and it can be activated only when required.

Initially, the radiating part of the copper monopole was replaced by EGaIn and the results were compared to the copper monopole. EGaIn presents lower efficiency as expected, 86 % of the copper down to 70 % of the EGaIn. Still, good performance was accomplished by the fluid monopole in terms of matching, polarisation, radiation pattern and gain. Frequency reconfiguration on the EGaIn monopole antenna was achieved by changing the fluid height.

Then, to determine the best ionised solution for our purposes, an experiment was setup to measure the dielectric properties for different ionised solutions and concentrations. Various concentrations of NaCl and KCl were measured and 2 mol KCl was selected as

the experimental ionised solution for design C because it presented the best permittivity properties to operate as a liquid switch.

Following the EGaIn monopole design, a reconfigurable KCl solution monopole design was proposed. It consisted of a 3D-printed tube and a panel-mount SMA connector. As an efficiency of 75 % using the fluid was achieved in simulation, a prototype was fabricated. From the measured results it can be deduced that the ionised solution is more lossy compared to a copper monopole as expected, although it allows very easy continuous tuning reconfiguration. The operating band changes from 7.0 GHz, to 5.7 GHz and down to 5.0 GHz for 20 mm, 30 mm and 40 mm ionised solution heights respectively. Further study and experimental verification is required for a full operational fluid monopole. However, with these experimental results the concept of reconfigurable fluid monopole was demonstrated: the KCl monopole changed its operating band by varying the height of fluid solution in the tube. Therefore, a low-cost ionised solution can replace a solid metal but the losses introduced by the fluid need to be taken into account.

In the second part of this chapter, a liquid-controlled reconfigurable Vivaldi antenna was proposed as design C to take advantage of the fluid characteristics previously proved. By integrating fluid channels into the Vivaldi antenna the operating band of the Vivaldi antenna can be continuously tuned. A case with an ionised solution of KCl was introduced at the position of the switch instead of the HMC550AE switch. There was no need for bias lines or layout contacts that affect the antenna RF performance as explained in section 3.1.1.1. The case was designed to be 3D-printed using a Formlabs Form1+ printer. A 3D printer was essential for fast prototyping as well as providing the freedom to produce shapes that are not possible with other techniques.

The prototype antenna was measured following the same procedure explained in the previous chapter. The antenna prototype presents two bands: a low band at 3.2 GHz with 11 dBi of gain and a high band at 4.5 GHz with 10.8 dBi of gain. The measured radiation patterns were in good agreement with the simulated results with only a 2° deviation for the high-band mode. There was good isolation between bands as for the rejected frequencies no current was propagated to the exponential flare achieving a minimum isolation of 14.5 dB in both bands.

Continuous frequency tuning in the proposed design can be achieved by using a different container shape to pump liquid at different points of the slot.

In conclusion, fluid antennas provide higher flexibility in terms of reconfiguration for an antenna, as the conductive liquid can easily be removed, can adopt any shape and self-heal. They are durable, easy to integrate and high-power handling. These reasons make fluid parts or fluid antennas the perfect candidate for the next-generation reconfigurable antennas. Moreover, the hybrid reconfigurable Vivaldi antenna prototype presented in this chapter demonstrates it is possible to replace a conventional RF switch by a liquid-controlled switch achieving good performance. This liquid switch can be used in many other designs easily providing continuously frequency tuning. To fully automate the antenna, a micropump is necessary to pump the ionised solution in or out of the case. For example, a GN series 42.9 L/min is sufficient as the amount of liquid to move is very low.

Chapter 6

Conclusion and Future Work

This chapter concludes this research thesis. It is divided in eight sections. First, the requirements of this research project are discussed along with the necessary equipment. Following, design A and B are analysed along with their limitations and suggestions to deal with these limitations. A design C is then discussed. Later, the project goals are reviewed to evaluate if they are met. Then, the novel contributions to research are presented. Finally, the future work is described.

6.1 Requirements of the project

The aim of this research project was to develop new designs of reconfigurable antennas that can operate across a wide frequency range while maintaining radiation characteristics, such as radiation pattern and polarisation, and fulfilling the industrial requirements. As the main application was spectrum surveillance, the industrial sponsors required the reconfigurable design to include:

- frequency tuning
- low cost
- low power consumption
- portability
- high gain
- wideband operation

- stable radiation patterns
- good isolation between bands

High gain was required to recognise attenuated communications of interest, while on the other hand a stable radiation pattern across a wide frequency range was essential because the antenna will be pointing to a specific direction in spectrum surveillance. If an antenna changes the direction of the main lobe in its operating band, the antenna needs to be realigned depending on the operating frequency and this is not a desirable feature.

The good isolation between bands was taken to be a minimum of 14 dB as it represents a power ratio of 25.

This thesis has covered the antenna design in terms of operation frequency, polarisation, impedance, gain and far-field radiation pattern at the frequencies of interest. Operating frequencies are found in the microwave spectrum between 1 GHz and 6 GHz. The antennas were designed so that they could be fabricated in the departmental workshop. In the workshop an etching machine which can fit designs of a maximum size of an A4 is used, although this technique is not limited by this size when a larger etching tank is utilised. Therefore, a planar design on a high performance substrate satisfied the requirement. The substrate needed to be low loss as the outcome requires high gain, so FR-4 substrate was not desirable. Low-cost materials were required. A wideband antenna was chosen as the basis of the reconfigurable design to provide consistent characteristics in all bands. The research covered the physical design of new reconfigurable antennas and established the switching mechanism, although the automated control of the switching mechanisms was outside the scope of this project.

To fulfil the stated aim, a Computational Electromagnetic tool was deemed necessary to perform the analysis of proposed designs. CST Microwave Studio was chosen for several reasons. First, a license for this software tool is already available in the Department of Electronic and Electrical Engineering at UCL. Second, this package encompasses a wide range of solvers that can be useful for simulating a wide range of reconfigurable antenna designs. Third, a lot of complementary tools work together with CST, such as Antenna Magus, which can aid and expedite the process of designing new antennas. And finally, CST was one of the most accurate full-3D EM simulator tool for time analysis antenna design and simulation currently available for designing antennas.

The designs proposed in this research project are not a one-component design, they are a combination of optimised parts that fit together to operate efficiently fulfilling

the goals of the project. The input port, the feed line, the stub-to-slot intersection, the resonating slot, the exponential flare and the tuning system are designed using different specialised tools of CST. Furthermore, the CST co-simulation enables the input of measured material characteristics and switch performances in the simulations.

Initially, in the design process each antenna system design requires assumptions about other system components because the system is not designed yet. During the design phase an understanding of the interaction between components, parts or subsystems is developed on how each component, material or part of the antenna design impacts the other parts. Likewise the material choices that are required for manufacture might change the requirements for the antenna itself. An understanding of these impacts takes time to evolve. Although once understood, each part or component design needs to be refined so that an understanding of these interactions is leveraged. Having multidisciplinary tools to analyse and evaluate each part of the system that are well integrated is crucial so that the process can be iterated efficiently.

Additionally, laboratory equipment was necessary for the test and antenna measurements, such as VNA, 3D printer, 3D-printer materials, reference antennas and the setup in the anechoic chamber to measure the gain and far-field radiation patterns.

6.2 Switched reconfigurable antennas

When analysing the state-of-the-art reconfigurable antennas it was observed that most of designs could only operate in a narrow frequency range. Thus, the radiation characteristics of the antenna were not preserved across a wide spectrum because of the different modes of resonance. The proposed reconfigurable designs in this thesis are based on a Vivaldi antenna because of its stability in the radiation characteristics across the operating frequency band.

Some designs for Vivaldi antennas had been proposed in the past, but most of them introduced some resonating element to achieve high isolation that compromised the gain severely. To avoid this gain loss, a Vivaldi antenna with a feed line that was matched only at the frequencies of interest was proposed. By controlling the feed line some frequencies could be rejected and a preferred band could be selected. RF switches were introduced in the feed line to tune the operating frequency of the antenna between frequency bands. These switches adjusted the length of the current path for the different bands. The operating bands could be easily changed by selecting the locations of the switches.

Several designs with two, three and four bands were presented, that covered the spectrum between 1.5 GHz and 6 GHz. All the proposed designs accomplished in-band stable high gain and several rejected frequencies which could be adjusted to block particular bands.

This low-cost method provided stable high gain and a rejected frequency just at the edge of the band with up to 36 dB rejection. A good isolation between bands combined with wide instant bandwidth can be very useful for spectrum surveillance.

After obtaining satisfactory simulation results, a prototype of design A was fabricated using RF-MEMS switches as switching mechanism. As the selected RF-MEMS switches proved to be difficult to integrate in the design, to solder and costly to operate, a design B was proposed using other RF switches: Hittite HMC550AE GaAs MMIC SPST switches. This prototype presented high gain and isolation, but RF switches are not easy to integrate into the antenna structure, they introduce bias lines, insertion losses and poor isolation in the design which deteriorates the overall gain.

The RF switches allow only a frequency switched tuning method, they add an extra cost to the system and the required bias lines alter the antenna RF performance. Therefore, alternative designs were considered and a novel liquid-switch was proposed next to prevent bias lines of an electronic switch to affect the design and allow continuous tuning.

Furthermore, a reproducible method was presented to calculate the antenna dimensions and switch positions. The method also calculates rejected frequencies of each band with a minimum accuracy of 96.6 % compared to simulation.

6.3 Hybrid reconfigurable antenna

Fluid antennas are a good alternative for reconfigurable antennas because, as fluids, they can be deformed without losing electric contact. Depending on the casing used, these antennas resist strain, deformation and can even self-heal in response to a sharp cut. Tuning a fluid reconfigurable antenna can be done by just pumping more fluid into the microchannels so that the area they cover is greater. They are easily conformed into the desired shape and even form a contact at room temperature without the need of soldering. On the other hand, fluids present lower conductivity compared to copper and there is a chance of leakage if the case is not properly sealed.

A summary of advantages and disadvantage of the fluid antennas is presented in Table 6.1.

Advantages	**Disadvantages**
- Can be reversibly deformed - Casing defines its mechanical properties - Mechanically tunable and sensitive to strain - Durable - Easily conformed into the desired shape - Can form a contact at room temperature without the need of soldering - Can self-heal in response to sharp cuts or cracks - Can have small RCS by draining the liquid when not in use - Fabrication is simple and fast by using 3D-printing techniques	- Lower conductivity than copper - Chance of leakage - Evaporation - Crystalisation - Operation change with temperature - Need of coupling feed to completely seal the case

TABLE 6.1: Advantages and disadvantages of fluid antennas.

In fluid antennas research, the most popular metal fluids are EGaIn and Galinstan, which provide high electric conductivity. Alternatives for low cost system are ionised solutions such as NaCl or KCl between others. Still, their conductivity is about three orders of magnitude below the copper conductivity. For high-efficiency designs it is preferable to use EGaIn to obtain the highest conductivity possible to minimise mismatches. A reconfigurable monopole was simulated using EGaIn accomplishing good performance closely related to a solid metal monopole. Furthermore, as fluid materials provide high permittivity, the antenna size can be reduced proportionally to its relative permittivity, which makes them excellent for biomedical and security applications.

As EGaIn is an expensive material, other water solutions were considered. KCl is chosen because it is non-toxic, non-corrosive, soluble in water and its solutions in water can be more conductive compared to pure water. KCl is an element widely found in seawater and, therefore, this project demonstrates seawater can also be used as a radiator too.

A KCl solution monopole is simulated in CST and good performance is obtained with efficiency of up to 75 %. The liquid state of the radiating part allows easy frequency reconfiguration by adjusting the amount of liquid in a container. A 3D printer is used for rapid prototyping of the liquid antenna model. Because it allows complicated and bespoke shapes for watertight container designs.

A new concept was introduced: “antennas on demand”. A design to display this concept was proposed using multiple fluid monopoles in a PDMS encasing reconfigurable antenna. But this concept can be extrapolated to any desirable design. It was based on a 3D-printed elastomer that included certain predefined microchannels for a conductive

fluid. It required three input ports to activate each of the monopoles. The conductive fluid could be pumped or drained as desired, thus achieving frequency reconfiguration for each monopole. Moreover, considering the position of each monopole is in a different direction, the antenna provides polarisation diversity: vertical, horizontal and diagonal or a combination of them. Additionally, when one or more of the antennas were not in use, the fluid could be drained to suppress coupling, making the design ideal for applications where stealth is crucial. This idea is based on a new technology for touchable keyboards that can trigger buttons that rise out of the surface using liquid. When the buttons are not in use the buttons are pushed back and surface becomes flat. One difficulty for this design will be the implementation of the excitation ports, where high-efficiency coupling ports are required. This technology can become essential for modern demanding applications in terms of multiple operating frequency, high isolation and low cost antenna requirements.

After proving a liquid solution can be used in antennas to define the effective length of a monopole and thus reconfigure its operating frequency, a liquid-switch was proposed as a switching mechanism for a hybrid reconfigurable Vivaldi antenna (design C). A 2 mol KCl solution was introduced as a low-cost liquid to replace an electronic switch. The liquid switch can dynamically adjust the operating frequency and it provides a low-cost highly flexible alternative to the conventional RF switch.

Design C presented higher losses compared to design B as expected, although the high gain and direction of the main lobe was preserved. Isolation between bands was better for design B as the conductivity of copper is higher than the ionised solution conductivity. Although the difference was 9 dB in high-band mode and 0.5 dB in low-band mode, the requirements of the project were met. Design C extended the operating band of the antenna as the liquid-switch operates like an absorber of EM waves by slowly absorbing the waves instead of creating a short circuit. An extended band can be useful in applications where a dynamic wide spectrum needs to be monitored.

To conclude, the liquid-switch hybrid Vivaldi antenna met the requirements of this research project while providing the possibility of continuous frequency tuning if needed. A pumping system such as a diaphragm can provide advantages to the design by being able to dynamically control the antenna while not degrading the antenna performance. The pumping system can be fabricated using a 3D-printing technique. This liquid switch can be used in many other designs easily providing continuous frequency tuning which conventional RF switches cannot.

6.4 Fulfilling the project aim

The aim of this research project was to develop new designs of reconfigurable antennas that are able to work across a wide frequency range while maintaining radiation characteristics, such as radiation pattern and polarisation, and fulfilling the industrial requirements.

Three designs have been proposed: a band-switching Vivaldi antenna using RF-MEMS switches (design A), a band-switching Vivaldi antenna using a GaAs MMIC switch (design B) and a hybrid Vivaldi antenna using a novel liquid-switch (design C). The first two used RF switches to tune the frequency band while the third design used a novel liquid-switch designed in this project achieving less coupling from the bias lines. Design B and design C fulfil the industrial requirements of:

- **Frequency tuning maintaining radiation characteristics** as they can tune their operating frequency maintaining the direction of main radiation and polarisation of the antenna.
- **Low cost** as these planar antennas are designed on a substrate and can be fabricated using etching techniques and a 3D printer for the liquid switch case in design C. The ionised solution utilised is KCl solution, although it can be replaced by seawater achieving similar results.
- **Portability** as the antennas measure 250 mm x 150 mm.
- **High-gain** as both antennas present a minimum of 11 dBi in low-band mode and a minimum of 10.8 dBi in high-band mode.
- **Good isolation between bands** as the minimum isolation achieved by design C is 14.5 dB and the minimum isolation achieved by design B is 25.7 dB. An isolation of 14 dB means there is a ratio of 25 between the gain at the operating band and the gain at the rejected band.

Thus, the aim of this project has been fulfilled by the design of two novel reconfigurable antennas based on a Vivaldi antenna. The first approach allows an RF switch to tune the operating frequency while maintaining the radiation characteristics, while the second approach introduces a novel tuning mechanism which can be applied to other antennas as well. This was accomplished by a study of a low-cost KCl solution to replace the existing expensive liquid metals like EGaIn or Galinstan currently employed in fluid antennas.

6.5 Novel contributions to research

The main novel contributions to research of this project are as follows:

1. Introduced a novel technique to tune the operating frequency of a Vivaldi antenna that preserves high gain, efficiency and the radiation pattern.
2. Provided strong empirical evidence that a KCl solution can be utilised as radiating part of a highly flexible reconfigurable antenna.
3. Tested a novel liquid switch which can be utilised for other antenna designs to tune various antenna characteristics.
4. Introduced a new concept of antennas-on-demand which can be advantageous to security applications, meaning antennas can be made available or non-radiating to eliminate detection and interferences when necessary.

6.6 Future work

A number of areas can be explored in order to continue in line with this research project.

- The "antennas-on-demand" novel concept was proposed in this thesis. The concept is displayed in a planar antenna using multiple fluid monopoles, but it can be extrapolated to any desirable design. This design includes three monopoles in different directions so as to provide polarisation diversity. As explained in chapter 5, a coupled feed is needed as an SMA connector creates a fissure in a sealed encasing material for a radiating fluid causing a possible leakage. Coupled feeds will need to be investigated to achieve efficient power coupling. Flexible resin can be used to accommodate different shapes for the fluid, but the actual design needs to be investigated and then tested. Additionally, the best approach to pump in and out water needs to be studied, either by pumping in water that pushes air out and then pumping air in to push water out or by creating a vacuum and pump water in and out. Moreover, for future designs a study of micropumps available in the market is required to compare cost, chemical resistance, flow rates and size.
- Although some KCl solutions and NaCl solutions have already been investigated in this research project, further research including other solutions is required in this topic. A complete study can determine what solution provides the highest

conductivity. Additionally, a test comparison with seawater from different places can establish a model for the utilisation of seawater in fluid antennas.

- The evaporation and crystallisation problems need to be addressed either by proposing other enclosing cases or by introducing another element into the solution to mitigate these problems.

- The hybrid Vivaldi antenna that currently operates in two bands should be expanded to more bands. A hybrid Vivaldi antenna with multiple bands could cover all bands in the wide operating band of the Vivaldi antenna design. Multiple liquid-switches can be introduced at different positions of the slot. Later, a continuous frequency tuning can be achieved by introducing the liquid in the slot at any requested point. A liquid switch for the stub may be necessary to match all the operating bands.

- The liquid container needs further research to ensure it is leakproof as for this project silicone was used to block any leak. A complete study is required to determine the best mechanical design.

- Further research in the KCl solution monopole is required to study how the impedance is altered with the type of liquid solution introduced and the amount of liquid in the monopole and leverage this understanding.

- The dielectric properties of a KCl solution change with temperature, which means the performance of the liquid switch may be degraded depending on the environmental conditions. Although temperature change can be compensated using a pump, a full test and analysis is required in this topic.

- Finally, in-depth study of the best shape for the liquid switch is required. By analysing the best approach and dimensions of the liquid switch using CST Microwave Studio a full understanding can be leveraged to produce the most efficient case. Furthermore, different pumping techniques should be analysed such as a diaphragm to determine the fastest and most efficient for the design.

Bibliography

[1] Jeanette Wannstrom. LTE-Advanced, May 2012. URL `http://www.3gpp.org/LTE-Advanced`.

[2] C.G. Christodoulou, Y. Tawk, S.A. Lane, and S.R. Erwin. Reconfigurable antennas for wireless and space applications. *Proceedings of the IEEE*, 100(7): 2250–2261, July 2012. ISSN 0018-9219. doi: 10.1109/JPROC.2012.2188249.

[3] D. Peroulis, K. Sarabandi, and L. P B Katehi. Design of reconfigurable slot antennas. *IEEE Transactions on Antennas and Propagation*, 53(2):645–654, 2005. ISSN 0018-926X. doi: 10.1109/TAP.2004.841339.

[4] Droneshield. Dronegun, a highly effective drone countermeasure, Nov 2016. URL `https://www.droneshield.com/dronegun`.

[5] Yong Zeng, Rui Zhang, and Teng Joon Lim. Wireless communications with unmanned aerial vehicles: opportunities and challenges. *IEEE Communications Magazine*, 54(5):36–42, 2016.

[6] G. Crespo, G. Glez de Rivera, J. Garrido, and R. Ponticelli. Setup of a communication and control systems of a quadrotor type unmanned aerial vehicle. In *Design of Circuits and Integrated Systems*, pages 1–6, Nov 2014. doi: 10.1109/DCIS.2014.7035590.

[7] Andrew L. Drozd. Spectrum-secure communications for autonomous UAS/UAV platforms, Nov 2016. URL `http://www.afcea.org/events/documents/MILCOM2015PPTDrozd-ANDROIII.pdf/`.

[8] M.A. Bedford. Unmanned aircraft system (UAS) service demand 2015-2035.

[9] L.C. Cadwallader N.B. Morley, J. Burris and M.D. Nornberg. *GaInSn usage in the research laboratory*, volume 79. Rev. Sci. Instrum., May 2008.

[10] P. Ahlberg, S. H. Jeong, M. Jiao, Z. Wu, U. Jansson, S. L. Zhang, and Z. B. Zhang. Graphene as a diffusion barrier in galinstan-solid metal contacts. *IEEE*

Transactions on Electron Devices, 61(8):2996–3000, Aug 2014. ISSN 0018-9383. doi: 10.1109/TED.2014.2331893.

[11] T. Someya. *Stretchable Electronics*. Wiley, 2012. ISBN 9783527647002. URL https://books.google.co.uk/books?id=41CkG7tcgvsC.

[12] P. J. Gibson. The Vivaldi aerial. In *9th European Microwave Conference, 1979.*, pages 101–105, 1979. doi: 10.1109/EUMA.1979.332681.

[13] IEEE. IEEE standard definitions of terms for antennas. *IEEE Std 145-1983*, pages 1–31, 1983. doi: 10.1109/IEEESTD.1983.82386.

[14] C. A. Balanis. *Antenna theory: analysis and design*. John Wiley & Sons, 2016.

[15] J.T. Bernhard. *Reconfigurable Antennas*. Synthesis Lectures on Antennas and Propagation Series. Morgan & Claypool Publishers, 2007. ISBN 9781598290264. URL http://books.google.co.uk/books?id=3v-ypGOeUKIC.

[16] Y. Rahmat-Samii, L. I. Williams, and R. G. Yaccarino. The UCLA bi-polar planar-near-field antenna-measurement and diagnostics range. *IEEE Antennas and Propagation Magazine*, 37(6):16–35, Dec 1995. ISSN 1045-9243. doi: 10.1109/74.482029.

[17] S. Saunders and A. Aragón-Zavala. *Antennas and Propagation for Wireless Communication Systems: 2nd Edition*. John Wiley & Sons, 2007. ISBN 9780470848791. URL https://books.google.co.uk/books?id=D1WF5Z1Yz7YC.

[18] C. Drentea. *Modern Communications Receiver Design and Technology*. Artech House intelligence and information operations series. Artech House, 2010. ISBN 9781596933101. URL https://books.google.co.uk/books?id=9juUwbKP-58C.

[19] W.L. Stutzman and G.A. Thiele. *Antenna Theory and Design*. Antenna Theory and Design. Wiley, 2012. ISBN 9780470576649. URL https://books.google.co.uk/books?id=xhZRA1K57wIC.

[20] Griffiths Hugh D. Baker-Chris J. Adamy Dave Stimson, George W. Institution of Engineering and Technology, 2014. ISBN 978-1-61353-022-1.

[21] C.A. Balanis. *Antenna Theory: Analysis and Design*. Wiley, 2012. ISBN 9780471714613. URL http://books.google.co.uk/books?id=whbVW29sbxcC.

[22] Physics-2000. Electromagnetic waves. http://www.colorado.edu/physics/2000/waves_particles/images/fig14.jpg, July 2013.

[23] Thomas A Milligan. *Modern antenna design*. John Wiley & Sons, 2005.

[24] Zhi Ning Chen. *Handbook of Antenna Technologies*. Springer, 2015.

[25] E. Pancera. UWB antennas and channel characteristics. In *2010 IEEE International Conference on Wireless Information Technology and Systems (ICWITS)*, pages 1–1, 2010. doi: 10.1109/ICWITS.2010.5611870.

[26] Guan-Yu Chen, Jwo-Shiun Sun, Sheng-Yi Huang, Guan-Yu Chen, and Cheng-Hung Lin. Characteristics of UWB antenna and wave propagation. In *Proceedings of 2005 International Symposium on Intelligent Signal Processing and Communication Systems, 2005. ISPACS 2005.*, pages 713–716, 2005. doi: 10.1109/ISPACS.2005.1595509.

[27] Liuqing Yang and G.B. Giannakis. Ultra-wideband communications: an idea whose time has come. *IEEE Signal Processing Magazine*, 21(6):26–54, 2004. ISSN 1053-5888. doi: 10.1109/MSP.2004.1359140.

[28] Zhi Ning Chen. UWB antennas: Design and application. In *6th International Conference on Information, Communications Signal Processing, 2007*, pages 1–5, 2007. doi: 10.1109/ICICS.2007.4449887.

[29] A.A. Kishk, Xuan Hui Wu, and K. S. Ryu. UWB antenna for wireless communication and detection applications. In *2012 IEEE International Conference on Ultra-Wideband (ICUWB)*, pages 72–76, 2012. doi: 10.1109/ICUWB.2012.6340457.

[30] Hans Schantz. Ultrawideband antennas. *Artech House, Inc*, 2005.

[31] T. Zwick, W. Wiesbeck, J. Timmermann, and G. Adamiuk. *Ultra-wideband RF System Engineering*. EuMA High Frequency Technologies Series. Cambridge University Press, 2013. ISBN 9781107015555. URL `https://books.google.co.uk/books?id=-UqyAAAAQBAJ`.

[32] W. Wiesbeck, G. Adamiuk, and C. Sturm. Basic properties and design principles of UWB antennas. *Proceedings of the IEEE*, 97(2):372–385, Feb 2009. ISSN 0018-9219. doi: 10.1109/JPROC.2008.2008838.

[33] D. Lamensdorf and L. Susman. Baseband-pulse-antenna techniques. *IEEE Antennas and Propagation Magazine*, 36(1):20–30, Feb 1994. ISSN 1045-9243. doi: 10.1109/74.262629.

[34] Antenna Magus. Antenna magus. the leading antenna design tool, Nov 2014. URL `http://www.antennamagus.com/`.

[35] D. A. Burrell and J.T. Aberle. Characterization of Vivaldi antennas utilizing a microstrip-to-slotline transition. In *Digest Antennas and Propagation Society International Symposium, 1993*, pages 1212–1215 vol.3, 1993. doi: 10.1109/APS.1993.385130.

[36] J. Fisher. Design and performance analysis of a 1-40 GHz ultra-wideband antipodal Vivaldi antenna. In *Proceedings of the German Radar Symposium GRS*, pages 237–241, 2000.

[37] Joon Shin and D. H. Schaubert. A parameter study of stripline-fed Vivaldi notch-antenna arrays. *IEEE Transactions on Antennas and Propagation*, 47(5): 879–886, May 1999. ISSN 0018-926X. doi: 10.1109/8.774151.

[38] Norhayati Hamzah and Kama Azura Othman. Designing Vivaldi antenna with various sizes using CST software. In *Proceedings of the World Congress on Engineering*, volume 2, pages 6–8, 2011.

[39] E.R. Brown. On the gain of a reconfigurable-aperture antenna. *IEEE Transactions on Antennas and Propagation*, 49(10):1357–1362, 2001. ISSN 0018-926X. doi: 10.1109/8.954923.

[40] B.A. Cetiner, Hamid Jafarkhani, Jiang-Yuan Qian, Hui Jae Yoo, A. Grau, and F. De Flaviis. Multifunctional reconfigurable MEMS integrated antennas for adaptive MIMO systems. *IEEE Communications Magazine*, 42(12):62–70, 2004. ISSN 0163-6804. doi: 10.1109/MCOM.2004.1367557.

[41] E. Bruce and A. C. Beck. Experiments with directivity steering for fading reduction. *The Bell System Technical Journal*, 14(2):195–210, April 1935. ISSN 0005-8580. URL `http://bstj.bell-labs.com/BSTJ/images/Vol14/bstj14-2-195.pdf;http://www.alcatel-lucent.com/bstj/vol14-1935/articles/bstj14-2-195.pdf`.

[42] J. Kiriazi, H. Ghali, H. Ragaie, and H. Haddara. Reconfigurable dual-band dipole antenna on silicon using series mems switches. In *IEEE Antennas and Propagation Society International Symposium, 2003.*, volume 1, pages 403–406 vol.1, June 2003. doi: 10.1109/APS.2003.1217482.

[43] Gabriel M Rebeiz. *RF MEMS: theory, design, and technology.* John Wiley & Sons, 2004.

[44] L.N. Pringle, P.H. Harms, S.P. Blalock, G.N. Kiesel, E.J. Kuster, P.G. Friederich, R.J. Prado, J.M. Morris, and G.S. Smith. A reconfigurable aperture

antenna based on switched links between electrically small metallic patches. *IEEE Transactions on Antennas and Propagation*, 52(6):1434–1445, 2004. ISSN 0018-926X. doi: 10.1109/TAP.2004.825648.

[45] Francis H Stites. Solid state transmit/receive switch, June 25 1985. US Patent 4,525,863.

[46] J. M. Kovitz, H. Rajagopalan, and Y. Rahmat-Samii. Practical and cost-effective bias line implementations for reconfigurable antennas. *IEEE Antennas and Wireless Propagation Letters*, 11:1552–1555, 2012. ISSN 1536-1225. doi: 10.1109/LAWP.2012.2234076.

[47] G. H. Huff and J. T. Bernhard. Integration of packaged rf mems switches with radiation pattern reconfigurable square spiral microstrip antennas. *IEEE Transactions on Antennas and Propagation*, 54(2):464–469, Feb 2006. ISSN 0018-926X. doi: 10.1109/TAP.2005.863409.

[48] J. R. De Luis and F. De Flaviis. Frequency agile switched beam antenna array system. *IEEE Transactions on Antennas and Propagation*, 58(10):3196–3204, Oct 2010. ISSN 0018-926X. doi: 10.1109/TAP.2010.2055813.

[49] I. Kim and Y. Rahmat-Samii. Rf mems switchable slot patch antenna integrated with bias network. *IEEE Transactions on Antennas and Propagation*, 59(12): 4811–4815, Dec 2011. ISSN 0018-926X. doi: 10.1109/TAP.2011.2165512.

[50] J.L. Freeman, B.J. Lamberty, and G.S. Andrews. Optoelectronically reconfigurable monopole antenna. *Electronics Letters*, 28(16):1502–1503, 1992. ISSN 0013-5194. doi: 10.1049/el:19920954.

[51] C.J. Panagamuwa, A. Chauraya, and J.C. Vardaxoglou. Frequency and beam reconfigurable antenna using photoconducting switches. *IEEE Transactions on Antennas and Propagation*, 54(2):449–454, 2006. ISSN 0018-926X. doi: 10.1109/TAP.2005.863393.

[52] H. Mirzaei and G. V. Eleftheriades. A wideband metamaterial-inspired compact antenna using embedded non-foster matching. In *2011 IEEE International Symposium on Antennas and Propagation (APSURSI)*, pages 1950–1953, July 2011. doi: 10.1109/APS.2011.5996885.

[53] P. Bhartia and I.J. Bahl. A frequency agile microstrip antenna. In *Antennas and Propagation Society International Symposium, 1982*, volume 20, pages 304–307, 1982. doi: 10.1109/APS.1982.1148900.

[54] J.-C. Langer, J. Zou, C. Liu, and J.T. Bernhard. Micromachined reconfigurable out-of-plane microstrip patch antenna using plastic deformation magnetic actuation. *IEEE Microwave and Wireless Components Letters*, 13(3):120–122, 2003. ISSN 1531-1309. doi: 10.1109/LMWC.2003.810123.

[55] Luyi Liu and R. Langley. Electrically small antenna tuning techniques. In *Antennas Propagation Conference, 2009. LAPC 2009. Loughborough*, pages 313–316, 2009. doi: 10.1109/LAPC.2009.5352518.

[56] O.H. Karabey, S. Bildik, S. Strunck, A. Gaebler, and R. Jakoby. Continuously polarisation reconfigurable antenna element by using liquid crystal based tunable coupled line. *Electronics Letters*, 48(3):141–143, February 2012. ISSN 0013-5194. doi: 10.1049/el.2011.3526.

[57] C.W. Jung, Y.J. Kim, Y.E. Kim, and F. De Flaviis. Macro-micro frequency tuning antenna for reconfigurable wireless communication systems. *Electronics Letters*, 43(4):201–202, 2007. ISSN 0013-5194. doi: 10.1049/el:20073906.

[58] Guoan Wang, T. Polley, A. Hunt, and J. Papapolymerou. A high performance tunable RF MEMS switch using barium strontium titanate (BST) dielectrics for reconfigurable antennas and phased arrays. *IEEE Antennas and Wireless Propagation Letters*, 4:217–220, 2005. ISSN 1536-1225. doi: 10.1109/LAWP.2005.851065.

[59] Fan Yang and Y. Rahmat-Samii. A reconfigurable patch antenna using switchable slots for circular polarization diversity. *IEEE Microwave and Wireless Components Letters*, 12(3):96–98, 2002. ISSN 1531-1309. doi: 10.1109/7260.989863.

[60] P. J. Rainville and F.J. Harackiewicz. Magnetic tuning of a microstrip patch antenna fabricated on a ferrite film. *IEEE Microwave and Guided Wave Letters*, 2(12):483–485, 1992. ISSN 1051-8207. doi: 10.1109/75.173402.

[61] Kin-Fai Tong and Jingjing Huang. New proximity coupled feeding method for reconfigurable circularly polarized microstrip ring antennas. *IEEE Transactions on Antennas and Propagation*, 56(7):1860–1866, 2008. ISSN 0018-926X. doi: 10.1109/TAP.2008.924736.

[62] P.J.B. Clarricoats and H. Zhou. The design and performance of a reconfigurable mesh reflector antenna. In *7th IEEE International Conference on Antennas and Propagation, 1991. ICAP 91*, pages 322–325 vol.1, 1991.

[63] Jung-Chih Chiao, Yiton Fu, Iao Mak Chio, M. DeLisio, and Lih-Yuan Lin. MEMS reconfigurable Vee antenna. In *IEEE MTT-S International Microwave Symposium Digest, 1999*, volume 4, pages 1515–1518 vol.4, 1999. doi: 10.1109/MWSYM.1999.780242.

[64] S. Nikolaou, R. Bairavasubramanian, Cesar Lugo, I. Carrasquillo, D. Thompson, G.E. Ponchak, J. Papapolymerou, and M.M. Tentzeris. Pattern and frequency reconfigurable annular slot antenna using PIN diodes. *IEEE Transactions on Antennas and Propagation*, 54(2):439–448, 2006. ISSN 0018-926X. doi: 10.1109/TAP.2005.863398.

[65] S. Zhang, G.H. Huff, J. Feng, and J.T. Bernhard. A pattern reconfigurable microstrip parasitic array. *IEEE Transactions on Antennas and Propagation*, 52 (10):2773–2776, 2004. ISSN 0018-926X. doi: 10.1109/TAP.2004.834372.

[66] Radant MEMS. SPST RF-MEMS switch, October 2014. URL `http://www.radantmems.com/radantmems.data/Library/Radant-Datasheet101_2.0.pdf`.

[67] Infineon. Silicon PIN diode, July 2014. URL `http://www.mouser.com/ds/2/196/Infineon-BAR88SERIES-DS-v01_01-en-767951.pdf`.

[68] Hittite. HMC550 datasheet, December 2014. URL `http://www.analog.com/media/en/technical-documentation/data-sheets/hmc550.pdf`.

[69] Skyworks. SKY13286, July 2016. URL `http://www.skyworksinc.com/uploads/documents/SKY13286_359LF_200570J.pdf`.

[70] M.R. Hamid, P. Gardner, P.S. Hall, and F. Ghanem. Switched-band Vivaldi antenna. *IEEE Transactions on Antennas and Propagation*, 59(5):1472–1480, May 2011. ISSN 0018-926X. doi: 10.1109/TAP.2011.2122293.

[71] Merrill Skolnik. *Introduction to radar*. Radar Handbook, 1990.

[72] M.R. Hamid, P. Gardner, P.S. Hall, and F. Ghanem. Reconfigurable Vivaldi antenna with tunable stop bands. In *International Workshop on Antenna Technology (iWAT), 2011*, pages 54–57, March 2011. doi: 10.1109/IWAT.2011.5752361.

[73] X. Artiga, J. Perruisseau-Carrier, P. Pardo-Carrera, I. Llamas-Garro, and Z. Brito-Brito. Halved Vivaldi antenna with reconfigurable band rejection. *IEEE Antennas and Wireless Propagation Letters*, 10:56–58, 2011. ISSN 1536-1225. doi: 10.1109/LAWP.2011.2108992.

[74] J.H. Schaffner, D.F. Sievenpiper, R.Y. Loo, J.J. Lee, and S.W. Livingston. A wideband beam switching antenna using RF MEMS switches. In *IEEE Antennas and Propagation Society International Symposium, 2001.*, volume 3, pages 658–661 vol.3, July 2001. doi: 10.1109/APS.2001.960182.

[75] J.H. Schaffner, R.Y. Loo, D.F. Sievenpiper, F.A. Dolezal, G.L. Tangonan, J.S. Colburn, J.J. Lynch, J.J. Lee, S.W. Livingston, R.J. Broas, and M. Wu. Reconfigurable aperture antennas using RF MEMS switches for multi-octave tunability and beam steering. In *IEEE Antennas and Propagation Society International Symposium, 2000.*, volume 1, pages 321–324 vol.1, July 2000. doi: 10.1109/APS.2000.873826.

[76] Ali El-Hajj Lise Safatly, Mohammed Al-Husseini and Karim Y. Kabalan. A reduced-size antipodal Vivaldi antenna with a reconfigurable band notch. *PIERS Proceedings*, pages 220–224, 2012.

[77] M. Bitchikh and F. Ghanem. UWB to 30 narrow sub-bands frequency reconfigurable antipodal Vivaldi antenna. *Electronics Letters*, 52(19):1580–1582, 2016. ISSN 0013-5194. doi: 10.1049/el.2016.2067.

[78] Amit Qusba-Gerard J. Hayes Gianluca Lazzi Michael D. Dickey Ju-Hee So, Jacob Thelen. Reversibly deformable and mechanically tunable fluidic antennas. *Advanced Functional Materials*, 19(22):3632–3637, 2009.

[79] A. Traille and M.M. Tentzeris. Liquid RF antennas, electronics and sensors: A modeling challenge. In *URSI General Assembly and Scientific Symposium, 2011*, pages 1–4, Aug 2011. doi: 10.1109/URSIGASS.2011.6050624.

[80] G.J. Hayes, Ju-Hee So, A. Qusba, M.D. Dickey, and G. Lazzi. Flexible liquid metal alloy (EGaIn) microstrip patch antenna. *IEEE Transactions on Antennas and Propagation*, 60(5):2151–2156, May 2012. ISSN 0018-926X. doi: 10.1109/TAP.2012.2189698.

[81] A. Pourghorban Saghati, J. Batra, J. Kameoka, and K. Entesari. A microfluidically-tuned dual-band slot antenna. In *IEEE Antennas and Propagation Society International Symposium (APSURSI), 2014*, pages 1244–1245, July 2014. doi: 10.1109/APS.2014.6904949.

[82] P. Sen and C. J. C. Kim. Microscale liquid-metal switches - a review. *IEEE Transactions on Industrial Electronics*, 56(4):1314–1330, April 2009. ISSN 0278-0046. doi: 10.1109/TIE.2008.2006954.

[83] A. Pourghorban Saghati, J. Batra, J. Kameoka, and K. Entesari. A microfluidically-switched CPW folded slot antenna. In *IEEE Antennas and Propagation Society International Symposium (APSURSI), 2014*, pages 557–558, July 2014. doi: 10.1109/APS.2014.6904609.

[84] M. Cosker, F. Ferrero, L. Lizzi, R. Staraj, and J. M. Ribero. 3D flexible antenna realization process using liquid metal and additive technology. In *2016 IEEE International Symposium on Antennas and Propagation (APSURSI)*, pages 809–810, June 2016. doi: 10.1109/APS.2016.7696113.

[85] M. COSKER, L. Lizzi, F. Ferrero, R. Staraj, and J. M. RIBERO. Realization of 3D flexible antennas using liquid metal and additive printing technologies. *IEEE Antennas and Wireless Propagation Letters*, PP(99):1–1, 2016. ISSN 1536-1225. doi: 10.1109/LAWP.2016.2615568.

[86] W. Su, R. Bahr, S. A. Nauroze, and M. M. Tentzeris. 3D printed reconfigurable helical antenna based on microfluidics and liquid metal alloy. In *2016 IEEE International Symposium on Antennas and Propagation (APSURSI)*, pages 469–470, June 2016. doi: 10.1109/APS.2016.7695943.

[87] S.J. Kar, A. Chakrabarty, and B.K. Sarkar. Fluid antennas. In *IEEE Middle East Conference on Antennas and Propagation (MECAP), 2010*, pages 1–6, Oct 2010. doi: 10.1109/MECAP.2010.5724209.

[88] Lei Xing, Yi Huang, S.S. Alja'afreh, and S.J. Boyes. A monopole water antenna. In *Antennas and Propagation Conference (LAPC), 2012 Loughborough*, pages 1–4, Nov 2012. doi: 10.1109/LAPC.2012.6402985.

[89] A. A. H. Ameri, G. Kompa, and A. Bangert. Study about tem horn size reduction for ultrawideband radar application. In *2011 German Microwave Conference*, pages 1–4, March 2011.

[90] David M Pozar. *Microwave engineering*. John Wiley & Sons, 2009.

[91] Taconic. Taconic RF-43 datasheet, Sep 2014. URL `https://www.4taconic.com/uploads/ADD%20Technical%20Data%20Sheets/1472069478_Taconic%20RF-41%20RF-43%20RF-45%20Technical%20Data%20Sheet.pdf`.

[92] Taconic. General processing guidelines, Sep 2014. URL `https://www.4taconic.com/uploads/ADD%20Processing%20Information/1448390815_RF%2041%20Processing%20Information.pdf`.

[93] Chittajit Sarkar. Some parametric studies on Vivaldi antenna. *International Journal of u-and e-Service, Science and Technology*, 7(4):323–328, 2014.

[94] Keysight Technologies. E5071C ENA Network Analyzer. `http://literature.cdn.keysight.com/litweb/pdf/5989-5479EN.pdf?id=862560`, July 2016.

[95] J. Bird. *Electrical Principles and Technology for Engineering*. Elsevier Science, 2013. ISBN 9781483293240. URL `https://books.google.co.uk/books?id=KG0vBQAAQBAJ`.

[96] John D Kraus and Ronald J Marhefka. Antenna for all applications. *Upper Saddle River, NJ: McGraw Hill*, 2002.

[97] Dielectric Laboratories. B033ND5S, Jun 2016. URL `http://www.mouser.co.uk/ProductDetail/Dielectric-Laboratories/B033ND5S`.

[98] S. Yang, C. Zhang, H. K. Pan, A. E. Fathy, and V. K. Nair. Frequency-reconfigurable antennas for multiradio wireless platforms. *IEEE Microwave Magazine*, 10(1):66–83, February 2009. ISSN 1527-3342. doi: 10.1109/MMM.2008.930677.

[99] C. Murray and R.R. Franklin. Independently tunable annular slot antenna resonant frequencies using fluids. *IEEE Antennas and Wireless Propagation Letters*, 13:1449–1452, 2014. ISSN 1536-1225. doi: 10.1109/LAWP.2014.2341232.

[100] Michael D Dickey. Emerging Applications of Liquid Metals Featuring Surface Oxides. *ACS Applied Materials & Interfaces*, 6(21):18369–18379, 2014.

[101] A. Petosa, A. Ittipiboon, Y.M.M. Antar, D. Roscoe, and M. Cuhaci. Recent advances in dielectric-resonator antenna technology. *IEEE Antennas and Propagation Magazine*, 40(3):35–48, Jun 1998. ISSN 1045-9243. doi: 10.1109/74.706069.

[102] Ju-Hee So. Controlling the shape and interfacial properties of eutectic gallium indium, 2012. URL `http://search.proquest.com/docview/1513589964?accountid=14511`. Copyright - Copyright ProQuest, UMI Dissertations Publishing 2012; Last updated - 2014-05-28; First page - n/a.

[103] G.P. Junker, A.A. Kishk, and A.W. Glisson. Input impedance of dielectric resonator antennas excited by a coaxial probe. *IEEE Transactions on Antennas*

and Propagation, 42(7):960–966, Jul 1994. ISSN 0018-926X. doi: 10.1109/8.299598.

[104] Mark A. Eddings, Michael A. Johnson, and Bruce K. Gale. Determining the optimal PDMS-PDMS bonding technique for microfluidic devices. *Journal of Micromechanics and Microengineering*, 18(6):067001+, June 2008. ISSN 0960-1317. doi: 10.1088/0960-1317/18/6/067001. URL `http://dx.doi.org/10.1088/0960-1317/18/6/067001`.

[105] A. Traille, Li Yang, A. Rida, and M. M. Tentzeris. A novel liquid antenna for wearable bio-monitoring applications. In *2008 IEEE MTT-S International Microwave Symposium Digest*, pages 923–926, June 2008. doi: 10.1109/MWSYM.2008.4632984.

[106] R.S. Yaduvanshi, H. Parthasarathy, A. De, and R. Gupta. Fluid frame magneto-hydrodynamic antenna. In *International Conference on Communication Systems and Network Technologies (CSNT), 2012*, pages 5–9, May 2012. doi: 10.1109/CSNT.2012.10.

[107] Tactus Technology. A new dimension of touch. `http://tactustechnology.com/wp-content/uploads/2014/08/White-Paper-New-Tagged-PDF.pdf`, October 2012.

[108] C.M. Ciesla. System and methods for raised touch screens, October 1 2013. URL `https://www.google.com/patents/US8547339`. US Patent 8,547,339.

[109] Formlabs. High-resolution 3D printer. `http://formlabs.com/products/form-1-plus/`, February 2015.

[110] D. Kalisz. Stereolithography: speeding time to market. In *WESCON/94. Idea/Microelectronics. Conference Record*, pages 286–290, Sep 1994. doi: 10.1109/WESCON.1994.403586.

[111] Bo Tan Hamsapriya Selvaraj and K Venkatakrishnan. Maskless direct micro-structuring of PDMS by femtosecond laser localized rapid curing. *Journal of Micromechanics and Microengineering*, 21(7):075018+, July 2011. doi: 10.1088/0960-1317/21/7/075018. URL `http://dx.doi.org/10.1088/0960-1317/21/7/075018`.

[112] A. G. Dickson and C. Goyet. *Handbook of methods for the analysis of the various parameters of the carbon dioxide system in sea water*. DOE, 1994.

[113] Agilent. 85070E Dielectric Probe Kit. http://literature.cdn.keysight.com/litweb/pdf/5989-0222EN.pdf?id=364444, July 2016.

[114] Jinqi Wang, Shuchang Liu, Z. Valy Vardeny, and Ajay Nahata. Liquid metal-based plasmonics. *Opt. Express*, 20(3):2346–2353, Jan 2012. doi: 10.1364/OE.20.002346. URL http://www.opticsexpress.org/abstract.cfm?URI=oe-20-3-2346.

[115] L. Xing, Y. Huang, Y. Shen, S. Al Ja'afreh, Q. Xu, and R. Alrawashdeh. Further investigation on water antennas. *IET Microwaves, Antennas Propagation*, 9(8): 735–741, 2015. ISSN 1751-8725. doi: 10.1049/iet-map.2014.0298.

[116] T. Weiland and M. Clemens. Discrete electromagnetism with the finite integration technique. *Progress In Electromagnetics Research*, 32:65–87, 2001.

[117] T. Weiland. Time domain electromagnetic field computation with finite difference methods. *International Journal of Numerical Modelling: Electronic Networks, Devices and Fields*, 9(4):295–319, 1996. ISSN 1099-1204. doi: 10.1002/(SICI)1099-1204(199607)9:4⟨295::AID-JNM240⟩3.0.CO;2-8. URL http://dx.doi.org/10.1002/(SICI)1099-1204(199607)9:4<295::AID-JNM240>3.0.CO;2-8.

[118] Mark A Richards, James A Scheer, and William A Holm. *Principles of modern radar*. Citeseer, 2010.

[119] Thomas Weiland. On the unique numerical solution of Maxwellian eigenvalue problems in three dimensions. *Part. Accel.*, 17(DESY-84-111):227–242, 1984.

[120] S. Chamaani, S. A. Mirtaheri, and M. S. Abrishamian. Improvement of time and frequency domain performance of antipodal Vivaldi antenna using multi-objective particle swarm optimization. *IEEE Transactions on Antennas and Propagation*, 59(5):1738–1742, May 2011. ISSN 0018-926X. doi: 10.1109/TAP.2011.2122290.

[121] D. y. Kim, J. W. Lee, C. S. Cho, and T. K. Lee. Design of a compact tri-band pifa based on independent control of the resonant frequencies. *IEEE Transactions on Antennas and Propagation*, 56(5):1428–1436, May 2008. ISSN 0018-926X. doi: 10.1109/TAP.2008.922667.

Appendix A

Software package

To fulfil the stated aim, a Computational Electromagnetic tool is deemed necessary to perform the analysis of proposed designs. **CST Microwave Studio** is chosen for several reasons. First, a license for this software tool is already available in the Department of Electronic and Electrical Engineering from UCL. Second, this package encompasses a wide range of solvers that can be useful for simulating a wide range of reconfigurable antenna designs. Third, a lot of complementary tools work together with CST, such as Antenna Magus, which can aid and expedite the process of designing new antennas. And finally, CST is the most accurate full-3D EM simulator tool for time analysis antenna design and simulation currently available for designing antennas.

As explained in [116] CST Transient Solver uses the Finite Integration Technique (FIT) to discretise Maxwell's equation in their integral form, based on the technique developed by Weiland in 1977 [117]. The resulting discretised fields in matrix equations are suitable for computers to efficiently simulate real-world electromagnetic field problems with complex geometries.

The first step for the FIT discretisation is to restrict the EM field open-boundary problem to a simply connected and bounded space region that contains the region of interest. The next step is to decompose the computational domain into a locally finite number of cells fitting to each other. Then, the matrix equations can be applied to each cell to solve it.

A.1 Equations

Maxwell's equations describe the electric fields which are produced by charged particles (Gauss's law for electricity) and by time varying magnetic fields (Faraday's law), magnetic fields produced by time varying electric fields but also moving charges produce currents (Ampere's law) [118].

$$\oint_{\delta A} \vec{E} \cdot \vec{ds} = -\int_{A} \frac{\delta \vec{B}}{\delta t} \cdot d\vec{A} \tag{A.1}$$

$$\oint_{\delta \tilde{A}} \vec{H} \cdot \vec{ds} = \int_{A} \left(\frac{\delta \vec{D}}{\delta t} + \vec{J} \right) \cdot d\vec{A} \tag{A.2}$$

$$\oint_{\delta V} \vec{B} \cdot d\vec{A} = 0 \tag{A.3}$$

$$\oint_{\delta V} \vec{D} \cdot d\vec{A} = \int_{V} \rho dV \tag{A.4}$$

Maxwell's Grid Equations (MGE) come from applying the dual interlaced grids $\left\{ G - \tilde{G} \right\}$ to the integral form of Maxwell's equations, presented in equations A.1 A.2 A.3 A.4, where:

$$\begin{cases} \vec{E} & electric\, field\, intensity \\ \vec{H} & magnetic\, field\, intensity \\ \vec{D} & electric\, flux\, density \\ \vec{J} & electric\, current\, density \\ \vec{B} & magnetic\, flux\, density \\ \rho & charge\, density \end{cases} \tag{A.5}$$

The discretisation's algebraic properties enable the development of long-term stable numerical time integration schemes and accurate eigenvalue solvers avoiding spurious modes, considering that basic properties of analytical fields are maintained when moving from R^3 to the grid doublet $\left\{ G - \tilde{G} \right\}$ since the set of matrix equations created by the FIT is a consistent discrete representation of the original field equations.

The FIT is a discretisation technique that transforms the integral form of Maxwell's Grid Equations (equations A.6 A.7 A.8 A.9) onto a dual grid cell complex, resulting in a set of discrete matrix equations as shown in equations A.10 A.11 A.12 A.13 [117].

$$\iint_A -\frac{\delta}{\delta t}\vec{B}\cdot d\vec{A} = \oint_{\delta A}\vec{E}\cdot\vec{dr} \tag{A.6}$$

$$\iint_{\delta V}\vec{B}\cdot d\vec{A} = 0 \tag{A.7}$$

$$\iint_{\tilde{A}}\left(\vec{J}+\frac{\delta}{\delta t}\vec{D}\right)\cdot\vec{d\tilde{A}} = \oint_{\delta\tilde{A}}\vec{H}\cdot\vec{d\tilde{r}} \tag{A.8}$$

$$\int_{\delta\tilde{V}}\vec{D}\cdot\vec{d\tilde{A}} = \iiint_{\tilde{V}}\rho d\tilde{V} \tag{A.9}$$

$$-D_A\dot{b} = CD_s e \tag{A.10}$$

$$SD_A b = 0 \tag{A.11}$$

$$\tilde{D}_A\left(i + D_e\dot{e}\right) = \tilde{C}\tilde{D}_s D_\mu^{-1} b \tag{A.12}$$

$$\tilde{S}\tilde{D}_A D_e e = q \tag{A.13}$$

This set of matrix equations is a one-to-one translation of Maxwell's equations from R^3 to a grid space doublet $\left\{G - \tilde{G}\right\}$. Combining these matrix equations a general real-valued algebraic eigenvalue problem is obtained. Hence, it is possible to find unique solutions [119].

A.2 Validation

Many published papers in journals, such as IEEE Transactions, have reported the use of CST Microwaves Studio and compared their simulation results to their experimental results, getting up to 5 to 10 % variation [120, 121].

As part of this research project a number of CST simulation results have been validated in order to determine reliability of the CST Microwave Studio simulation results. The measured and simulated results were found to be principally coincident, although some variations at certain frequencies were found of a difference up to 2 dB. These discrepancies can be explained by environment unaccounted reflections in the measurements and material inaccuracies because of limitations in characterising materials to be introduced in the software tool.

Appendix B

Relation between antenna design equations and frequency

The relation between antenna design parameters calculated for different frequencies are presented here. The design parameters include: Slot length (L_{slot}) in Figure B.2, Stub length (L_{stub}) in Figure B.3 and Stub position (Pos_{stub}) in Figure B.4, as shown in Figure B.1.

The following equations describe the relation between L_{slot}, L_{stub} and Pos_{stub} across frequency, when frequency is introduced in GHz.

$$L_{slot}\ (f(GHz)) = \frac{0.75}{4 \cdot f} \tag{B.1}$$

$$L_{stub}\ (f(GHz)) = \frac{0.15}{4 \cdot f} \tag{B.2}$$

$$Pos_{stub}\ (f(GHz)) = \frac{0.25}{4 \cdot f} \tag{B.3}$$

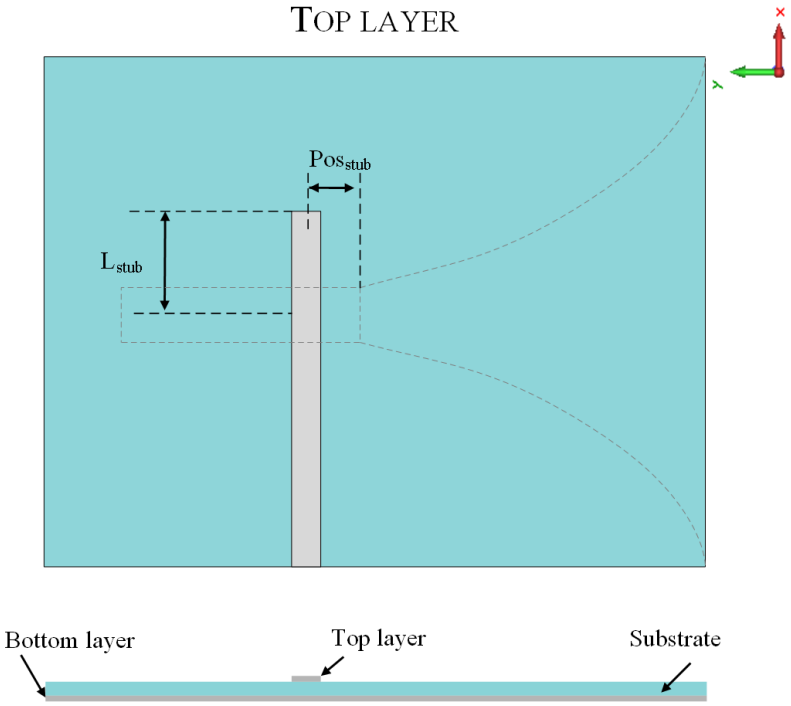

(A) Top view

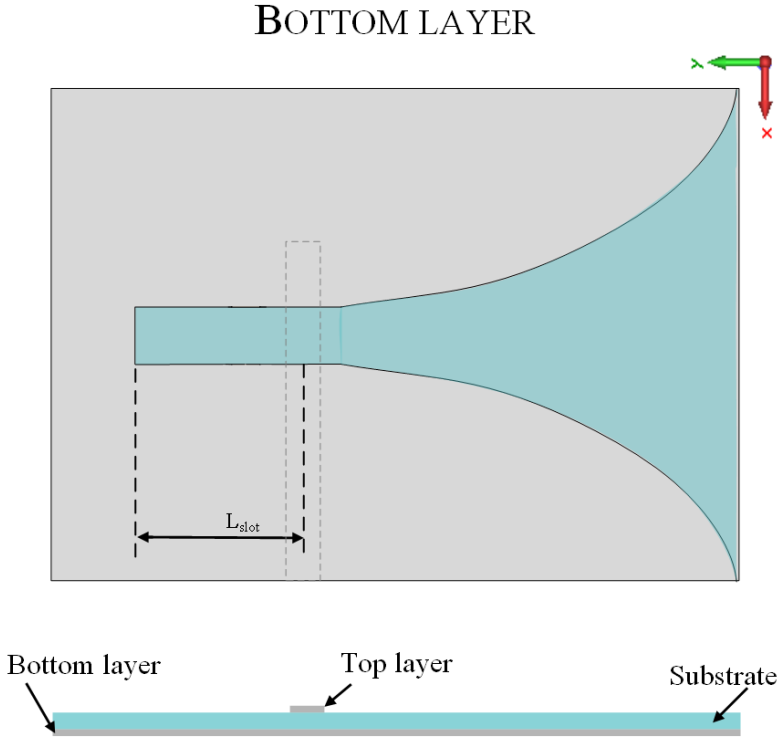

(B) Bottom view

FIGURE B.1: Top and bottom view of the Vivaldi antenna with design parameters.

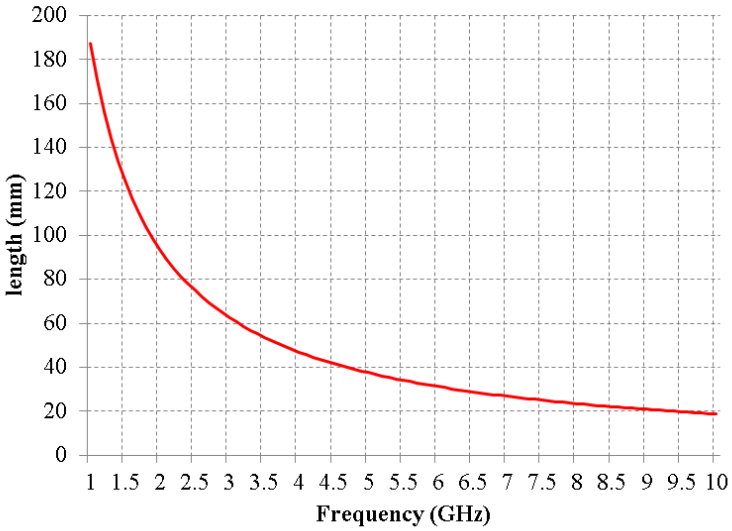

FIGURE B.2: Relation between slot length and frequency described in equation B.1.

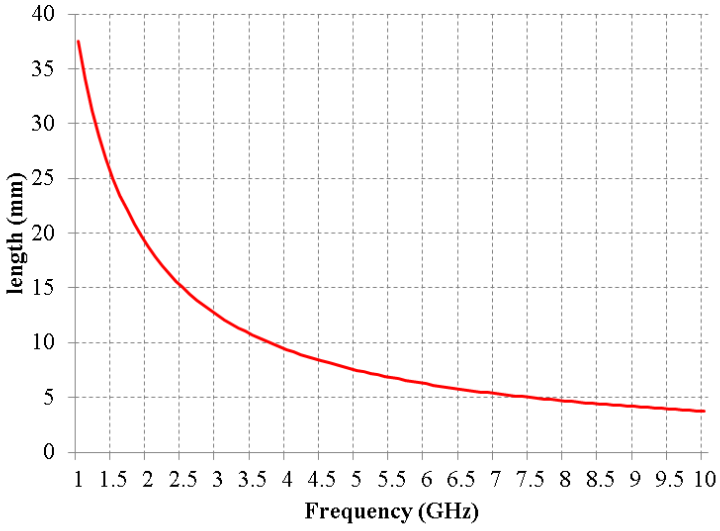

FIGURE B.3: Relation between stub length and frequency described in equation B.2.

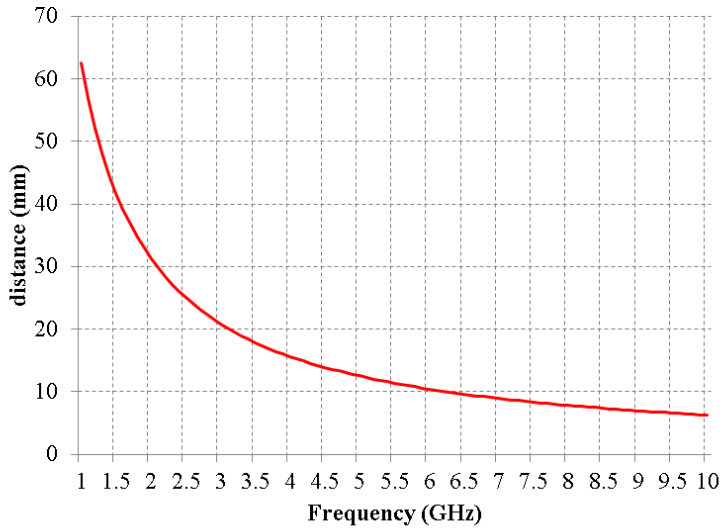

FIGURE B.4: Relation between stub position and frequency described in equation B.3.